DYNAMIC ELASTOGRAPHY WITH FINITE ELEMENT-BASED INVERSION

by

MOHAMMAD HONARVAR

B.Sc., Sharif University of Technology, Tehran, IRAN, 2007
M.Sc., Sharif University of Technology, Tehran, IRAN, 2009

A THESIS SUBMITTED IN PARTIAL FULFILLMENT OF
THE REQUIREMENTS FOR THE DEGREE OF

DOCTOR OF PHILOSOPHY

in

THE FACULTY OF GRADUATE AND POSTDOCTORAL STUDIES

(Mechanical Engineering)

THE UNIVERSITY OF BRITISH COLUMBIA
(Vancouver)

February 2015

Abstract

Tissue stiffness is often correlated to its pathological state and can be used as a basis for initial recognition of many tissue abnormalities. The term elastography refers to the class of medical imaging techniques that non-invasively measure the viscoelastic properties of soft tissue. Elastography involves deforming the tissue using an exciter, measuring the deformations using an imaging technique such as ultrasound (US) or magnetic resonance imaging (MRI), and then calculating the tissue elasticity distribution by solving an inverse problem. The focus of this thesis is on the inverse problem. Specifically, this thesis studies the inverse problem of elastography using direct finite element methods under the condition of applying continuous harmonic excitation to measure the absolute value of the elasticity. First, the "mixed-FEM" inversion technique that solves for both the shear modulus and the pressure is considered. Different regularization techniques are investigated for this method. New sparsity and strain-based regularization techniques, which improve the accuracy, robustness to noise, and speed of the reconstruction, are developed. A comparison of the iterative and direct FEM techniques is performed using simulations. The results show the superiority of the direct method over the iterative method. In order to reduce the number of unknowns, the pressure parameters are removed using the curl operator in a new curl-based direct FEM technique (c-FEM). In this technique, unlike in all previous curl-based methods, the local homogeneity assumption is not used. One of the main observations of this thesis is the importance of the deleterious effect of the tissue homogeneity assumption on the reconstruction results for regions with large variations in the elasticity of the region. A new simplified direct FEM technique without the homogeneity assumption (shear-FEM) is also developed for cases where only partial displacement data is available, such as in US elastography. It is shown that using multi-frequency excitations in both c-FEM and shear-FEM techniques is beneficial by providing multiple measurements of the shear waves and reducing the problem of low-amplitude nodes. To conclude the thesis, the methods developed in this thesis, plus two other established reconstruction algorithms, are compared using simulations, phantoms, ex-vivo and in-vivo data.

Preface

This thesis is based and expanded from several manuscripts, resulting from the collaboration between multiple researchers. The material from the publications has been modified to make the thesis coherent. Ethical approval for conducting this research has been provided by the Clinical Research Ethics Board (CREB), certificate numbers: H09-03163, H08-02696.

A version of Chapter 2 has been published in:

- M. Honarvar, R. Sahebjavaher, S. Salcudean and R. Rohling, "Sparsity regularization in dynamic elastography," Phys. Med. Biol., vol. 57, pp. 5909, 2012.

The contribution of the author was in developing, implementing, evaluating the method and writing the manuscript. Ramin Sahebjavaher, Professor's Salcudean's doctoral student, assisted with MRE data collection. Profs. Rohling and Salcudean assisted with their valuable suggestions and editing the manuscript.

A version of Chapter 5 has been published in:

- M. Honarvar, R. Sahebjavaher, R. Sinkus, R. Rohling and S. Salcudean, "Curl-based finite element reconstruction of the shear modulus without assuming local homogeneity: time harmonic case," IEEE Trans Med Imaging, vol. 32, pp. 2189-2199, 2013.

The contribution of the author was in developing, implementing, evaluating the method and writing the manuscript. Ramin Sahebjavaher assisted with MRE data collection. Prof. Sinkus helped with the development of the MRE acquisition system. Profs. Rohling and Salcudean assisted with their valuable suggestions and editing the manuscript.

A version of Chapter 6 has been submitted as:

- M. Honarvar, J. Lobo, O. Mohareri, S. Salcudean and R. Rohling, "Direct Vibro-Elastography FEM inversion in Cartesian and cylindrical coordinate systems without the local homogeneity assumption," 2014.

The contribution of the author was in developing, implementing, evaluating the method and writing the manuscript. Mr. Lobo, a research engineer working with Profs. Salcudean and Rohling, and Mr. Mohareri, Prof. salcudean's doctoral student, assisted with US data collection from the prostate phantom and the patient. Profs. Rohling and Salcudean assisted with their valuable suggestions and editing the manuscript.

A version of Chapter 3 is ready to be submitted as:

- M. Honarvar, R. Rohling and S. Salcudean, "Strain-based regularization in dynamic elastography," 2015.

The contribution of the author was in developing, implementing, evaluating the method and writing the manuscript. Prof. Salcudean suggested the idea of using quasi-static strain image in regularization. Profs. Rohling and Salcudean assisted with their valuable suggestions and editing the manuscript.

A version of Chapter 4 is ready to be submitted as:

- M. Honarvar, R. Rohling and S. Salcudean, "A comparison of direct and iterative finite element inversion techniques in dynamic vibro-elastography," 2015.

The contribution of the author was in developing, implementing, evaluating the method and writing the manuscript. Prof. Salcudean suggested that this comparison be carried out. Profs. Rohling and Salcudean assisted with their valuable suggestions and editing the manuscript.

A version of Chapter 7 is ready to be submitted as:

- M. Honarvar, R. Sahebjavaher, R. Rohling and S. Salcudean, " A comparison of state-of-the-art inversion techniques in dynamic elastography," 2015.

The contribution of the author was in developing, implementing, evaluating the method and writing the manuscript. The suggestion of this comparison and much of the data was provided from a clinical study carried out by doctoral student Ramin Sahebjavaher under Prof. salcudean's supervision. Profs. Rohling and Salcudean assisted with their valuable suggestions and editing the manuscript.

Table of Contents

List of Tables

List of Figures

Glossary

1D/2D/3D	one/two/three dimensional
AIDE	Algebraic Inversion of Differential Equation
ARFI	Acoustic Radiation Force Impulse
B-mode	Brightness mode
c-DI	curl-based Direct Inversion
c-FEM	curl-based Finite Element Method
CNR	Contrast to Noise Ratio
CT	Computed Tomography
DCT	Discrete Cosine Transform
DI	direct inversion
FEM	Finite Element Method
IVUSe	Intravascular ultrasound elastography
LFE	local frequency estimation
MRE	magnetic resonance elastography
MRI	magnetic resonance imaging
PC	Personal Computer
PDE	Partial Differential Equation
PVC	Polyvinyl Chloride
RMS	Root Mean Square
ROI	region of interest
SA-DCT	Shape Adaptive Discrete Cosine Transform
SMURF	Spatially Modulated Ultrasound Radiation Force

SNR	signal to noise ratio
SSI	Supersonic Shear Imaging
STD	Standard Deviation
SWEI	Shear Wave Elasticity Imaging
TWE	traveling wave expansion
US	Ultrasound

Acknowledgements

I would like to thank Professor Rohling and Professor Salcudean for their valuable supervision and insight into my research during the course of this thesis.

I am also thankful to all the former and current members of the RCL lab at UBC: Ali, Reza, Hani, Sara, Ramin, Jeff, Julio, Omid, Mohammad, Narges, Hamid, Parmida, Guy, Caitlin, Siavash, Saman, Samira, Hussam, Amin, Sabrina, Philip, Julie, Angelica and Corey.

I would like to acknowledge the fellowships and grants that supported my research during the course of my studies: the National Science and Engineering Council of Canada (NSERC), and the UBC FYF Graduate scholarship.

Last but not least, I would like to thank my parents whose unconditional support and love helped me accomplish this and many other milestones throughout my life

Chapter 1 - Introduction

1.1 Motivation

Medical imaging methods for viewing the internal structures of the body are widely used for clinical purposes such as disease diagnosis and monitoring and studying anatomy and physiology. X-ray, ultrasound and MRI are three of the most commonly used medical imaging techniques. In each technique a specific tissue characteristic is used to produce contrast in an image. For example, in X-ray images, the contrast is a function of the X-ray's absorption coefficient for tissue; in MRI images, contrast depends on proton density and the time-constants of the dipoles' spins; and in ultrasound it is a function of acoustic impedance and the scattering properties of the tissue from mechanical pressure waves.

Tissue elasticity is often correlated to its pathological state. For example cancerous tumors are usually stiffer than the surrounding tissue. This makes palpation the basis for initial recognition of many breast, thyroid, prostate and liver abnormalities. But the targets which are small or far from the surface may not be detected by palpation. Moreover, some of these abnormalities are not visible in conventional medical images. This motivates us to develop a new modality of medical imaging measuring the elasticity of the soft tissue and using this for contrast in images, which in turn should lead to better detection of such abnormalities.

The imaging of the viscoelastic properties of tissues is currently gaining significant interest in the medical field. Elasticity, viscosity, density, anisotropy, poroelasticity and nonlinearity are some examples of mechanical properties which describe the deformation and mechanical behaviour of tissue when tissue undergoes a static or dynamic force or displacement excitation. The term elastography refers to the class of medical imaging technique which non-invasively measures the viscoelastic properties of soft tissue.

Several groups have investigated different clinical applications of elastography such as cancer diagnosis in liver [1, 2], breast [3-7], prostate [8, 9], thyroid [10] and diagnosis of brain diseases [11-13], cardiac and vascular diseases [14-16] and musculoskeletal diseases [17, 18].

1.2 Background

A range of elastography techniques have been developed and most of them consist of three main steps: 1- mechanical excitation, 2- motion measurement and 3- inverse problem (Figure 1-1). First, the tissue is deformed by a mechanical exciter. During the deformation, a conventional imaging system such as ultrasound (US) or magnetic resonance imaging (MRI), adopted for motion measurement, is used to find the tissue

deformation map. And finally the deformation or displacement map is used in an inverse problem to find the elasticity map.

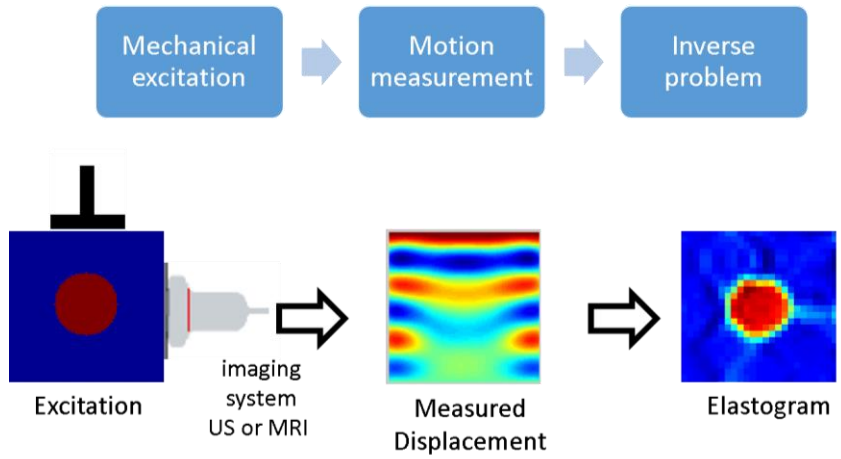

Figure 1-1. Three main steps of most elastography techniques.

The focus of this thesis is on the inverse problem. In order to solve the inverse problem, a mathematical model should be used to simulate the behaviour of the soft tissue. For infinitesimal deformations, it can be assumed that soft tissues exhibit linear elastic behaviour. However, when soft tissues undergo a finite deformation, they display a nonlinear behaviour due to geometry and material nonlinearity [19-23]. In this thesis, we assume the deformations are small and therefore the linear model is used.

1.2.1 Linear elasticity

In this thesis, normal fonts denote scalar parameters while vectors are shown in italic bold and matrices in roman bold. In indicial notation, Einstein summation convention implies that repeated indices are summed over.

Linear elasticity is a mathematical model which describes the behaviour of solid objects and their deformation under loading condition. Infinitesimal strains or "small" deformations and linear relationships between the components of stress and strain are two fundamental assumptions of linear elasticity. When displacements $\boldsymbol{u}$ and gradients of displacements $\nabla\boldsymbol{u}$ are small compared to unity, the non-linear or second order terms of the finite strain tensor can be neglected. In that case the Lagrangian finite strain tensor $\mathbf{E}$ and the Eulerian finite strain tensor $\mathbf{e}$ are approximately the same and can be approximated by infinitesimal strain tensor [24].

$$\mathbf{E} \approx \mathbf{e} \approx \boldsymbol{\varepsilon} = \frac{1}{2}\left((\nabla\boldsymbol{u})^T + \nabla\boldsymbol{u}\right) \quad or \quad \varepsilon_{ij} = \frac{1}{2}\left(u_{i,j} + u_{j,i}\right) \tag{1-1}$$

Having small strains, we can assume linear relation between the components of stress and strain. This behaviour is represented by Hooke's law:

$$\boldsymbol{\sigma} = \mathbf{C}:\boldsymbol{\varepsilon} \quad or \quad \sigma_{ij} = C_{ijkl}\,\varepsilon_{kl} \tag{1-2}$$

where $\boldsymbol{\sigma}$ is the Cauchy stress tensor and C is the fourth-order stiffness tensor. Due to the symmetry of the stress tensor, strain tensor, and stiffness tensor, only 21 elastic coefficients are independent. For isotropic materials this number reduces to two independent parameters and the Hooke's law can be expressed as follows:

$$\boldsymbol{\sigma} = \lambda\, tr(\boldsymbol{\varepsilon})\mathbf{I} + 2\mu\boldsymbol{\varepsilon} \quad or \quad \sigma_{ij} = \lambda\varepsilon_{kk}\delta_{ij} + 2\mu\varepsilon_{ij} \tag{1-3}$$

where λ and μ are the Lamé constants. The shear modulus or μ is the parameter we are interested to find in elastography imaging. μ and λ are related to Young modulus (E) and Poisson ratio (ν) via:

$$\mu = \frac{E}{2(1+\nu)} \quad , \quad \lambda = \frac{\nu E}{(1+\nu)(1-2\nu)} \ . \tag{1-4}$$

For nearly incompressible materials, the Poisson ratio is almost 0.5 ($\nu \approx 0.5$) and therefore the Young modulus is almost three times the shear modulus ($E \approx 3\mu$). Therefore these two parameters are mentioned interchangeably throughout this thesis and the term elasticity is sometimes used in general.

For dynamic deformation, according to Newton's second law, we can derive the equation of motion as follows:

$$\nabla \cdot \boldsymbol{\sigma} = \rho\ddot{\boldsymbol{u}} \quad or \quad \sigma_{ij,j} = \rho\partial_{tt}u_i \tag{1-5}$$

in which ρ is the density of the material. Substituting equation (1-3) into equation (1-5) yields the elastodynamic wave equation:

$$\nabla \cdot [\mu(\nabla\boldsymbol{u} + (\nabla\boldsymbol{u})^T) + \lambda(\nabla \cdot \boldsymbol{u})\mathbf{I}] = \rho\ddot{\boldsymbol{u}} \tag{1-6}$$

For harmonic deformations, the time-independent equations in the frequency domain can be used:

$$\nabla \cdot [\mu(\nabla\boldsymbol{u} + (\nabla\boldsymbol{u})^T) + \lambda(\nabla \cdot \boldsymbol{u})\mathbf{I}] = -\rho\omega^2\boldsymbol{u} \tag{1-7}$$

where ω is the angular frequency of the excitation.

One of the re-occurring concepts addressed in this thesis is "homogeneity". In a homogeneous region, the mechanical properties of the material are constant in space which means ($\lambda_{,i} = \mu_{,i} \approx 0$). In this case, the wave equation can be written as:

$$\mu\nabla^2\boldsymbol{u} + (\mu + \lambda)\nabla(\nabla \cdot \boldsymbol{u}) = -\rho\omega^2\boldsymbol{u} \tag{1-8}$$

Throughout this thesis two types of waves are mentioned repeatedly: shear waves and compressional waves. When a viscoelastic material is excited, these two types of waves are always generated and start propagating inside the material. The shear waves usually travel with a slower speed and therefore have a smaller wavelength, but the compressional waves have a much higher speed and longer wavelength. According to Helmholtz's decomposition theorem, any square-integrable vector field $\boldsymbol{u}$ can be decomposed into curl-free and divergence-free components [25]:

$$\boldsymbol{u} = \nabla\varphi + \nabla \times \boldsymbol{\psi} \tag{1-9}$$

where the curl-free component is the gradient of a scalar potential function (φ) and the divergence-free component is the curl of a vector potential function ($\boldsymbol{\psi}$). We can show that the displacement field $\boldsymbol{u}$ satisfying equation (1-8) can be decomposed according to (1-9). Using the identity $\nabla^2\boldsymbol{u} = \nabla(\nabla \cdot \boldsymbol{u}) - \nabla \times \nabla \times \boldsymbol{u}$, equation (1-8) can be written in the following form

$$-\mu\nabla \times \nabla \times \boldsymbol{u} + (\lambda + 2\mu)\nabla(\nabla \cdot \boldsymbol{u}) = -\rho\omega^2\boldsymbol{u} \tag{1-10}$$

Rearranging this equation results in:

$$\boldsymbol{u} = -\frac{(\lambda + 2\mu)}{\rho\omega^2}\nabla(\nabla \cdot \boldsymbol{u}) + \frac{\mu}{\rho\omega^2}\nabla \times \nabla \times \boldsymbol{u} = \boldsymbol{u}_L + \boldsymbol{u}_T \tag{1-11}$$

Comparing (1-9) with (1-11) we can conclude:

$$\varphi = -\frac{(\lambda + 2\mu)}{\rho\omega^2}\nabla \cdot \boldsymbol{u} \quad , \quad \boldsymbol{\psi} = \frac{\mu}{\rho\omega^2}\nabla \times \boldsymbol{u} \tag{1-12}$$

It can be shown that these potential functions also satisfy the Helmholtz equation:

$$\nabla^2\varphi = -\frac{\omega^2}{c_d^2}\varphi \quad , \quad \nabla^2\boldsymbol{\psi} = -\frac{\omega^2}{c_s^2}\boldsymbol{\psi} \quad , \tag{1-13}$$

where $c_d = \sqrt{\frac{(\lambda+2\mu)}{\rho}}$ is the compressional wave speed and $c_s = \sqrt{\frac{\mu}{\rho}}$ is the shear wave speed. Not only the potential functions φ and $\boldsymbol{\psi}$, but also the displacement fields $\boldsymbol{u}_L$ and $\boldsymbol{u}_T$ satisfy the same Helmholtz equations:

$$\nabla^2 \boldsymbol{u}_L = -\frac{\omega^2}{c_d^2}\boldsymbol{u}_L \quad , \quad \nabla^2 \boldsymbol{u}_T = -\frac{\omega^2}{c_s^2}\boldsymbol{u}_T \, . \tag{1-14}$$

In fact $\boldsymbol{u}_L$ and $\boldsymbol{u}_T$ are the compressional wave and shear wave components that were mentioned earlier.

In nearly incompressible materials, such as soft tissues, λ is orders of magnitude larger than μ. This means the compressional wave speed is much larger than the shear wave speed. Later in this thesis we will discuss this property further.

1.2.2 Viscosity

Viscoelastic materials, such as soft tissue, exhibit a strain rate dependence on time. This causes dissipation of energy in the material undergoing dynamic loading. The viscoelastic behaviour can be modeled using a linear combinations of springs and dashpots [26]. There are different models such as the Maxwell model, Kelvin-Voigt model and Standard linear solid model. Each model uses a different arrangement of springs and dashpots. It has been shown that for many soft tissues, the Kelvin-Voigt model, also called the Voigt model, describes the dynamic behaviour of the material more accurately [27]. The relation between the stress and strain of a simple Voigt model consisting of a spring and dashpot in parallel is as follows:

$$\sigma = E\varepsilon(t) + \eta\dot{\varepsilon}(t) \ , \tag{1-15}$$

where E is the modulus of elasticity and η is the viscosity. In frequency domain equation (1-15) becomes:

$$\sigma = E\ \varepsilon(\omega) + i\eta\omega\ \varepsilon(\omega) = (E + i\eta\omega)\ \varepsilon(\omega) = E^*\ \varepsilon(\omega)\ , \tag{1-16}$$

where $\varepsilon(\omega)$ is the Fourier transform of $\varepsilon(t)$. Therefore, for dynamic cases, the complex modulus E^* can be used in which its real and imaginary components are related to elasticity and viscosity respectively.

For Newtonian materials, viscosity is independent of frequency but for non-Newtonian materials η is also dependent on frequency . Different models can be used to relate the viscosity to frequency. Power law is one of the models often used as follows:

$$\eta = \eta_c \omega^n. \tag{1-17}$$

The Voigt model can also be applied on the wave equation (1-7) by replacing the Lamé parameters λ and μ with the complex Lamé parameters $\lambda^* = (\lambda + i\lambda')$ and $\mu^* = (\mu + i\mu')$ where λ' and μ' are related to compressional and shear viscosities. Throughout this thesis, the complex displacement phasor can be used with the FEM methods developed here and the resulting shear modulus is a complex shear modulus.

In some elastography approaches, the shear modulus and viscosity are calculated from the shear wave speed $c_s = \omega\Delta r/\Delta\phi_s$ and wave attenuation $\alpha_s = \ln(A_1/A_2)/\Delta r$. These values can be related to the shear modulus and viscosity using equation (1-14). Based on this equation the complex shearwave number k_s equals:

$$k_s = \sqrt{\frac{\rho\omega^2}{\mu^*}}. \tag{1-18}$$

By substituting μ^* into (1-18) and considering the fact that $c_s = \omega/\mathrm{Re}(k_s)$ and $\alpha_s = \mathrm{Im}(k_s)$ the following equations can be obtained for the shearwave speed and attenuation:

$$c_s = \sqrt{2\left(\frac{\mu^2 + \omega^2\eta^2}{\rho\left(\mu + \sqrt{\mu^2 + \omega^2\eta^2}\right)}\right)} \quad , \alpha_s = \sqrt{\frac{\rho\omega^2\sqrt{\mu^2 + \omega^2\eta^2} - \mu}{2(\mu^2 + \omega^2\eta^2)}} \tag{1-19}$$

Therefore, using these equations, one can find the shear modulus and shear viscosity from the shear wave speed and wave attenuation.

1.2.3 Elastography techniques

Most of the previous elastography techniques developed to date can be categorized based on the methods used in each of the three main steps shown in Figure 1-1. Table 1-1 shows a summary of some of previous studies categorized accordingly.

1.2.3.1 Mechanical excitation

The mechanical excitation can be either internal or external. For example respiratory motion or heart beat can used as a source of internal excitation [28-30]. Acoustic radiation force is another example of internal excitation [31-35]. If the deformation is caused by a force applied on the surface of the tissue, for example using a voice coil or hand motion, it is considered as an external excitation [36-39]. The mechanical excitation can also be categorized based on its frequency content. It can be static [40-45], harmonic [36, 37, 39, 46-50] or transient [33, 51-54]. Other mechanical excitations are possible and sometimes used e.g. broadband, multi-frequency, chirp.

Table 1-1. Summary of the different elastography techniques

<table>
<tr><td rowspan="4">Excitation</td><td colspan="3">Internal</td><td colspan="3">External</td></tr>
<tr><td colspan="3">[30], [29], [28], [35], [34], [33], [32], [31]</td><td colspan="3">[39], [38], [36], [37]</td></tr>
<tr><td colspan="2">Static</td><td colspan="2">Harmonic</td><td colspan="2">Transient</td></tr>
<tr><td colspan="2">[45], [44], [43], [42], [41], [40]</td><td colspan="2">[50], [49], [48], [39], [47], [46], [37], [36]</td><td colspan="2">[33], [54], [53], [52], [51]</td></tr>
<tr><td rowspan="2">Motion Measurement</td><td>US</td><td>MRI</td><td>Optical</td><td>Acoustic</td><td>X-Ray</td></tr>
<tr><td>[45] , [52], [55], [56], [57]</td><td>[38], [58], [47], [59], [37], [36]</td><td>[60], [61], [62]</td><td>[63], [31], [64], [65]</td><td>[66]</td></tr>
<tr><td rowspan="3">Inverse problem</td><td colspan="2">Static</td><td colspan="2">Harmonic</td><td>Transient</td></tr>
<tr><td>Direct</td><td>Iterative</td><td>Direct</td><td>Iterative</td><td>Direct</td></tr>
<tr><td>[45], [44], [67], [68], [69], [70], [71], [40], [72], [41], [73], [74], [75]</td><td>[42], [43], [76], [77], [78], [79], [62], [80], [21]</td><td>[81], [82], [83], [50], [84], [85], [86], [83], [87], [88], [89], [90],: [46], [91], [47], [92], [93], [3], [94], [95], [49], [96]</td><td>[97], [98], [48], [39]</td><td>[35], [55], [34], [33], [32], [99], [100], [54], [101], [102], [53], [52], [51]</td></tr>
</table>

1.2.3.2 Motion measurement

Different imaging modalities have been adopted for measuring the motion. The most common ones are US [45, 52, 55-57] and MRI [36-38, 47, 58, 59]. If the MRI imaging is used for motion measurement, in literature it is called MR Elastography (MRE). Optical coherence imaging [60-62], CT and X-ray imaging [66] have also been used for motion or strain imaging but are not as popular as US and MRI.

The displacements measured using MRI are the most accurate and complete set of data. MRI can measure all three components of displacement in a 3D volume while US can only measure one component of displacement accurately which is called the axial component as is along with the ultrasound beam. This measurement can be done on a 2D plane or a 3D volume depending on the type of the ultrasound transducer used. The lateral component of displacement can also be measured using different ultrasound techniques such as beam steering, 2D motion tracking or using multiple probes from different angles, but the accuracy of that is one order of magnitude less than the axial displacement measurement. Although US has those limitations compared to MRI, it is more easily available, cheaper and faster than MRI.

1.2.3.3 Inverse problem

The measured displacement data should be further processed to find an image representing the distribution of the mechanical properties of the tissue. Different inversion techniques have been suggested to find the mechanical properties, mostly the elasticity, depending on the type of the excitation and the displacement data available.

(a) Static:

Strain imaging is one of the first and simplest methods used in elastography [45]. It was first developed as an ultrasound imaging technique and later extended to MR imaging as well [69, 103]. Strain imaging and its clinical applications have been well established in the literature [45, 104, 105]. In this technique, an external or internal source is used to deform the tissue and create strain within it. Assuming a constant uniaxial stress, the relative Young's modulus of the tissue can be estimated from the reciprocal of the measured strain based on Hooke's law. But the assumption of constant stress field in the medium is not truly achievable due to tissue heterogeneity and stress concentration. Therefore, the resulting artifacts can affect the diagnostic performance of the images. Some researchers have tried to compensate for these effects by estimating the stress distribution within the region [68, 106-108] but they can only compensate for the hardening artifact as a function of compressor size and shape and still the stress concentration near the inclusion boundaries cannot be reliably predicted. However, strain imaging can provide reasonable relative images of stiffness for cases where the exact value of the shear modulus is not essential.

In order to correct for the boundary conditions and heterogeneity artifacts in strain imaging, an elasticity inverse problem needs to be solved. However, these techniques usually decrease the spatial resolution of the image [109]. Based on the equilibrium equation, having the displacement distribution, one can solve for the shear modulus. In the static case, if the force boundary conditions are known, the absolute values of the shear modulus can be found but usually the forces are difficult to measure therefore only the relative values of the shear modulus can be calculated.

The methods used for solving the inverse problem are either direct or iterative. A few examples will be described. Raghavan and Yagle [73] proposed a direct method in which the equilibrium equation for the 2D plane strain case is discretized using finite difference and rearranged into a linear system of equations with the elasticity and pressure parameters as the unknowns. The problem with this method is that the pressure boundary condition needs to be known which is not possible to measure for internal boundaries, and also, since the strains are calculated using finite difference, the method is sensitive to noise. However as mentioned before, if the pressure or force boundary condition are not available, the relative shear modulus can be obtained. Bishop *et al* [74] proposed a similar method to find the relative shear modulus by eliminating the pressure unknowns using matrix partitioning. It was shown that this method is still sensitive to noise and ill-conditioned, so Tikhonov regularization was used to constrain the solution. Some researchers have used the

finite element method (FEM) instead of finite differences to discretize the equilibrium equation and solved it directly for the shear modulus in a similar manner. Halliwell *et al* [40] introduced a direct FEM method for finding the relative shear modulus by assigning the value of one to the shear modulus of the elements on one edge. They formulated the mixed displacement-pressure (u-p) FEM for the forward problem and rearranged the resulting system of equations with respect to the shear modulus and pressure unknowns. Then they eliminated the pressure unknowns using the equations between the displacements and pressure. In fact they replaced the pressure with $\lambda(\nabla.u)$. But the problem with this approach is that, for nearly incompressible materials, the divergence of the displacement cannot be calculated accurately from the noisy displacement data. There are other similar approaches [72], [41] using a direct method with pure displacement FEM in which the divergence of the displacement has to be calculated.

The other group of methods consider the inverse problem as an optimization problem in which the shear modulus is changed iteratively to minimize the error between measured displacement and the simulated displacement assuming the current elasticity distribution. This optimization problem may be solved using one of a large number of optimization algorithms such as the Gauss-Newton method [42, 43, 62, 79], gradient-based algorithms [21, 77, 78] or non-gradient approaches [76, 110]. Some algorithms such as Gauss-Newton require the value of the functional, the gradient and the Hessian matrix, but some other algorithms require only the value of the functional and the gradient. Those methods which use the Hessian have a higher convergence rate than algorithms which use the gradient only. But, on the other hand, the computational cost in each iteration of Hessian-based methods is higher than gradient-based methods. In gradient-based methods the adjoint method can be used to compute the gradient efficiently [77]. The uniqueness of the inverse problem solution was investigated for both iterative and direct differential methods [111]. It was shown that in addition to the strain measurement, either the stress distribution or the elastic stiffness must be measured along a sufficient portion of the boundary in order to have a unique solution.

(b) Harmonic:

When the excitation is not static, the acceleration term or the inertial force on the right hand side of equation (1-6) is not zero and this equation can be used to find the absolute modulus without having to measure the forces on the boundaries as required in static techniques. Like quasi-static elastography, harmonic elastography was first implemented with ultrasound imaging and later extended to magnetic resonance imaging. Harmonic excitation was first used in a method called sonoelastography [50, 85]. Basically an external vibration at low frequencies (10-1000 Hz) was used to induce oscillations within soft tissues, and the motion was detected by Doppler ultrasound. The results from this method were only qualitative and were displayed in a format resembling conventional Doppler color flow mapping. The concept is that stiff tissues will respond differently to an applied mechanical vibration than normal tissues. Later on, more advanced methods were developed for estimating quantitative values of the shear modulus. To obtain the full inversion

of the wave equation, one needs all components of the displacement field in a 3D volume, which are not readily available in all cases such as ultrasound elastography. Therefore, the problem is simplified in some approaches by assuming that the gradients of the pressure and shear modulus are negligible. This results in an independent Helmholtz equation for each component of the displacement. In this way, measuring just one displacement component is sufficient to solve for the shear modulus. For example, the Local Frequency Estimator (LFE) [81, 82] uses these assumptions. This technique is based on estimating the local spatial frequency of shear waves using filter banks. The local spatial frequency is related to the shear modulus according to the Helmholtz equation (1-14). The same technique has been used in Crawling Wave Imaging [83]. In this technique, two opposing shear vibration sources vibrate at slightly different frequencies ω and $\omega + \Delta\omega$, respectively. The resulting interference patterns measured by ultrasound move at an apparent velocity of $v_m = \frac{\Delta\omega}{\omega} v_s$, where v_s is the shear wave speed. Therefore the apparent wavelength can be measured using LFE and converted to actual shear wavelength using the ratio $\frac{\Delta\omega}{\omega}$. McAleavey *et al* [89] proposed a method called spatially modulated ultrasound radiation force (SMURF) in which instead of applying an excitation of known temporal frequency, they use spatially modulated radiation force to generate a shear wave of known spatial frequency (wavelength) and measure the temporal frequency of the propagating shear wave to determine the shear modulus of the material. There are other methods which use the wave equation more directly to find the elasticity. For example Oliphant *et al* [46] proposed the algebraic inversion of differential equation (AIDE) in which they solve the Helmholtz equation locally by estimating local derivatives of displacement using a least squares polynomial fit or finite window filters [91]. There are other methods which use the complete form of the wave equation instead of the simplified Helmholtz equation. Such methods require a complete set of displacement data which is available in MRE. For example Sinkus *et al* [47] used a linear system of PDE derived from the full wave equation to find the entire symmetric elasticity tensor at each point. In another work, Romano *et al* [94] used a variational form of the wave equation to solve for both μ and λ locally at each point. The mentioned methods using the full wave equation require the calculation of the displacement divergence. As mentioned before, since soft tissue is nearly incompressible, this value is small and cannot be calculated accurately from the noisy displacement data. Sinkus *et al* [93] suggested using the curl operator to eliminate the divergence term and solve the resulting Helmholtz equation of the curl of displacement using their direct method. However, taking the curl of the equation results in third order derivatives of the displacement, which is also challenging with noisy data. FEM has also been used with harmonic data. Park and Maniatty [49] described a direct mixed-FEM technique in which both the shear modulus and pressure parameters are found from the displacement data. Eskandari et al [96] used a similar method but with a standard pure displacement formulation of FEM and with only the shear modulus as unknown. Similar to its static counterpart, the inverse problem can also be solved using iterative methods for the harmonic case [39, 48, 97, 98].

(c) Transient:

By using an ultrafast ultrasound scanner, it is possible to capture high frame rate data which enables real time imaging of transient shear wave generated in the body. One way to generate the transient shear wave is to use the acoustic radiation force (ARF). For example, in a method called acoustic radiation force imaging (ARFI) [35, 55], the radiation force is applied at each point and the relative stiffness is estimated from the inverse of the magnitude of the displacement at that point. Similarly, in shearwave elasticity imaging (SWEI) [33], acoustic radiation force is used to generate a transient shearwave and the elasticity is calculated by measuring either the speed of the wave front or the required time for the displacement to reach a maximum at the focal point. In another work, Sandrin *et al* [53] used an external electromagnetic vibrator attached to the sides of a linear ultrasound probe to induce a symmetric shearwave in the image plane and a high frame rate ultrasound system (1000 frames/s) was used to measure the displacement. The excitation used was one or two cycles of a sinusoid (typically 50 Hz) and the shear modulus was computed as the mean of the ratio between the temporal and spatial second order derivatives using a simplified 2D Helmholtz equation (1-20).

$$\mu(x,z) = \rho \frac{1}{N} \sum_{n=1}^{N} \frac{\left(\frac{\partial^2 u_z}{\partial t^2}\right)_{x,z}}{\left(\frac{\partial^2 u_z}{\partial x^2} + \frac{\partial^2 u_z}{\partial z^2}\right)_{t=nT}} \tag{1-20}$$

Bercoff *et al* [52] use a similar approach but they shake the ultrasound probe to generate the wave and use the same equation (1-20) but in frequency domain by taking the Fourier transform of the displacements (1-21).

$$\mu(x,z) = \frac{\rho}{\Delta\omega} \int \frac{\left| FT\left\{\frac{\partial^2}{\partial t^2} u_z(x,z,t)\right\}\right|}{\left| FT\left\{\frac{\partial^2}{\partial x^2} u_z(x,z,t) + \frac{\partial^2}{\partial z^2} u_z(x,z,t)\right\}\right|} d\omega \tag{1-21}$$

Bercoff *et al* [32] also developed a new way of generating plane shear waves called supersonic shear wave imaging (SSI). The idea of SSI is to create a shear source moving through the medium at a supersonic speed. This shear source, which moves faster than the shear waves it induces, is created by successively focusing the ultrasonic “pushing” beam at different depths. All resulting shear waves interfere constructively along a Mach cone creating two plane and intense shear waves propagating in opposite directions. An ultrafast scanner is used to both generate this supersonic source and image (5000 frames/s) the propagation of the resulting shear waves. They use the same equation (1-21) to find the shear modulus. The shear modulus has also been estimated using the shear wave arrival time and the Eikonal equation which relates the spatial gradient of the arrival time to the shear modulus [51, 101, 102].

The time reversal method [54, 99, 100] is another technique used in transient elastography. The idea is that if the displacement response of a pulse excitation is measured at any point p, and the time reversed of that

response signal with the length of T is reapplied at the point of excitation, the measured displacement at that point would have a peak at time T. If the responses of adjacent points at time T are plotted in space, according to the Rayleigh criterion, there would be a peak at point p and the focal spot width is directly related to the shear wavelength and therefore the elasticity at that point.

In summary, elastography is an important ongoing field of research, and numerous research groups are concurrently attempting to discover and develop better imaging techniques to capture the mechanical properties of living tissue, although these methods have yet to be improved and reach widespread acceptance among clinical practitioners. Although simple strain imaging or relative elasticity imaging can be useful in detection of some abnormalities, determining the different stages of a disease or monitoring progress of a treatment would benefit from knowledge of the *absolute* value of the tissue elasticity. Among the methods measuring the absolute elasticity, those using harmonic excitation are popular due to the relatively simple system required to measure the harmonic motions compared to the transient motions. Therefore, in this thesis we study the inverse problem of elastography under the condition of applying continuous harmonic excitation and then analysing the measured displacements in the phasor domain.

1.3 Thesis objectives

The objective of this work is to develop novel techniques to quantitatively and accurately measure the absolute value of the shear modulus of soft tissue using both US and MRE systems. To achieve this goal, the specific objectives of this thesis are as follows:

1. Improve the existing FEM-based inversion techniques to find a robust and efficient method for accurately measuring the absolute shear modulus of tissue and tissue mimicking material samples using full displacement phasors which can be obtained from MRE techniques.
2. Find appropriate regularization techniques for the ill-posed inverse problem of elasticity and incorporating prior knowledge from quasi-static strain images in shear modulus reconstruction.
3. Develop a FEM-based inversion technique to be used with partial displacement data from US motion measurement system.
4. Extend the proposed FEM inversion technique to cylindrical coordinate systems used for volumetric US data captured on a cylindrical mesh.
5. Study the performance of these techniques using both simulation and experimental data and comparing them with other state of the art techniques.
6. Construct more complex tissue-mimicking phantoms for validation purposes.

1.4 Thesis outline

Chapter 2 describes a new sparsity regularization technique combined with the direct mixed-FEM inversion technique for solving the inverse problem of elasticity. The method is tested on simulation and experiment data and the results are compared with the most common regularization technique, Tikhonov regularization.

In Chapter 3 the potential use of quasi-static strain images as a prior knowledge of the shear modulus distribution is investigated for regularizing the inverse problem. Simulations are used to test three different ways of using strain images for constraining the unknown parameters. In two of the methods, the strain image is used to segment the region and then either hard or soft constraints are applied on the parameters of each segment. In the third method, the sparsity pattern used in sparsity regularization is selected based on the strain image.

In Chapter 4 the two forms of direct and iterative FEM inversion techniques commonly used in dynamic elastography are compared using simulations. The performance and spatial resolution of the methods are investigated for different excitation frequencies and inclusion sizes and contrasts.

Chapter 5 describes a new curl-based FEM inversion technique in which the curl operator is used to remove the pressure term without using the homogeneity assumption. The method is validated using simulations and phantom studies and the results are compared with the method that does use the homogeneity assumption.

In Chapter 6 a direct FEM method is developed to be used with partial displacement data. In order to be able to use partial data, the coupling terms in the wave equation are ignored but still the local homogeneity assumption is avoided. This method is also extended to cylindrical coordinate systems typical of US volumetric displacement data captured on a cylindrical mesh. The method is tested on simulation, phantom and in-vivo patient data.

Chapter 7 compares all the three FEM-based inversion techniques developed in previous chapters with two other commonly used inversion techniques, LFE and c-DI. These methods are compared using simulations, phantoms and ex-vivo and in-vivo data.

Chapter 2 - Sparsity regularization in dynamic elastography

2.1 Introduction

As summarized in previous chapter, elasticity imaging, or elastography, is an emerging technique in medical imaging [45]. The goal is to accurately depict the differences in elastic modulus of tissues in order to distinguish them based on tissue composition and pathology.

In dynamic elastography, having inertial forces inside the tissue enables the calculation of the absolute values of shear modulus. Having the displacement measurements, the elasto-dynamic wave equation is used to solve the inverse problem. To obtain the full inversion of the wave equation, one needs all components of the displacement field in a 3D volume, which are not readily available in all cases such as ultrasound elastography. Therefore, the problem is simplified in those cases [82, 112], by assuming local homogeneity and neglecting the pressure term. Park and Maniatty [49] showed that neglecting the pressure gradient term in heterogeneous media introduces inaccuracy in the modulus estimates.

The finite element method (FEM) is one of the most commonly used method for solving the inverse problem. The FEM can be solved directly [41, 49] or iteratively [39, 77] in both dynamic and quasi-static elastography to obtain the shear modulus distribution. With the FEM, the equation of motion can be used without any simplification, which means that the gradients of pressure or shear modulus are not assumed to be negligible. However, for nearly incompressible materials with Poisson's ratio of close to 0.5, using a low-order FEM with a standard displacement-based formulation is prone to the so-called 'locking' problem which results in poor convergence and instability [113]. The typical solution to this problem is to use a mixed formulation of FEM. In [49], a mixed finite element based direct inversion method has been used to solve the inverse problem for linear, isotropic, elastic materials. This method is fast since it solves for the shear modulus directly, without any iterations. Furthermore, with this method there is no need to know the boundary conditions. However, a mixed FEM inversion technique solves for both pressure and shear modulus distributions so it has more unknowns than a standard formulation. This makes the inverse problem more ill-conditioned, and therefore it is necessary to utilize regularization techniques when solving for the unknowns

The most common regularization method is Tikhonov regularization [114]. In this method, the low-order spatial derivatives of the solution are penalized which results in smooth solutions. This reduces the resolution and structural detail of the reconstruction. Tikhonov regularization confines the variation of the reconstructed values, and this usually results in underestimation of the parameters. In the geophysics literature, an alternative approach to regularization was developed that uses a sparse representation of the original variables [115]. In this method the original variables are transformed into another set of variables using an appropriate transformation which results in sparse representation of the original variables. The goal is to use a small subset of new variables to provide a good approximation of the original field. This technique is generally used in image compression [116]. Applying this transformation on the problem's variables and then using truncating approximation on the new variables results in a new inverse problem with fewer unknowns and improved conditioning. This technique could be helpful in cases where the number of measurement points is limited, such as the problem of assessing subsurface structures from limited surface measurements. Jafarpour and colleagues [115] used sparsity regularization in solving the subsurface inverse problem. They used a discrete cosine transform (DCT) as the sparsifying transform and solved the inverse problem using an iterative method to minimize the sum of an l_2-norm measurement misfit term and an l_1-norm regularization term.

The goal of this chapter and the next chapter is to find a more efficient way of regularizing the parameters in the inverse problem of elasticity to achieve more accurate results with higher robustness to noise and possibly faster performance. In this chapter, for the first time, we use the direct mixed FEM technique with DCT-based sparsity regularization. In the next chapter, we will investigate the use of quasi-static strain images as prior knowledge of elasticity for the purpose of regularization. In this chapter the results are compared with traditional Tikhonov regularization. The rest of this chapter is organized as follows. In Section 2.2 the theory of mixed finite elements and inverse problems are described. Then sparsity regularization is introduced and discussed in Section 2.3. Simulation results are presented in Section 2.4 and Section 2.5 concludes the chapter.

2.2 Finite element formulation

The governing equation of motion for linear, isotropic, elastic materials with a time harmonic excitation is as follows:

$$\nabla \cdot [\mu(\nabla \boldsymbol{u} + (\nabla \boldsymbol{u})^T) + \lambda(\nabla \cdot \boldsymbol{u})\mathbf{I}] = -\rho\omega^2 \boldsymbol{u} \qquad in\ \Omega \tag{2-1}$$

$$\boldsymbol{u} = \hat{\boldsymbol{u}} \qquad on\ \Gamma_1 \tag{2-2}$$

$$[\mu(\nabla \boldsymbol{u} + (\nabla \boldsymbol{u})^T) + \lambda(\nabla \cdot \boldsymbol{u})\mathbf{I}] \cdot \boldsymbol{n} = \widehat{\boldsymbol{T}} \qquad on\ \Gamma_2 \tag{2-3}$$

where Ω is the region of interest in which the boundary is $\Gamma = \Gamma_1 \cup \Gamma_2$ and the displacement field $\boldsymbol{u}(x)$ is measured as a function of position ($x \in \Omega$). $\boldsymbol{n}$ is the unit normal vector on Γ. μ and λ are Lamé parameters and the vector $\widehat{\boldsymbol{T}}$ is a traction vector on a part of boundary denoted by Γ_2, and $\widehat{\boldsymbol{u}}$ is the prescribed displacement vector on a part of boundary denoted by Γ_1. In another words, Γ_1 is related to the displacement boundary condition, and Γ_2 is related to the force boundary condition.

Lamé parameters μ and λ are related to Young modulus (E) and Poisson ratio (ν) via:

$$\mu = \frac{E}{2(1+\nu)} \quad , \quad \lambda = \frac{\nu E}{(1+\nu)(1-2\nu)} \ . \tag{2-4}$$

For nearly incompressible materials, the limit $\lambda \to \infty, \nu \to 0.5$ implies that $\nabla \cdot \boldsymbol{u} \to 0$. This effect causes the locking problem in the FEM forward problem. This also causes a similar problem in solving the inverse problem. Since the divergence of the displacement is close to zero, this term cannot be calculated directly from the noisy displacement data. In order to overcome this problem, a mixed formulation of the FEM is used in which pressure is introduced as a new variable:

$$p = \lambda\,(\nabla \cdot \boldsymbol{u})\ . \tag{2-5}$$

This variable is determined independently of the displacement. Substituting (2-5) into both (2-1) and (2-3) gives

$$\nabla \cdot [\mu(\nabla \boldsymbol{u} + (\nabla \boldsymbol{u})^T) + p\mathbf{I}] = -\rho\omega^2 \boldsymbol{u} \qquad in\ \ \Omega \tag{2-6}$$

$$\boldsymbol{u} = \widehat{\boldsymbol{u}} \qquad on\ \Gamma_1 \tag{2-7}$$

$$[\mu(\nabla \boldsymbol{u} + (\nabla \boldsymbol{u})^T) + p\mathbf{I}] \cdot \boldsymbol{n} = \widehat{\boldsymbol{T}}\ . \qquad on\ \Gamma_2 \tag{2-8}$$

The following formulation follows the direct inversion approach suggested by Park and Maniatty [49]. To solve (2-6) numerically, it should be discretized, which can be done using the FEM. According to Galerkin's method, equations (2-6)-(2-8) are written in a weak formulation or integral form, which involves multiplying (2-6) with a test function $\boldsymbol{w} \in \mathbb{R}^3$ and integrating over the entire domain. If $\{\boldsymbol{u}(x), p(x)\}$ is a solution of the boundary value problem (2-6)-(2-8), then for any smooth function $\boldsymbol{w}$ that is zero on Γ_1 we have:

$$\int_{\Omega} \nabla \cdot [\mu(\nabla \boldsymbol{u} + (\nabla \boldsymbol{u})^T)] \cdot \boldsymbol{w}\, d\Omega + \int_{\Omega} \nabla p \cdot \boldsymbol{w}\, d\Omega = -\rho\omega^2 \int_{\Omega} \boldsymbol{u} \cdot \boldsymbol{w}\, d\Omega \tag{2-9}$$

Conversely, if $\{\boldsymbol{u}(x), p(x)\}$ satisfies (2-9) for every smooth function $\boldsymbol{w}$, then one may show that this solution will solve (2-6). After performing integration by parts, which reduces one order of the derivatives of the displacement, we obtain:

$$\begin{aligned} -\int_{\Omega} [\mu(\nabla \boldsymbol{u} + (\nabla \boldsymbol{u})^T)] : \nabla \boldsymbol{w}\, d\Omega - \int_{\Omega} p\, \nabla \cdot \boldsymbol{w}\, d\Omega \\ + \int_{\Gamma_2} [\mu(\nabla \boldsymbol{u} + (\nabla \boldsymbol{u})^T) + p\mathbf{I}] \cdot \boldsymbol{n} \cdot \boldsymbol{w}\, d\Gamma = -\rho\omega^2 \int_{\Omega} \boldsymbol{u} \cdot \boldsymbol{w}\, d\Omega \end{aligned} \tag{2-10}$$

By substituting the traction boundary condition (2-8) into (2-10) we have:

$$\int_{\Omega} [\mu(\nabla \boldsymbol{u} + (\nabla \boldsymbol{u})^T)] : \nabla \boldsymbol{w}\, d\Omega + \int_{\Omega} p\, \nabla \cdot \boldsymbol{w}\, d\Omega = \rho\omega^2 \int_{\Omega} \boldsymbol{u} \cdot \boldsymbol{w}\, d\Omega + \int_{\Gamma_2} \widehat{\boldsymbol{T}} \cdot \boldsymbol{w}\, d\Gamma \tag{2-11}$$

Then the infinite dimensional problem (2-11) is replaced with a finite dimensional version

$$\begin{aligned} \int_{\Omega} \left[\mu^h \left(\nabla \boldsymbol{u}^h + \left(\nabla \boldsymbol{u}^h\right)^T\right)\right] : \nabla \boldsymbol{w}^h\, d\Omega + \int_{\Omega} p^h\, \nabla \cdot \boldsymbol{w}^h\, d\Omega \\ = \rho\omega^2 \int_{\Omega} \boldsymbol{u}^h \cdot \boldsymbol{w}^h\, d\Omega + \int_{\Gamma_2} \widehat{\boldsymbol{T}} \cdot \boldsymbol{w}^h\, d\Gamma\ , \end{aligned} \tag{2-12}$$

where μ^h, p^h, $\nabla \boldsymbol{u}^h$, $\boldsymbol{u}^h$ and $\boldsymbol{w}^h$ are finite dimensional approximations of the actual values. In the finite element method, a finite number of nodes are considered on the region for each of the parameters and these values are approximated over the region using finite element shape functions:

$$\mu^h(x) = \sum_{\alpha=1}^{N_\mu} \bar{\mu}_\alpha \psi_\alpha^\mu(x)\ , \tag{2-13}$$

$$p^h(x) = \sum_{\beta=1}^{N_p} \bar{p}_\beta \psi_\beta^p(x)\ , \tag{2-14}$$

$$\boldsymbol{u}^h(x) = \sum_{\gamma=1}^{N_u} \bar{\boldsymbol{u}}_\gamma \psi_\gamma^u(x)\ , \tag{2-15}$$

$$\nabla \boldsymbol{u}^h(x) = \sum_{\gamma=1}^{N_u} \overline{\nabla \boldsymbol{u}}_\gamma \psi_\gamma^u(x) \,, \tag{2-16}$$

where ψ_α^μ, ψ_β^p and ψ_γ^u are shape functions for shear modulus, pressure and displacement respectively and $\bar{\mu}_\alpha$, $\bar{p}_\beta$, $\overline{\boldsymbol{u}}_\gamma$ and $\overline{\nabla \boldsymbol{u}}_\gamma$ are nodal values of the parameters. N_μ, N_p, N_u are the numbers of shear modulus, pressure and displacement nodes. The shape functions have a value of one at their corresponding node and a value of zero at all other nodes. Normally in a finite element formulation, when solving the forward problem, the gradient of displacement $\nabla \boldsymbol{u}^h$ is approximated by differentiating the displacement shape functions in (2-15), but in the case of an inverse problem where we have noisy displacement measurements, it is better to take the derivatives of the displacements separately using a more robust method, such as the least squares method, and then use them in the formulation.

In Galerkin's method, the test functions $\boldsymbol{w}^h$ are also approximated using the displacement shape functions as:

$$\boldsymbol{w}^h(x) = \sum_{\alpha=1}^{N_w} \overline{\boldsymbol{w}}_\alpha \psi_\alpha^u(x) \,, \tag{2-17}$$

Since equation (2-12) must be satisfied for an arbitrary $\overline{\boldsymbol{w}}_\alpha$, then $\overline{\boldsymbol{w}}_\alpha$ can be factored out and eliminated, resulting in:

$$\int_\Omega \left[\mu^h \left(\nabla \boldsymbol{u}^h + \left(\nabla \boldsymbol{u}^h\right)^T\right)\right] \cdot \nabla \boldsymbol{\psi} \, d\Omega + \int_\Omega p^h \, \nabla \boldsymbol{\psi} \, d\Omega = \rho \omega^2 \int_\Omega \boldsymbol{u}^h \boldsymbol{\psi} \, d\Omega + \int_{\Gamma_2} \widehat{\boldsymbol{T}} \boldsymbol{\psi} \, d\Gamma \,, \tag{2-18}$$

where $\boldsymbol{\psi}$ is a row vector of all the displacement shape functions:

$$\boldsymbol{\psi} = \left[\psi_1^u \,, \psi_2^u \,, \dots, \psi_{N_u}^u\right] \tag{2-19}$$

$$\nabla \boldsymbol{\psi} = \begin{bmatrix} \psi_{1,1}^u \,, \psi_{2,1}^u \,, \dots, \psi_{N_u,1}^u \\ \psi_{1,2}^u \,, \psi_{2,2}^u \,, \dots, \psi_{N_u,2}^u \\ \psi_{1,3}^u \,, \psi_{2,3}^u \,, \dots, \psi_{N_u,3}^u \end{bmatrix}. \tag{2-20}$$

There is one point about the test function which should be mentioned here. The second term on the right hand side of the equation (2-12) contains the traction vector on the boundary which we are not able to measure. By setting the interpolation functions for the test functions $\boldsymbol{w}^h$ to be zero at the nodes on the boundary, the equations associated with the boundary nodes are eliminated.

It should be mentioned that the order of shear modulus and pressure shape functions should be chosen to be equal or less than the order of the displacement shape functions in order to have enough equations to solve for

the unknowns [49]. In this study, we use constant shape functions for shear modulus and pressure, and Lagrange polynomials of the first order [117] for displacement shape functions and the test function. Figure 2-1 shows the Lagrange polynomials of the first order for a 2D rectangular element.

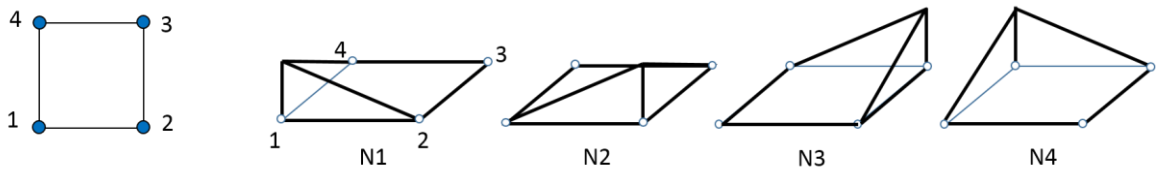

Figure 2-1. Sample Lagrange first order shape functions for a 2D rectangular element.

In elastography, the displacement distribution is known from measurements. The unknown is the shear modulus distribution. Therefore, equation (2-12) should be rearranged with respect to shear modulus and pressure unknowns and written in matrix form as follows:

$$[\mathbf{A} \quad \mathbf{C}] \begin{Bmatrix} \overline{\boldsymbol{\mu}} \\ \overline{\boldsymbol{p}} \end{Bmatrix} = \{\boldsymbol{f}'\}\,, \tag{2-21}$$

in which vectors $\overline{\boldsymbol{\mu}}$ and $\overline{\boldsymbol{p}}$ are the global shear modulus and pressure vectors, and the ith column of the matrices **A** and **C** and the vector $\boldsymbol{f}'$ are defined as follows:

$$\mathbf{A}^i = reshape\left(\int_\Omega \left[\psi_i^\mu \left(\nabla \boldsymbol{u}^h + \left(\nabla \boldsymbol{u}^h\right)^T\right)\right] \cdot \nabla \boldsymbol{\psi}\, d\Omega\right)\,, \tag{2-22}$$

$$\mathbf{C}^i = reshape\left(\int_\Omega \psi_i^p\, \nabla \boldsymbol{\psi}\, d\Omega\right)\,, \tag{2-23}$$

$$\boldsymbol{f}' = reshape\left(\rho\omega^2 \int_\Omega \boldsymbol{u}^h \boldsymbol{\psi}\, d\Omega\right)\,, \tag{2-24}$$

where *reshape(.)* of a matrix means all the elements of that matrix are regarded as a single column.

After defining the system of equations (2-21), the question that arises is whether this system of equations is solvable. First of all, as explained before, since we are eliminating the boundary force term in equation (2-12) by using the test functions which have zero value on the boundary, we are not able to find the absolute value of the pressure. The reason is that eliminating the boundary forces means we are not considering equation (2-8). Equation (2-6) alone has only information about the gradient of the pressure. Therefore, only the

relative values of pressure can be determined by that equation and, in order to solve for pressure, we need to determine the value of pressure in at least one element. Moreover, depending on the order of the shape functions and the number of nodes used for unknown parameters and the displacements, the number of equations might be less or more than the number of the unknown parameters. Therefore, the system might be under or over determined. For example, in the 2D case with a mesh size of $(n+1)\times(n+1)$, if we use rectangular 4-node elements with constant shape functions for shear modulus and pressure and linear shape function for displacements, we will have $n\times n$ elements therefore $2n^2$ unknowns and $2(n-1)^2$ equations (2 equations for each interior node). In this case the system is under-determined. But for the 3D case, using the same type of element and shape functions, the number of unknowns would be $2n^3$ and the number of equations would be $3(n-1)^3$. In this case for $n>7$ we have more equations than unknowns. Yet even in this case, the system is rank deficient due to the pressure term and a constraint needs to be added to the pressure parameters to make the system determined.

Removing the boundary equations not only decreases the rank of matrix $\mathbf{C}$ but also degrades the condition number of the matrices $\mathbf{A}$ and $\mathbf{C}$. Furthermore, the existence of noise and points of small displacements or small derivatives of displacements degrades the conditioning of the inverse problem. Therefore, a degree of regularization is always needed to improve the condition of the inverse problem and make the problem solvable.

In the following section, different ways of adding constraints to the problem parameters are discussed.

2.3 Regularization

2.3.1 Tikhonov regularization

As mentioned before, regularization is necessary to add constraints on the system parameters to make the system determined and well-conditioned. A common approach is Tikhonov regularization in which the objective function of the inverse problem is changed to a sum of two terms: a data misfit term and a regularization term [49]. The regularization consists of the norm of the parameters plus the norm of the low-order spatial derivatives of the parameters. So, in that case, the new inverse problem becomes:

$$\min_{\bar{\boldsymbol{\mu}},\bar{\mathbf{p}}}[(\mathbf{A}\bar{\boldsymbol{\mu}}+\mathbf{C}\bar{\boldsymbol{p}}-\boldsymbol{f}')^T(\mathbf{A}\bar{\boldsymbol{\mu}}+\mathbf{C}\bar{\boldsymbol{p}}-\boldsymbol{f}')+\alpha(\mathbf{G}\bar{\boldsymbol{\mu}})^T(\mathbf{G}\bar{\boldsymbol{\mu}})+\beta_1\bar{\boldsymbol{p}}^T\bar{\boldsymbol{p}}+\beta_2(\mathbf{G}\bar{\boldsymbol{p}})^T(\mathbf{G}\bar{\boldsymbol{p}})]\,, \qquad (2\text{-}25)$$

where α, β_1 and β_2 are regularization parameter weights and $\mathbf{G}$ is the differential operator. The reason the norm of the pressure parameter and its gradient are penalized, while only the norm of the spatial derivatives of the shear modulus is penalized, is the rank deficiency of the matrix $\mathbf{C}$. This deficiency, inhibiting our ability to determine the absolute value of the pressure, was created after removal of the boundary equations. However, the absolute values can be still determined for the shear modulus, and there is no need to add an absolute

constraint for the shear modulus. Differentiating equation (2-25) with respect to the unknown parameters and setting it equal to zero, we obtain the new system of equations as follows:

$$\begin{bmatrix} \mathbf{A}^T\mathbf{A} + \alpha\mathbf{G}^T\mathbf{G} & \mathbf{A}^T\mathbf{C} \\ \mathbf{C}^T\mathbf{A} & \mathbf{C}^T\mathbf{C} + \beta_1\mathbf{I} + \beta_2\mathbf{G}^T\mathbf{G} \end{bmatrix} \begin{Bmatrix} \overline{\boldsymbol{\mu}} \\ \overline{\boldsymbol{p}} \end{Bmatrix} = \begin{Bmatrix} \mathbf{A}^T\boldsymbol{f}' \\ \mathbf{C}^T\boldsymbol{f}' \end{Bmatrix}. \tag{2-26}$$

2.3.2 Sparsity regularization

The proposed alternative regularization is to use a sparse transformation. Depending on the structure of the underlying field of parameters, a suitable sparsifying transform should be chosen so that only a small subset of the new parameters in the transformed field can provide a good approximation of the original field. The discrete cosine transform (DCT) is often used for audio (MP3) and image (JPEG) compression because it has a strong energy compaction property. The 1D DCT of a signal $x(n)$ of length N is as follows:

$$X(k) = \sum_{n=0}^{N-1} x(n)\, cos\left[\frac{\pi}{N}\left(n + \frac{1}{2}\right)k\right] \qquad k = 0, \dots, N-1 \ . \tag{2-27}$$

To make this transform orthonormal, the first term X(0) should be multiplied by $\frac{1}{\sqrt{N}}$ and the other terms should be multiplied by $\sqrt{\frac{2}{N}}$. For the 2D case it is simply a separable product of DCTs along each dimension:

$$X(k_1, k_2) = \sum_{n_1=0}^{N_1-1} \sum_{n_2=0}^{N_2-1} x(n_1, n_2)\, cos\left[\frac{\pi}{N_1}\left(n_1 + \frac{1}{2}\right)k_1\right] cos\left[\frac{\pi}{N_2}\left(n_2 + \frac{1}{2}\right)k_2\right] \ . \tag{2-28}$$

For illustration, Figure 2-2(a) and (d) show two different sample elasticity maps. One map has an inclusion with a Gaussian profile and the other a circular inclusion with a step profile. We can see from Figure 2-2(b) and (e), which show the logarithm of the absolute values of the DCT coefficients, that elasticity maps with sharp edges are less sparse after transformation than maps which are smooth. Figure 2-2(c) and (f) show the inverse DCT of the truncated coefficients located inside the square region shown in Figure 2-2(b) and (e). As we can see, by using only $\frac{1}{16}$ of the low frequency DCT coefficients, we can reconstruct the original map with a very good approximation. In Figure 2-3, the upper row shows cross section profiles of the reconstructed maps obtained from truncated DCT coefficients using different cut-off ratios $r = N_s/N_t$ which is the ratio of the size of the selected region to the original region. The second row in Figure 2-3 shows the reconstructed map after penalizing the spatial derivatives of the map similar to what happens in Tikhonov regularization. This is done by minimizing the functional below:

$$\min_{\boldsymbol{E}}[(\boldsymbol{E}-\boldsymbol{E}^*)^T(\boldsymbol{E}-\boldsymbol{E}^*)+\alpha(\mathbf{G}\boldsymbol{E}^*)^T(\mathbf{G}\boldsymbol{E}^*)] \tag{2-29}$$

in which $\boldsymbol{E}^*$ is the original elasticity map in a vector and $\mathbf{G}$ is the differential operator and α is regularization parameter. After minimization we have the system of equations as follows:

$$[\mathbf{I}+\alpha\mathbf{G}^T\mathbf{G}]\{\boldsymbol{E}\}=\{\boldsymbol{E}^*\}\,. \tag{2-30}$$

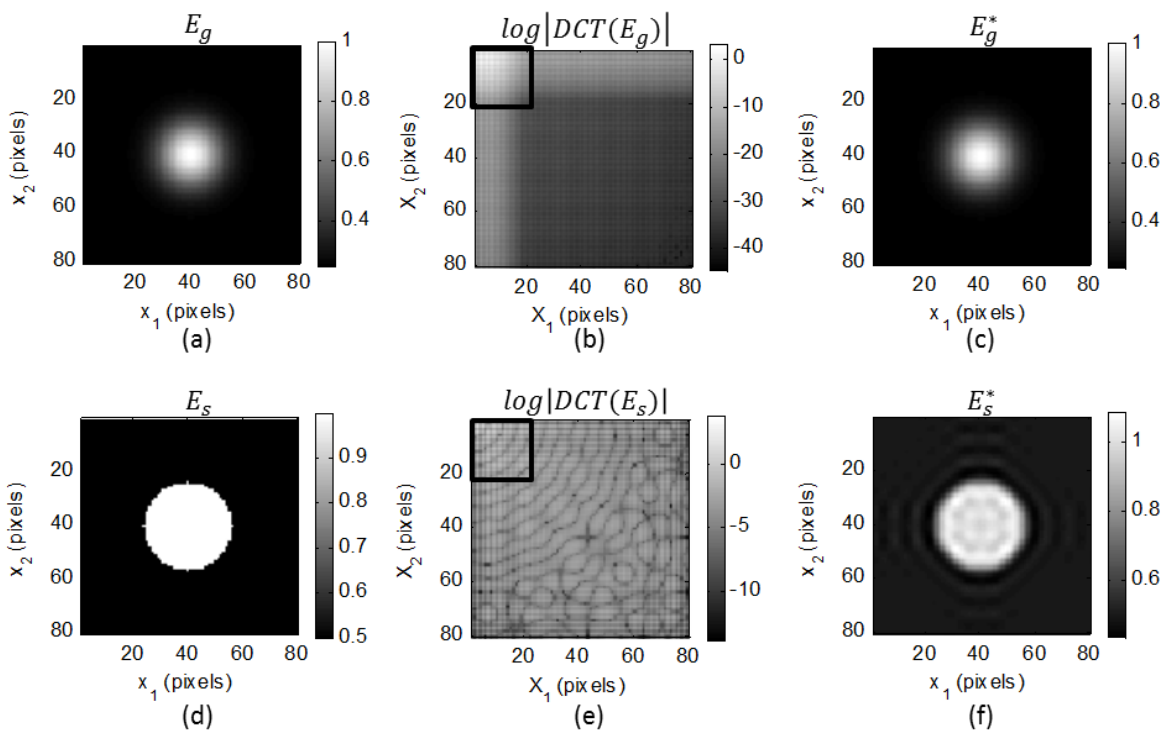

Figure 2-2. Two sample maps with (a) Gaussian and (d) step distribution. Logarithm of the absolute value of DCT coefficients for (b) Gaussian and (e) step distributions. Reconstructed (c) Gaussian (f) step distributions maps from truncated DCT coefficients i.e. the coefficients inside the square region in (b) and (e)..

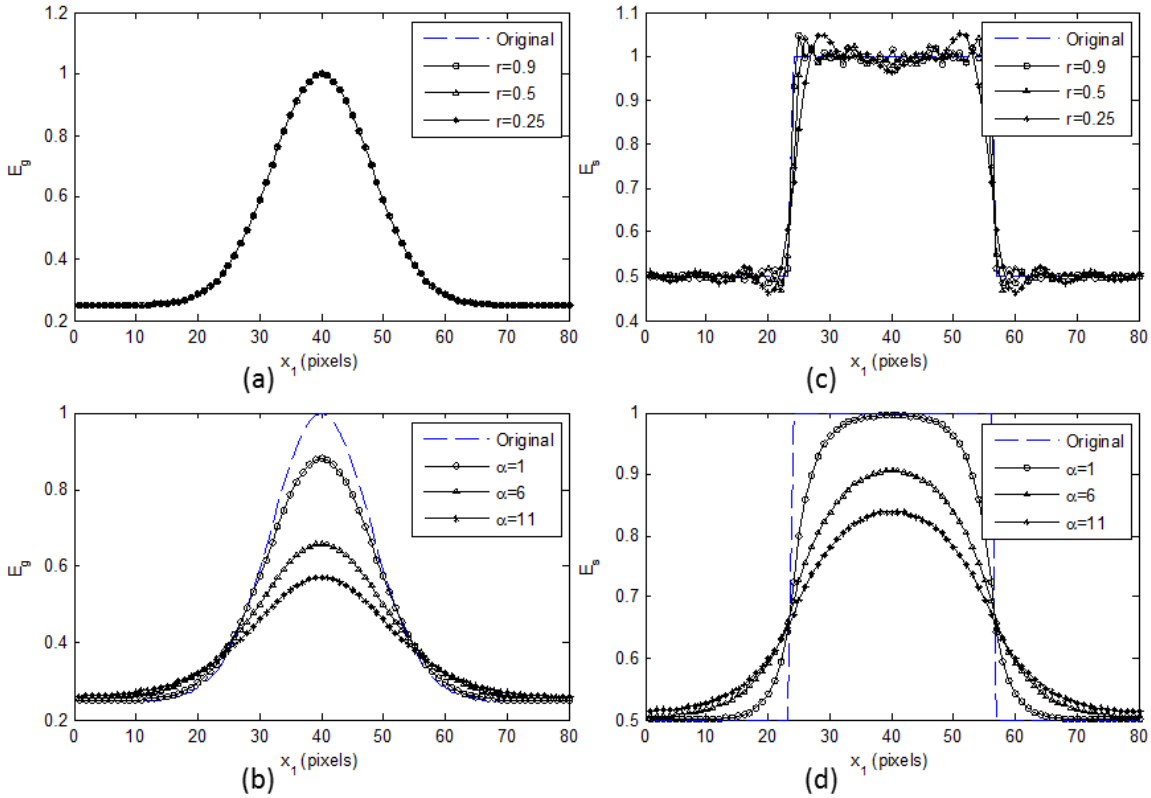

Figure 2-3. Profile of the reconstructed maps using truncated DCT coefficients of the (a) Gaussian map and (c) circular step map with different cut-off ratios of *r*. The resulting profiles using Tikhonov regularization which penalizes the gradient of the original parameters for maps with (b) Gaussian and (d) step inclusions for different values of regularization parameters *α*.

As shown in Figure 2-3(a) and (c), the reproduced image of Gaussian profile using truncated DCT coefficients is almost exact but the step profile has some ringing artifacts. Although there are some oscillations around the exact values, the contrast between the inclusion and background is almost exact on average and we do not see any reduction in contrast. But if we use Tikhonov regularization to limit the spatial gradient of the variables this will cause a reduction in contrast as shown in Figure 2-3(b) and (d).

It is anticipated that for smooth fields, the DCT is a suitable sparsifying transform which can be used to approximate the field with significantly fewer variables. Therefore, using sparsity regularization with the DCT as a sparsifying transform can be helpful by decreasing the number of variables and consequently improving the condition of the inverse problem for such fields. Moreover, the other advantage of this method is its higher speed. Since the number of the unknowns is reduced significantly, the system of equations can be solved significantly faster than the original system of equations.

Since the DCT is a linear transform, it can be written in matrix form:

$$\boldsymbol{X} = \mathbf{T}\boldsymbol{x} \tag{2-31}$$

in which $\mathbf{T}$ is the DCT transform matrix, $\boldsymbol{x}$ is a vector containing original field variables, and $\boldsymbol{X}$ is the transform-domain vector. We can reconstruct $\boldsymbol{x}$ from $\boldsymbol{X}$ using the inverse of $\mathbf{T}$.

$$\boldsymbol{x} = \mathbf{T}^{-1}\boldsymbol{X} \ . \tag{2-32}$$

Since $\boldsymbol{X}$ is sparse, we can choose a small number of dominant coefficients with large values and assume the others to be zero. This means we can choose the appropriate columns of $\mathbf{T}^{-1}$ corresponding to those selected dominant coefficients and call the new matrix $\mathbf{R} \equiv (\mathbf{T}^{-1})^*$ and let $\boldsymbol{X}^*$ be the truncated transform-domain vector. In this way:

$$\boldsymbol{x} \approx (\mathbf{T}^{-1})^*\boldsymbol{X}^* = \mathbf{R}\boldsymbol{X}^* \ . \tag{2-33}$$

In order to apply the sparsity regularization on the direct FEM inverse problem explained in the previous section, we need to replace the vectors $\overline{\boldsymbol{\mu}}$ and $\overline{\boldsymbol{p}}$ in equation (2-21) with approximated vectors obtained by using equation (2-33). So the new regulated system of equations becomes:

$$\begin{bmatrix} (\mathbf{AR}_1)^T(\mathbf{AR}_1) & (\mathbf{AR}_1)^T(\mathbf{CR}_2) \\ (\mathbf{CR}_2)^T(\mathbf{AR}_1) & (\mathbf{CR}_2)^T(\mathbf{CR}_2) \end{bmatrix} \begin{Bmatrix} \overline{\boldsymbol{\mu}} \\ \overline{\boldsymbol{p}} \end{Bmatrix} = \begin{Bmatrix} (\mathbf{AR}_1)^T\boldsymbol{f}' \\ (\mathbf{CR}_2)^T\boldsymbol{f}' \end{Bmatrix}, \tag{2-34}$$

in which $\mathbf{R}_1$ and $\mathbf{R}_2$ are appropriate selected transforms for shear modulus and pressure variables respectively. The challenging part of sparsity regularization is determining how to choose the dominant transformed variables. Depending on the structure of the field, the maximum coefficients of the transformed field are placed in different positions. If prior knowledge of the structure of unknown variables is available, it can be used to find the pattern of DCT coefficients distribution. For example, assuming a smooth distribution of variables, we can conclude that most of the larger coefficients in the DCT domain are located in the lower frequency part of the domain. So in this study, we roughly select the coefficients located in a rectangular window at the lower frequency corner of the domain as shown in Figure 2-2(b).

2.4 Results

2.4.1 Numerical simulations

A 2D $20mm \times 20mm$ region under plane strain is used to create the synthetic data. The region is bounded from the top and left as shown in Figure 2-4 and excited from the bottom with a harmonic displacement excitation. There are two Gaussian hard inclusions with the distribution:

$$E(x,y) = 10 + 15 \times \mathrm{e}^{\left(-\frac{(x-10)^2}{6.6} - \frac{(y-5)^2}{6.6}\right)} + 30 \times \mathrm{e}^{\left(-\frac{(x-10)^2}{6.6} - \frac{(y-15)^2}{6.6}\right)} \tag{2-35}$$

E is the Young modulus value in kPa. A constant density of 1000 kg/m^3 is assumed for the medium and the Poisson ratio is assumed to be $\nu = 0.4995$. While typical values for μ and λ for soft tissue are 10 kPa and 2 GPa, respectively, which lead to the Poisson ratio of $\nu = 0.499997$, we have used a smaller Poisson ratio of 0.4995 in all of our computations. To justify this use, we have solved the forward problem for different values of the Poisson ratios, and found that for Poisson ratios greater than 0.4995, changes in the results are negligible. The forward problem is solved using four-node square elements with a mesh size of $L = 0.25mm$ (80×80) to obtain synthetic data. The element size used in solving the inverse problem should be larger than the element size used in forward problem so that the discretization error of the forward problem is small compared to discretization error of the inverse problem. Therefore, the generated data is first down-sampled to a coarser mesh size of (30×30) then used in the inverse problem. The sample data generated with excitation frequency of 100 Hz are shown in Figure 2-5.

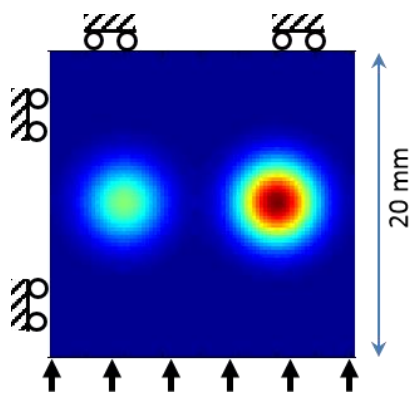

Figure 2-4. Schematic showing geometry and boundary conditions of the model used. The region is subjected to a harmonic excitation from the bottom and a sliding constraint at the top and left edges.

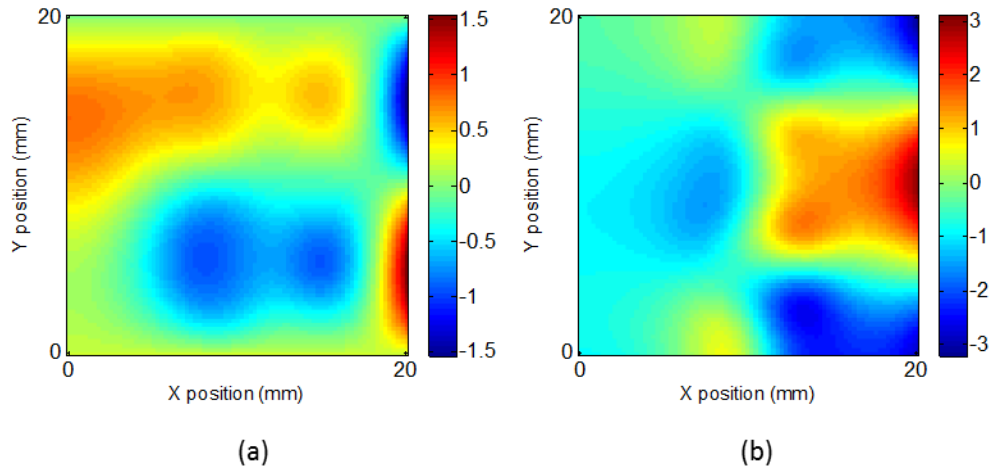

Figure 2-5. (a) The axial displacement (mm) and (b) pressure distributions (kPa) using an excitation frequency of 100Hz .

The elasticity reconstruction is performed using the direct mixed FEM technique with both Tikhonov regularization and sparsity regularization. In order to complete the rank of matrix $\mathbf{C}$, in sparsity regularization, $p^*(0,0)$, which is the coefficient of the constant base function in the DCT domain, is assumed to be zero and is removed from the unknowns. In Tikhonov regularization, the term which minimizes the norm of the pressure deals with this problem. The reconstructed Young modulus and pressure for the excitation frequency of 100 Hz, using sparsity regularization with cut-off ratios of $r_\mu = 0.4$ and $r_p = 0.9$ for shear modulus and pressure respectively, are shown in Figure 2-6. Figure 2-7 shows the reconstructed Young's modulus using both sparsity and Tikhonov regularizations for two different excitation frequencies. As one can see, parameter settings for Tikhonov regularization in one case may not work for a different case, for example when the frequency of excitation or boundary conditions are changed. In this example the parameters of the Tikhonov regularization were set for the excitation frequency of 150 Hz ($\alpha = 10^{-17}, \beta_1 = 10^{-14}, \beta_2 = 10^{-21}$) and then the same parameters were used for the excitation frequency of 200 Hz. The parameters are optimized by performing a full search on a discretized domain to minimize the RMS error for Young's modulus. As the results show in Figure 2-7(b) the Tikhonov regularization is not working as well at 200 Hz and the regularization parameters need to be readjusted while sparsity regularization does not need any changes. The elasticity reconstruction was performed for different excitation frequencies and different boundary conditions using both regularization methods, and the RMS error was calculated for each case using equation (2-36).

$$RMS = \sqrt{\frac{1}{m}\sum_{i=1}^{m}\frac{\left(E_i - E_i^0\right)^2}{(E_i^0)^2}} \tag{2-36}$$

The mean of RMS errors for the sparsity regularization and the Tikhonov method are 0.064 and 0.148 respectively with the standard deviations of 0.027 and 0.0363. The mean and standard deviation for the sparsity regularization is smaller than for the Tikhonov method, which shows that the Tikhonov method is more dependent on the frequency and boundary condition.

As discussed in the previous section and shown in Figure 2-2(e), in the case of Young's modulus patterns with sharp edges, the transformed variables in the DCT domain are not as sparse as when the Young's modulus pattern is smooth and without discontinuity. This can affect the performance of the sparsity regularization and cause artifacts in the reconstruction results. In order to investigate the effect of discontinuities in Young's modulus distribution, a region with circular step inclusion has been used to create synthetic data with the same boundary conditions as in Figure 2-4, with an excitation frequency of 200Hz. White Gaussian noise was added to the data to achieve an SNR of 35 dB, and the inverse problem was solved using both regularization methods. The regularization parameters were optimized for both methods. The parameters obtained for Sparsity regularization are ($r_\mu = 0.6$, $r_p = 0.9$), and for Tikhonov regularization are ($\alpha = 10^{-17}, \beta_1 = 10^{-13}, \beta_2 = 10^{-25}$). Figure 2-8 shows the reconstructed results. To show the effect of the regularization parameters, these parameters were changed around the optimized value and the inverse problem was solved. For this test, only the parameters related to the shear modulus were changed and the others were kept constant. The figures in the central column show the results when the optimized parameters are used, and the left and right columns show the results of under- and over-regularized conditions respectively. The two plots in Figure 2-8 (g) and (h) show the RMS errors as the regularization parameters change. As can be seen, for under-regularized conditions, errors appear and some artifacts related to discretization error and noise appear in the results with both methods. For over-regularized conditions the results are smooth and, as expected, Tikhonov regularization reduces the contrast but sparsity regularization only causes some ringing artifacts but does not reduce the contrast.

In another test, white Gaussian noise was added to the displacement data, obtained from both models with Gaussian and step inclusion, to achieve SNR of 25 dB and the inverse problem was solved for different values of excitation frequencies using both regularization methods. For each case, the model was simulated 30 times and the means and standard deviations of the RMS error for Young's modulus are shown in Figure 2-9. The regularization parameters which were used are the ones optimized for the excitation frequency of 200Hz. As can be seen from this figure, the mean RMS values for the Tikhonov method are higher than for the sparsity regularization and also are much more dependent on the excitation frequency. The standard deviation of RMS errors for sparsity regularization is smaller than for the Tikhonov method which shows the higher stability of this method compared to that of the Tikhonov method in the presence of noise. As expected, it can

also be seen that sparsity regularization works better for the region with Gaussian inclusion, due to its higher level of sparsity.

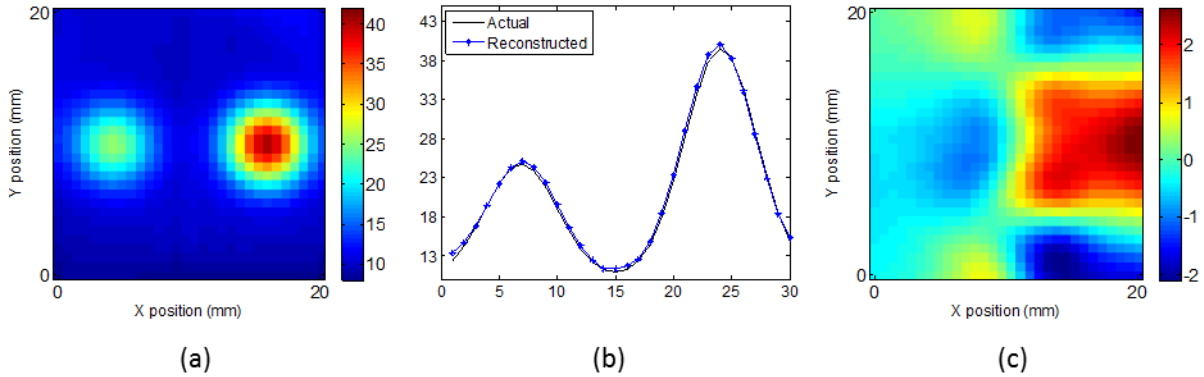

Figure 2-6. (a),(b) Reconstructed Young's modulus (kPa) and (c) pressure (kPa + constant) using our sparsity regularization method with cut-off ratios of $r_\mu = 0.4, r_p = 0.9$ and excitation frequency of 100 Hz.

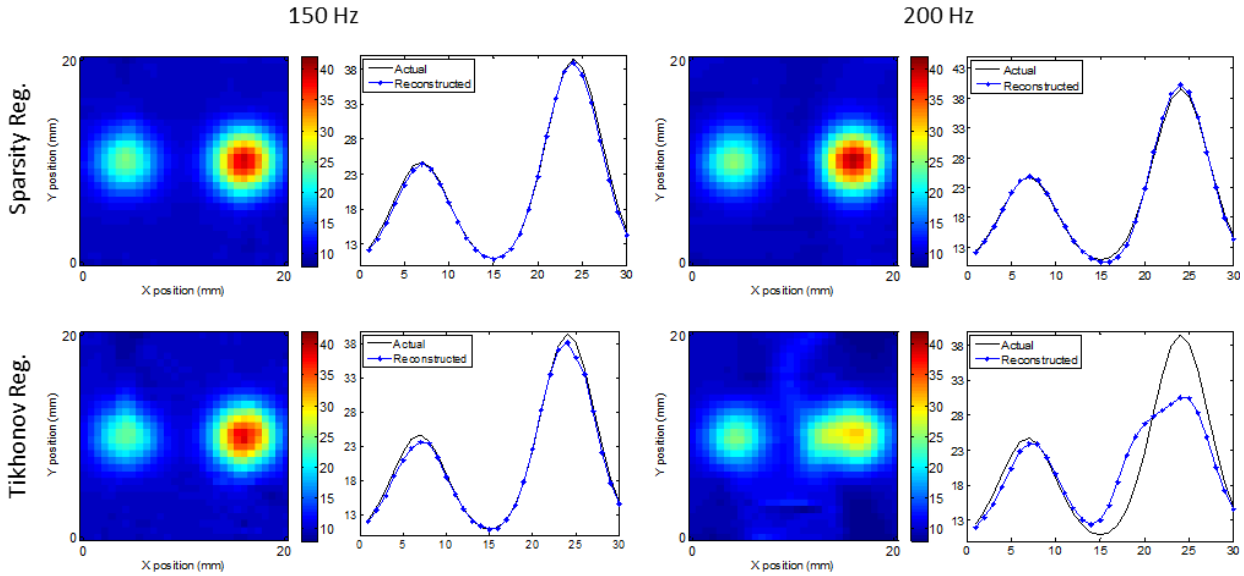

Figure 2-7. Reconstructed Young's modulus (kPa) using sparsity (top row) and Tikhonov (bottom row) regularization methods for 150 Hz and 200 Hz excitation frequencies.

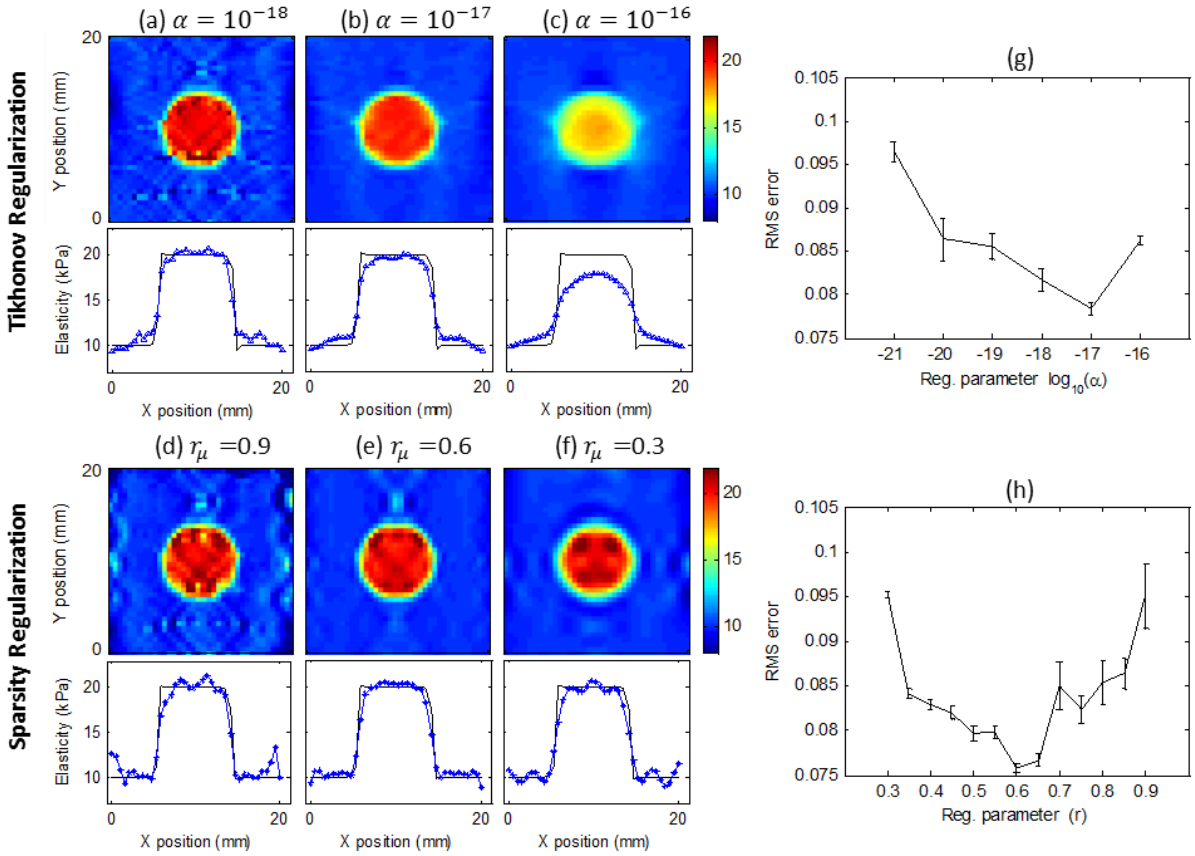

Figure 2-8. The reconstructed Young's modulus of the region with circular step inclusion using Tikhonov regularization (upper row (a)-(c)) and sparsity regularization (lower row (d)-(f)). For the middle column the optimized parameters are used and the left and right columns are the results of under-regularized and over-regularized conditions respectively. (g) and (h) are the RMS error versus regularization parameters for Tikhonov and sparsity regularization methods.

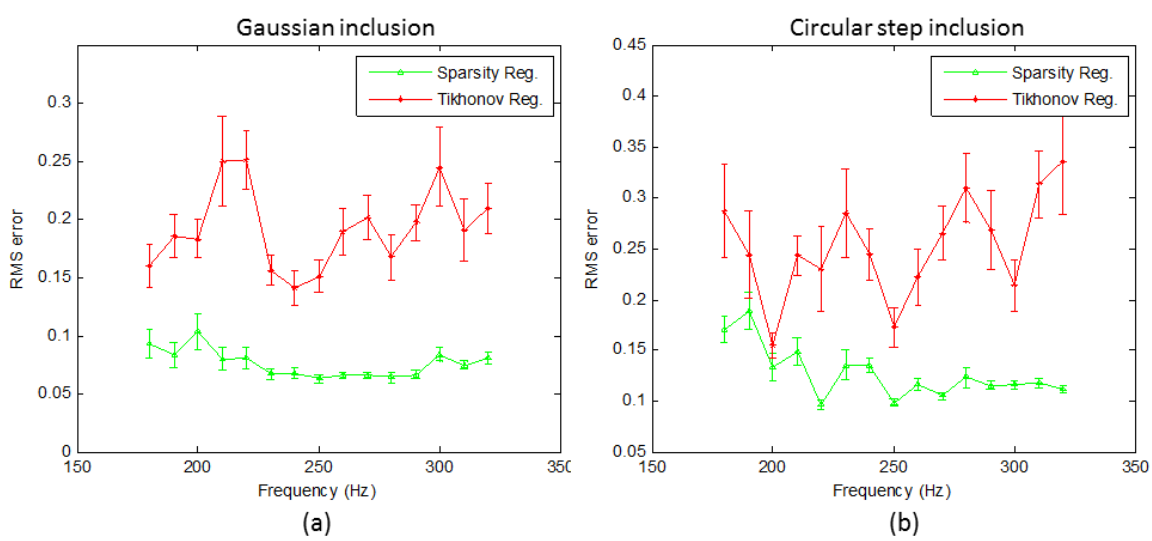

Figure 2-9. The RMS error for Young's modulus versus excitation frequency (a) Gaussian inclusion (b) Circular step inclusion.

2.4.2 MRE experiment data

The direct mixed FEM inversion technique with sparsity regularization was applied to the MRE experiment data captured from a CIRS elastography phantom model 049 (CIRS Inc., Norfolk, VA, USA). The phantom has 8 spherical inclusions with different values of elasticity and sizes as shown in Figure 2-10. The assumed values of Young's modulus for background and inclusions are reported by the manufacturer shown in Table 2-1. The sizes of the inclusions are 10mm and 20mm in diameter. The material used in this phantom is Zerdine®, a patented solid elastic water based polymer which simulates the ultrasound characteristics of human liver tissue. This material does not simulate the poroelastic property of real tissue which mean there is no fluid freely moving through the material. The phantom was excited with a frequency of 200 Hz in the Z-direction using a MRI compatible actuator developed in our lab [118].

Table 2-1. Young's modulus values of inclusions and background for CIRS phantom reported by the manufacturer. (The density is equal to the density of water)

Region	Young's modulus (kPa)
Type I	6
Type II	17
Type III	54
Type IV	62
Background	29

The MRE images were acquired using a 2D multi-slice multi-shot SE-EPI method with turbo factor 11 [119]. A single sinusoidal cycle was used as the motion encoding gradient with strength of 60mT/m, which captured 8 states of the mechanical motion. The displacements in time domain were converted to complex phasors using the Discrete Fourier Transform and used in the inverse problem. All three components of displacement were aquired on a 224×112×48 matrix with 1.5mm isotropic voxel size. Total image acquisition time was about 5 min. The acquisition matrix was cropped to 96×48×32, which includes the four larger inclusions as shown in Figure 2-10 (b). Figure 2-11 shows all the three components of the displacement in a plane normal to Y-direction. From this figure, especially the displacement in Z-direction, the reader can recognize the position of the actuator where the displacement is maximum. The displacements are attenuated further away from the excitation source because of the damping effect in the material.

The signal to noise ratio (SNR) of the measured displacement data for this experiment is about 28dB. SNR can be estimated using the following equation:

$$\mathrm{SNR_{db}} = 20\log_{10}\frac{\overline{U_{\mathrm{signal}}}}{\overline{U_{\mathrm{noise}}}}, \tag{2-37}$$

In which $\overline{U_{\mathrm{signal}}}$ and $\overline{U_{\mathrm{noise}}}$ are the root mean square of the displacement and noise respectively over the region of interest. The noise can be estimated as the error between the temporal displacement measurement and the sinusoid function fitted onto this data. Basically, it is assumed that all Fourier components other than the fundamental frequency are due to noise.

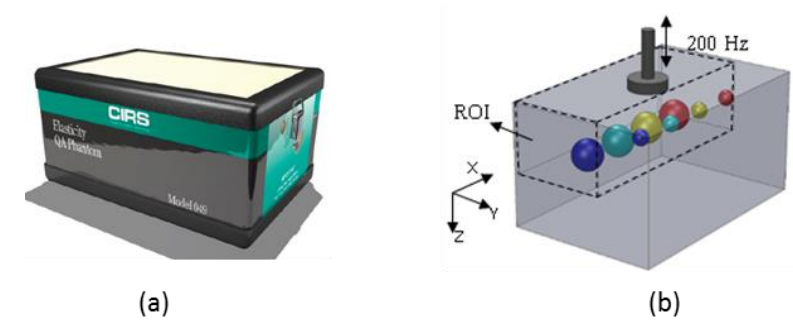

Figure 2-10. (a) CIRS elastography phantom, (b) Schematic showing the region of interest and the exciter position.

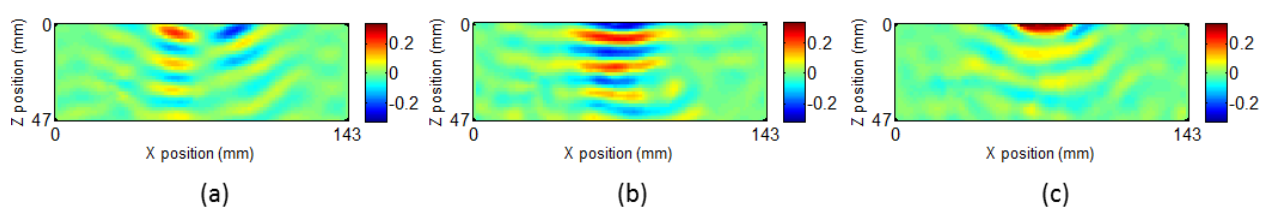

Figure 2-11. All three components of displacement (mm) data in a plane normal to Y-direction. (a), (b) and (c) show X, Y and Z directional displacements respectively.

The region of interest is divided into overlapping sub-domains of size $15 \times 15 \times 15$ to decrease the processing time. The sub-domains are overlapped by 3 pixels and the values in the overlapping region are averaged to retain the uniformity of the reconstructed shear modulus. The derivatives of the displacements used in the reconstruction are calculated using a planar fit on overlapping windows of size $4 \times 4 \times 4$. A

constant density of 1000 kg/m^3 is assumed. The sparsity regularization is used for both shear modulus and pressure. The sparsity pattern or the selected new coefficients in the transformed domain are the lower frequency coefficients located in a rectangular window of size $\frac{2}{3}$ of the entire domain which in this case is $10\times 10 \times 10$.

Figure 2-12 shows the reconstructed Young's modulus on different cross-sections. All the inclusions are visible with similar shapes, sizes and elasticities as the manufacturer's values. The regions are segmented by assuming spheres of radius 10 mm, locating them manually in each region and moving them around the assigned positions to minimize Young's modulus error. The mean and standard deviation of the Young's modulus of each region are calculated and compared with the values reported by the manufacturer. The quantitative results are shown in Figure 2-13. In order to estimate the size of the inclusions in the reconstructed Young's modulus map, the average of the Young's modulus of the elements located at a distance r from the estimated centers are plotted in Figure 2-14. Then, the radius of the inclusion is defined at the midpoint between the points of maximum curvature. The estimated radii of the inclusions 1, 2, 3 and 4 are 10.6 mm, 11.4 mm, 9.5 mm and 9.9 mm, respectively, which are close to the manufacturer's nominal value of 10 mm.

The processing time for this case using sparsity regularization was approximately 30 minutes while the Tikhonov regularization took approximately 5 hours to process. Since similar quality results can be obtained using Tikhonov regularization by adjusting the regularization parameters properly; only the results from sparsity regularization are shown here. The estimated Young's modulus values are slightly different from the values reported by the manufacturer. For hard inclusions we have an underestimation of the true parameters and for soft inclusions we have an overestimation of the true parameters. The same discrepancy has also been reported by Baghani *et al.* [120]. The reasons for this discrepancy can be the difference in temperature, excitation frequency or the changes of the material properties due to aging.

As mentioned before, only the relative values of the pressure distribution can be evaluated. Since we are using small overlapping windows and the pressure values obtained are not absolute values, the pressure distribution is not continuous at the boundaries of the overlapping windows as shown in Figure 2-15 (a). In order to be able to show a continuous pressure distribution for the entire domain we down-sampled the data to $\frac{2}{3}$ of the original mesh size and solved the inverse problem for the entire domain at once without dividing it into smaller windows. Figure 2-15 (b) shows the reconstructed pressure distribution for this case. Unlike the shear modulus, the unit of the pressure depends on the unit of the displacement data but since only the shear modulus value is of our interest in this study, we are not concerned about the unit of the pressure obtained. However, from this figure we can see that the gradient of the pressure is not negligible in some areas especially near the boundaries and this term should be considered in the reconstruction formulation as

reported by Park and Maniatty in [49]. Also from the pressure distribution the position of the actuator is easily detectable, in the middle at top where the pressure concentration is higher. This shows the consistency of the pressure solution.

In order to show the effect of windowing on the reconstruction, the down-sampled data which was used to solve the inverse problem without windowing was also used in the window-based reconstruction method using overlapping windows of size $15 \times 15 \times 15$ and the results were compared. The mean and standard deviation of the RMS error between these two results are 0.0179 and 0.0142 respectively. This shows that the results obtained from the windowing method are very close to the results obtained when the whole region is processed at once.

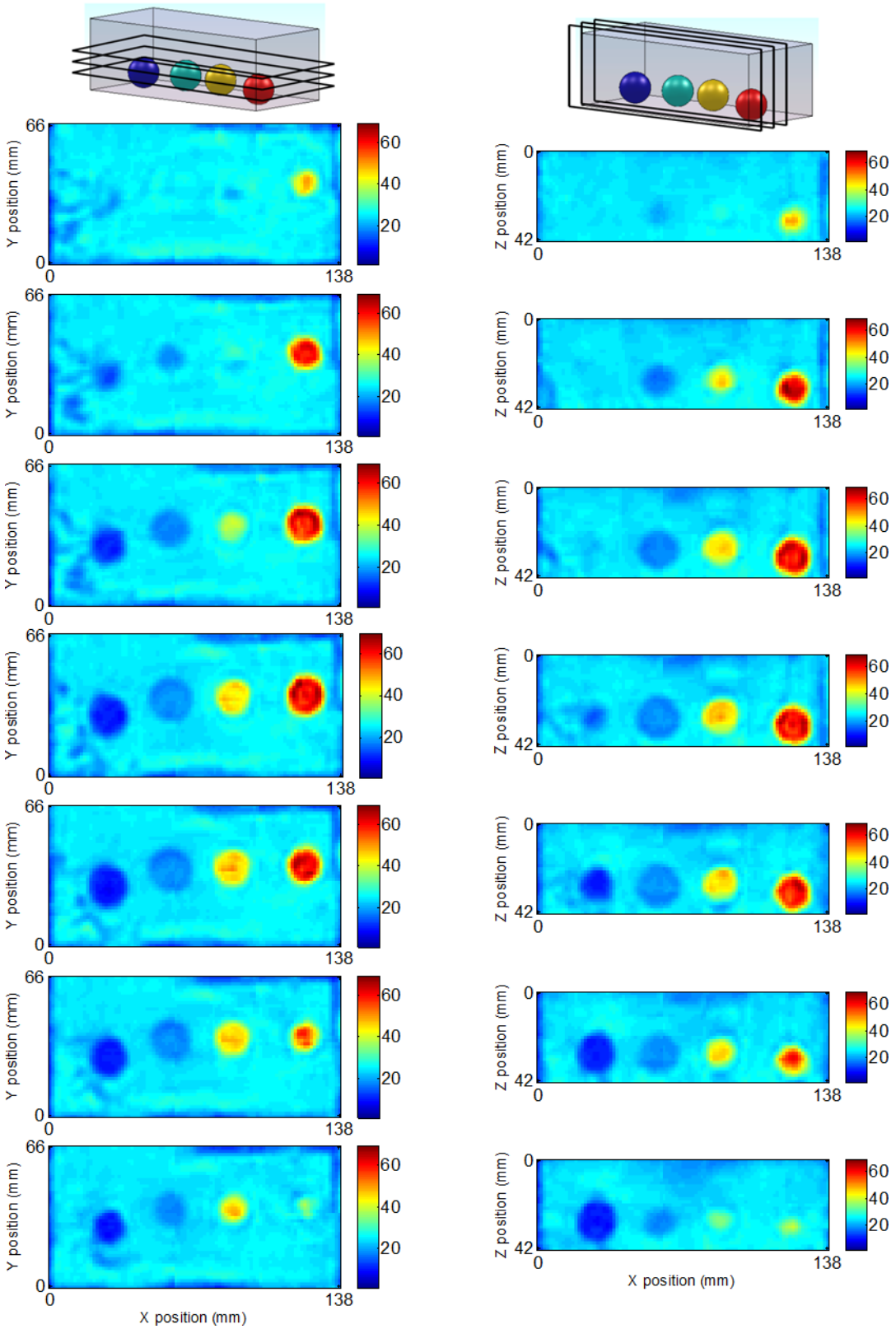

Figure 2-12. The reconstructed Young's modulus (kPa) using sparsity regularization. The reconstructed Young's modulus distribution on different cross-sections normal to Z-direction (left column) and Y-direction (right column) are shown.

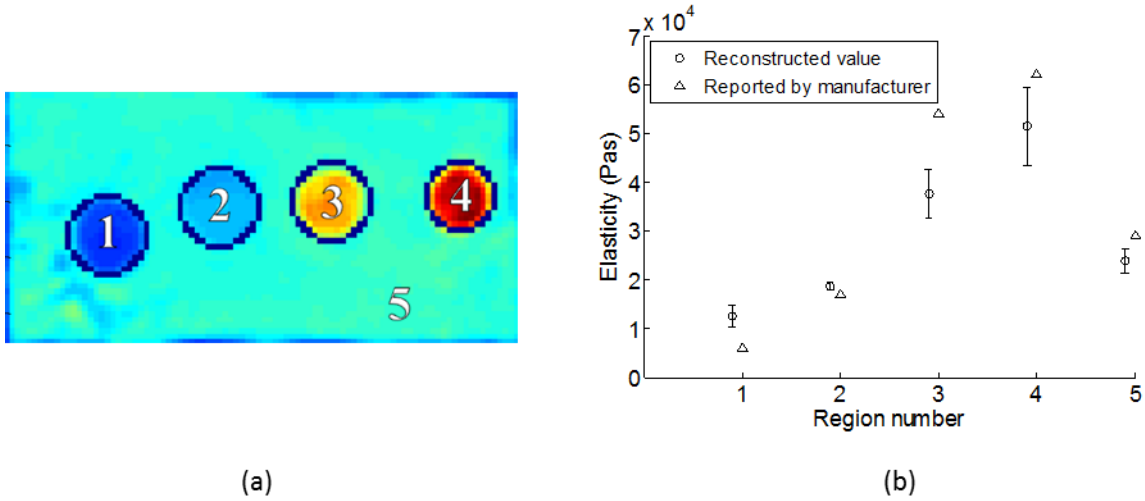

Figure 2-13. (a) The segmented regions with different elasticity (b) The mean and standard deviation of the Young's modulus over each region compared to the values reported by the manufacturer.

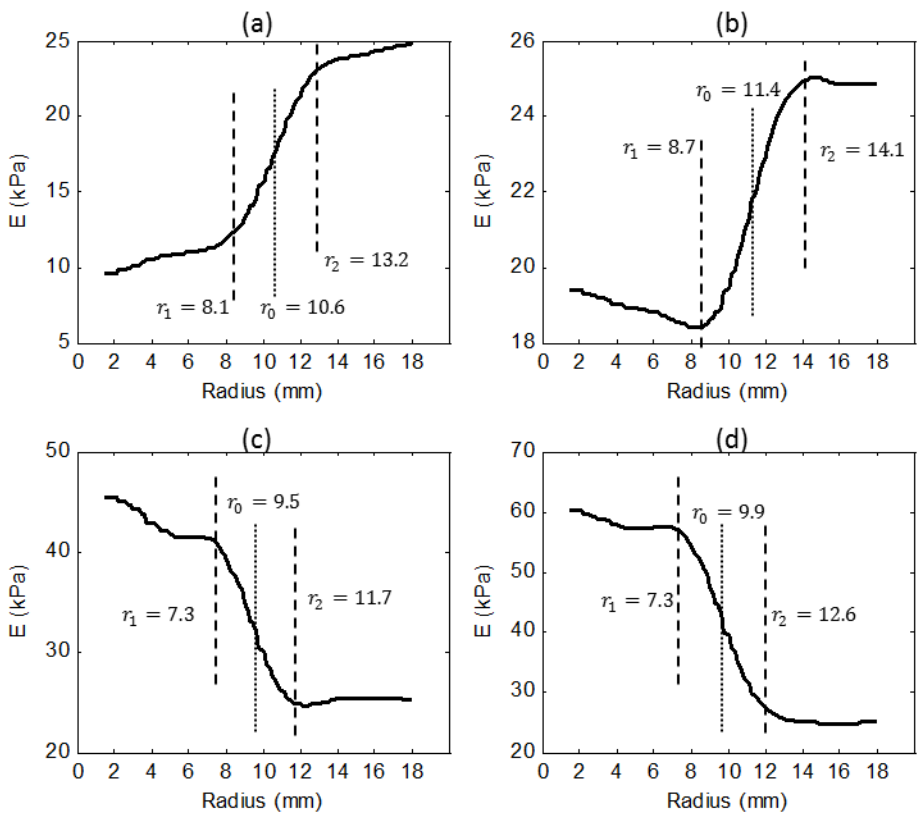

Figure 2-14. Profiles of the average Young's modulus versus distance from the center of the inclusions (a) type I (b) type II (c) type III (d) type IV

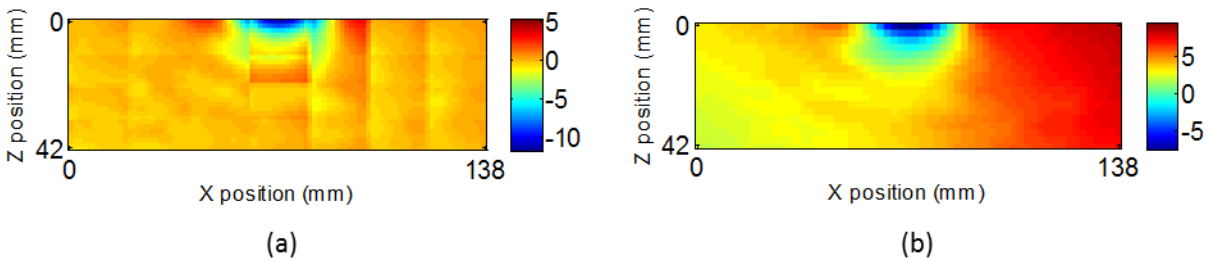

Figure 2-15. The reconstructed pressure distribution (a) using small overlapping windows (b) using one large window covering the entire region.

2.5 Conclusion

In this chapter a comparison of sparsity and Tikhonov regularization in solving the inverse problem of tissue elasticity using a direct finite element based algorithm with mixed u-p formulation was presented. Synthetic data was generated using different boundary conditions and excitation frequencies and the reconstructed results from sparsity and Tikhonov regularization were compared. The results show the higher dependency of Tikhonov regularization on the excitation condition and the higher dependence of its results on the regularization parameters. Sparsity regularization is independent of the boundary conditions and excitation and no readjustment is needed in this method. The noise analysis shows the higher robustness of the sparsity regularization compared to that of the Tikhonov regularization method. The results also show the higher speed of the proposed method. Results from MRE experiment data were also presented. The data was captured from a CIRS elastography phantom. All the inclusions were discernible as spherical inclusions with identifiable edge locations within 1.4 mm of the expected edge, and absolute Young's modulus values for each inclusion matching the order from smallest to highest provided by the manufacturer. Some discrepancies in absolute Young's modulus remain, likely due to differences in test conditions or aging of the phantom material, as reported previously.

Chapter 3 - Strain-based regularization in dynamic elastography

3.1 Introduction

In Chapter 2 it was shown that regularization is essential for stabilizing the solution and improving the conditioning of the inverse problem. Regularization techniques apply constraints on the parameters based on a prior knowledge about the unknown parameters. For example in Tikhonov regularization the smoothness of the solution is the prior assumption. Sparsity regularization was introduced in Chapter 2 in which it is assumed the solution is sparse in DCT domain with the significant parameters located in the lower frequency portion of the domain. It was shown that this method is more stable and faster than Tikhonov regularization and does not require application-specific tuning of the regularization parameters. But it was shown that the efficiency of the sparsity regularization method drops when there are discontinuities in the elasticity distribution which makes the parameters in DCT domain less sparse.

There are other approaches to constrain the solution in elastography which use the structural information obtained from other sources for example by segmenting the images obtained from conventional US [121], MRI [122] or optical coherence tomography (OCT) imaging [123]. A potential choice is a strain image. Simple quasi-static strain imaging can provide high resolution images showing the existence of hard inclusions but it is not an exact representative of elasticity, usually contains artefacts, and merely shows relative stiffness distribution. But these images can be used in dynamic elastography as prior knowledge of the shear modulus distribution for the purpose of regularization. In previous studies, strain images have been used for regularization in intravascular ultrasound elastography (IVUSe) [124, 125]. But those methods use iterative FEM inversion techniques with static displacement data.

In this chapter we investigate different ways of using quasi-static strain images as prior knowledge for the purpose of regularization in dynamic elastography with direct FEM inversion technique. The methods are tested on both simulation and phantom data.

3.2 Methods

3.2.1 Inverse problem

For the reconstruction, the direct FEM inversion technique with a mixed (displacement-pressure) formulation, as presented in Chapter 2, is used. In this method, the equation of motion is discretized and written in matrix form as in (3-1) and solved directly for the shear modulus $\overline{\boldsymbol{\mu}}$ and pressure parameters $\overline{\boldsymbol{p}}$:

$$[\mathbf{A} \quad \mathbf{C}] \begin{Bmatrix} \overline{\boldsymbol{\mu}} \\ \overline{\boldsymbol{p}} \end{Bmatrix} = \{\boldsymbol{f}'\} , \tag{3-1}$$

3.2.2 Sparsity regularization

Sparsity regularization was proposed in Chapter 2, and a brief summary is provided here for convenience. The basic idea is to use a sparsifying transform on the problem's parameters, resulting in a sparse representative of the original variables. In the new domain, a small subset of variables can be chosen and used to reconstruct the original variables with a very good approximation. Therefore the new inverse problem has a smaller number of variables compared to the number of equations resulting in improved conditioning.

It was shown that the discrete cosine transform (DCT) can be used as the sparsifying transform for this purpose. The DCT of a 1D signal $x(n)$ of length N is defined in (3-2); for higher dimensions it is just a separable product of DCTs along each dimension.

$$X(k) = \sum_{n=0}^{N-1} x(n) \cos\left[\frac{\pi}{N}\left(n + \frac{1}{2}\right)k\right] \qquad k = 0, \dots, N-1 \ . \tag{3-2}$$

The DCT is a linear transform and it can be written in matrix form as:

$$\boldsymbol{X} = \mathbf{T}\boldsymbol{x} \tag{3-3}$$

in which $\mathbf{T}$ is the DCT transform matrix, $\boldsymbol{x}$ is a vector containing original field variables, and $\boldsymbol{X}$ is the transform-domain vector. We can reconstruct $\boldsymbol{x}$ from $\boldsymbol{X}$ using the inverse of $\mathbf{T}$.

$$\boldsymbol{x} = \mathbf{T}^{-1}\boldsymbol{X} \ . \tag{3-4}$$

Since $\boldsymbol{X}$ is sparse, we can choose a small number of dominant coefficients with large values and assume the others to be zero. This means we can choose the appropriate columns of $\mathbf{T}^{-1}$ corresponding to those selected

dominant coefficients and call the new matrix $\mathbf{R} \equiv (\mathbf{T}^{-1})^*$ and let $\boldsymbol{X}^*$ be the truncated transform-domain vector. In this way:

$$\boldsymbol{x} \approx (\mathbf{T}^{-1})^* \boldsymbol{X}^* = \mathbf{R}\boldsymbol{X}^* \,. \tag{3-5}$$

This approximation can be replaced with the original variables in (3-1) as follows:

$$\bar{\boldsymbol{\mu}} \approx \mathbf{R}_1 \bar{\boldsymbol{\mu}}^* \,, \bar{\boldsymbol{p}} \approx \mathbf{R}_2 \bar{\boldsymbol{p}}^* \tag{3-6}$$

So the new regulated system of equations becomes

$$[\mathbf{A}\mathbf{R}_1 \quad \mathbf{C}\mathbf{R}_2] \begin{Bmatrix} \bar{\boldsymbol{\mu}}^* \\ \bar{\boldsymbol{p}}^* \end{Bmatrix} = \{\boldsymbol{f}'\} \,. \tag{3-7}$$

3.2.3 Strain-based regularization

As mentioned before, in this method information from quasi-static strain images is used as prior knowledge of the shear modulus distribution. It can be assumed that in regions where the strain is approximately constant, the shear modulus is likely constant. Here we investigate three different ways of applying such a constraint on shear modulus parameters: 1- Hard constraint, 2- Soft constraint and 3- sparsity pattern selection based on strain image.

3.2.3.1 Hard constraint

In this method, first the region is segmented into sub-regions based on the structural information in the strain image and then constraints are added to the parameters of each region separately. In the hard constraint method, all the parameters of a region are lumped together. This greatly reduces the number of the unknowns and therefore improves the conditioning of the problem. I.e., for a single inclusion segmented from a background there can be as few as two shear modulus parameters to identify: inclusion and background. The segmentation of the strain image into sub-regions can be performed using thresholding or any other segmentation method. For the pressure parameters, we still use sparsity regularization described in Chapter 2.

Having m segmented regions Ω^i $(i = 1, \dots, m)$ each with n_i elements, applying these constraints on the system of equations (3-1) results in:

$$\begin{bmatrix} \mathbf{B} & \mathbf{C}\mathbf{R}_p \end{bmatrix} \begin{Bmatrix} \bar{\bar{\boldsymbol{\mu}}} \\ \bar{\boldsymbol{p}}^* \end{Bmatrix} = \{\boldsymbol{f}'\} \,, \tag{3-8}$$

where $\bar{\bar{\boldsymbol{\mu}}}$ is a vector containing lumped shear modulus of each region and $\mathbf{R}_p$ is the sparsity filter for the pressure parameters. The ith column of matrix **B** is calculated from the columns of matrix **A** as follows:

$$B^i = \sum_{j=1}^{n_i} A^{d_j^i} \ , \tag{3-9}$$

where d_j^i is the global index number of the jth element in region Ω^i .

One of the expected drawbacks of strain-based regularization with a hard constraint is that the misclassification of the parameters on the boundaries of the sub-regions can cause considerable error in the absolute values of the reconstructed shear modulus. In order to avoid the expected errors caused by misclassification, the elements located on the boundaries are separated from both segments and considered as separate individual elements. For example, Figure 3-1 shows a sample shear modulus pattern, the corresponding strain image and the segmented region. In that case, equation (3-8) becomes:

$$\begin{bmatrix}\mathbf{B} & \mathbf{B}^s & \mathbf{C}\mathbf{R}_p\end{bmatrix}\begin{Bmatrix}\bar{\bar{\boldsymbol{\mu}}} \\ \bar{\boldsymbol{\mu}}^s \\ \bar{\boldsymbol{p}}^*\end{Bmatrix} = \{\boldsymbol{f}'\}\,, \tag{3-10}$$

where matrix $\mathbf{B}^s$ contains the columns of matrix **A** corresponding to individual elements located on the boundaries of the regions that are left without regularization.

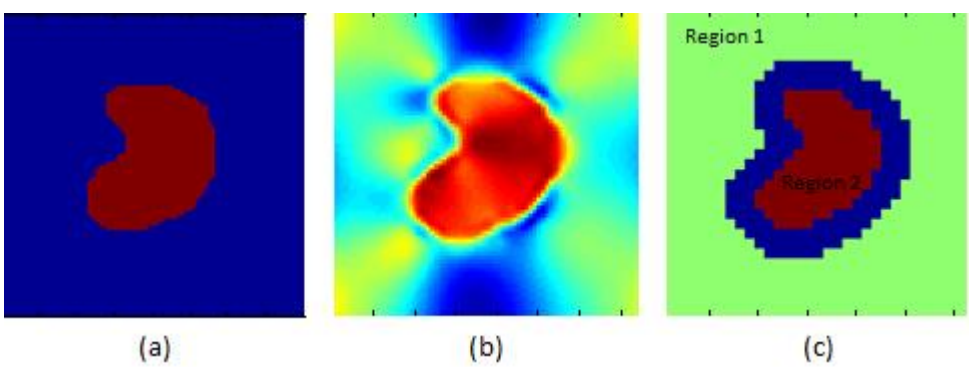

Figure 3-1. (a) Sample shear modulus pattern (b) the corresponding quasi-static strain image (c) the segmented region based on the strain image.

3.2.3.2 Soft constraint

Another drawback of strain-based regularization with a hard constraint is that the parameters of one region may not necessarily be identical as assumed with a hard constraint. For example, in the investigated region, there might be an inclusion with smooth edges that was not detected by the segmenting algorithm. Therefore, that inclusion will be considered as part of its surrounding segment and not seen in the elastogram.

An alternative way is to apply a soft constraint instead of lumping all the parameters of a region. In this way the parameters of a region are allowed to differ by a certain amount. Richards and Doyley [121] suggested using soft constraints in IVUSe problem. They derived the spatial priors from manually segmented IVUS sonograms and applied the Tikhonov regularization on each segment separately. In another work, McGarry *et al* [122] used MRI T1 images to segment the region and apply a soft constraint on the parameters of each region. They solved the inverse problem using the iterative FEM method and the constraint was applied by adding a regularization term to the misfit function, which minimizes the norm of the difference between the Young's modulus of each element and the average of the Young's modulus of the other elements in the same segmented region. An alternative way suggested here is to apply the sparsity regularization on each sub-region derived from segmented quasi-static strain images. We call this method regional sparsity regularization. Since the regions are segmented so that the high variation areas are located on the boundaries of the regions, therefore within the regions there is no sudden change in shear modulus and no ringing artifacts resulting from ignoring the higher frequency coefficients in DCT domain. This idea is inspired from the shape-adaptive DCT algorithm (SA-DCT) proposed by Sikora and Makai [126, 127] in the field of image processing used for compression of segmented images. That algorithm is capable of encoding arbitrary-shaped segments. Using that algorithm we can apply our sparsity regularization separately on each segmented region obtained from the strain image. The only similarity between our implementation of a soft constraint and the previous work by McGarry *et al* [122] is that in both methods the region is segmented based on features from another imaging modality and a constraint is applied to the elements of the each segment separately. Otherwise they are different in other aspects. We are applying the method on the direct FEM inversion but they used it with an iterative technique. Also the constraints applied are different. Using sparsity regularization in our method reduces the number of the parameters significantly and improves the efficiency and robustness.

In order to implement this technique, the region of interest is segmented into sub-regions of low strain gradients similar to the previous section. For this purpose, an edge detection algorithm based on the gradient of the strain is used to segment the region with high gradients along the boundaries between tissue types. In order to avoid the expected errors caused by misclassification, the elements located on the boundaries are again separated from both segments and considered as separate individual elements.

The next step is to define the DCT filter for irregular-shaped segments using the SA-DCT. First the forward SA-DCT is explained and the inverse SA-DCT needed for the sparsity regularization is simply implemented as the same processing steps but performed in reverse order. Here we explain SA-DCT for 2D regions but the method can be extended to higher dimensions. For 2D regions there are four steps to be applied. Figure 3-2 shows the schematic of these four steps. Similar to the regular 2D transform, first the 1D transform is applied in one direction and then again another 1D transform is applied on the other direction on the resulting

parameters from the previous transform. But the difference here is the elements of the region should be shifted prior to the transformation.

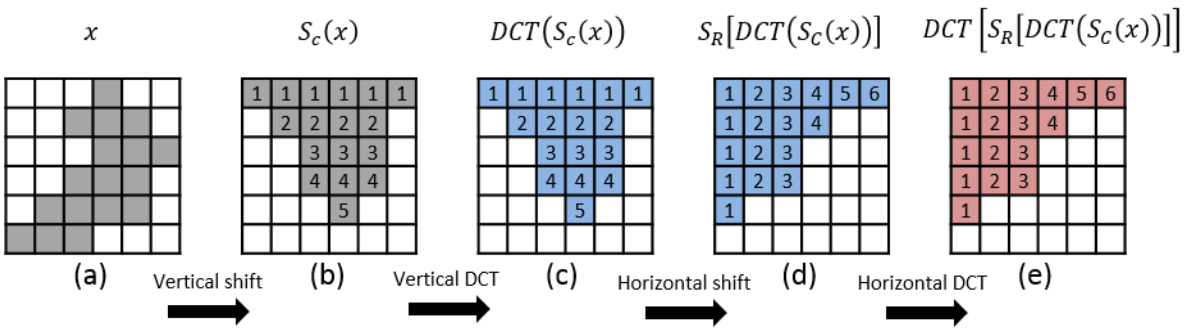

Figure 3-2. The four steps for performing the forward SA-DCT transform on an irregular shape region.

Here we first apply the vertical transform and then the horizontal. Therefore, in order to make the columns of the region connected, the columns are shifted vertically to the most upper position as in Figure 3-2(b). Then the one dimensional DCT transform is applied to each column based on the length of the column. In the next step, the elements of each row are shifted to the most left position as in Figure 3-2(d) and finally the one dimensional DCT is applied to each row depending on the length of the row.

Again since this is a linear transform, it can be written in matrix form as in equations (3-3) and (3-4). Then similar to the regular sparsity regularization technique, the parameters are approximated by truncating the transformed variables in the frequency domain, as done before in (3-5). This approximation can be applied to each region separately. For the pressure parameters, the regular sparsity regularization is used. Therefore the new system of equations becomes:

$$\left[\widetilde{\mathbf{A}}_1\mathbf{R}_1 \quad \widetilde{\mathbf{A}}_2\mathbf{R}_2 \quad \cdots \quad \widetilde{\mathbf{A}}_m\mathbf{R}_m \quad \widetilde{\mathbf{A}}^s \quad \mathbf{C}\mathbf{R}_p\right]\begin{Bmatrix}\overline{\boldsymbol{\mu}}_1^* \\ \overline{\boldsymbol{\mu}}_2^* \\ \vdots \\ \overline{\boldsymbol{\mu}}_m^* \\ \overline{\boldsymbol{\mu}}^s \\ \overline{\boldsymbol{p}}^*\end{Bmatrix} = \{\boldsymbol{f}'\}, \tag{3-11}$$

where $\widetilde{\mathbf{A}}_i$ $(i = 1..m)$ are matrices formed from selected columns of matrix $\mathbf{A}$ corresponding to elements of region Ω^i , $\mathbf{R}_i$ $(i = 1..m)$ are the regional sparsity filters for the region Ω^i , $\mathbf{R}_p$ is the sparsity filter for the pressure parameters, and matrix $\widetilde{\mathbf{A}}^s$ is formed from the columns of matrix $\mathbf{A}$ corresponding to the individual elements located on the boundaries of the regions which are left without regularization.

A by-product of this section is the sparsity filter for irregular shaped regions. In most real tissue cases, the region of interest is an irregular shaped region instead of a rectangular region. For example, in prostate elastography we cannot cover the whole prostate gland using a rectangular region of interest. In these cases, using the filter developed in this section, we can still apply the sparsity regularization on the parameters of the irregular shaped region and solve the inverse problem.

3.2.3.3 Sparsity pattern selection based on strain image

The two methods explained in the previous sections require segmenting the region based on the strain image which will inevitably contain errors especially along poorly-defined borders. In a different approach, we propose to use the strain image to find an optimal sparsity pattern for the regular sparsity regularization. In sparsity regularization, the challenging part is to determine an appropriate sparsity pattern in the new domain. In Chapter 2, we used a rectangular or circular pattern at the lower frequency part of the DCT domain, as in Figure 3-3(d), considering the fact that the majority of the parameters with significant magnitude are located in the lower frequency part of the DCT domain. But a possible better approach is to choose an optimal sparsity pattern based on the prior knowledge of the unknown parameters. In order to find the sparsity pattern for the shear modulus parameters, we use the strain image as an appropriate representation of the shear modulus distribution. Basically, the DCT transform of the strain image is calculated and the parameters with higher magnitudes are selected to be inside the sparsity pattern. For example, Figure 3-3(a) shows a circular hard inclusion excited with a 10 Hz vibration and Figure 3-3(b) shows the resulting strain image. Figure 3-3(c) shows the sparsity pattern obtained from the strain image. This pattern is obtained by taking the DCT transform of the strain image and then selecting a number of pixels with highest magnitude. This pattern can be used in deriving the filter $\mathbf{R}_1$ in (3-7). For deriving the filter $\mathbf{R}_2$, which is for the pressure parameters, we still use the circular pattern (Figure 3-3(d)) since we do not have any specific prior knowledge of the pressure distribution.

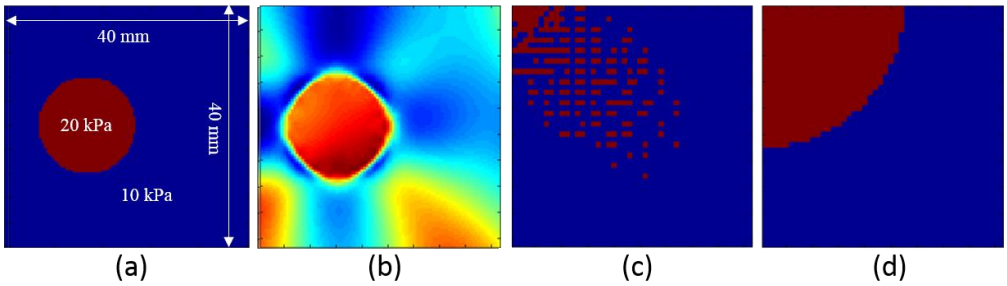

Figure 3-3. (a) actual Young's modulus pattern (b) quasi-static strain image. (c) sparsity pattern obtained from the strain image, (d) circular sparsity pattern

3.3 Results

3.3.1 Numerical simulations

Simulation data is used to investigate the effectiveness of each regularization technique. In the first test we show the effect of hard constraint on the reconstructed results. A 2D $25mm \times 25mm$ region under the plane strain assumption is used to create the synthetic data. The region is fixed at the top and left edges with sliding constraints and excited from the bottom as shown in Figure 3-4. Both static and harmonic excitations (250 Hz) are applied. The static data is used to calculate the axial strain image for segmenting the region and the dynamic data is used for reconstructing the absolute shear modulus values. A constant density of 1000 kg/m^3 and a Poisson ratio of 0.4995 are assumed for the medium. The Young's modulus for the background and the inclusions are 10 kPa and 20 kPa respectively. The forward problem is solved using four-node square elements with a mesh size of $L = 0.25mm$ to obtain synthetic data. Then the displacements inside a smaller square region of size $20\ mm$ are selected and down-sampled to be used in the inverse problem.

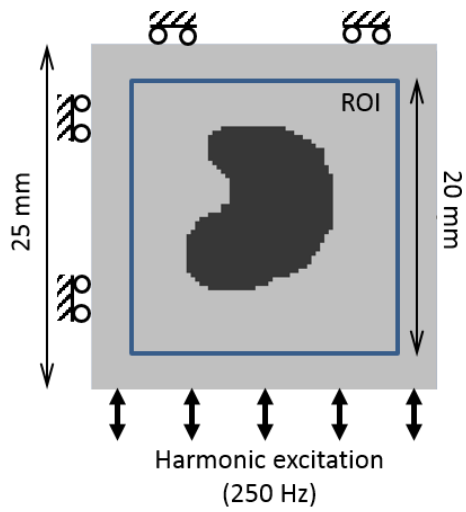

Figure 3-4. The schematic of the region used for generating the synthetic data

White Gaussian noise was added to the displacement data to achieve a SNR of 30 dB and then used in the inverse problem. Figure 3-5 shows the reconstructed Young's modulus maps using the regular sparsity (described in Chapter 2) and two of the strain-based regularization techniques. In both cases, the sparsity regularization is used for the pressure parameter. On the one hand, for sparsity regularization, since there is a discontinuity in the Young's modulus map, the cut-off ratio r_μ should be large enough to include sufficient high frequency parameters to reduce the ringing artifacts. On the other hand, to reduce the effect of noise and achieve a more stable result, the cut-off ratio needs to be smaller. Thus, there is a trade-off in choosing this

parameter. Figure 3-5(b) shows the result for the optimum cut-off ratio ($r_\mu = 0.5$) with the minimum RMS error for Young's modulus. As it can be seen, due to the small value of the cut-off ratio, the ringing artifacts appear in the result. Figure 3-5(c) shows the reconstructed Young's modulus using the hard constraint. As discussed before, the misclassification of the parameters in the strain-based regularization with a hard constraint results in a significant error in the estimated values. Since the borders of the segmented regions are not precisely coincident with the inclusion boundary, some elements of the background are included in the inclusion segment and vice versa. As it can be seen, this has caused a significant underestimation of the inclusion's Young's modulus. To overcome this problem, as suggested before, the elements located on the border of the regions are separated from both segments and considered as individual elements with different Young's modulus values. Figure 3-5(d) shows the result after separating the boundary elements. As it can be seen, after this modification, the values obtained for the inclusion and background segments are close to the specified values.

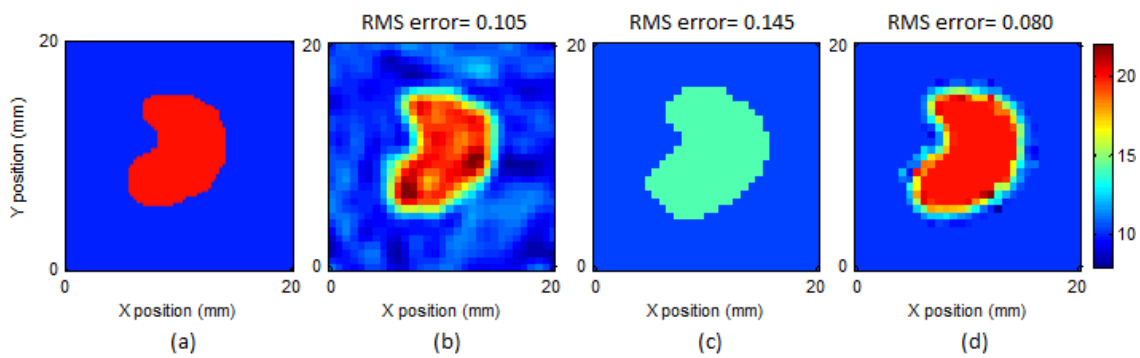

Figure 3-5. (a) The specified Young's modulus map. (b) The reconstructed Young's modulus map using conventional sparsity regularization, (c) strain-based regularization with a hard constraint (d) strain-based regularization when boundary elements are considered as individual separate elements.

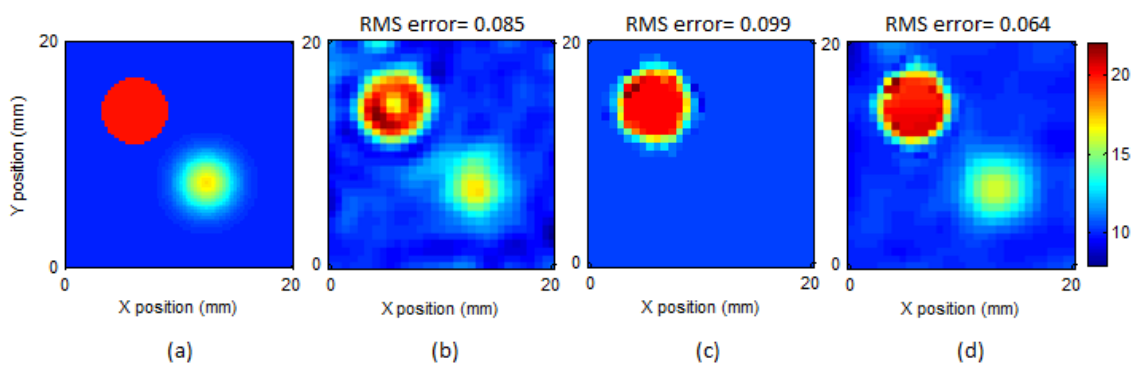

Figure 3-6. (a) The specified Young's modulus map. (b) The reconstructed Young's modulus map using regular sparsity regularization, (c) strain-based regularization with hard constraint (d) regional sparsity regularization.

As explained before, the drawback of a hard constraint is that it does not consider the possible elasticity variation inside the segments. This can cause detection problems for inclusions with gradual elasticity changes at their boundaries since these inclusions may not be detected in segmentation of the strain image. This can be solved by using a soft constraint instead of hard constraint. To show this effect, a region with both Gaussian and circular step inclusions (Figure 3-6(a)) is used to generate the synthetic data using the same boundary condition as shown in Figure 3-4. Figure 3-6(b) shows the reconstructed Young's modulus map using the regular sparsity regularization. Figure 3-6(c) and Figure 3-6(d) show the results for strain-based regularization with a hard constraint and regional sparsity regularization respectively. Since the Gaussian inclusion has a smooth edge it cannot be detected in segmentation of the strain image. Therefore, it is included in the background segment and cannot be recovered when the hard constraint is used. It can be seen that by using regional sparsity regularization the Gaussian inclusion in the background is also detected. Moreover, since the regularization is applied to each segment separately, the discontinuity is not a problem here. The cut-off ratio of the sparsity regularization can be chosen smaller than when the conventional sparsity regularization is used and still avoid the ringing artifacts. The optimized cut-off ratios found for this case were $r_\mu = 0.5$ for the conventional sparsity and $r_\mu = 0.3$ for the regional sparsity regularization.

As mentioned before, the segmentation of the region based on the strain image will inevitably contain errors which can drastically affect the performance of the segment-based regularization techniques. Here we show how the third suggested strain-based sparsity regularization can benefit the strain image without having to explicitly segment the region. In order to show the efficiency of the proposed method we used simulation data obtained from a region with a circular step inclusion as shown in Figure 3-3(a). We used both the strain-based selected sparsity pattern and the circular pattern for deriving the sparsity filter. We changed the number of parameters selected in the sparsity patterns and solved the inverse problem and calculated the RMS error for the shear modulus for each case. The RMS result is shown in Figure 3-7. We also added 30 dB white Gaussian noise to the displacement data and repeated the same experiment. The lines with error bars in Figure 3-7 show the mean and standard deviation of the RMS error for this case. It can be seen from this figure that the strain-based pattern selection is more efficient. For example, in the case without noise, the strain-based method using only 180 parameters leads to the same level of error as using 800 parameters in the circular pattern. Also, from the noise analysis result, we can see the strain-based method is less affected by noise than using the circular pattern. Figure 3-8 shows an example of shear modulus reconstructed result using 180 parameters with the circular sparsity pattern (a) and the strain-based pattern selection method (b). This simulation results show that by using sparsity regularization with strain-based sparsity pattern selection we can efficiently find the shear modulus parameters by solving a system of equations with fewer unknowns. For example in this case we used only 180 unknown parameters instead of $45 \times 45 = 2025$ parameters.

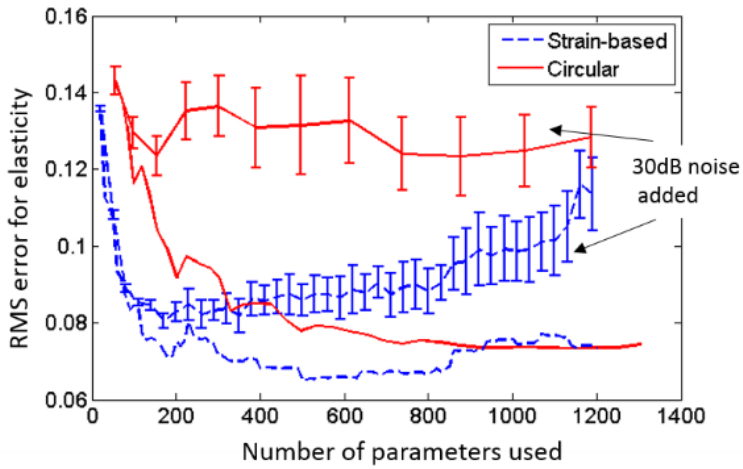

Figure 3-7. The RMS error with respect to the number of parameters used in the inverse problem using both circular sparsity pattern and strain-based sparsity pattern.

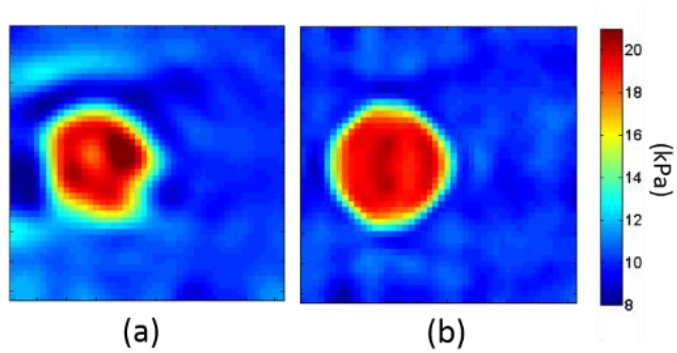

Figure 3-8. Sample shear modulus reconstruction using (a) circular sparsity pattern and (b) strain-based sparsity pattern with 180 parameters for a region of size 45×45

3.3.2 MRE experiment data

The proposed regularization techniques were also tested on the MRE experiment data captured from a CIRS elastography phantom model 049 (CIRS Inc., Norfolk, VA, USA). The phantom has 8 spherical inclusions with different values of Young's modulus and sizes. Table 2-1 shows the values of Young's modulus for the background and for the inclusions as reported by the manufacturer. The sizes of the inclusions are 10 mm and 20 mm in diameter. For this experiment the region of interest was selected around the hardest inclusion (Type IV) with 20 mm diameter. The phantom was excited with two different frequencies of 150 Hz and 200 Hz using a MRI compatible actuator developed in our lab [118]. To obtain the quasi-static strain image, a lower excitation frequency is required. Based on the elasticity of the region, the frequency of the excitation should

be low enough to generate waves with a long wavelength compared to the region of interest (at least twice the size of the region of interest). However the lowest frequency data available was 150 Hz and it was low enough to generate strain images with good contrast for the hardest inclusion in this phantom. For cases where the exciter has a large footprint and applies compressional deformation, the axial strain is used for the strain image. But for point excitations, we have observed that the maximum shear strain produces higher contrast images. The maximum shear strain γ_{max} is given by:

$$\gamma_{max} = \frac{1}{2}(\varepsilon_{11} - \varepsilon_{33}) , \tag{3-12}$$

where ε_{11} and ε_{33} are the maximum and minimum principal normal strain components calculated from the Cauchy's strain tensor. This value can be calculated only when all the three components of the displacement are available as in MRE data. Figure 3-9(a) shows the normalized reciprocal of the maximum shear strain obtained from the data with frequency of 150 Hz. As it can be seen, the inclusion is detected clearly in this image. Figure 3-9(b) shows the regions segmented manually based on the strain image and Figure 3-9(c) shows the same regions when the boundary elements are separated.

Table 3-1. Young's modulus values of inclusions and background for CIRS phantom reported by the manufacturer. (The density is equal to the density of water)

Region	Young's modulus (kPa)
Type I	6
Type II	17
Type III	54
Type IV	62
Background	29

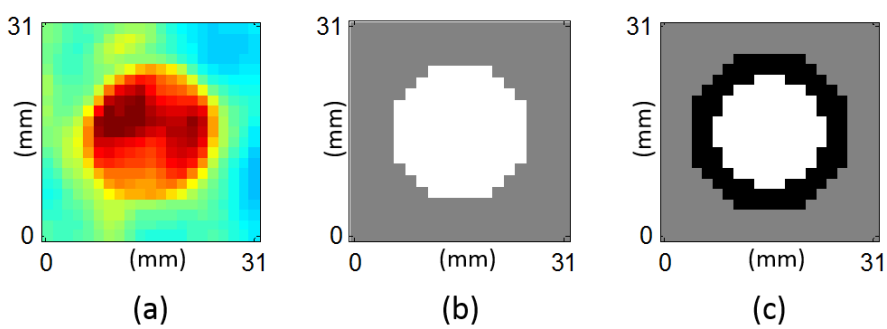

Figure 3-9. (a) Reciprocal of the maximum shear strain, (b) the segmented region based on the strain image, (c) the segmented region with separated boundary elements.

All different regularization techniques introduced in this chapter are used with mixed-FEM method to reconstruct the Young's modulus. A sample test case is shown in Figure 3-10. Since our data had a very high SNR of 28dB, in order to show the efficiency of different methods for lower SNR values, 10% white Gaussian noise was also added to the data to achieve a SNR of 20dB and used in the reconstruction. The first row shows the results for the case without noise and the second row shows the results for the case in which noise was added. In all the methods that involve sparsity regularization (i.e. all the methods except the hard constraint methods) only 10% of the total parameters in the sparse domain are used in the reconstruction. Table 3-2 shows the mean and standard deviation of the reconstructed Young's modulus of the inclusion and background, and the CNR value for each method. For the hard constraint methods since the standard deviation of the Young's modulus of regions is zero, the CNR value cannot be calculated. Figure 3-11 shows the CNR value versus the percentage of the parameters used in the sparsity domain with circular and strain-based patterns for the cases of with and without noise.

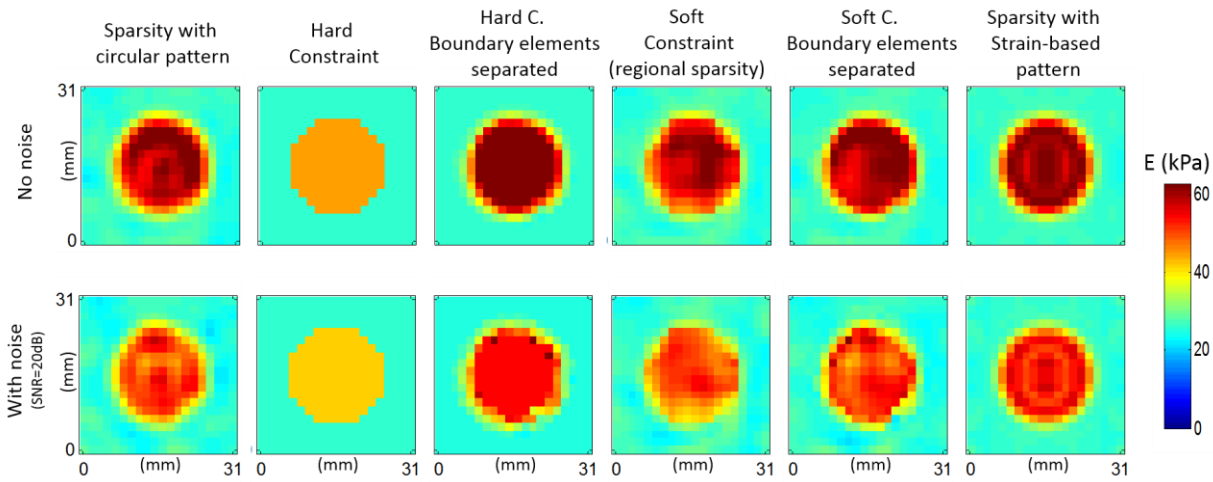

Figure 3-10. Reconstructed Young's modulus using mixed-FEM with different regularization techniques for the cases of with and without noise. The displacement SNR for the case with noise is 20 dB

As it can be seen in Figure 3-10, the misclassification error with the hard constraint method caused a significant underestimation of the inclusion's Young's modulus, as expected from simulation results. But when the boundary elements are separated, we can see that the hard constraint method produces Young's modulus values very close to the values reported by the manufacturer. This method works well for this case since the regions are actually homogeneous and assuming one value of Young's modulus for each segment is a valid assumption. Therefore using a soft constraint in this case is not necessary and it does not improve the

results compared to the hard constraint method. As it can be seen, the misclassification error has also affected the soft constraint method and separating the boundary elements improves the results in this method. However we do not see very much improvement comparing the results of the conventional sparsity regularization with a circular pattern and the regional sparsity regularization method when the boundary elements are separated. But the advantage of the regional sparsity method is that we can reduce the percentage of the parameters used in the sparsity domain much more than the conventional sparsity method without seeing the ringing artifacts in the results. In fact by reducing the number of parameters in the regional sparsity method, the results converge to the results of the hard constraint method which are the best here. Comparing the results of the conventional sparsity with the circular pattern and the sparsity with the strain-based pattern, we can see some improvements. This is also visible in the CNR plot shown in Figure 3-11.

Table 3-2. Mean and standard deviation of the reconstructed Young's modulus of the inclusion and background and CNR value using different regularization techniques. The region of interest includes only the hardest inclusion of the CIRS phantom. The displacement SNR for the case with noise is 20 dB

		Sparsity with circular pattern	**Hard constraint**	**Hard c. Boundary elements separated**	**Soft constraint (regional sparsity)**	**Soft c. Boundary elements separated**	**Sparsity with strain-based pattern**
$\boldsymbol{E_{inclusion}}$ **(kPa) (mean±std)**	No noise	59.3±3.9	45.0±0	61.4±0	56.7±4.2	59.6±2.8	59.4±2.6
	With noise	51.2±3.6	42.3±0	53.8±0	49.2±3.2	51.7±3.1	52.3±2.3
$\boldsymbol{E_{background}}$ **(kPa) (mean±std)**	No noise	28.2±6.0	27.8±0	28.4±0	28.2±5.6	28.5±6.6	28.1±5.9
	With noise	27.3±4.8	27.2±0	27.8±0	27.3±4.7	27.6±5.5	27.4±4.9
CNR	No noise	37.5	---	---	33.1	37.8	46.0
	With noise	30.9	---	---	29.6	29.1	41.1

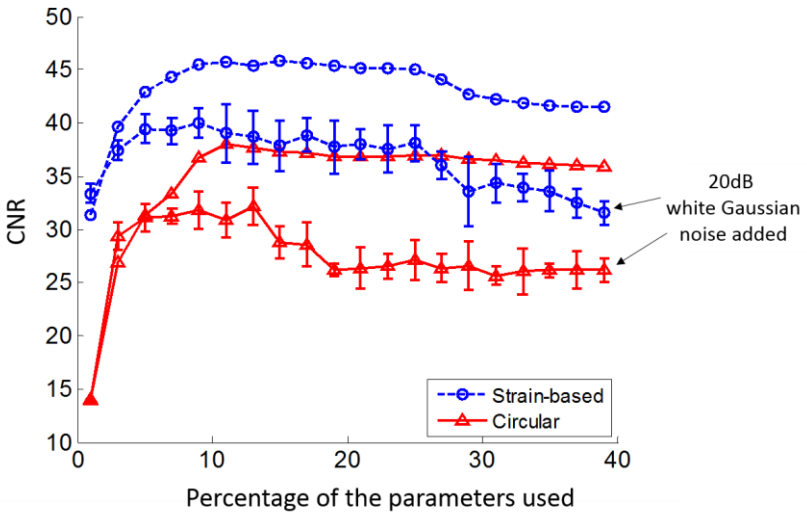

Figure 3-11. The CNR value with respect to the percentage of the parameters used in the inverse problem using both circular sparsity pattern and strain-based sparsity pattern.

3.4 Conclusion

In this chapter the feasibility of using quasi-static strain images for regularizing the elasticity parameters in the inverse problem was investigated. Three different ways using the strain image for regularization were developed and compared. The methods were tested on simulation data. The results showed that the hard constraint can significantly improve the conditioning of the inverse problem but, on the other hand, introduces errors due to region misclassification and also missing inclusions with smooth boundaries. It was shown that using soft constraint by applying regional sparsity regularization on each region separately, the problem of inclusions with smooth boundaries can be solved. But, with these methods, the misclassification of boundary elements is still problematic and separating boundary elements and leaving them without regularization is increasingly challenging as noise increases. The third method however overcomes this problems since there is no need to segment the region in this method. The results showed that selecting the sparsity pattern based on the strain image improves the robustness to noise, accuracy and efficiency of the inverse problem significantly.

Chapter 4 - A comparison of direct and iterative finite element inversion techniques in dynamic elastography

4.1 Introduction

In dynamic elastography, the tissue is excited usually by a harmonic motion and the displacement distribution is measured using ultrasound or magnetic resonance (MR) imaging techniques. Then an inverse problem is solved to find the Young's modulus distribution from the measured displacements.

The finite element method (FEM) is one of the most commonly used methods for solving the inverse problem which can be solved directly [41, 49] or iteratively [39, 43, 77]. Each of these methods has its own advantages and disadvantages which will be addressed in this chapter. In the iterative methods the inverse problem is considered as an optimization problem in which the shear modulus is changed iteratively to minimize the error between measured displacement and the simulated displacement assuming the current elasticity distribution. The iterative method was suggested for the static case first [21, 42, 43, 77] and later applied on harmonic data. In this thesis we focus on harmonic cases. Several groups have used different forms of the iterative FEM method with harmonic data. For example Van Houten et al [128] used a similar approach suggested by Kallel and Bertrand [42] in the static case, except that they applied the method on harmonic MRE data and suggested an overlapping subzone technique in which the region of interest is divided into subzones and reconstruction objective is defined as a sum of minimizations rather than a single minimization of sums. They used the standard pure displacement formulation of FEM to discretize the region and use 2D plane stress and plane strain assumptions. The minimization was performed using the Newton's method. No regularization term was added to the cost function and instead they used spatial filtering at each iteration to suppress local fluctuations in the shear modulus and achieve a convergent solution. Later they expanded their method to include Maxwellian viscoelastic behavior [129, 130] and also 3D volumes [48, 98, 131, 132].

Using the pure displacement formulation of FEM for nearly incompressible materials causes instability in the forward problem's solution. In order to avoid this problem the mixed formulation of FEM can be used instead. McGarry et al [133, 134] from the same group used mixed u-p FEM with their iterative method and

this time they also included Rayleigh damping in their formulation. Eskandari et al [39] also developed a similar iterative FEM using Voigt model for damping.

FEM has also been used to solve the inverse problem directly in both static and harmonic cases. In these methods since the discretized system of equations for the forward problem is also linear with respect to the shear modulus or Young's modulus, it can be rearranged with respect to those parameters and solved directly. Different implementations of the direct method have been suggested by different groups. In some approaches that use the pure displacement formulation [40, 41, 72, 96] the divergence of the displacement is required to be calculated. But since for nearly incompressible materials the volume change is very small, it is not feasible to calculate the divergence from the noisy displacement data. This problem can be avoided using the mixed formulation [49] as mentioned in Chapter 2.

In this chapter we try to clarify the differences and similarities between the direct and iterative FEM approaches which will help in deciding which approach to choose. For simplicity, in this chapter we do not consider the viscosity and assume pure elasticity. The iterative method used here is similar to the method used in [134] except that we do not consider viscosity. The mixed u-p formulation is used and minimization is done using Gauss-Newton method. We do not use spatial filtering as done in [134] but we use our sparsity regularization to stabilize the problem. The direct method used here is the mixed-FEM method with sparsity regularization as explained in Chapter 2.

As mentioned before, in dynamic elastography, due to the existence of inertial forces which can be calculated from the measured displacement phasors, we are able to find the absolute values of the Young's modulus. This cannot be done in static cases without measuring the boundary forces which is difficult to do in practice. That being said, one can conclude that the higher the frequency of the excitation, the more inertial forces will be present and therefore the better estimation of the absolute Young's modulus can be achieved. But there are other limitations in both methods which limit the highest frequency that can be used. One of the limitations is the data's spatial resolution which itself is limited to the acquisition time and the resolution of the imaging device. The spatial sampling frequency should be at least twice the spatial frequency of the wave to meet the Nyquist criteria. In other words, we should have at least two nodes per wavelength, preferably more. The selected resolution also determines the size of the smallest detectable inclusion in the region which is an important criteria for diagnosis such as early cancer detection.

In this chapter we present a performance analysis of the direct versus iterative FEM inverse methods. We study the performance of the two methods for different ratios of the wavelength to the voxel size. Consequently the spatial resolution and inclusion detectability of these methods are evaluated using the contrast to noise ratio (CNR) performance metric for different values of inclusion size and contrast.

4.2 Methods

The equation used in dynamic elastography is the equation of motion for linear, elastic, isotropic material in the frequency domain:

$$\left[\mu\left(u_{i,j}+u_{j,i}\right)\right]_{,j}+\left(\lambda u_{k,k}\right)_{,i}=-\rho\omega^2 u_i \tag{4-13}$$

in which u_i is the displacement phasor, ρ is the density and ω is the frequency of excitation. μ and λ are the Lamé parameters which are related to Young's modulus (E) and Poisson ratio (ν) via:

$$\mu=\frac{E}{2(1+\nu)} \quad , \qquad \lambda=\frac{\nu E}{(1+\nu)(1-2\nu)} \ . \tag{4-14}$$

Equation (4-13) can be discretized using the FEM method. Equation (4-15) shows the resulting system of equations which can be used to solve the forward problem of elasticity. The details about the forward problem formulation are presented in the Appendix A.

$$[\mathbf{K}-\omega^2\mathbf{M}]\{\boldsymbol{u}\}=\{\boldsymbol{f}\} \tag{4-15}$$

In this equation, matrix **K**, which is the stiffness matrix, is a function of Young's modulus and Poisson ratio, matrix **M** is a function of density, and $\boldsymbol{f}$ is a vector of external forces which are nonzero only on the boundary nodes. As mentioned before, for nearly incompressible materials ($\nu \rightarrow 0.5$), using this formulation with low order elements causes the locking problem in the FEM forward problem [113]. In order to overcome this problem, a mixed formulation of the FEM is used in which pressure is introduced as a new variable p [117]:

$$\lambda u_{k,k}=p \tag{4-16}$$

The resulting system of equations will be:

$$\begin{bmatrix}\widehat{\mathbf{K}}-\omega^2\mathbf{M} & \mathbf{C}\\ \mathbf{B} & -\mathbf{D}\end{bmatrix}\begin{Bmatrix}\boldsymbol{u}\\ \boldsymbol{p}\end{Bmatrix}=\begin{Bmatrix}\boldsymbol{f}\\ \mathbf{0}\end{Bmatrix}. \tag{4-17}$$

In this equation $\widehat{\mathbf{K}}$ is a function of μ and the second line is the discretized form of (4-16).

4.2.1 Iterative method

In the iterative method, the inverse problem is posed as follows: given the measured displacement $\boldsymbol{u}^m$, find the shear modulus distribution $\mu(x)$ as a function of spatial location x such that the norm of an error functional

$$\Pi(\boldsymbol{u};\mu) = \frac{1}{2}\|\boldsymbol{u}(\mu) - \boldsymbol{u}^m\|^2 \tag{4-18}$$

is minimized. This optimization problem may be solved using one of a large number of optimization algorithms such as the Gauss-Newton method or steepest descent algorithms [39, 43, 77]. In each iteration, the shear modulus parameters are updated as follows:

$$\boldsymbol{\mu}^{k+1} = \boldsymbol{\mu}^k + \Delta\boldsymbol{\mu}^k \tag{4-19}$$

where k is the iteration number and $\Delta\boldsymbol{\mu}^k$ is determined according to the method used for optimization.

In this study we use the Gauss-Newton method in which the shear modulus update is calculated using the equation below:

$$(\mathbf{J}^T\mathbf{J} + \alpha\mathbf{I})\,\Delta\boldsymbol{\mu}^k = -\mathbf{J}^T(\boldsymbol{u} - \boldsymbol{u}^m) \tag{4-20}$$

where **J** is the Jacobian matrix and **I** is the identity matrix. The Jacobian matrix is defined as:

$$\mathbf{J} = \mathbf{J}^u = [J_{ij}] = \frac{\partial u_i}{\partial \mu_j}. \tag{4-21}$$

In order to find the Jacobian matrix, equation (4-17) is differentiated with respect to the shear modulus parameters:

$$\begin{bmatrix} \widehat{\mathbf{K}} - \omega^2\mathbf{M} & \mathbf{C} \\ \mathbf{B} & -\mathbf{D} \end{bmatrix} \begin{Bmatrix} \dfrac{\partial \boldsymbol{u}}{\partial \mu_i} \\ \dfrac{\partial \boldsymbol{p}}{\partial \mu_i} \end{Bmatrix} = \begin{Bmatrix} \dfrac{-\partial \widehat{\mathbf{K}}}{\partial \mu_i}\boldsymbol{u} \\ \mathbf{0} \end{Bmatrix}. \tag{4-22}$$

Therefore the Jacobian matrix for the displacement $\mathbf{J}^{\boldsymbol{u}}$ can be obtained using the following equation:

$$\begin{bmatrix} \mathbf{J}^{\boldsymbol{u}} \\ \mathbf{J}^{\boldsymbol{p}} \end{bmatrix} = \begin{bmatrix} \widehat{\mathbf{K}} - \omega^2\mathbf{M} & \mathbf{C} \\ \mathbf{B} & -\mathbf{D} \end{bmatrix}^{-1} \begin{bmatrix} \mathbf{H} \\ \mathbf{0} \end{bmatrix}, \tag{4-23}$$

$$\mathbf{H} = [\boldsymbol{h}^1\ \boldsymbol{h}^2 \dots \boldsymbol{h}^N], \quad \boldsymbol{h}^I = \frac{-\partial \widehat{\mathbf{K}}}{\partial \mu_I}\boldsymbol{u}. \tag{4-24}$$

In each iteration of the optimization problem, the estimated displacement vector $\boldsymbol{u}$ is found by solving the forward problem (4-17) assuming the current shear modulus distribution $\boldsymbol{\mu}^k$. For solving the forward problem, since the boundary forces are not available, they are replaced with the displacement boundary condition.

There is another point about the iterative method which makes it more limited in terms of the frequency used for a specific mesh size. Looking at equation (4-17), the matrix that should be inverted for solving the forward problem in each iteration of the iterative method contains $[\widehat{\mathbf{K}} - \omega^2\mathbf{M}]$. To ensure the convergence of this problem, a minimum number of nodes per wavelength is required. It can be shown that a higher mesh density is required for the problem to converge when we have $[\widehat{\mathbf{K}} - \omega^2\mathbf{M}]$ on the left side compared to when there is only $[\widehat{\mathbf{K}}]$, and this mesh density is dependent on the wavelength. In order to be able to use a lower mesh density, since we have the measured displacements, we propose to consider the inertial forces as the external force and move $\omega^2\mathbf{M}\boldsymbol{u}$ to the right side of the equation and replace $\boldsymbol{u}$ with $\boldsymbol{u}^m$. Therefore the equation which should be solved in each iteration for the forward problem will be:

$$\begin{bmatrix} \widehat{\mathbf{K}} & \mathbf{C} \\ \mathbf{B} & -\mathbf{D} \end{bmatrix} \begin{Bmatrix} \boldsymbol{u} \\ \boldsymbol{p} \end{Bmatrix} = \begin{Bmatrix} \boldsymbol{f} + \omega^2\mathbf{M}\boldsymbol{u}^m \\ \mathbf{0} \end{Bmatrix}. \tag{4-25}$$

We call the former version of the iterative method (Iterative (I) based on (4-17)) and the new modified version (Iterative (II) based on (4-25)).

4.2.2 Direct method

As a brief review, in the direct FEM method, since equation (4-13) is linear with respect to the shear modulus, the resulting system of equations after discretization can be rearranged with respect to the shear modulus. Also, for the nearly incompressible materials, the divergence of the displacement is almost zero and difficult to calculate from the noisy data, so again the product of λ and the divergence is defined as a new variable p, and solved together with the shear modulus. Therefore the resulting system of equations is:

$$[\mathbf{A} \quad \mathbf{C}] \begin{Bmatrix} \boldsymbol{\mu} \\ \boldsymbol{p} \end{Bmatrix} = \{\acute{\boldsymbol{f}}\} \tag{4-26}$$

where the term $\mathbf{A}\,\boldsymbol{\mu}$ is the discretized form of the first term in (4-13) and $\mathbf{C}\,\boldsymbol{p}$ the second term and $\acute{\boldsymbol{f}}$ the term on the right hand side of the equation. $\acute{\boldsymbol{f}}$ also contains the external forces which are nonzero only on the boundary nodes. But since those forces are not available, the equations related to boundary nodes are removed from the system of equations and there is still a sufficient number of equations left to solve for the unknown shear modulus and relative pressure parameters.

4.2.3 A comparison of the iterative and direct methods

As shown in previous sections, the system of equations used in the direct (4-26) and iterative (4-25) methods are both derived from the same equation (4-13). By comparing these equations we can conclude that:

$$\mathbf{A}\boldsymbol{\mu} = \widehat{\mathbf{K}}\boldsymbol{u}^m \tag{4-27}$$

$$\acute{\boldsymbol{f}} = \boldsymbol{f} + \omega^2 \boldsymbol{M}\boldsymbol{u}^m \,. \tag{4-28}$$

This means the equations used in both direct and iterative methods are the same but arranged in a different way. The most important difference between the iterative and direct methods is the way the equations are solved or the way the optimization problem is defined. We can consider that both methods perform a constrained optimization. In the iterative method, the optimization problem is defined as:

$$\begin{gathered} \min_{\mu} \Pi(\boldsymbol{u};\mu) = \frac{1}{2}\|\boldsymbol{u}(\mu) - \boldsymbol{u}^m\|^2 \\ subject\ to \\ \left[\mu\left(u_{i,j} + u_{j,i}\right)\right]_{,j} + p_{,i} = -\rho\omega^2 u_i \end{gathered} \tag{4-29}$$

But in the direct method, the optimization problem is defined as:

$$\begin{gathered} \min_{\mu,p} \left\| \left[\mu\left(u_{i,j} + u_{j,i}\right)\right]_{,j} + p_{,i} + \rho\omega^2 u_i \right\|^2 \\ subject\ to \\ \boldsymbol{u} = \boldsymbol{u}^m \end{gathered} \tag{4-30}$$

Therefore in these problems the objective function and the constraint are swapped. However the minimization in (4-30) is not done by the usual methods used for solving constrained optimization problems. This optimization problem can be solved by just substituting $\boldsymbol{u}_m$ with $\boldsymbol{u}$ in the objective function and solving the resulting system of equations which would be (4-26).

Therefore, in the ideal case where we have no noise in displacements and the optimization is done perfectly and reaches the global minimum, which is zero, both methods will reach to the same final result but from different paths. However the optimization problems are always terminated before getting to a zero minimum. In addition, the regularization terms used in both methods also cause deviations between the two method's results. These differences make them behave slightly differently in different situations.

There is also another important difference between the two sides of equation (4-27). Normally in FEM the derivatives of the parameters are estimated using the derivatives of the shape functions. For example if the displacement u_i is estimated by $u_i = \sum_k \bar{u}_i^k \psi_k$ where $\bar{u}_i^k$ are the displacement nodal values and ψ_k are the displacement shape functions, the derivatives of the displacement are estimated using $u_{i,j} = \sum_k \bar{u}_i^k \psi_{k,j}$. This

means an exact polynomial fit to the displacement nodal values and the derivatives of the fitted polynomial are used to approximate the derivatives of the data. Curve-fitting can also be done using least-squares where smoothing is required due to the existence of noise. In situations where the parameter to be differentiated is part of the unknowns of the resulting system of equations, for example the displacement in the forward problem, the exact fit should be used to avoid an underdetermined system. This is what is happening on the right hand side of equation (4-27) which is used in the forward problem. But in the inverse problem since we have the displacements from the measurement and it is not part of the unknowns, it is better to use the least-squares to find the derivatives. In that case the left hand side of equation (4-27) which is used in the direct inverse problem can be different from the right hand side and therefore the reconstruction results using direct and iterative methods will be different.

Another difference between the direct and iterative method is that, in the iterative method, the value of either the Poisson ratio or the Lamé parameter λ should be assumed for solving the forward problem in each iteration, but in the direct method those values are not required. And finally the last difference is the computational cost of these methods. In each iteration of the iterative method one forward problem needs to be solved. For example, for a 2D case, if a mesh grid of size $N \times N$ is used, the number of unknowns for each forward problem is approximately $3N^2$. Also, in each iteration, another system of equations with the same size should be solved to find the Jacobian matrix. Finally the entire processing time of each step should be multiplied by the number of iterations. But in the direct method only one system of equations with $2N^2$ unknowns needs to be solved. For example Figure 4-12 shows the processing time required to solve the inverse problem using the direct and iterative methods for a 2D region with grid size of $N \times N$. The processing is done in Matlab® using a standard (Intel® Core2 Duo 2.93GHz) PC with 8GB RAM.

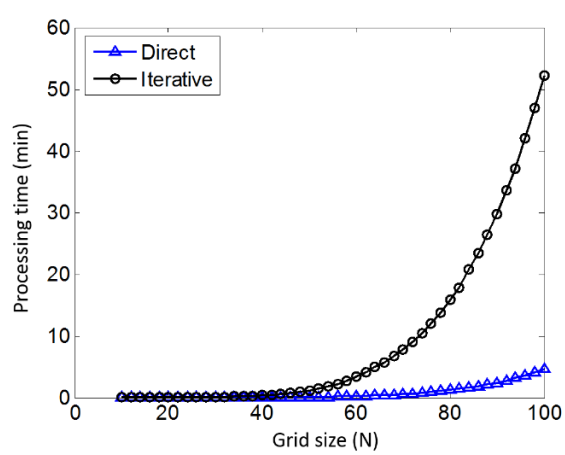

Figure 4-12. The processing time required to solve the inverse problem using the direct and iterative methods for a 2D region with mesh grid size of $N \times N$.

4.2.4 Regularization

The inverse problem of elasticity is usually ill-conditioned and it is necessary to use regularization techniques in order to stabilize the problem. We introduced sparsity regularization in Chapter 2 in which the original variables are transformed into another set of variables using a sparsifying transformation (e.g. DCT) which results in a sparse representative of the original variables. Therefore, in the new domain, only a small number of the parameters have significant magnitude and the rest of the parameters can be removed, resulting in a system of equations with fewer unknowns and greater stability. Basically, in this method, the original parameters are replaced with their approximations as follows:

$$\boldsymbol{x} \approx \mathbf{R}\boldsymbol{X}^* \tag{4-31}$$

in which $\boldsymbol{x}$ is the original parameter, $\mathbf{R}$ is the sparsity filter and $\boldsymbol{X}^*$ is the truncated new parameter in the transformed domain. This regularization can be applied to the direct method as follows:

$$[\mathbf{AR}_1 \quad \mathbf{CR}_2]\begin{Bmatrix}\boldsymbol{\mu}^* \\ \boldsymbol{p}^*\end{Bmatrix} = \begin{Bmatrix}\acute{\boldsymbol{f}} \\ 0\end{Bmatrix}. \tag{4-32}$$

Sparsity regularization can also be used with the iterative method by replacing the Jacobian matrix $\mathbf{J}$ with $\mathbf{J}^*$ which is calculated from $\mathbf{J}$ as follows:

$$\mathbf{J}^* = \mathbf{JR} \tag{4-33}$$

Therefore the updated shear modulus will be $\Delta\boldsymbol{\mu}^*$ which should be converted back to the original parameter using (4-31). For all the simulations in this chapter, sparsity regularization with the circular sparsity pattern was used. The cut-off ratio of $r = 0.8$ was used which means the radius of the circular pattern is 0.8 times the size of the domain side.

4.3 Results

4.3.1 Comparison

First we compare the performance of Iterative (I), Iterative (II) and the direct method for the case without noise. In order to show the similarities of the direct and iterative method, first we use the direct method with derivatives taken using the exact fit similar to what happens in the iterative method. We used simulation data obtained from the model shown in Figure 4-13.

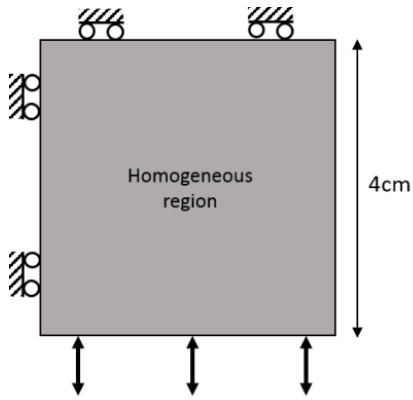

Figure 4-13. Schematic showing the shape and boundary conditions of the model used for generating 2D synthetic data.

To have a single wavelength over the entire region, we used a homogeneous region with a Young's modulus of 10 kPa. The simulation was performed on a fine mesh of size 200*200 and the displacement data was down-sampled into a coarser mesh (40*40) and used in the inverse problem. The simulation was run for different values of the excitation frequency, ranging from 10Hz to 400Hz, and the inverse problem was solved using direct and iterative methods for each case and the RMS error was calculated. The elements used in both methods are 4-node rectangular linear elements. Figure 4-14 shows the results. In this plot the RMS error is plotted versus the ratio of the voxel size (L) to the wavelength (Λ) : $r_m = L/\Lambda$. The wavelength is calculated from the shearwave speed ($\Lambda = \frac{2\pi}{\omega}\sqrt{\frac{\mu}{\rho}}$).

From Figure 4-14 we can see that, as mentioned before, Iterative (I) has comparable errors to the other methods only for lower ratios of r_m , $r_m < 0.035$, and it becomes unstable for ratios above this value. This means for this method to work we need at least 30 nodes per wavelength. This limitation does not apply to the Iterative (II) or the direct method. However this number is only for this specific type of the element used and it will be different for higher order elements. Therefore this result shows that a lower mesh density is required using Iterative (II) instead of Iterative (I). From hereafter we use only the Iterative (II) for the rest of the study since it always outperforms Iterative (I).

From Figure 4-14 we can also see that both direct and iterative methods show increasing errors at very low frequencies which was predictable as all dynamic methods rely on inertial forces which decrease with frequency. As the ratio r_m increases, the RMS error for both methods increases with a gentle slope. Also this result shows when the displacement derivatives are taken the same way in iterative and direct methods the results of these methods almost match.

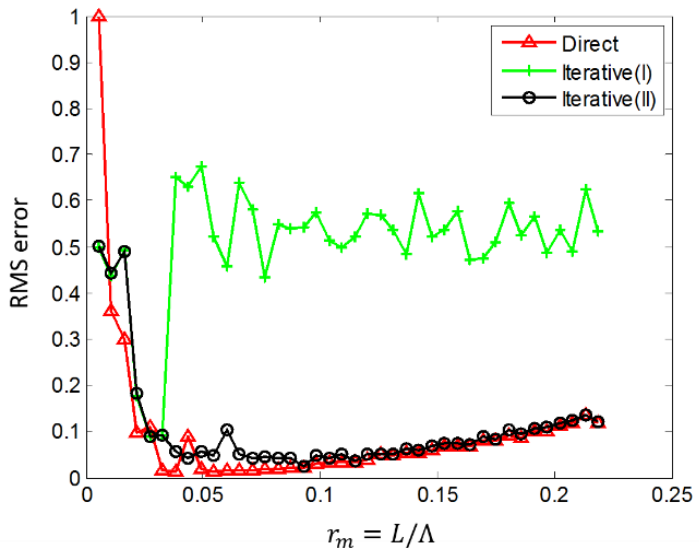

Figure 4-14. RMS error versus the ratio of voxel size / wavelength for different methods.

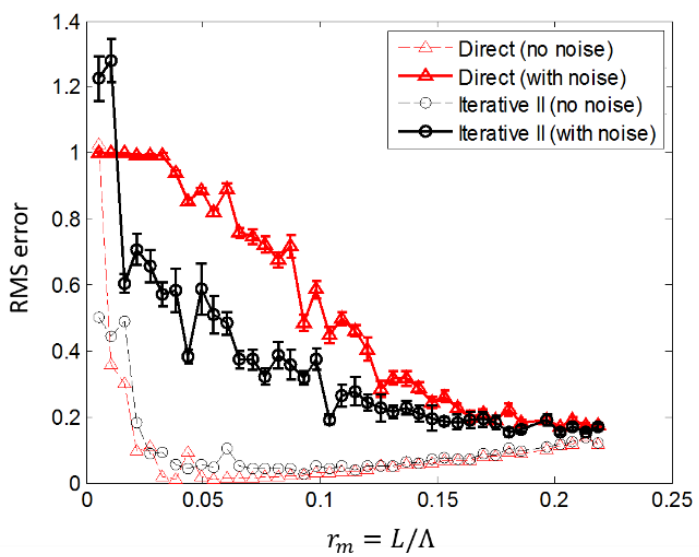

Figure 4-15. RMS error versus the ratio of voxel size / wavelength for different methods. (White Gaussian noise was added to achieve an SNR of 25 dB)

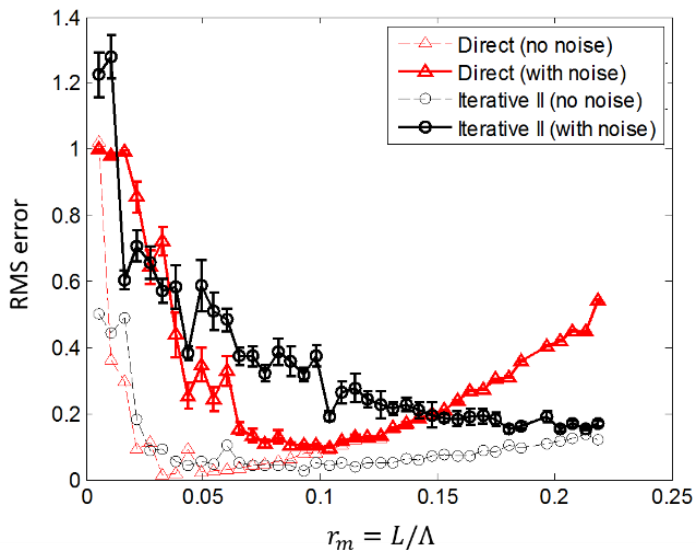

Figure 4-16. RMS error versus the ratio of voxel size / wavelength for different methods. For the direct method the derivatives are taken using least-squares. (White Gaussian noise was added to achieve an SNR of 25 dB)

In order to investigate the effect of noise, white Gaussian noise was added to the displacement data to achieve a SNR of 25dB and the same experiment was repeated. The results are shown in Figure 4-15. The solid lines are the results after adding the noise and the dash lines are the previous results without noise. It can be seen that both methods are very sensitive to noise. The sensitivity is greater at lower r_m ratios and it becomes less when the ratio increases. However the results of the two methods do not match as for the case without noise and it seems the iterative method is less sensitive to noise than the direct method with the derivatives taken using an exact fit. Conversely Figure 4-16 shows how the least-squares fit, instead of an exact fit, can improve the stability of the direct method compared to the iterative method. This figure summarizes the same experiment except that the direct method calculates the derivatives by fitting a first order polynomial onto a window of $3 \times 3 \times 3$ and the value is assigned to the center node. Then the derivatives are interpolated over the whole region using their own shape functions as $u_{i,j} = \sum_k \bar{u}_{i,j}^k \psi_k$. As it can be seen, using the least-squares fit makes the direct method more robust to noise but on the other hand gives rising errors for higher r_m ratios. This in fact is not a random error; it is caused from a systematic shift in estimated Young's modulus. Figure 4-17 shows the mean and standard deviation of the estimated Young's modulus using direct method. As it can be seen, the estimated value increases as the ratio r_m increases. This effect is from the error in estimating the derivatives. Basically, as the ratio r_m increases, the variation or the curvature of the displacement phasor also increases within a specific window size used for curve fitting and the fit cannot capture the curvature properly. This leads to an underestimation of the Laplacian of the displacement which causes the increase in the shear modulus.

These results suggest that, when using the robust form of the direct method with least squares fit, there is an optimal value for the frequency of the excitation which results in a minimum error. This optimal value depends on the noise level of the displacement data. For example for the SNR of 25dB the optimal ratio found is $r_m = 0.1$ which means about 10 nodes per wavelength. In practice, the region of interest may not be homogenous for most of the cases but we can always set the parameters based on the average shear modulus of the background which we may know from previous statistics. Therefore having the optimal ratio r_m^{opt} and the average shear modulus μ_{ave} we can find the optimal value of $L\omega$ as follows:

$$L\omega = 2\pi\, r_m^{opt} \sqrt{\frac{\mu_{ave}}{\rho}}. \tag{4-34}$$

Then we pick a value for either L or ω based on the limits on the maximum possible frequency or maximum possible resolution (minimum L) and find the value of the other parameter based on (4-34).

This experiment is also repeated for a region with a circular inclusion as shown in Figure 4-18. The Iterative (II) and the direct method with least-squares fit are used for the reconstruction. The results are shown in Figure 4-19. For this graph the wavelength Λ is calculated based on the background shear modulus. In this figure a similar pattern to the homogeneous case is observed. Therefore although there is a harder inclusion in the region the optimal ratio r_m is almost unchanged, so equation (4-34) can still be applied.

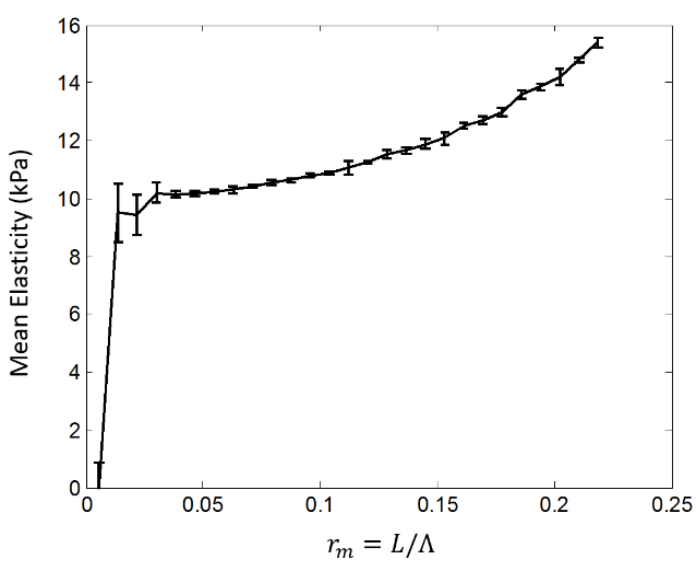

Figure 4-17. Average Young's modulus versus the ratio of voxel size / wavelength using the direct method with least-squares fit.

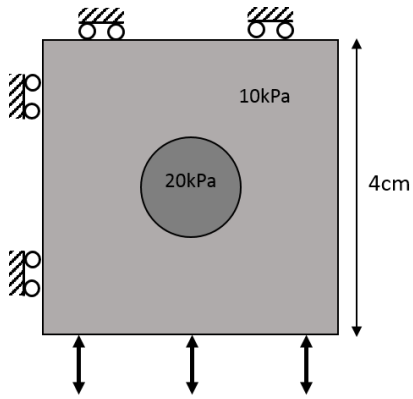

Figure 4-18. Schematic showing the shape and boundary conditions of the model with circular inclusion used for generating 2D synthetic data.

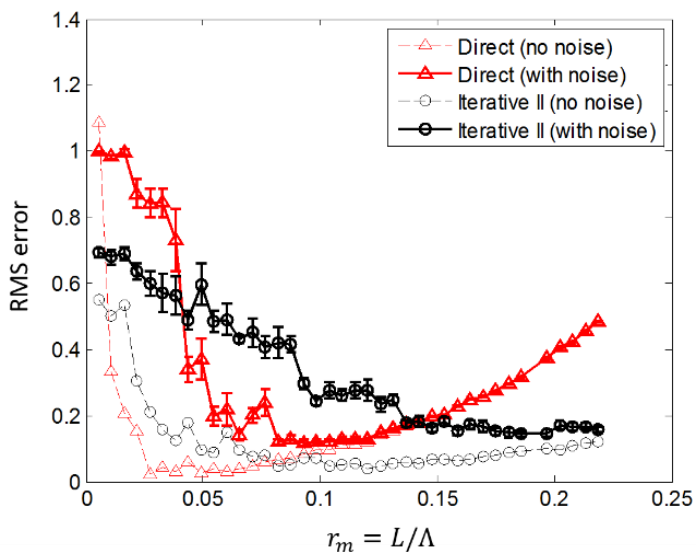

Figure 4-19. RMS error versus the ratio of voxel size / wavelength for the region with circular inclusion using different methods. For the direct method the derivatives are taken using least-squares. (White Gaussian noise was added to achieve an SNR of 25 dB)

4.3.2 Detectability and spatial resolution

In the previous section we showed that the direct method with an exact fit for calculating derivatives has similar behaviour as the iterative method and using the least-squares fit in the direct method makes this method more robust to noise but on the other hand causes a shift in estimated Young's modulus at higher r_m ratios. In this section we investigate the detectability and spatial resolution of the direct method with either exact fit and least-squares fit. We assume the iterative method would give a similar result as the direct method with exact fit based on previous results. The simulation is done at two ratios of $r_m = 0.1$ and $r_m = 0.2$ for the

cases of with and without noise. The metric used to measure the detectability of an inclusion in an elastogram is the contrast to noise ratio (CNR). This metric is defined as follows:

$$CNR = \frac{2(m_1 - m_2)^2}{\sigma_1^2 + \sigma_2^2} \tag{4-35}$$

where m_1 and m_2 are the means and σ_1 and σ_2 are the standard deviations of the estimated Young's modulus of the background and the inclusion.

For this study we used the same model shown in Figure 4-18 and changed the size and contrast of the inclusion and generated the synthetic data which was later down-sampled and used in the inverse problem with the mentioned methods. The diameter of the inclusion varies from 0.4mm to 15 mm and the inclusion contrast varies from 1.1 to 3. In order to make the result independent of the mesh size used in the inverse problem, the inclusion diameter is converted to the units of voxels by dividing it by the voxel size. For the case with noise, white Gaussian noise was added to the data to achieve an SNR of 25 dB.

Figure 4-20 and Figure 4-21 show the CNR results for the direct method with exact fit and least-squares fit respectively. In these figures, the first row images are for the case without noise and the second row images are for the case with noise. In the first column, the r_m ratio is 0.1, and in the second column, the ratio is 0.2. For easier comparison, the contour lines at the CNR values of 1 and 2 are also displayed in these images as the CNR values less than 1 means the inclusion is not detectable at all. It is apparent from these figures that the direct method with exact fit has a higher CNR value compare to the direct method with least-squares fit in the absence of noise. Also, the CNR increases at higher frequency but, as expected from previous results, the direct method with exact fit is much more sensitive to noise evidenced by how the CNR value drops significantly when the noise is added. From Figure 4-21 we can see that, for the direct method with least-squares fit, the CNR value changes very little when the noise is added and also, as opposed to the method with exact fit, increasing the frequency only decreases the CNR value slightly.

In order to have a better sense of the spatial resolution of the reconstructed Young's modulus, the reconstructed profiles of the inclusions are also plotted for these methods. Figure 4-22 and Figure 4-23 show the profile of the inclusion reconstructed using the direct method with exact fit and direct method with least-squares fit respectively for different inclusion sizes and contrasts. Each profile is calculated by radially averaging the Young's modulus around the center of the inclusion. The plots on the left side show inclusions with the contrast of 2 and different sizes; the plots on the right side show inclusions with the radius of 5 pixels and different contrasts.

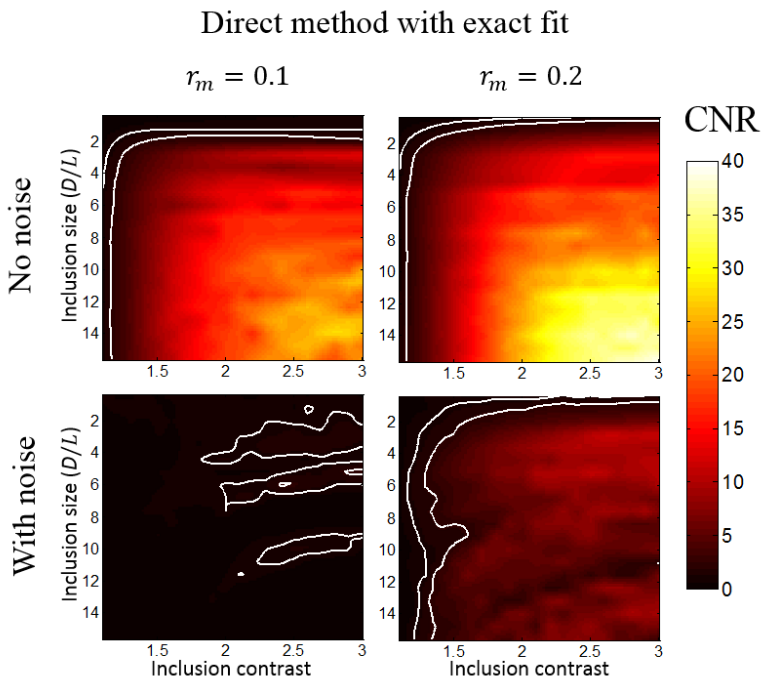

Figure 4-20. The CNR value for different sizes of inclusion and inclusion contrasts using the direct method with exact fit. The contour lines at the CNR values of 1 and 2 are also displayed in these images

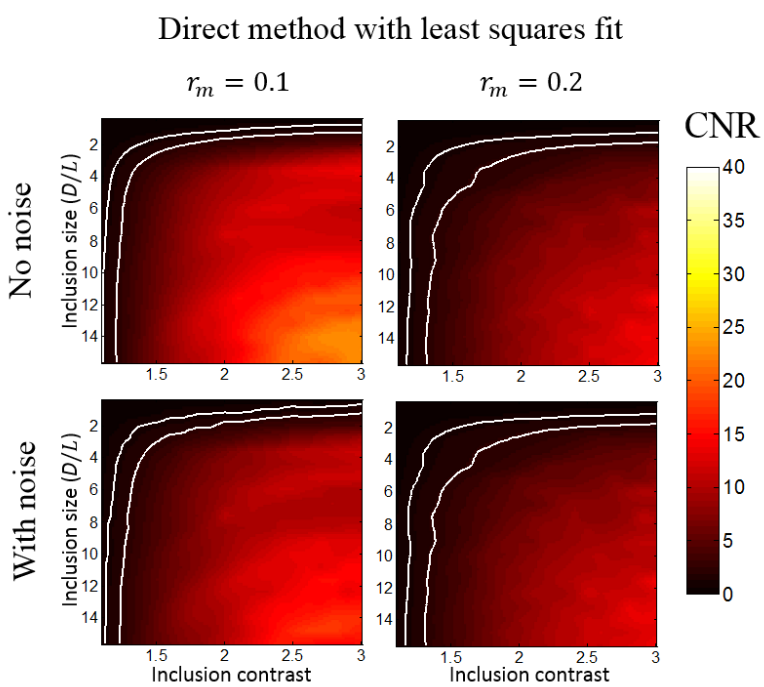

Figure 4-21. The CNR value for different sizes of inclusion and inclusion contrasts using the direct method with least-squares fit. The contour lines at the CNR values of 1 and 2 are also displayed in these images

As it can be seen from these figures, the edge of the inclusion is sharper when the exact fit is used compared to when the least-squares fit is used. In order to measure this value, two endpoints of the edge ramp, where the curve has maximum curvature, are chosen and the distance between them is measured. These values are 2.5 pixels for the direct method with exact fit and 3.4 pixels for the direct method with least-squares fit and it is mostly independent of the contrast or size of the inclusion. Of course these values are dependent on the least-squares kernel size and also the regularization parameters. These measured values determine the minimum size of an inclusion that these methods can correctly estimate its peak value or the closest distance two inclusions can be without merging into each other in the reconstructed result. Although this result shows that the direct method with exact fit has less blurring of the boundary, as shown in Figure 4-20, this method is more sensitive to noise.

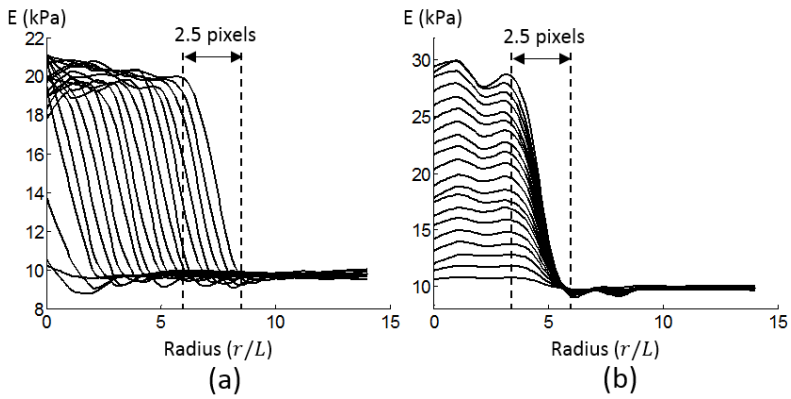

Figure 4-22. The radially averaged profile of the reconstructed inclusion using the direct method with exact fit (a) inclusions of different sizes and contrast of 2 (b) inclusions of different contrast and radius of 5 pixels.

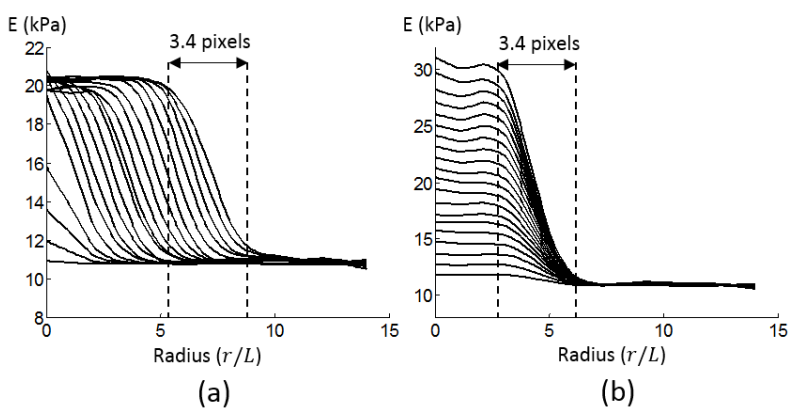

Figure 4-23. The radially averaged profile of the reconstructed inclusion using the direct method with least-squares fit (a) inclusions of different sizes and contrast of 2 (b) inclusions of different contrast and radius of 5 pixels.

4.4 Conclusion

In this study, the two forms of direct and iterative FEM inversion techniques used in dynamic elastography were compared. It was shown that the formulations used in these methods are quite similar but solved in a different way. The results show that if (in the direct method) the displacement derivatives are calculated using an exact fit, the reconstruction results are quite similar to the iterative method but it seems the iterative method has a lower RMS error compared to this version of the direct method in the presence of noise, although the errors are quite high in both cases. It was shown that using a least-squares fit in the direct method makes this method more stable and accurate compared to the iterative method in the presence of noise but, on the other hand, because of using a larger kernel size it increases the effect of elasticity overestimation at higher frequencies and therefore limits the acceptable wavelength to the voxel size ratio around the optimal ratio. We proposed a formula for choosing the best frequency and data resolution based on the optimal r_m ratio and the average shear modulus of the region. However, choosing the maximum frequency is also limited due to the existence of viscosity, which limits the penetration of mechanical wave at higher frequencies since higher frequency waves experience greater attenuation. This fact is an important limiting factor in achieving higher spatial resolution elastograms in real tissue applications.

Also the detectability study results show the higher stability of the direct method with least-squares fit compared to the method with exact fit which is similar to the iterative method but on the other hand causing a lower CNR value due to the smoothing effect and overestimation of the softer material.

The presented results in this chapter show that overall the direct method with least-squares fit outperforms the iterative method in terms of stability and accuracy in presence of noise. Also considering the fact that the performance of the iterative method is dependent on the initial guess of the elasticity and also that there is a significant difference in the computational cost of these methods, makes it easier to choose between these methods. However it should be mentioned that the only case for which the iterative method must be used and the direct method cannot be used is when a nonlinear elasticity model is used.

Chapter 5 - Curl-based finite element reconstruction of the shear modulus without assuming local homogeneity

5.1 Introduction

As mentioned in previous chapters, the linear elastic wave equation is typically used to relate the measured displacements with the mechanical properties of the tissue. In the frequency domain, it is given by (repeated from (1-7) and (2-1)):

$$\nabla \cdot \left[\mu\left(\nabla \boldsymbol{u} + (\nabla \boldsymbol{u})^{\mathrm{T}}\right) + \lambda(\nabla \cdot \boldsymbol{u})\mathbf{I}\right] = -\rho\omega^2 \boldsymbol{u} \tag{5-1}$$

There are several approaches for reconstruction of tissue elasticity based on the wave equation. In many previous approaches it is assumed that the shear modulus is locally constant or that the spatial derivatives of the shear modulus are negligible [91, 94, 120, 135, 136]. This simplifies the wave equation and the inverse problem but causes biases in regions where the elasticity variation is high [137]. The other simplifying assumption which is usually made is the incompressibility assumption ($\nabla . \boldsymbol{u} = 0$) [52, 82, 91, 138]. This removes the coupling term in the wave equation and results in a Helmholtz equation in which the displacement components are decoupled. Therefore, only one displacement component is sufficient to solve the inverse problem and to find the shear modulus. This is particularly useful with ultrasound imaging of the axial displacement of tissue. Although the divergence of the displacement is small for nearly incompressible materials, λ is large, and therefore their product ($\lambda \nabla . \boldsymbol{u}$, the pressure term) is not negligible. Several groups use finite elements with a standard formulation in which the incompressibility assumption is not used [39, 41-43, 129]. These methods are either iterative or direct. In iterative methods, the forward problem needs to be solved at each iteration. Using a standard pure displacement FEM formulation with a Poisson's ratio near 0.5 causes the so-called 'locking' problem which results in poor convergence and instability. Therefore such methods typically use arbitrarily lower values of Poisson's ratio. In addition, in such direct methods, the divergence of the displacement is required but cannot be calculated from noisy displacement data since it is beyond typical measurement accuracy. The mixed displacement-pressure FEM has been used to overcome this problem [49], and explored in Chapters 2, 3, 4.

Park and colleagues [49] introduced a direct "mixed FEM" technique in which the entire product $\lambda\nabla.\boldsymbol{u}$ is considered as unknown. They solved for both shear modulus and pressure distribution directly and showed that neglecting the pressure term causes artifacts and underestimation of the shear modulus. In their method, pressure parameters are added to the unknowns which results in higher computational cost and processing time than when only the shear modulus is unknown. Adding the pressure term also increases the ratio of the number of unknowns to the number of the equations which degrades the condition number of the inverse problem. In Chapter 2, a sparsity regularization technique was combined with the mixed-FEM method. The sparsity regularization was shown to be more efficient and robust compared with the traditional Tikhonov regularization technique.

An alternative solution to mixed-FEM is to eliminate the pressure term explicitly in the equations by taking the curl of the wave equation [93]. In this method, first the local homogeneity assumption is used, and then the curl operator is applied to remove the pressure term. The homogeneity assumption leads to imaging biases, while taking the curl leads to third order derivatives of the displacement data and associated noise amplification. In order to consider the spatial variation of the shear modulus, Sinkus and co-workers [137] took the first order spatial derivatives of the real-part of the shear modulus into account by estimating the real part of shear modulus with a linear function, using this in the wave equation and then applying the curl operator to remove the pressure term. But in that method, only the variation of the real part of the shear modulus is considered. Furthermore, the third order spatial derivatives of the displacement are still required.

Reducing the number of unknowns and increasing the computational speed by eliminating the pressure parameters motivated us to combine the direct FEM introduced in Chapter 2 [36] with the idea of using the curl operator [93]. In this chapter, we develop a new curl-based FEM method (c-FEM) based on taking the curl of the original form of the wave equation without using the assumption of local homogeneity. Then we solve the inverse problem directly for the shear modulus using the finite element method, without having to consider the pressures as unknowns. We employ our sparsity regularization [36] when solving the inverse problem.

In addition, having only the shear modulus as the unknown enables us to use multi-frequency techniques to improve the conditioning of the inversion. Multi-frequency approaches have been shown to be effective in overcoming the lack of information at amplitude nulls [120, 138, 139]. In this approach the data from different frequencies are combined and solved simultaneously for the unknowns. Since in the mixed-FEM method both the shear modulus and pressure are considered as unknowns and the pressure distribution changes with frequency, in order to combine the equations from different frequencies, we have to add one set of pressure parameters for each frequency. Therefore, the number of unknowns also increases as we add more equations, which does not really improve the condition of the problem. But with the new curl-based FEM, we

have only the shear modulus as an unknown; since it does not change with frequency, the equations can be combined without having to increase the number of unknowns.

5.2 Methods

First we start with the equation of motion for linear isotropic elastic materials with a time harmonic excitation at frequency ω (5-1). This equation in indicial notation is as follows:

$$\left[\mu\left(u_{i,j}+u_{j,i}\right)\right]_{,j}+\left(\lambda u_{k,k}\right)_{,i}=-\rho\omega^2 u_i \qquad in\ \Omega \tag{5-2}$$

where Ω is the region of interest with boundary Γ and the displacement field $\boldsymbol{u}(x)$ is measured as a function of position ($x \in \Omega$). μ and λ are the Lamé parameters and the Einstein summation convention implies that repeated indices are summed over.

$\lambda u_{k,k}$ is called the pressure term. Since the divergence of displacement for nearly incompressible materials is almost zero ($u_{k,k} \approx 0$), this term cannot be calculated reliably directly from the noisy displacement data. In (5-2), the gradient of the pressure term appears. Since the curl of the gradient of any scalar function is always zero, the curl operator can be used to eliminate the pressure term.

In previous work using this method [93], first the local homogeneity assumption was used which results in:

$$\mu u_{i,jj}+(\lambda+\mu)\left(u_{k,k}\right)_{,i}=-\rho\omega^2 u_i\,. \tag{5-3}$$

After applying the curl operator, the second term, which is the gradient of a scalar field, was eliminated and resulted in the Helmholtz equation

$$\mu q_{i,jj}=-\rho\omega^2 q_i\,, \tag{5-4}$$

in which **q** is the curl of the displacement. This equation can be solved for the shear modulus at each point using either algebraic inversion of the wave equation [46], [91] or a finite element method.

5.2.1 Curl-based FEM without homogeneity (c-FEM)

As a new approach to this problem, in order to consider the spatial derivatives of the shear modulus, we remove the local homogeneity assumption and apply the curl operator directly to the original equation of motion (5-2). Therefore, we obtain the following equation:

$$\varepsilon_{lmi}\left[\mu\left(u_{i,j}+u_{j,i}\right)\right]_{,jm}=-\rho\omega^2\varepsilon_{lmi}u_{i,m}\ , \tag{5-5}$$

where ε denotes the Levi-Civita symbol. The second term in (5-2) which is the gradient of the pressure is eliminated by taking the curl. We use the FEM to discretize (5-5) in order to solve it numerically. According to Galerkin's method [117], this equation can be written in a weak formulation or integral form, which involves multiplying (5-5) with a test function w and integrating over the entire domain Ω.

$$\int_{\Omega}\ \varepsilon_{lmi}\left[\mu\left(u_{i,j}+u_{j,i}\right)\right]_{,jm}w\ \mathrm{d}\Omega=-\rho\omega^2\int_{\Omega}\ \varepsilon_{lmi}u_{i,m}\ w\ \mathrm{d}\Omega \tag{5-6}$$

Integrating by parts both sides of the (5-6) we obtain:

$$\begin{aligned}-\int_{\Omega}\ \varepsilon_{lmi}\left[\mu\left(u_{i,j}+u_{j,i}\right)\right]_{,j}w_{,m}\ \mathrm{d}\Omega+\int_{\Gamma}\ \varepsilon_{lmi}\left[\mu\left(u_{i,j}+u_{j,i}\right)\right]_{,j}n_m w\ d\Gamma\\ =\rho\omega^2\int_{\Omega}\ \varepsilon_{lmi}u_i\ w_{,m}\ \mathrm{d}\Omega-\rho\omega^2\int_{\Gamma}\ \varepsilon_{lmi}u_i\ n_m\ w\ \mathrm{d}\Gamma\end{aligned} \tag{5-7}$$

where $\boldsymbol{n}$ is the unit normal vector on the boundary Γ. If the test function w has a zero value on Γ, the boundary integrations in (5-7) become zero. Then the first term in the left-hand-side of (5-7) can be integrated by parts again which results in:

$$\int_{\Omega} \varepsilon_{lmi}\mu\left(u_{i,j}+u_{j,i}\right)w_{,mj}\,\mathrm{d}\Omega - \int_{\Gamma} \varepsilon_{lmi}\mu\left(u_{i,j}+u_{j,i}\right)n_j w_{,m}\,d\Gamma = \rho\omega^2 \int_{\Omega} \varepsilon_{lmi}u_i\, w_{,m}\,\mathrm{d}\Omega \tag{5-8}$$

If, in addition to the zero boundary value, the test function also has zero first order derivatives on Γ, the second term in the left-hand-side of (5-8) would also become zero. Therefore, after performing the integration by parts twice, only the first derivatives of the displacement remain in the equation. The next step is to replace the infinite dimensional problem with a finite dimensional version:

$$\int_{\Omega} \varepsilon_{lmi}\mu^h\left(u^h_{i,j}+u^h_{j,i}\right)w^h_{,mj}\,\mathrm{d}\Omega = \rho\omega^2 \int_{\Omega} \varepsilon_{lmi}u^h_i\, w^h_{,m}\,\mathrm{d}\Omega \tag{5-9}$$

where μ^h, u^h_i and w^h are finite dimensional approximations of the actual values. Within each element of the discretized domain, these values are interpolated from the element nodes by using shape functions:

$$\mu^h(x) = \sum_{\alpha=1}^{N_\mu} \bar{\mu}_\alpha \psi^\mu_\alpha(x) \tag{5-10}$$

$$\boldsymbol{u}^h(x) = \sum_{\beta=1}^{N_u} \overline{\boldsymbol{u}}_\beta \psi^u_\beta(x) \tag{5-11}$$

$$\nabla\boldsymbol{u}^h(x) = \sum_{\beta=1}^{N_u} \overline{\nabla\boldsymbol{u}}_\beta \psi^u_\beta(x) \tag{5-12}$$

where ψ^μ_α and ψ^u_β are shape functions for the shear modulus and displacement respectively, and $\bar{\mu}_\alpha$, $\overline{\boldsymbol{u}}_\beta$ and $\overline{\nabla\boldsymbol{u}}_\beta$ are the nodal values of the parameters. N_μ, N_u are the numbers of shear moduli and displacement nodes, respectively. The shape functions have values of one at their corresponding node and value of zero at all other nodes. As mentioned in Chapter 4, when solving the forward problem with the FEM, the gradient of the

displacement $\nabla \boldsymbol{u}^h$ is approximated by differentiating the displacement shape functions in (5-11). However, in the inverse FEM problem, when we have noisy displacement measurements, if we use the shape functions to calculate the derivatives, the noise is amplified because we are doing an exact fit to the noisy data and then taking the derivatives of the fitted function. There are two solutions to this problem: one is to filter the data first and then use it with usual FEM formulation; the other is to calculate the derivatives by using other robust methods such as a least-squares curve-fitting method and then interpolate the derivatives using basis functions. We found the second method to be more accurate and robust (Chapter 2, Chapter 4) [36]. Therefore, the first order derivatives of the displacement are calculated by fitting a first order polynomial on small overlapping windows using the least squares method. Then, the same shape functions used for displacements are used to approximate the derivatives between the nodes.

As mentioned before, the test functions w^h and their derivatives should be zero on the boundaries. Moreover, since the second order derivatives of the test function appear in the formulation, the test functions should be polynomials of degree higher than one. The base functions that we use here to approximate the test functions w^h, are fourth order polynomials of the form [140]:

$$\psi_c^w = (1-\bar{x}^2)^2(1-\bar{y}^2)^2(1-\bar{z}^2)^2 \tag{5-13}$$

where $\bar{x} = \frac{x-x_c}{L_x}, \bar{y} = \frac{y-y_c}{L_y}, \bar{z} = \frac{z-z_c}{L_z}$ and (x_c, y_c, z_c) is the position of the center node of the base function and L is the distance between the nodes. Since the test function w^h is arbitrary, (5-9) should hold for every ψ_c^w. Lagrange polynomials of the second order are used as the displacement and shear modulus shape functions. Figure 5-1 shows an example of the shape functions and the test functions in the 1D case. The test function and the shape functions corresponding to node number 3 are drawn with solid line.

The integrals in (5-9) are calculated for each base function ψ_c^w as follows:

$$\hat{A}_{l\alpha}^c = \int_{\Omega_c} \varepsilon_{lmi} \psi_\alpha^{\mu} \left(u_{i,j}^h + u_{j,i}^h\right) \psi_{c,mj}^w \, \mathrm{d}\Omega \tag{5-14}$$

$$\hat{f}_l^c = \rho\omega^2 \int_{\Omega_c} \varepsilon_{lmi} u_i^h \, \psi_{c,m}^w \, \mathrm{d}\Omega \tag{5-15}$$

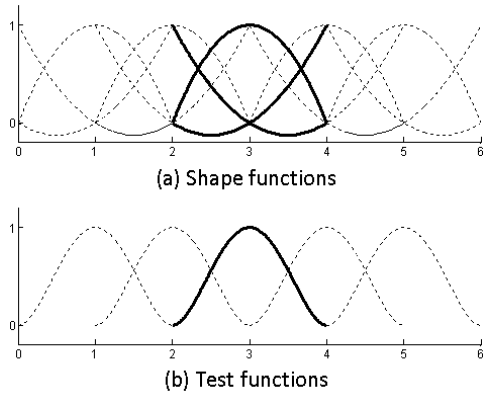

Figure 5-1. An example of 1D shape functions (a) and test functions (b) which should be used in solving the inverse problem.

where Ω_c is the volume where the corresponding base function ψ_c^w is non-zero. For example in Figure 5-1 for the base function ψ_c^w shown in the solid line, Ω_c is the area between nodes 2 and 4.

Then, the matrices $\widehat{\mathbf{A}}^c$ and the vectors $\hat{\boldsymbol{f}}^c$ of all the base functions are assembled in the global matrix $\widehat{\mathbf{A}}$ and the vector $\hat{\boldsymbol{f}}$ and the system of equations (5-16) is solved for the nodal values of the shear modulus $\overline{\boldsymbol{\mu}}$.

$$\widehat{\mathbf{A}}\overline{\boldsymbol{\mu}} = \hat{\boldsymbol{f}} \,. \tag{5-16}$$

For the 3D case, where all three displacement components are available in a 3D volume, with a mesh size of $\times\, n \times n$, we have $3(n-2)^3$ equations and n^3 unknowns. Therefore, for $n > 6$ there are more equations than unknowns and the system is over-determined. If the equations are linearly independent, they can be solved using the least squares method. But for the 2D case, under the plane-strain assumption, only two displacement components are available in a 2D region, and only one component of the curl is non-zero. Therefore we have $(n-2)^2$ equations and n^2 unknowns. In this case the system of equations is under-determined and cannot be solved without parameter regularization. Sparsity regularization (Chapter 2) [36, 115, 141, 142] can be used to decrease the number of unknowns and make the system determined. Alternatively, multi-frequency data can be used to increase the number of equations and make the system determined.

5.2.2 Multi-frequency technique

In multi-frequency technique, we assume that there is no significant dispersion in the elasticity in the range of frequencies considered. Therefore, the frequencies should be chosen sufficiently similar so frequency does not

significantly affect the elasticity values while causing enough change in the displacement pattern to give us different sets of data. In scanning *in-vivo*, this range will need to be selected appropriately for a given tissue type. Given two frequencies ω_1 and ω_2, the corresponding systems of equations for these two sets of data are:

$$\widehat{\mathbf{A}}_1\overline{\boldsymbol{\mu}} = \hat{\boldsymbol{f}}_1 \,, \widehat{\mathbf{A}}_2\overline{\boldsymbol{\mu}} = \hat{\boldsymbol{f}}_2 \ . \tag{5-17}$$

If we assume that the shear modulus does not change with frequency, we can combine these two sets of equations and solve them simultaneously:

$$\begin{bmatrix} \widehat{\mathbf{A}}_1 \\ \widehat{\mathbf{A}}_2 \end{bmatrix} \overline{\boldsymbol{\mu}} = \begin{bmatrix} \hat{\boldsymbol{f}}_1 \\ \hat{\boldsymbol{f}}_2 \end{bmatrix} . \tag{5-18}$$

5.2.3 Sparsity regularization

In the sparsity regularization method, as described in Chapter 2, the original variables are transformed into another, sparse, set of variables using an appropriate transformation. For example, the discrete cosine transform (DCT) has a strong energy compaction property and can be used for this purpose. Since the DCT is a linear transform, it can be written in matrix form:

$$\boldsymbol{X} = \mathbf{T}\boldsymbol{x} \tag{5-19}$$

where $\mathbf{T}$ is the DCT transform matrix, $\boldsymbol{x}$ is a vector containing the original field variables, and $\boldsymbol{X}$ is the transform-domain vector. We can reconstruct $\boldsymbol{x}$ from $\boldsymbol{X}$ using the inverse of $\mathbf{T}$.

$$\boldsymbol{x} = \mathbf{T}^{-1}\boldsymbol{X} \ . \tag{5-20}$$

Since $\boldsymbol{X}$ is sparse, we can choose a small number of dominant coefficients with large values and assume the others to be zero. This means we can choose the appropriate columns of $\mathbf{T}^{-1}$ corresponding to the selected dominant coefficients and call the new matrix $\mathbf{R} \equiv (\mathbf{T}^{-1})^*$. If $\boldsymbol{X}^*$ is the truncated transform-domain vector, we have:

$$\boldsymbol{x} \approx (\mathbf{T}^{-1})^* \boldsymbol{X}^* = \mathbf{R}\boldsymbol{X}^* . \tag{5-21}$$

The regularization is applied to this problem's unknowns by replacing the shear modulus vector $\overline{\boldsymbol{\mu}}$ with $\mathbf{R}\overline{\boldsymbol{\mu}}^*$:

$$[\widehat{\mathbf{A}}\mathbf{R}]\overline{\boldsymbol{\mu}}^* = \hat{\boldsymbol{f}} \tag{5-22}$$

Numerical experiments have shown that in the DCT domain, most of the energy is usually distributed in the lower frequency portion of the domain. Based on this, in this method we only consider the lower frequency variables and remove those of higher frequency from the system. For example a rectangular or circular region on the lower frequency corner of the domain can be selected. The selection of the DCT domain is based on the displacement SNR and the complexity of the elasticity pattern, and can be adjusted to improve imaging as discussed in Chapter 2 [36].

5.3 Simulation analysis

In this section numerical simulations are used to show the effectiveness of the proposed reconstruction algorithm. Our new c-FEM method and the curl-based method employing the local homogeneity assumption are used to estimate the elasticity images. For all the simulation results, the derivatives of the displacements for the noiseless case are calculated using a least squares planar fit on overlapping windows of relatively small size $3 \times 3 \times 3$ to retain high resolution. A slightly larger window size of $4 \times 4 \times 4$ was used when we performed the noise analysis, as a balance between resolution versus noise.

First, synthetic data from a 2D region with plane strain is used to show how the new proposed method removes the artifacts due to the local homogeneity assumption. 2D simulations are performed first because the 2D plane strain case highlights the benefits of the multi-frequency technique. Furthermore, 2D analysis is

of interest to ultrasound-based elastography techniques where all three components of the displacements are not available. Finally, the proposed method is tested on 3D synthetic data.

5.3.1 2D simulation data: single frequency

A 2D $20\text{mm} \times 20\text{mm}$ region under plane strain is used to create the synthetic data. The region is fixed from the top and is subjected to a harmonic horizontal excitation of the bottom surface as shown in Figure 5-2. The region has a harder inclusion with the Young's modulus of 20 kPa and the background has a Young's modulus of 10 kPa. A constant density of 1000 kg/m^3 is assumed for the medium and the Poisson ratio is assumed to be $\nu = 0.4995$. The forward problem is solved using four-node square elements with a mesh size of $L = 0.25\text{mm}$ (80×80) to obtain synthetic data. Later the obtained synthetic data is down-sampled to a coarser mesh size of (40×40) to be used in the inverse problem. This step is essential because, in the inverse problem, we should not use the same discretization as used in the forward problem. Since in simulations we are not considering viscosity, all the values including displacements and shear modulus values are real numbers.

First, the data obtained with an excitation frequency of 300 Hz is used to compare our method to the curl-based method with the local homogeneity assumption. In order to be able to solve the 2D problem using the c-FEM method, we use sparsity regularization to decrease the number of parameters. The results are shown in Figure 5-3. Figure 5-3(a) shows the actual distribution of the Young's modulus, Figure 5-3(b) shows the result using the local homogeneity assumption and Figure 5-3(c) shows the result using the c-FEM method. As it can be seen, using the local homogeneity assumption results in an underestimation of the Young's modulus value on the boundary of the inclusion which appears as a dark area around the inclusion. But no such dark area can be seen in the result from the c-FEM method. However, there are some artifacts in the c-FEM's results which are related to the inaccurate estimation of the curl at points of small curl. In the next sub-section it is shown that the artifact's pattern changes as the excitation frequency changes because the curl distribution changes with the excitation frequency. These artifacts are reduced in the 3D case since the curl is no longer constrained to a single direction and all three equations for the three directions of the curl can be used in solving the inverse problem. In the next sub-section it is shown how to overcome this problem in the 2D case by using the multi-frequency technique. This is especially useful for ultrasound-based measurement of motion since most ultrasound systems capture 2D images.

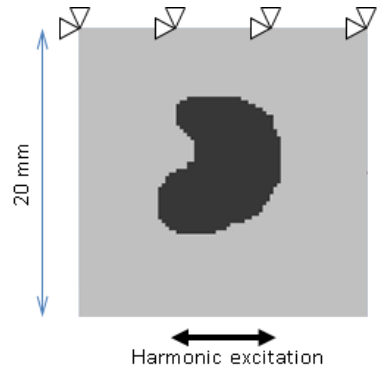

Figure 5-2. Schematic showing the shape and boundary conditions of the model used for generating 2D synthetic data.

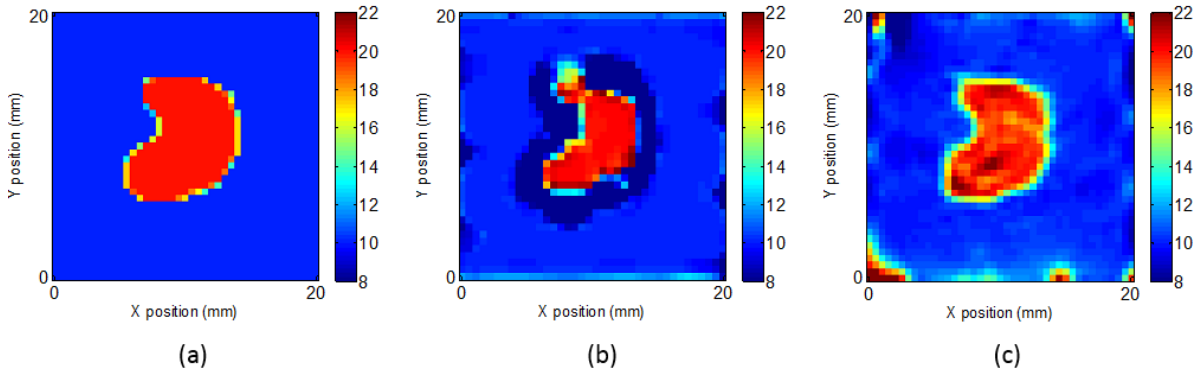

Figure 5-3. (a) The actual distribution of the Young's modulus (kPa) (b) the reconstructed Young's modulus using the curl-based method with local homogeneity assumption and (c) the result using the c-FEM method

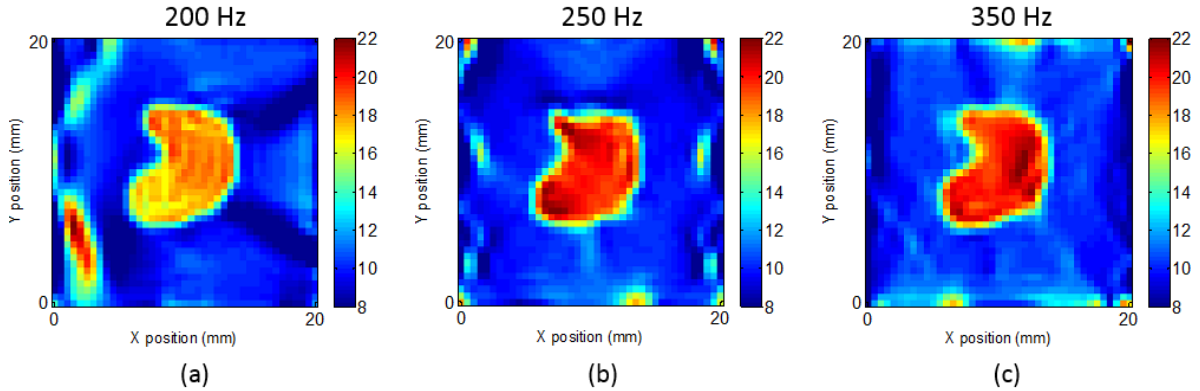

Figure 5-4. Reconstructed Young's modulus using c-FEM method for different values of excitation frequencies.

5.3.2 2D simulation: multi-frequency

Figure 5-4 shows the reconstructed Young's modulus for the different excitation frequencies of 200 Hz, 250 Hz and 350 Hz. As can be seen, all these images have artifacts which vary as the excitation frequency is changed. As explained before, these artifacts are related to the points of small curl. From Figure 5-4 it can also be seen that as the excitation frequency increases the artifacts are reduced. This can be explained by the fact that, as the excitation frequency increases, the shear wavelength decreases, which also decreases the wavelength of the curl of the displacement. Therefore areas of small displacement curl will be smaller and spread all over the region instead of concentrating in a larger connected area. Unfortunately, higher frequency waves experience higher attenuation in tissue, so frequencies greater than 400 Hz are infeasible in many clinical applications of elastography. It should also be mentioned that the c-FEM method, similarly to all other dynamic inversion techniques, relies on the inertial forces caused by the tissue acceleration. Therefore, as the frequency of excitation decreases, the inertial forces decrease and consequently the performance of the algorithm deteriorates.

To overcome this problem in the 2D case, we can use the data acquired at different excitation frequencies to increase the number of the equations compared to the number of unknowns and improve the conditioning of the inverse problem. In fact, since the position of the small curl area varies with the excitation frequency, the lack of information at some points at one frequency is compensated by the information from the data due to other excitation frequencies. Figure 5-5 shows the result obtained from stacking the equations of the data with the excitation frequencies of 200 Hz, 250 Hz, 300 Hz and 350 Hz. As it can be seen, the artifacts appearing in the single frequency results are effectively eliminated in the multi-frequency result.

As shown in the next section, in the 3D case, since we have the curl vector in all three directions and there are enough equations to solve for the unknowns, these artifacts do not appear in the results, even when a single excitation frequency is used.

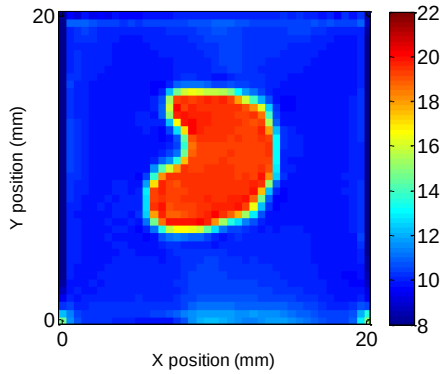

Figure 5-5. Reconstructed Young's modulus using c-FEM method and multi-frequency data with the frequencies of 200 Hz, 250 Hz, 300 Hz and 350 Hz

5.3.3 3D simulation data: single frequency

Even though for the 3D case we have three equations for each test function, and the number of the equations is larger than the number of unknowns for the mesh size of $n > 6$, it is not guaranteed that the system of equations is full rank. In fact, the system of equations depends on how the excitation and boundary conditions are applied. Similar to the 2D case, the results of this method are dependent on the distribution of the curl of the displacement which is also dependent on the excitation and boundary conditions. For example, if the boundary conditions and excitation are applied in such a way that the resulting curl vector is oriented mostly in one direction, similarly to the 2D case, then two of the three equations do not bring any new constraints and the system of equations becomes under-determined.

To show this effect, a 3D model with two different boundary conditions as shown in Figure 5-6 was simulated using ANSYS (ANSYS Inc., Canonsburg, USA). In one case, the top surface is fixed and the entire bottom surface is excited in the X-direction with the frequency of 75 Hz to produce plane shear waves in the X-Y plane. In the second case, a point excitation is used to excite the bottom surface in the Y-direction which results in a more non-uniform shear wave in all directions.

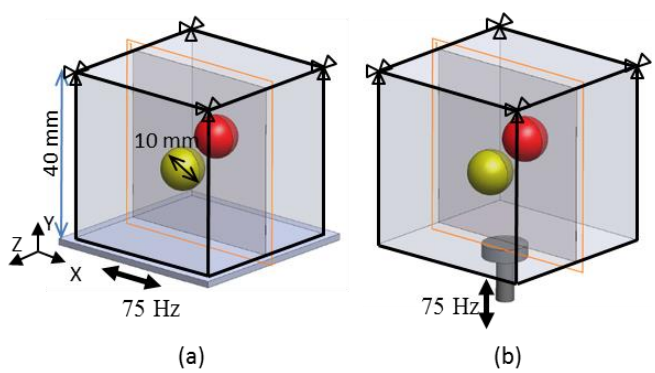

Figure 5-6. Schematic of the model used for generating 3D synthetic data with two different boundary conditions: (a) shear excitation in one direction close to plane strain condition (b) point excitation.

These two sets of data are used separately in the reconstruction without using any regularization of the parameters. The region of interest is divided into overlapping sub-domains of size $15 \times 15 \times 15$ to decrease the processing time [128]. The sub-domains are 30% overlapped and the values in the overlapping region are averaged. The results are shown in Figure 5-7. For the first data set, since the curl of the displacement is oriented mostly in the Z-direction, the system of equations is not full-rank and no meaningful result is obtained with our approach. But for the second case it can be seen that the system of equations is solvable and the inclusions are detected in the reconstruction.

Even with point excitation where the system of equations is full rank, the problem is still ill-conditioned. Sparsity regularization (Chapter 2) [36] can be used which globalizes the parameters and overcomes the local singularity points in the data. It also speeds up the inversion by decreasing the number of the parameters. Figure 5-8 shows the results after applying this type of regularization. The sparsity pattern or the selected new coefficients in the transformed domain are the lower frequency coefficients located in an ellipsoidal volume of equation

$$\left(\frac{x_1}{N_1}\right)^2 + \left(\frac{x_2}{N_2}\right)^2 + \left(\frac{x_3}{N_3}\right)^2 \leq 1 \tag{5-23}$$

where x_i is the index number of the new coefficients in the transformed domain and N_i is the size of the domain. The Young's modulus is shown in different cross-section planes from different directions. As it can be seen, the spherical shape of the inclusions and their Young's modulus values are detected accurately with this method.

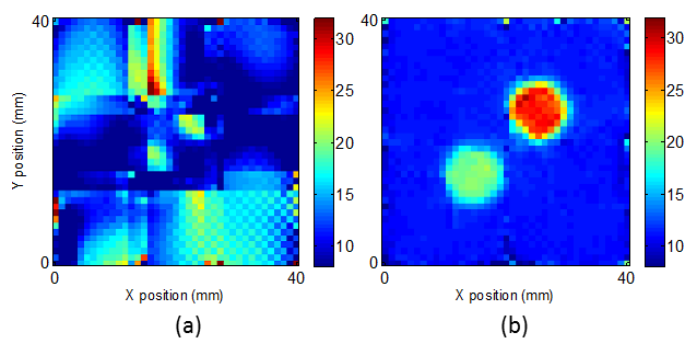

Figure 5-7. Reconstructed Young's modulus with c-FEM (a) using the data set with in plane shear excitation without using any regularization (b) using the data set with point excitation without any regularization

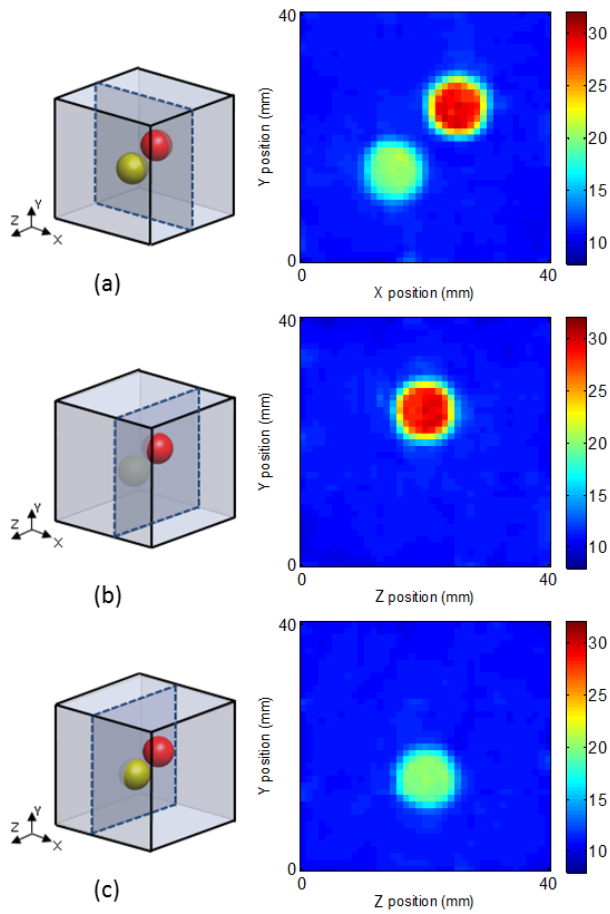

Figure 5-8. Different cross sections of the reconstructed Young's modulus map using the c-FEM method with sparsity regularization on the 3D data set with point excitation (Figure 5-6 (b))

5.3.4 2D simulation: noise analysis

The effect of noise on the results from the previous section are studied next. White Gaussian noise was added to the 2D displacement data obtained from the same model shown in Figure 5-2 and three methods: (1) the curl-based method with homogeneity assumption, (2) the c-FEM method using single excitation and (3) c-FEM using multi-frequency excitation were used to solve the inverse problem. For each case the inverse problem was solved 50 times and the normalized RMS error of the Young's modulus reconstruction were calculated for different values of the signal to noise ratio (SNR). The SNR is defined as the power ratio between the signal amplitude and the added noise amplitude and is expressed in dB:

$$\mathrm{SNR_{db}} = 20\log_{10}\frac{\overline{U_{\mathrm{signal}}}}{\overline{U_{\mathrm{noise}}}}. \tag{5-24}$$

It should be mentioned that in this analysis, the size of the window used for taking the spatial derivatives is fixed for all levels of noise while this window size should ideally be selected based on the noise level. However, for simplicity, we used a fixed window size of $4 \times 4 \times 4$ and therefore, in theory, the results should improve slightly with a more optimal window size.

For the single frequency test, the 300 Hz data set was used and for the multi-frequency test, data sets with excitation frequencies of 200 Hz, 250 Hz, 300 Hz and 350 Hz were used together. The results are shown in Figure 5-9.

From this figure it can be seen that the mean value of the normalized RMS error for the c-FEM method is lower than that obtained when the homogeneity assumption is used. However, the standard deviation of the RMS error is higher for the c-FEM method when only the single frequency data is used. However, using multi-frequency data with the c-FEM method improves the results significantly in terms of both accuracy and stability.

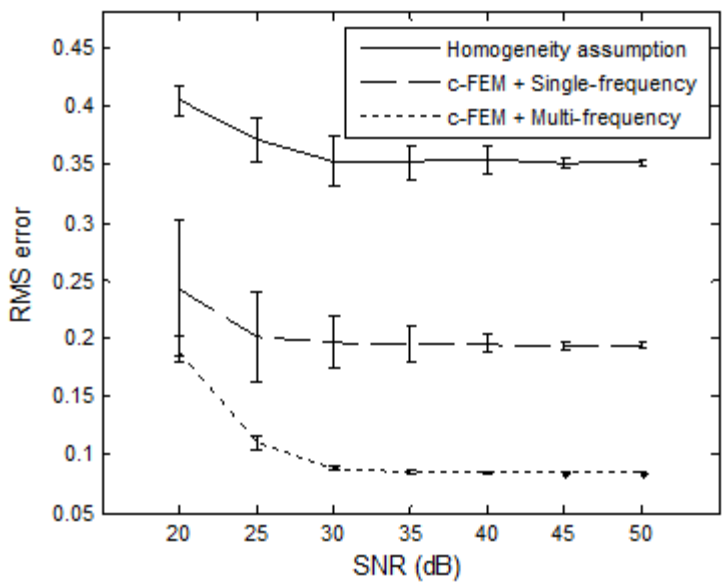

Figure 5-9. The normalized RMS error of the reconstructed Young's modulus versus different values of the SNR for the 2D case.

5.4 Experimental results

The c-FEM inversion technique with sparsity regularization was applied to 3D MRE experimental data. The data was collected from a CIRS elastography phantom model 049. Figure 5-10 shows a schematic of the

phantom and the exciter. The phantom has 8 spherical inclusions with different values of elasticity and diameters of 10mm and 20mm. As shown in Figure 5-10, the phantom was excited from the top in the Z-direction with the frequency of 200 Hz by an MRI compatible actuator [118].

The MRE images were acquired using a 2D multi-slice multi-shot SE-EPI method with turbo factor 11 [119]. A single sinusoidal cycle was used as the motion encoding gradient with strength of 60mT/m, which captured 8 states of the mechanical motion. The displacements in time domain were converted to complex phasors using the Discrete Fourier Transform and used in the inverse problem. All three components of displacement were aquired on a 224×112×48 matrix with 1.5mm isotropic voxel size. Total image acquisition time was approximately 5 min. The acquisition matrix was cropped to two smaller regions of interest ROI-1 and ROI-2 shown in Figure 5-10. A sample displacement distribution is shown in Figure 5-11 with all three components of the displacement in a plane normal to the Y-direction. The SNR for this data is 28dB as explained in Chapter 2.

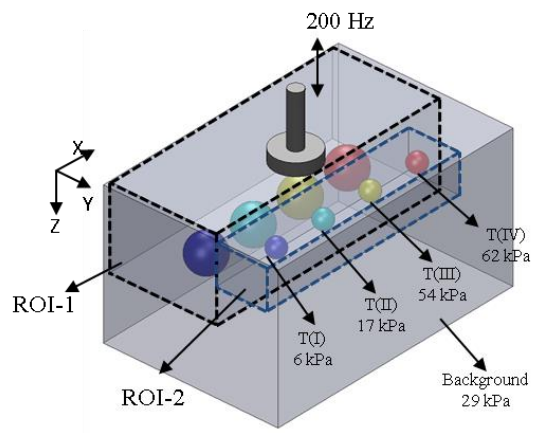

Figure 5-10. Schematic of the CIRS elastography phantom showing the region of interest and the exciter position.

In order to decrease the processing time the region of interest is divided into overlapping sub-domains of $15 \times 15 \times 15$ voxels. The sub-domains are overlapped to retain the uniformity of the reconstructed shear modulus and the values in the overlapping regions are averaged. The derivatives of the displacements used in the reconstruction are calculated using a planar fit on overlapping windows of $4 \times 4 \times 4$ voxels. A constant density of 1000 kg/m^3 is assumed. The sparsity regularization with the same ellipsoidal sparsity pattern as in (5-23) is used here as well. The processing time for this setting using the c-FEM method on ROI-1 using Matlab was approximately 15 minutes. Solving the same problem by using the mixed-FEM method using Matlab on the same PC took approximately 35 minutes to process. This example shows that removing the pressure parameters from unknowns in our suggested method decreases the processing time significantly.

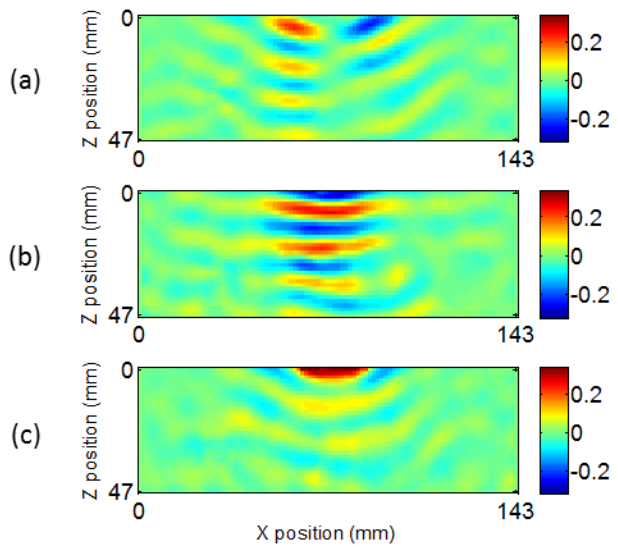

Figure 5-11. The real-part of all three components of displacement (mm) data in a plane normal to Y-direction. (a), (b) and (c) show X, Y and Z directional displacement respectively.

The real-part of the reconstructed Young's modulus maps at different cross-sections are shown in Figure 5-12 for ROI-1 which contains the larger inclusions. Figure 5-13 shows the same result for the smaller inclusions in ROI-2 at a cross-section normal to the z-axis. All the inclusions are visible with similar shapes, sizes and elasticities as the manufacturer's values. The regions are segmented manually and the mean and standard deviation of the real-part of the Young's modulus of each region are calculated and compared with the values reported by the manufacturer. The quantitative results are shown in Figure 5-15 for both large and small inclusions. The imaginary-part of the Young's modulus at the same cross-section as shown in Figure 5-12 is shown in Figure 5-14. Since the phantom has a low viscosity, the imaginary-part of the Young's modulus is much smaller than the real-part and because there is no viscosity inclusion in the phantom, the imaginary-part of the Young's modulus does not show any contrast correlating with the geometry of the inclusions.

The estimated Young's modulus values are slightly different from the values reported by the manufacturer. For hard inclusions we have an underestimation of the true parameters and for soft inclusions we have an overestimation of the true parameters. The same discrepancy has also been reported by Baghani *et al.* [120]. The reasons for this discrepancy can be the difference in temperature, excitation frequency or the changes of the phantom material properties due to aging.

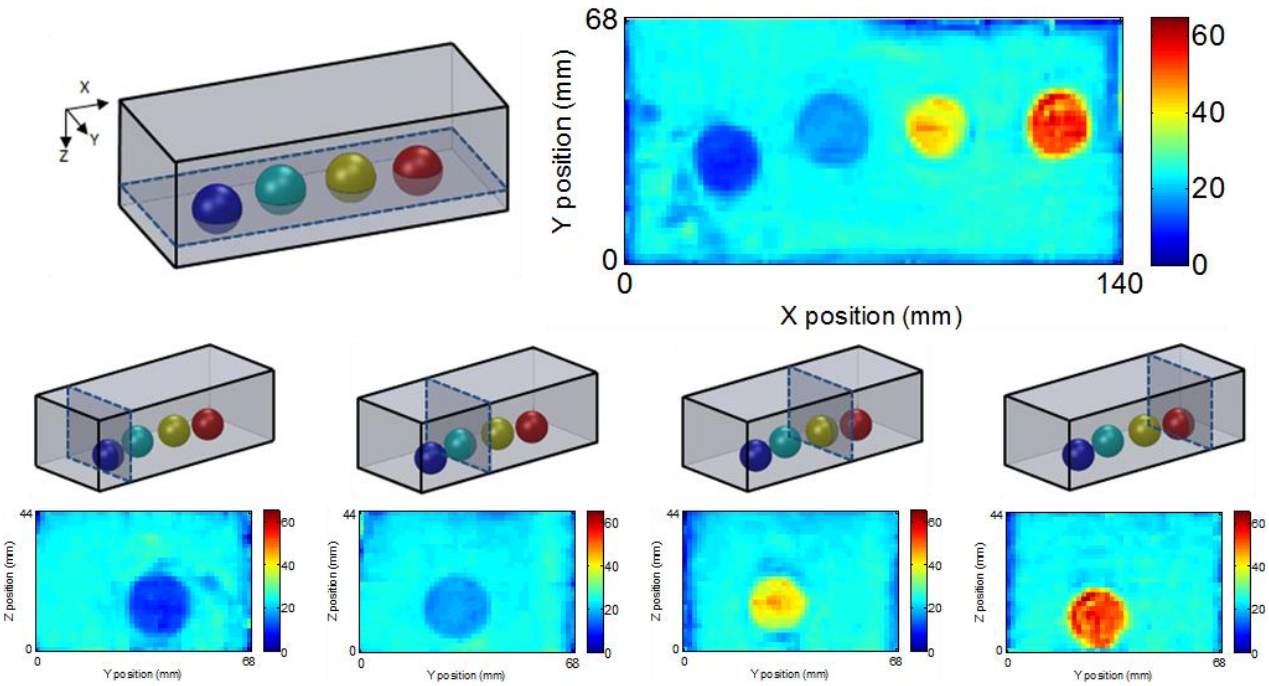

Figure 5-12. The phantom's reconstructed Young's modulus maps (kPa) on different cross-sections using c-FEM

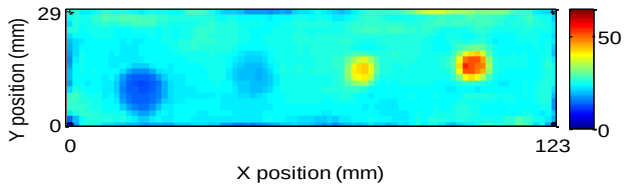

Figure 5-13. The real-part of the reconstructed Young's modulus (kPa) for the small inclusions using c-FEM

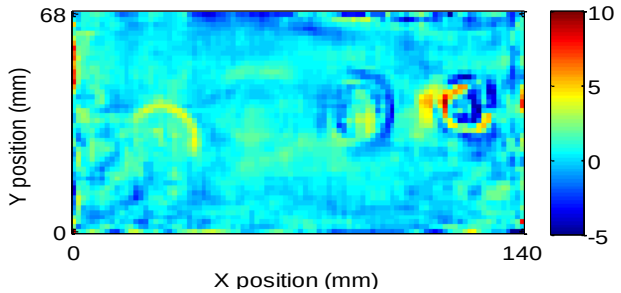

Figure 5-14. The imaginary part of the reconstructed Young's modulus (kPa) using c-FEM for the same cross-section shown in Figure 5-12

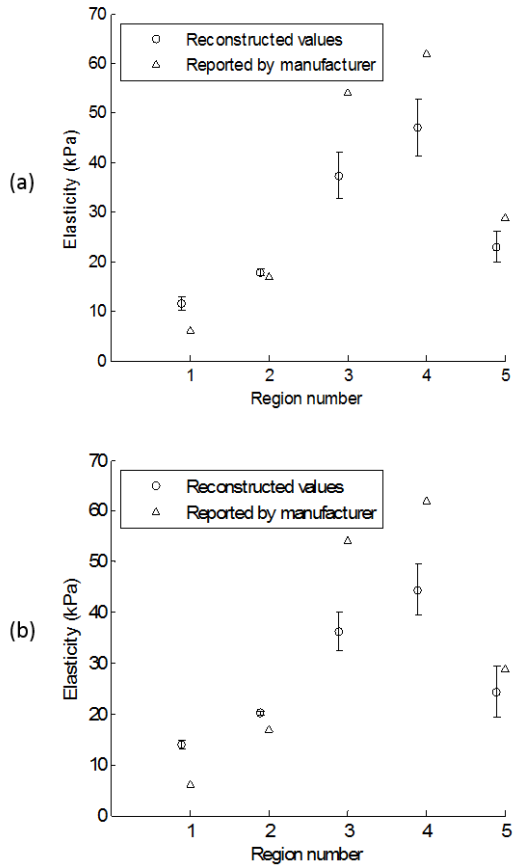

Figure 5-15. The mean and standard deviation of the Young's modulus using c-FEM over each region compared to the values reported by the manufacturer: (a) for the larger inclusions, (b) for the smaller inclusions.

Comparing this result to the mixed-FEM results presented in Chapter 2 shows the results are as good as those obtained with the mixed-FEM method. We note that there is a small degradation in the results due to the higher order of the derivative needed for the curl operator. However, we have shown that the c-FEM method is faster than the mixed-FEM and can be used with multi-frequency excitation in cases where one frequency data does not provide sufficient information. As explained previously, for this experiment the excitation and boundary conditions are such that even a single frequency dataset provides sufficient equations at all points. An in depth comparison of this method with some other methods will be presented in Chapter 7.

5.5 Conclusion

In order to remove the pressure term of the wave equation for linear isotropic materials and to solve for the shear modulus given the displacement data, we propose to take the curl of the wave equation without using the local homogeneity assumption. We developed a new specialized FEM formulation to discretize the resulting equation and solved it directly for the shear modulus. The pressure variable being removed from the

unknowns, the resulting system of equations can be solved faster than the direct mixed-FEM inversion technique [49] which solves for both shear modulus and pressure. It also enables us to use multi-frequency data to improve the resulting shear modulus reconstruction. This approach does not perform as well when the pressure was considered as an unknown since the pressure distribution changes with the frequency.

The method was tested on 2D and 3D simulation data sets. In the 2D case, the result from the curl-based method with local homogeneity assumption was compared to the result of the new method. Significant underestimation of the Young's modulus was observed on the edges of the inclusions when using the local homogeneity assumption. However, when using the c-FEM method the edges were detected clearly with less underestimation of the Young's modulus value. The 2D case is more challenging as compared to the 3D case because in the 2D case only one component of the curl exists, and there are not enough equations to solve for the unknowns without regularization. Even after regularization, there are still some artifacts due to the points of small curl. It was shown that this problem can be solved by using multi-frequency data which increases the number of the equations and compensates for the lack of information in areas of small curl by the information from other frequencies. This problem also occurs in the 3D case, if the boundary conditions and excitation are such that the curl vector is pointing mostly in one direction, similarly to the 2D case. However, in general in the 3D case, this special condition is unlikely to happen as irregular shapes cause the curl vector to vary in all the directions in space and therefore there are enough equations to solve for the unknowns.

A noise analysis was performed with 2D simulation data using the curl-based method with homogeneity assumption, and the c-FEM method with both single frequency and multi-frequency data. The results showed that the c-FEM method is more accurate than the method with homogeneity assumption but when using single frequency data it is less stable. Using multi-frequency data with the c-FEM method improves the accuracy and stability significantly.

The algorithm was demonstrated on MRE experimental data captured from a CIRS elastography phantom. All the inclusions were detected with clear sharp edges and spherical shape. The absolute Young's modulus values are almost matched with the values reported by the manufacturer. However a reduction in the overall contrast is observed which can be due to aging of the phantom or test condition differences. The same discrepancies have been reported previously [120]. The results show the high potential of this method in providing high quality MR elastograms of tissue *in-vivo* demonstrating the pathological state of the tissue which can be used in detection and staging of many diseases such as prostate cancer.

Unlike US elastography, MRE can provide high quality 3D displacement data which was used in this study. Using US with a single conventional transducer, at most 2D displacements in a 3D volume can be measured of which the lateral component is usually one order of magnitude less accurate than the axial component. Having two components of displacement in a 3D volume, one component of the curl can be obtained and can be used for the reconstruction with the presented algorithm. This is the subject of future work.

Chapter 6 - Ultrasound elastography: direct FEM inversion using simplified wave equations

6.1 Introduction

As mentioned in previous chapters, in order to fully solve the inverse problem using the complete wave equation, all three components of the displacement are required in a volume. Using MRI, it is possible to measure all three components of the displacement in a 3D volume. However, conventional ultrasound can only measure the axial component of the displacement accurately. Beam steering has been used by several groups to measure the lateral displacement using ultrasound [56, 143-145] but the accuracy of the lateral displacement is an order of magnitude less than the axial displacement. To measure the elevational component using beam steering a 2D array transducer is required but currently the most ultrasound systems do not support that kind of transducer. The cheaper price, more availability and faster speed of ultrasound systems compared to MRI has motivated many researchers to simplify the wave equation to adopt it for the limited data available with US. There are iterative FEM based methods [39, 43] in which the Young's modulus is iteratively changed to minimize the error between the measured displacement and simulated displacement from the forward problem. In such techniques, the boundary conditions are required in order to solve the forward problem at each step but such data is not fully available. In other methods, the equation of motion is simplified into a Helmholtz equation by using the local homogeneity assumption and ignoring the second term of the wave equation which is called the pressure term. The resulting equation holds for each component of the displacements independently. Therefore, with only one component of the displacement, the inverse problem can be solved to find the shear modulus. These assumptions have been widely used in many ultrasound based approaches [27, 46]. Methods using the local homogeneity assumption may work very well in areas where the elasticity is almost constant. However, it has been shown that this assumption can cause significant errors in regions where the elasticity variation is high (Chapter 5) [37].

In US elastography, the 3D volume data is usually captured by rotating a transducer array about a fixed axis of rotation and capturing a set of 2D image planes from different angles. In cases where a small angular range is sufficient to cover the volume, the image planes can be assumed to be approximately parallel to each other

and the inverse problem can be solved in a Cartesian coordinate system. However, there are many cases in which the angle range needed to cover a volume is large. For example in trans-rectal prostate ultrasound imaging [146], the angle of the transducer can easily cover 90° or more. Therefore the Cartesian coordinate system can no longer be used. For these cases the cylindrical coordinate system should be used instead.

In this chapter we introduce a new FEM based direct method that does not use the local homogeneity assumption. We call this method shear-FEM since it uses the shear wave equation without homogeneity assumption. This method is suitable for the limited unidirectional ultrasound displacement data. The method is developed for both Cartesian and cylindrical coordinate systems.

6.2 Method

6.2.1 Inverse problem

6.2.1.1 Cartesian coordinate system

We start with the equation of motion in the frequency domain (repeated from (5-2)):

$$\left[\mu\left(u_{i,j}+u_{j,i}\right)\right]_{,j}+\left(\lambda u_{k,k}\right)_{,i}=-\rho\omega^2 u_i \tag{6-1}$$

Expanding equation (6-1) we have:

$$\mu\left(u_{i,jj}+u_{j,ij}\right)+\mu_{,j}\left(u_{i,j}+u_{j,i}\right)+\lambda_{,i}\left(u_{k,k}\right)+\lambda u_{k,ki}=-\rho\omega^2 u_i \ . \tag{6-2}$$

In previous studies, in order to simplify equation (6-1), first the local homogeneity assumption ($\mu_{,i}=0$, $\lambda_{,i}=0$) was used which results in:

$$\mu u_{i,jj}+(\lambda+\mu)u_{k,ki}=-\rho\omega^2 u_i \ . \tag{6-3}$$

The second term in (6-3), which is the gradient of the pressure, has also been removed in prior work by using different justifications. Some groups use the incompressibility assumption and ignore $u_{k,k}$, which, being the divergence of the displacement, is small. But this justification does not hold because for nearly incompressible materials λ is large and the product of λ and the divergence of the displacement remains finite. Other groups use the fact that the compressional wavelength is very large compared to the size of the region of interest and therefore the gradient of the pressure is negligible. This assumption is not always valid since

the pressure distribution is dependent on the boundary conditions and heterogeneity of the region and can be large. Although neither of these justifications strictly holds true, in our work we have no other choice but to ignore this term because we only have one component of the displacement vector. We will show that the resulting artifacts can be reduced by using a multi-frequency technique.

Ignoring the second term in (6-3), which is also the coupling term, results in:

$$\mu u_{i,jj} = -\rho\omega^2 u_i \ . \tag{6-4}$$

The resulting equation (6-4) is a Helmholtz equation which is also called the shear wave equation. In this equation the displacement components u_i are decoupled and each one satisfies the equation independently.

As mentioned in the introduction, when all the three components of the displacement are available, as it is in MRE data, the full wave equation can be used without any simplifying assumptions. In such methods the pressure term has been dealt with differently. It has been considered as unknown and solved for the pressure together with the shear modulus as in Chapter 2, or it has been eliminated by using the curl operator as shown in Chapter 5. But in this chapter, we assume we have only one component of the displacement. In this case, the coupling terms or the pressure cannot be removed but they can be ignored. However the other simplifying assumption, the homogeneity assumption, can still be avoided which is a key point of this work.

In our proposed method, we only neglect the coupling terms in (6-2) but we do not use the local homogeneity assumption. If we rearrange equation (6-2) as follows

$$\underbrace{\left(\mu u_{i,j}\right)_{,j}}_{term\ 1} + \underbrace{\mu_{,j} u_{j,i}}_{term\ 2} + \underbrace{\mu u_{j,ji} + \left(\lambda u_{k,k}\right)_{,i}}_{term\ 3} = -\rho\omega^2 u_i \ , \tag{6-5}$$

term 3 is the compressional term and contains coupling terms that are neglected as done in many previous methods. *Term 2* is also a coupling term which has to be neglected in order to decouple the displacement components in this equation. This term was removed using the local homogeneity assumption in (6-3) however in our method we are not using the local homogeneity assumption for the first term in (6-5). Therefore the equation used in our method will be as follows:

$$\left(\mu u_{i,j}\right)_{,j} = -\rho\omega^2 u_i \ , \tag{6-6}$$

in which the shear modulus μ remains inside the bracket, unlike in previous methods using equation (6-4). Then we use the finite element method to discretize (6-6). This involves writing the equation in a weak form and taking integration by parts which results in:

$$\int_{\Omega} \mu u_{i,j}\, w_{,j}\, d\Omega - \int_{\Gamma} \mu u_{i,j}\, n_j w\, d\Gamma = \rho\omega^2 \int_{\Omega} u_i w\, d\Omega \ , \tag{6-7}$$

where w is a test function and Ω is the region of interest with the boundary of Γ and $\boldsymbol{n}$ is the unit normal vector on the boundary Γ. In the next step, all the parameters and functions are replaced with their finite dimensional approximations:

$$\mu \approx \mu^h = \bar{\mu}_\alpha \psi_\alpha^{\mu} \ , \qquad u_i \approx u_i^h = \bar{u}_{i\alpha} \psi_\alpha^{u} \ , \qquad w \approx w^h = w_\alpha \psi_\alpha^{w} \tag{6-8}$$

where ψ_α^{μ} and ψ_α^{u} are base functions for the shear modulus and displacement respectively, and $\bar{\mu}_\alpha$, $\bar{u}_{i\alpha}$ are the nodal values of the parameters. ψ_α^{w} are the base functions for approximating the test function which can be the same as ψ_α^{u}. Since w is any arbitrary function, (6-7) should hold for every ψ_α^{w}. In this study, we discretize the region with cubic elements with Lagrange polynomials of the first order [117] for displacement shape functions and the test function, and constant shape function for the shear modulus. We can eliminate the boundary integration by removing the equations in which ψ_α^{w} has nonzero values on the boundary. The resulting system of equations after discretization is rearranged with respect to the shear modulus nodal parameters as shown in (6-9) and it is solved directly for the shear modulus.

$$\widetilde{\mathbf{A}}\bar{\boldsymbol{\mu}} = \boldsymbol{f}' \ . \tag{6-9}$$

In the above equation, $\bar{\boldsymbol{\mu}}$ is a vector containing the nodal values of the shear modulus and $\widetilde{\mathbf{A}}$ and $\boldsymbol{f}'$ are a matrix and a vector respectively defined as follows:

$$\tilde{A}_{\alpha\beta} = \int_{\Omega} \psi_\beta^{\mu}\, u_{,j}^h\, \psi_{\alpha,j}^{w}\, \mathrm{d}\Omega \ , \quad f'_\alpha = \rho\omega^2 \int_{\Omega} u^h\, \psi_\alpha^{w}\, \mathrm{d}\Omega \ , \tag{6-10}$$

where u can be any of the components of the displacement.

If we were to discretize equation (6-4), which uses the assumption of local homogeneity, the resulting $\widetilde{\mathbf{A}}$ would be a vector instead, defined as follows:

$$\tilde{A}_\alpha = \int_{\Omega} u_{,jj}^h\, \psi_\alpha^{w}\, \mathrm{d}\Omega \tag{6-11}$$

We have also used this formulation in this study for the purpose of comparison.

In order to stabilize the inverse problem, we use the sparsity regularization explained in Chapter 2 [36] . Although avoiding the local homogeneity assumption improves the accuracy of the results, there still will be artifacts in the reconstructed results due to ignoring the pressure term and also due to lack of data at areas where the displacement is close to zero. Since these artifacts change as the wave pattern changes, it is possible to reduce the artifacts by using a multi-frequency technique [37, 138, 139] . One way to do this is to stack all the equations from different excitation frequencies and solve them together for the shear modulus. For example, given two frequencies ω_1 and ω_2, the corresponding systems of equations for these two sets of data are:

$$\widetilde{\mathbf{A}}_1\overline{\boldsymbol{\mu}} = \boldsymbol{f}'_1 \,, \widetilde{\mathbf{A}}_2\overline{\boldsymbol{\mu}} = \boldsymbol{f}'_2 \ . \tag{6-12}$$

If we assume that the shear modulus does not change within the frequency range of excitation, we can combine these two sets of equations and solve them simultaneously:

$$\begin{bmatrix} \widetilde{\mathbf{A}}_1 \\ \widetilde{\mathbf{A}}_2 \end{bmatrix} \overline{\boldsymbol{\mu}} = \begin{bmatrix} \boldsymbol{f}'_1 \\ \boldsymbol{f}'_2 \end{bmatrix} . \tag{6-13}$$

It should be mentioned that the shear modulus found in this method is a complex shear modulus; its real and imaginary components are related to elasticity and viscosity, respectively. In other methods where the shear modulus is calculated from the shear wave speed or shear wavelength using the shear wave speed equation ($\mu = \rho V_s^2 = \rho (L_s f)^2$), what is found is the apparent shear modulus which is dependent on viscosity and frequency. In those methods the multi-frequency technique should be used more carefully since the shear modulus found is dependent on frequency. However, in our method we compute the actual complex shear modulus. If the material is Newtonian, the complex shear modulus is independent of frequency. If the material is not Newtonian, the change in elasticity and viscosity is typically small for the small change in frequency (a few tens of Hertz) typically used with our multi-frequency technique.

6.2.1.2 Cylindrical coordinate system

The equation of motion in cylindrical coordinates in the radial direction is given by:

$$
\begin{gathered}
\mu\left(\frac{\partial^2 u_r}{\partial r^2}+\frac{1}{r^2}\frac{\partial^2 u_r}{\partial \theta^2}+\frac{\partial^2 u_r}{\partial z^2}\right)+ \\
2\frac{\partial \mu}{\partial r}\left(\frac{\partial u_r}{\partial r}\right)+\frac{1}{r}\frac{\partial \mu}{\partial \theta}\left(\frac{1}{r}\frac{\partial u_r}{\partial \theta}+\frac{\partial u_\theta}{\partial r}-\frac{u_\theta}{r}\right)+\frac{\partial \mu}{\partial z}\left(\frac{\partial u_r}{\partial z}+\frac{\partial u_z}{\partial r}\right)+ \\
\mu\frac{\partial}{\partial r}\left(\frac{\partial u_r}{\partial r}+\frac{1}{r}\frac{\partial u_\theta}{\partial \theta}+\frac{u_r}{r}+\frac{\partial u_z}{\partial z}\right)+ \\
\frac{\partial}{\partial r}\left(\lambda\left(\frac{\partial u_r}{\partial r}+\frac{1}{r}\frac{\partial u_\theta}{\partial \theta}+\frac{u_r}{r}+\frac{\partial u_z}{\partial z}\right)\right)+ \\
\frac{\mu}{r}\left(\frac{\partial u_r}{\partial r}-\frac{u_r}{r}-\frac{2}{r}\frac{\partial u_\theta}{\partial \theta}\right)=-\rho\omega^2 u_r\,.
\end{gathered}
\tag{6-14}
$$

Unlike in Cartesian coordinates, using the local homogeneity and incompressibility assumptions in cylindrical coordinates does not decouple the displacement components completely. Using the local homogeneity assumption, the second line in (6-14) can be removed and, by ignoring the pressure term, the third and fourth lines can be neglected. This results in:

$$
\mu\left(\frac{\partial^2 u_r}{\partial r^2}+\frac{1}{r^2}\frac{\partial^2 u_r}{\partial \theta^2}+\frac{\partial^2 u_r}{\partial z^2}+\frac{1}{r}\frac{\partial u_r}{\partial r}-\frac{u_r}{r^2}-\overbrace{\frac{2}{r^2}\frac{\partial u_\theta}{\partial \theta}}^{***}\right)=-\rho\omega^2 u_r\,. \tag{6-15}
$$

The highlighted term (***) in this equation contains the displacement component in the angular direction which means that the equation in the radial direction is still dependent on the angular component of the displacement. Therefore, in cylindrical coordinates, additional assumptions are required in order to decouple the displacement components.

Similarly to the Cartesian coordinates case, here we try to avoid the local homogeneity assumption. Rearranging equation (6-14) results in:

$$\frac{\partial}{\partial r}\left(\mu\frac{\partial u_r}{\partial r}\right)+\frac{1}{r}\frac{\partial}{\partial\theta}\left(\mu\frac{1}{r}\frac{\partial u_r}{\partial\theta}\right)+\frac{\partial}{\partial z}\left(\mu\frac{\partial u_r}{\partial z}\right)+$$
$$\frac{\partial\mu}{\partial r}\left(\frac{\partial u_r}{\partial r}\right)+\frac{1}{r}\frac{\partial\mu}{\partial\theta}\left(\frac{\partial u_\theta}{\partial r}-\frac{u_\theta}{r}\right)+\frac{\partial\mu}{\partial z}\left(\frac{\partial u_z}{\partial r}\right)+$$
$$\mu\frac{\partial}{\partial r}\left(\frac{\partial u_r}{\partial r}+\frac{1}{r}\frac{\partial u_\theta}{\partial\theta}+\frac{u_r}{r}+\frac{\partial u_z}{\partial z}\right)+ \tag{6-16}$$
$$\frac{\partial}{\partial r}\left(\lambda\left(\frac{\partial u_r}{\partial r}+\frac{1}{r}\frac{\partial u_\theta}{\partial\theta}+\frac{u_r}{r}+\frac{\partial u_z}{\partial z}\right)\right)+$$
$$\frac{\mu}{r}\left(\frac{\partial u_r}{\partial r}-\frac{u_r}{r}-\frac{2}{r}\frac{\partial u_\theta}{\partial\theta}\right)=-\rho\omega^2u_r\,.$$

Similar to what we did for the Cartesian coordinate system, the third and fourth lines can be neglected by ignoring the pressure term. Similar to the *term 2* in (6-5), the second line in (6-16) should also be neglected in order to decouple the displacement components. Also the remaining angular component which was highlighted in (6-15) should be neglected. Therefore the resulting equation will be:

$$\frac{\partial}{\partial r}\left(\mu\frac{\partial u_r}{\partial r}\right)+\frac{1}{r}\frac{\partial}{\partial\theta}\left(\mu\frac{1}{r}\frac{\partial u_r}{\partial\theta}\right)+\frac{\partial}{\partial z}\left(\mu\frac{\partial u_r}{\partial z}\right)+\frac{\mu}{r}\left(\frac{\partial u_r}{\partial r}-\frac{u_r}{r}\right)=-\rho\omega^2u_r\,. \tag{6-17}$$

Similarly to our approach in Cartesian coordinates, we write (6-17) in a weak form as follows:

$$\int_\Omega\left(\left(\frac{\partial}{\partial r}+\frac{1}{r}\right)\left(\mu\frac{\partial u_r}{\partial r}\right)+\frac{1}{r}\frac{\partial}{\partial\theta}\left(\mu\frac{1}{r}\frac{\partial u_r}{\partial\theta}\right)+\frac{\partial}{\partial z}\left(\mu\frac{\partial u_r}{\partial z}\right)\right)w\,\mathrm{d}\Omega$$
$$-\int_\Omega\frac{\mu}{r}\left(\frac{u_r}{r}\right)w\,\mathrm{d}\Omega=-\int_\Omega\rho\omega^2u_r\,w\,\mathrm{d}\Omega\,. \tag{6-18}$$

Then using Green's first identity for the first integral we have:

$$-\int_{\Omega} \left(\mu \frac{\partial u_r}{\partial r}\right)\left(\frac{\partial w}{\partial r}\right) + \left(\mu \frac{1}{r}\frac{\partial u_r}{\partial \theta}\right)\frac{1}{r}\frac{\partial w}{\partial \theta} + \left(\mu \frac{\partial u_r}{\partial z}\right)\frac{\partial w}{\partial z}\ \mathrm{d}\Omega$$

$$+\int_{\Gamma} \left(\left(\mu \frac{\partial u_r}{\partial r}\right) n_r + \left(\mu \frac{1}{r}\frac{\partial u_r}{\partial \theta}\right) n_\theta + \left(\mu \frac{\partial u_r}{\partial z}\right) n_z\right) w \mathrm{d}\Gamma - \tag{6-19}$$

$$\int_{\Omega} \frac{\mu}{r}\left(\frac{u_r}{r}\right) w\ \mathrm{d}\Omega = -\int_{\Omega} \rho\omega^2 u_r\, w\ \mathrm{d}\Omega\,.$$

As before, we replace all the parameters and functions with their finite dimensional approximations and we remove the boundary equations. The resulting K matrix and f vector are:

$$\tilde{A}_{\alpha\beta} = \int_{\Omega} \psi_\beta^{\mu} \left[\left(\frac{\partial u_r}{\partial r}\right)^h \frac{\partial \psi_\alpha^{\mathrm{w}}}{\partial r} + \left(\frac{u_r}{r^2}\right)^h \psi_\alpha^{\mathrm{w}} + \left(\frac{1}{r^2}\frac{\partial u_r}{\partial \theta}\right)^h \frac{\partial \psi_\alpha^{\mathrm{w}}}{\partial \theta} + \left(\frac{\partial u_r}{\partial z}\right)^h \frac{\partial \psi_\alpha^{\mathrm{w}}}{\partial z}\right]\ \mathrm{d}\Omega\ , \tag{6-20}$$

$$f'_\alpha = \rho\omega^2 \int_{\Omega} u_r^h\, \psi_\alpha^{\mathrm{w}}\ \mathrm{d}\Omega\ .$$

We can also use a multi-frequency technique as in the Cartesian formulation, as shown in (6-13), to improve the inversion.

6.2.2 Simulations, phantom and patient data collection

6.2.2.1 Simulation

We used simulations to investigate the effectiveness of the proposed method in a controlled and repeatable environment. First, the performance of the methods were tested on a simple homogeneous region to better see the effect of the simplifying assumptions and then the experiment was repeated for a region with a spherical inclusion. Therefore, we simulated two 3D models using ANSYS®, one with a homogeneous region and the other with a spherical inclusion. The boundary conditions used are shown in Figure 6-1. The inclusion has a Young's modulus of 30 kPa and a diameter of 12 mm and the Young's modulus of the background for both models is 10 kPa. The Poisson's ratio and density of the regions are 0.495 and 1000 $\mathrm{kg/m^3}$ respectively. The two adjacent (left and front) faces were confined in their normal directions and the bottom face was excited with harmonic motion. Different frequencies were used for the excitation. The region was discretized using 10-node tetrahedral elements (SOLID187) with element size of 0.5 mm and then the resulting data was

interpolated onto a coarser regular rectangular mesh and the formulation for Cartesian coordinate system was used to solve the inverse problem. A region of interest of size $25mm \times 25mm \times 25mm$ was considered in the center of the region to solve the inverse problem. In order to show the effect of different simplifying assumptions separately, different methods were used to solve the inverse problem. First the mixed-FEM method (Chapter 2) was used as a reference in which the complete form of the wave equation without any simplifying assumptions is used. In this method all three components of the displacement are used. The next method is the mixed-FEM method with local homogeneity assumption which shows only the effect of local homogeneity assumption on the results. This method is used only for the region with inclusion since it produces exactly the same results as the mixed-FEM without homogeneity assumption for the homogeneous region. In order to show only the effect of ignoring coupling terms, in the next method the shear-FEM without homogeneity assumption was used with all the three (X, Y, Z) components of the displacement. Therefore this method would be the same as mixed-FEM with the only difference that the coupling terms are ignored. For the rest of the methods only the axial component of the displacement in the Y-direction was used which is assumed to be the only component available. The local inversion of the Helmholtz equation was used for comparison as a previously used method for the situation under study. In this method the Helmholtz equation (6-4) in which both the homogeneity and incompressibility are assumed, is used. Two different sub-domain sizes of $4 \times 4 \times 4$ and $10 \times 10 \times 10$ were used for this method. Finally the shear-FEM without the homogeneity assumption proposed in this paper was used with only the Y-component of the displacement. For the FEM methods, we used 8-node cubic elements of size 1mm with linear displacement shape functions and constant shape functions for the shear modulus.

In order to test the formulation in cylindrical coordinate system, the data was interpolated on a cylindrical mesh and the radial component of the displacement was calculated for each node and used in the inverse problem (Figure 6-2). The displacement data is interpolated on a cylindrical mesh with the size of $\Delta r = 1mm, \Delta\theta = 2deg\ , \Delta z = 1mm$, and we assume the radius of the probe is 10mm, therefore the center of the mesh is 10mm away from the edge of the cube, (d=10mm) as shown in Figure 6-2. Then the formulation derived for cylindrical coordinates was used to reconstruct the Young's modulus.

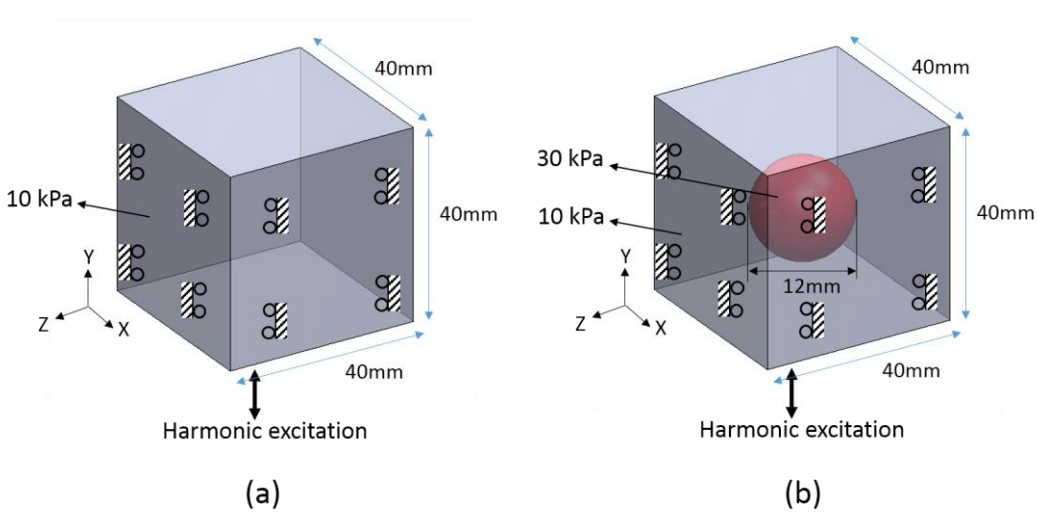

Figure 6-1. Schematic of the model used for generating 3D synthetic data. (a) for a homogenous region, (b) for a region with spherical inclusion. Two of the faces are confined in the normal direction and one face is excited with a harmonic motion.

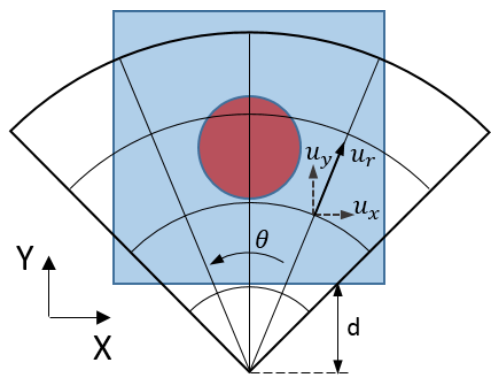

Figure 6-2. The displacement data is interpolated on a cylindrical mesh and radial component of the displacement is calculated.

6.2.2.2 CIRS phantoms

We also applied the proposed method to the experimental data captured from a CIRS elastography quality-assurance phantom (model 049, CIRS Inc, USA) using the ultrasound system developed in our lab for measuring fast steady-state tissue motion [147]. A 4DL14-5 linear 3D probe (Ultrasonix Medical Corp., Richmond, BC, Canada) with the center frequency of 6.5 MHz was used to measure the axial displacement phasor distribution in a volume. The excitation was applied using a voice coil as shown in Figure 6-3 with excitation frequencies of 200, 233, 267 Hz. The axial displacement was captured in different 2D planes using the sweep motion of the probe. Then the data was interpolated on a regular mesh with spacing of 1.5 mm for reconstruction. The radius of the sweep on the surface of the probe is 82mm. Although for this case it can be

assumed that the image planes are almost parallel, we used both the Cartesian and the cylindrical formulations for comparison. The CIRS phantom has eight spherical inclusions with different sizes and elasticity values. In this experiment the region of interest contains only the small hardest inclusion which has the Young's modulus of 62 kPa surrounded by the background material with Young's modulus of 29 kPa.

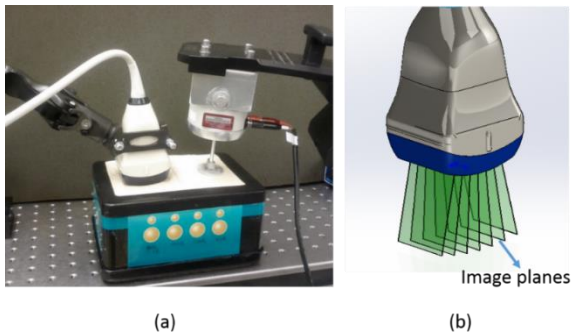

Figure 6-3. (a) The experiment setup showing the CIRS phantom, the 3D probe and the voice coil. (b) Showing the schematic of the set of 2D planes spanning a volume.

We also tested the proposed method in cylindrical coordinates using experimental data captured from a CIRS elastography prostate phantom (model 066, CIRS Inc, USA). The material used in this phantom is Zerdine®, a patented solid elastic water based polymer. In this phantom, the prostate, along with structures simulating the rectal wall, seminal vesicles and urethra, is contained within an 11.5 x 7.0 x 9.5 cm clear plastic container. This phantom contains 3 isoechoic lesions with diameter of 10 mm that are at least two times stiffer than the simulated prostate tissue (Figure 6-4).

A BK 8848 4-12 MHz TRUS linear transducer (BK Medical, Herlev, Denmark)) was used to measure the axial displacement phasor distribution in a volume. Due to limited control of the imaging sequence in the BK system, we could not use here the sector based tissue motion measurement technique developed for the Ultrasonix system [147]. We used instead a band-pass sampling algorithm described by Eskandari et al. [148]. This approach allows phase and amplitude reconstruction with sampling frequencies that are lower than the excitation frequencies. The excitation was applied using a voice coil as shown in Figure 6-5 with excitation frequencies of 144, 165, 181 Hz. We used a previously designed TRUS roll robot [149] for sweeping the volume by rolling the TRUS probe in 0.9° increments. The radius of the sweep for this probe is 10mm on the surface of the transducer therefore larger angle change is required for this case to cover the desired volume. The CIRS phantom used in this experiment has three spherical stiff inclusions. Unfortunately, the elasticity values are not reported by the manufacturer for this model of the phantom. Therefore, the absolute values of the Young's modulus cannot be validated for this case.

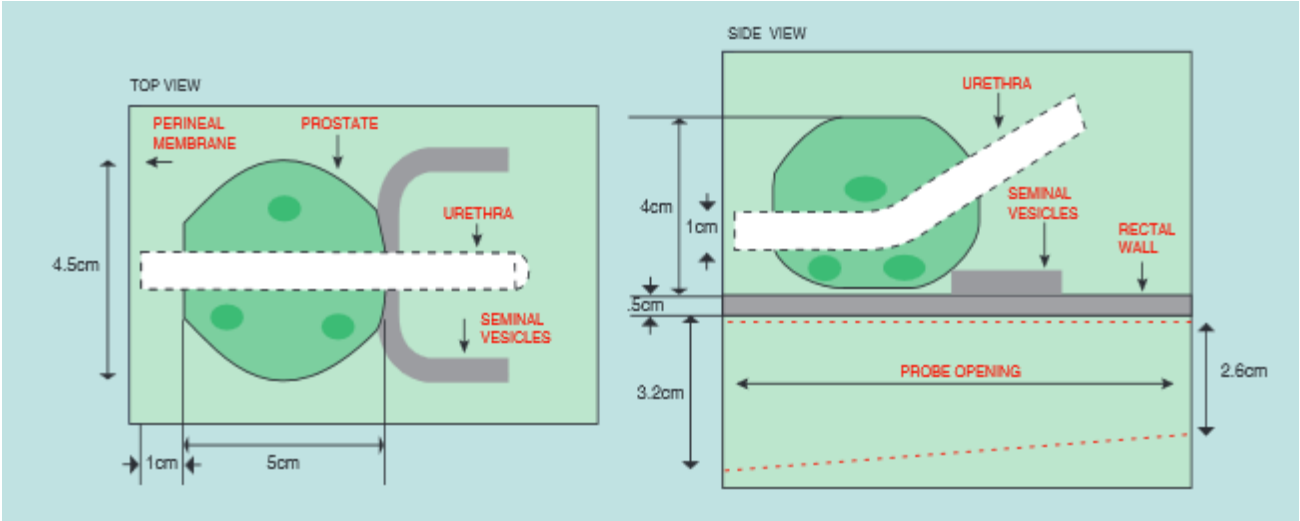

Figure 6-4. The schematic of the CIRS prostate phantom model 066. (www.cirsinc.com)

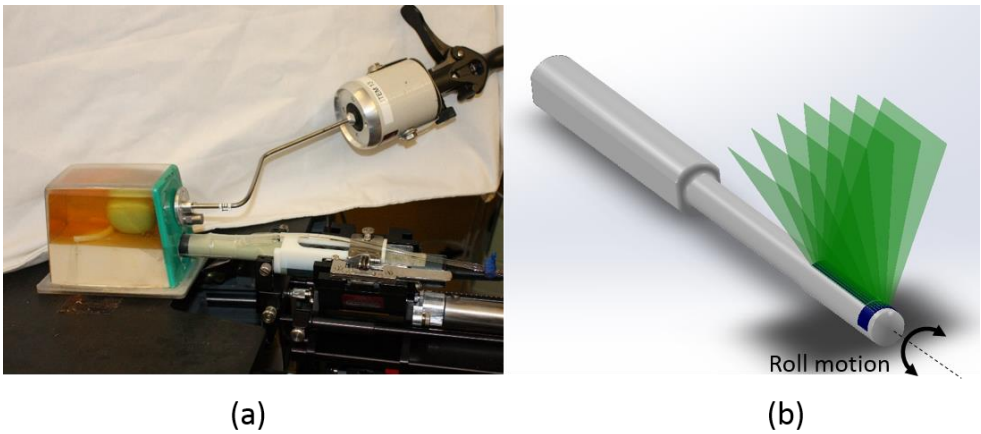

Figure 6-5. (a) The experiment setup showing the CIRS prostate phantom, the TRUS probe and the shaker, (b) Showing the schematic of the TRUS probe and 2D planes on which the data was captured over a volume.

6.2.2.3 Patient

We used the same system that was used for the prostate phantom experiments to collect data from a 70 year old patient with biopsy confirmed cancer. Excitation frequencies of 72, 75, 80 Hz were used. The patient was scheduled for radical prostatectomy due to prostate cancer at Vancouver General Hospital (VGH) and the Elastography scan was preformed right before the surgery. Institutional Research Ethics Board approval and patient consent were obtained.

6.3 Results

6.3.1 Simulations

6.3.1.1 Cartesian coordinate system

Figure 6-6 shows the normalized magnitude of the Y-component of the displacement for the mid-plane of the two different regions. Figure 6-7 shows the reconstructed results for the homogeneous region and Figure 6-8 shows the results for the region with the spherical inclusion.

In Table 6-1, the RMS error, mean and standard deviation of the Young's modulus of the homogeneous region are reported for different inversion techniques and different frequencies. For the region with the spherical inclusion, the RMS error and CNR values are reported in Table 6-2. The RMS error and CNR were calculated for each case using equations (6-21) and (6-22) respectively.

$$RMS = \sqrt{\frac{1}{m}\sum_{i=1}^{m}\frac{\left(E_i - E_i^0\right)^2}{(E_i^0)^2}} \tag{6-21}$$

$$CNR = \frac{2(m_1 - m_2)^2}{\sigma_1^2 + \sigma_2^2} \tag{6-22}$$

where E and E^0 are the estimated and actual elasticities, m_1 and m_2 are the means and σ_1 and σ_2 are the standard deviations of the estimated Young's modulus of the background and the inclusion.

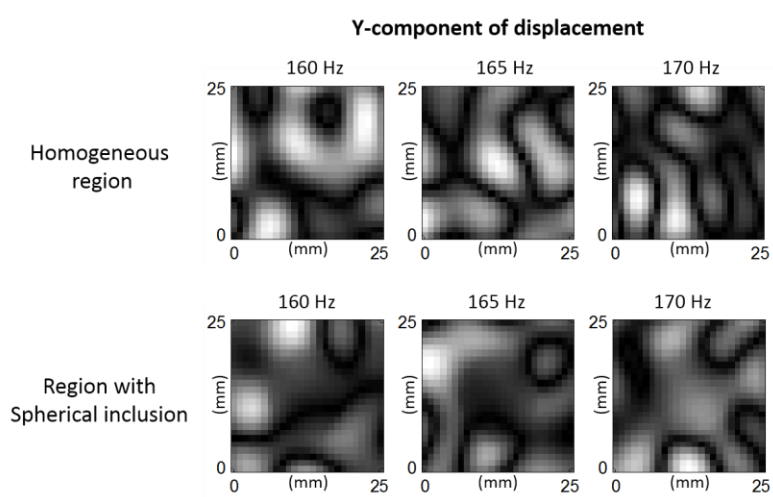

Figure 6-6. Simulated Y-component for both regions shown in Figure 6-1. The normalized magnitude of the displacement in the mid-plane is shown in these images.

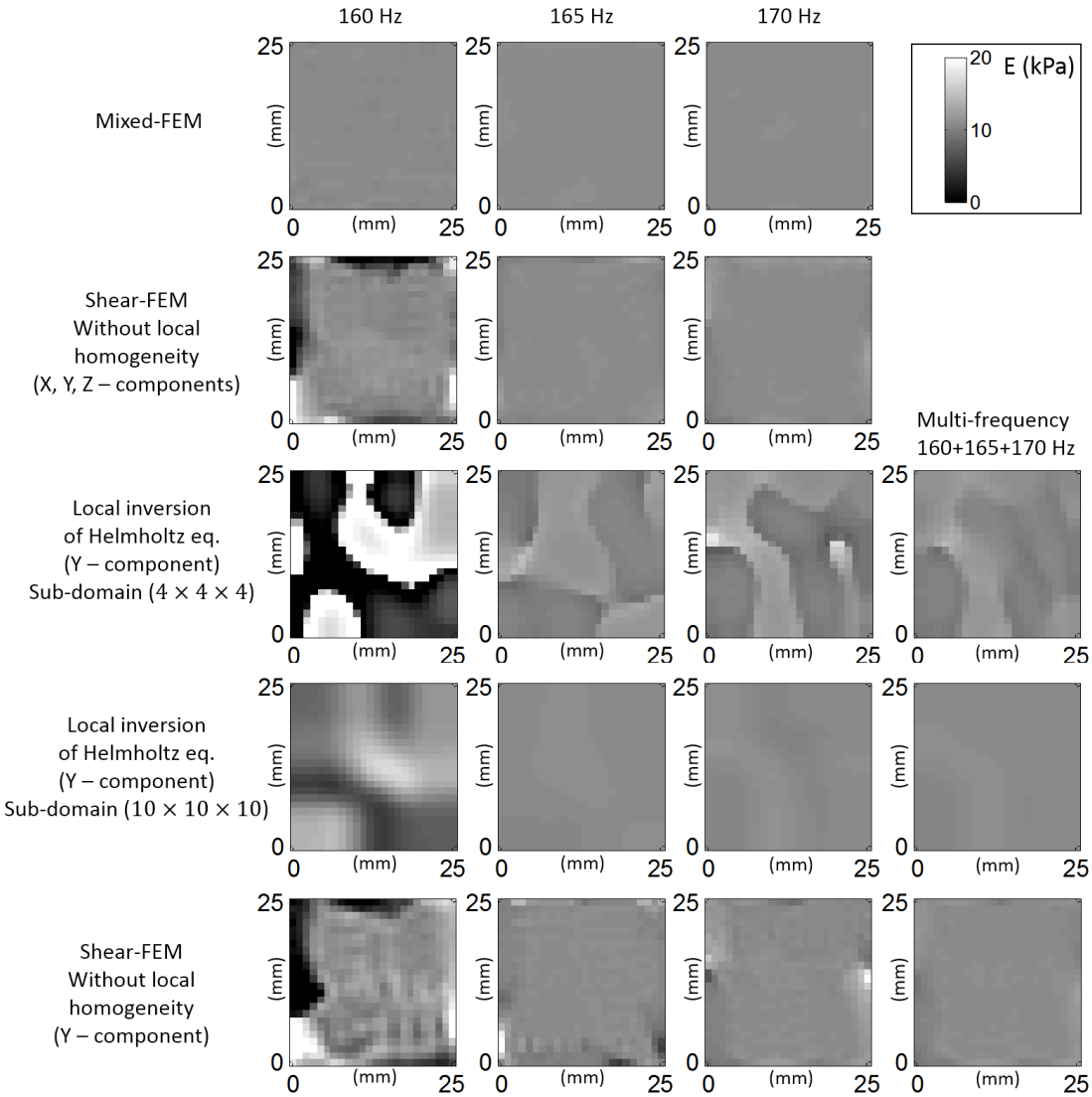

Figure 6-7. The reconstructed Young's modulus from simulation data for the homogeneous region using different methods and excitation frequencies

Table 6-1. The RMS error, mean and standard deviation of the reconstructed Young's modulus for the homogeneous region using different methods and frequencies

Method	Frequency (Hz)	RMS error	Mean E (kPa)	Std E (kPa)
Mixed-FEM	160	0.082	10.79	0.22
	165	0.090	10.90	0.05
	170	0.083	10.82	0.05
Shear-FEM (X, Y, Z – components)	160	0.586	10.85	5.80
	165	0.104	10.94	0.45
	170	0.114	10.95	0.63
Local inversion of Helmholtz eq. (Y – component) $(4 \times 4 \times 4)$	160	1.256	10.82	12.53
	165	0.133	10.92	0.95
	170	0.195	10.97	1.69
	160+165+170	0.125	10.92	0.85
Local inversion of Helmholtz eq. (Y – component) $(10 \times 10 \times 10)$	160	0.350	10.66	3.43
	165	0.095	10.92	0.23
	170	0.096	10.88	0.37
	160+165+170	0.090	10.88	0.22
Shear-FEM (Y – component)	160	0.914	10.87	9.10
	165	0.145	10.91	1.13
	170	0.184	11.03	1.52
	160+165+170	0.110	10.89	0.64

Table 6-2. The RMS error and CNR values of the reconstructed Young's modulus for the region with spherical inclusion using different methods and frequencies.

Method	Frequency (Hz)	RMS error	CNR
Mixed-FEM	160	0.134	18.68
	165	0.122	16.82
	170	0.141	18.09
Mixed-FEM With local homogeneity	160	0.266	0.20
	165	0.231	0.22
	170	0.232	0.15
Shear-FEM (X, Y, Z – components)	160	0.271	13.34
	165	0.184	9.76
	170	0.358	9.03
Local inversion of Helmholtz eq. (Y – component) $(4 \times 4 \times 4)$	160	0.860	0.14
	165	0.851	0.10
	170	0.899	2.39
	160+165+170	0.408	1.50
Local inversion of Helmholtz eq. (Y – component) $(10 \times 10 \times 10)$	160	0.240	0.90
	165	0.232	0.10
	170	0.253	2.61
	160+165+170	0.199	1.93
Shear-FEM (Y – component)	160	0.444	8.44
	165	0.349	4.99
	170	0.622	4.04
	160+165+170	0.203	17.64

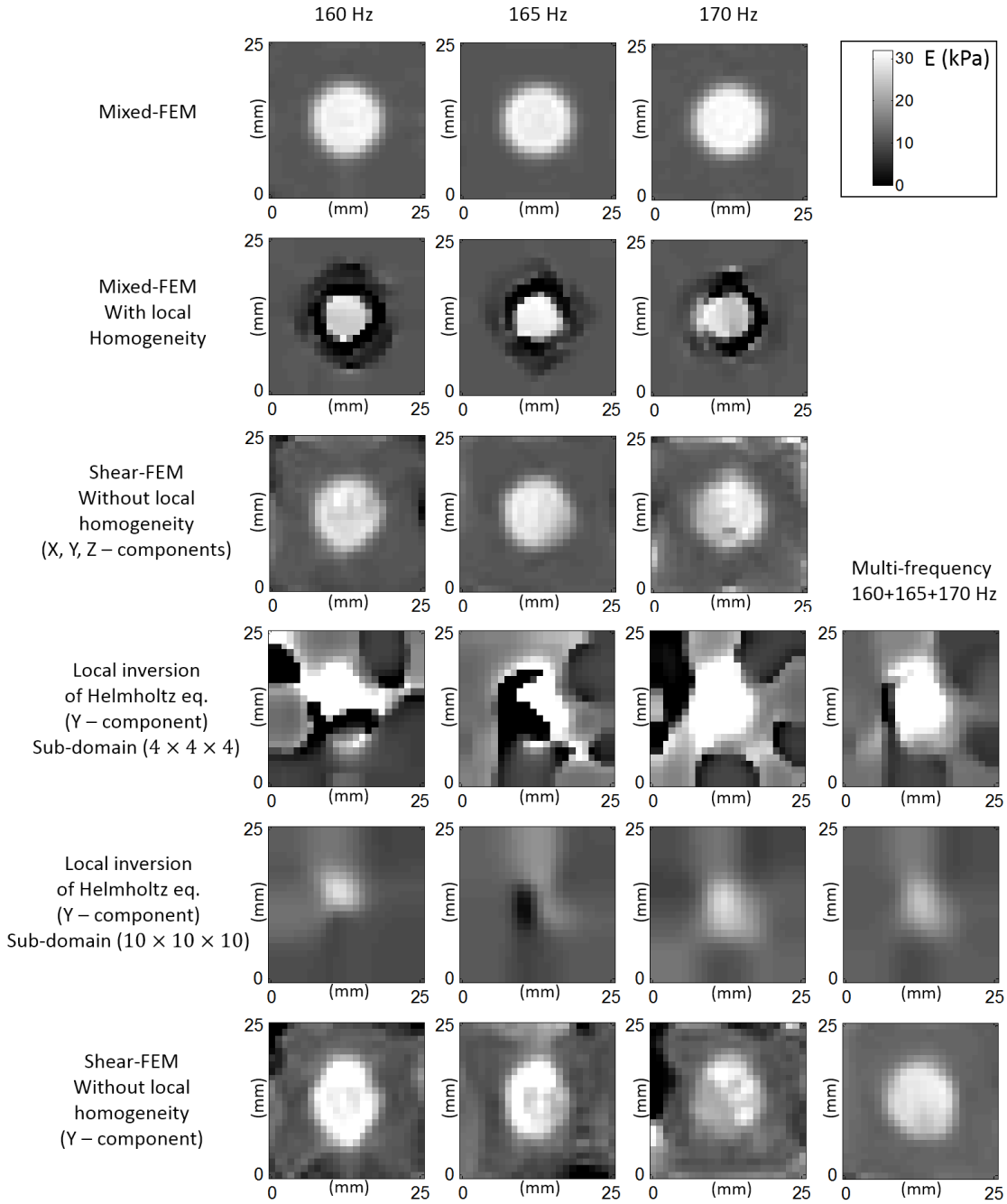

Figure 6-8. The reconstructed Young's modulus from simulation data for the region with spherical inclusion using different methods and excitation frequencies.

6.3.1.2 Cylindrical coordinate system

Figure 6-9(a) shows the reconstructed Young's modulus of the middle plane using cylindrical formulation with multi-frequency data. In order to show the importance of the use of cylindrical formulation for such cases, the same data is used with Cartesian formulation assuming the image planes are parallel. The distance at the mid-point in radial direction is used as the distance between the planes. The result is shown in Figure 6-9(b). The RMS errors of the results obtained using cylindrical and Cartesian formulations are 0.2 and 0.43 respectively.

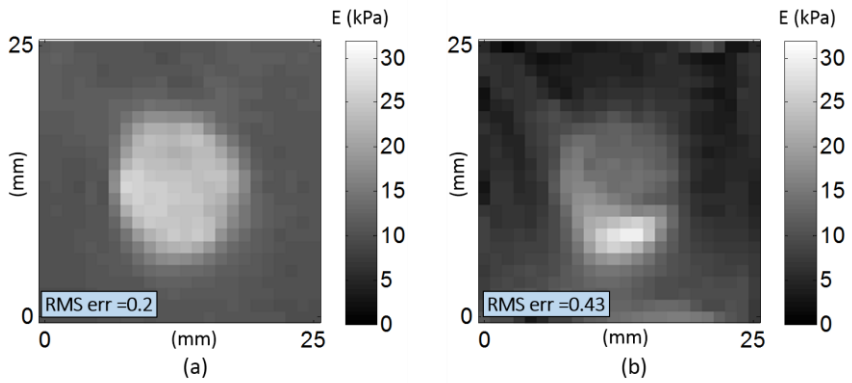

Figure 6-9. (a) The reconstructed Young's modulus using the formulation for cylindrical coordinate system, (b) using the Cartesian coordinate system.

6.3.2 Experiment

6.3.2.1 CIRS elastography phantom

Figure 6-10 shows the sample B-mode image and the normalized measured displacement in one of the planes.

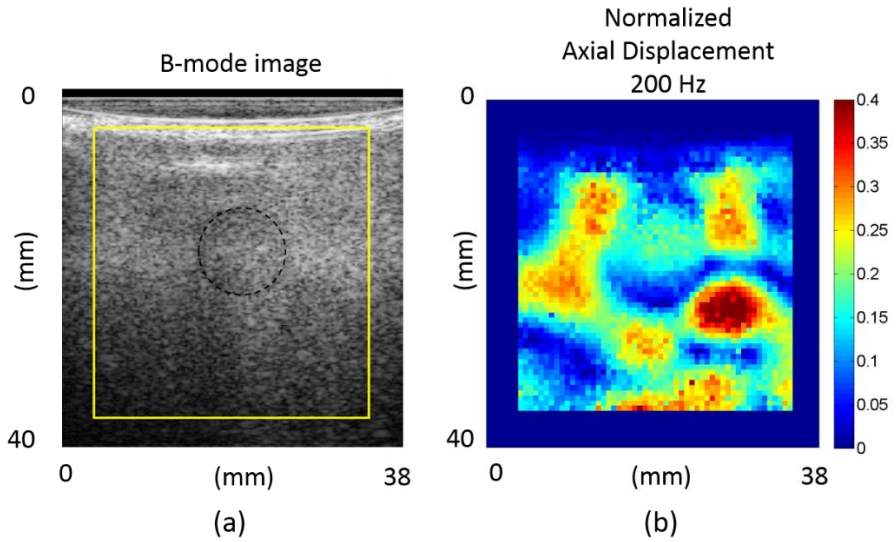

Figure 6-10. Sample B-mode image and the absolute values of the normalized displacement phasors in the mid-plane.

The two methods, with and without the local homogeneity assumption, with Cartesian formulation, were used to reconstruct the Young's modulus map. The results are shown in Figure 6-11 for different frequencies. For comparison, the result using the cylindrical formulation is also presented in this figure. The inclusion was manually segmented and the mean and standard deviation of the Young's modulus for each region was calculated and from that the CNR values were calculated for each case and are reported under each image in Figure 6-11. With the Cartesian formulation without homogeneity assumption and with multi-frequency data, the mean and standard deviation of the Young's modulus are 43.8 ± 4.9 kPa and 26.2 ± 2.7 kPa (mean $\pm$ standard deviation) for the inclusion and the background, respectively. With the cylindrical formulation the corresponding values are 43.7 ± 5.2 and 23.5 ± 2.8.

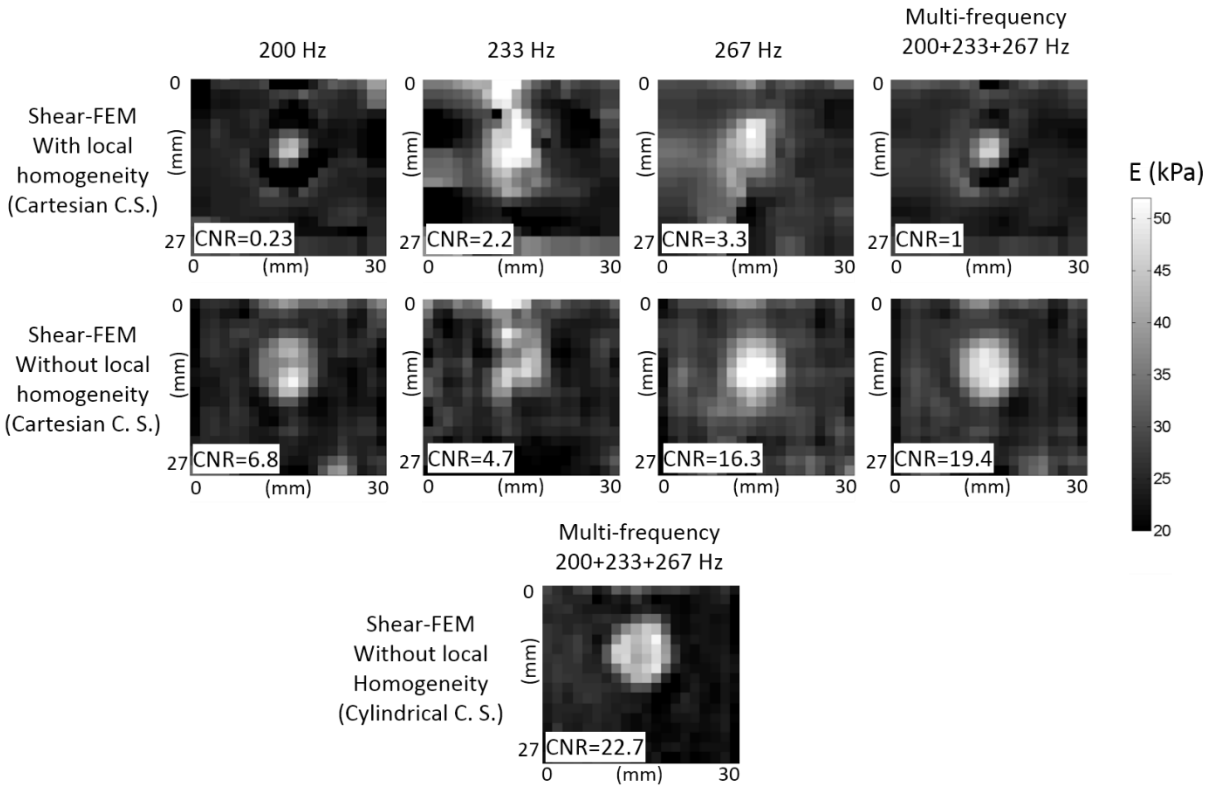

Figure 6-11. The reconstructed Young's modulus from experimental data for different excitation frequencies and the multi-frequency data using the FEM method with and without local homogeneity assumption in Cartesian and Cylindrical coordinate systems.

6.3.2.2 CIRS prostate phantom

Figure 6-12 shows the sample normalized displacement data for the excitation frequency of 181 Hz and the B-mode image for one of the planes. Figure 6-13(a) shows the reconstructed Young's modulus using the cylindrical formulation with multi-frequency data. We also processed the same data using the formulation in Cartesian coordinate system assuming the image planes are parallel. Figure 6-13(b) shows the result for the Cartesian formulation.

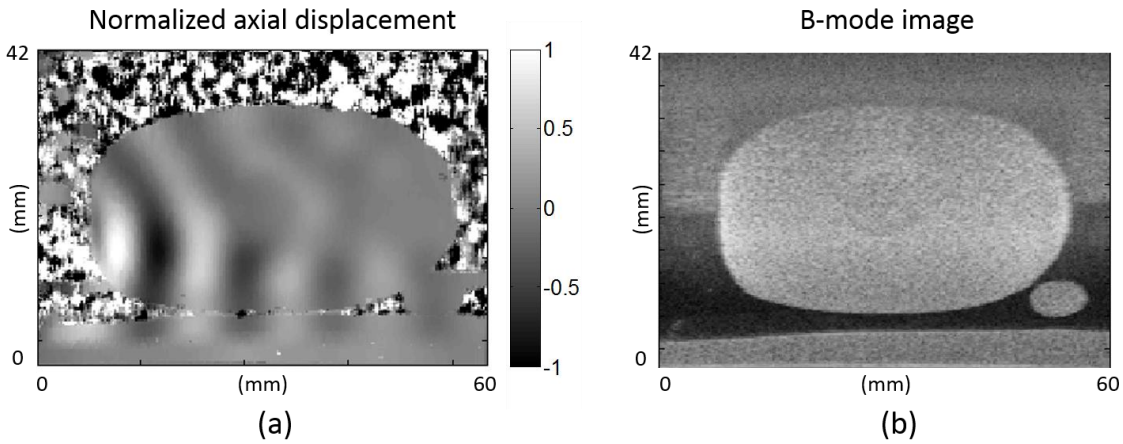

Figure 6-12. (a) Sample displacement data captured from CIRS prostate phantom. (b) B-mode image of the prostate phantom.

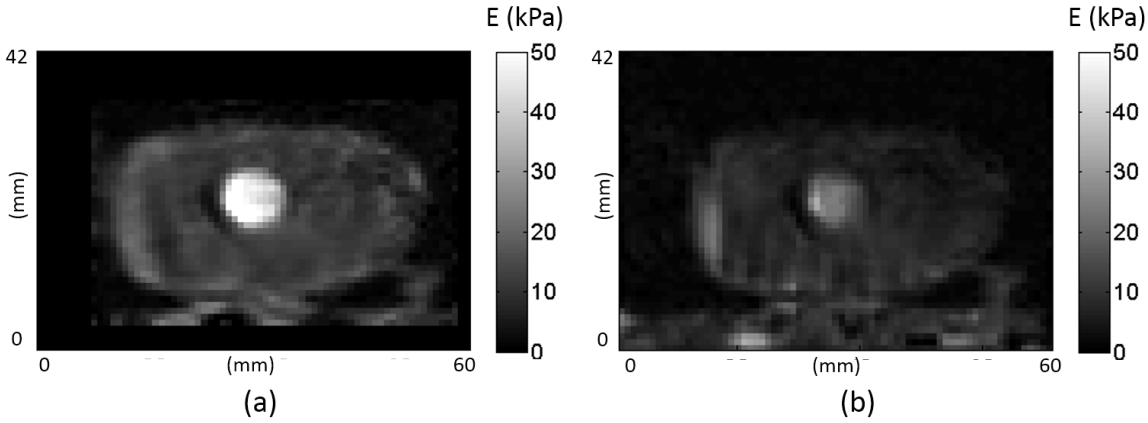

Figure 6-13. (a) The reconstructed Young's modulus using the formulation for cylindrical coordinate system, (b) using the Cartesian coordinate system.

6.3.3 Patient results

The Young's modulus map was obtained using the multi-frequency cylindrical formulation as explained before. Figure 6-14 shows the elastograms and B-mode images for one sagittal and one transverse planes. For comparison and to show the effect of the homogeneity assumption in a real tissue case, the local inversion of the Helmholtz equation was also applied to this data and the results are shown in Figure 6-15. In the first row, overlapping sub-domains of size $4 \times 4 \times 4$ are used and in the second row sub-domains of size $10 \times 10 \times 10$.

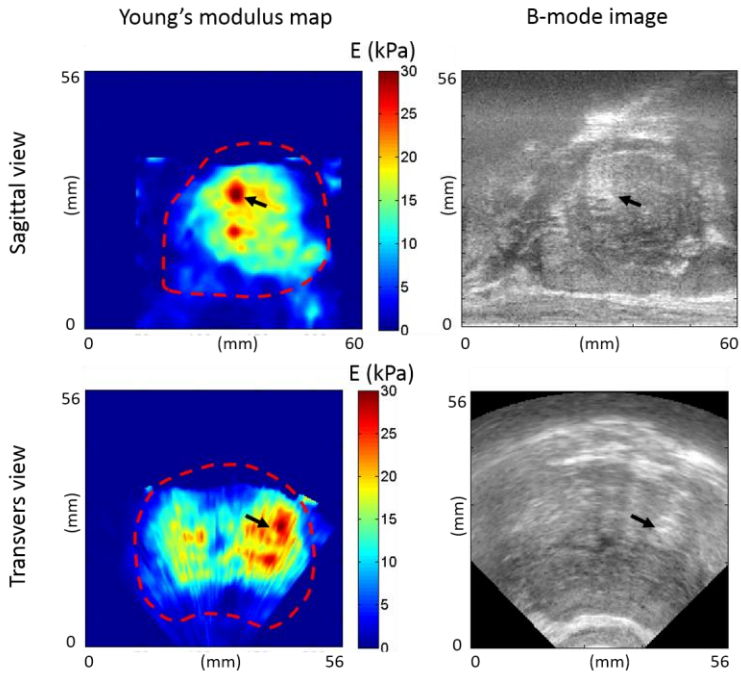

Figure 6-14. The reconstructed Young's modulus using shear-FEM without homogeneity assumption with cylindrical formulation and the corresponding B-mode image in a sagittal and transverse plane.

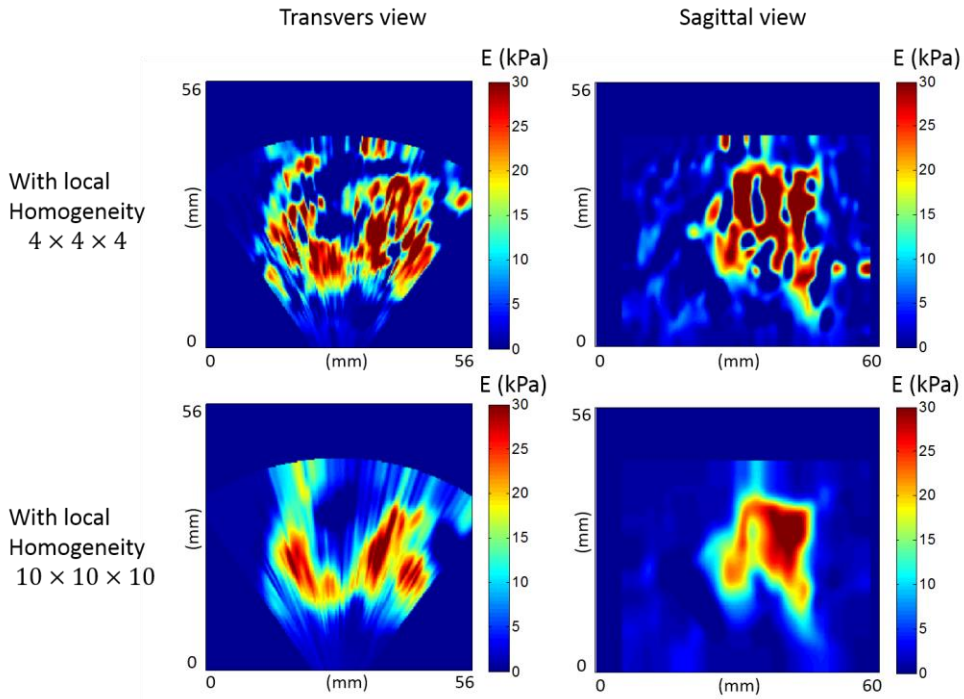

Figure 6-15. The reconstructed Young's modulus using the local inversion of the Helmholtz equation in the same sagittal and transverse planes as in Figure 6-14. Two different sub-domain sizes were used.

6.4 Discussions

In the simulation results of the homogeneous region, it can be seen that the mixed-FEM is producing uniform results with a very low standard deviation. The mean value is slightly higher than the assumed value of 10 kPa which is related to the chosen ratio of voxel size to the wavelength and its effect on the derivatives calculation as discussed in [150]. This effect appears in all other methods as well. The second row in Figure 6-7 shows the deviation from the mixed-FEM results when only the coupling terms of the wave equation are ignored. As it can be seen, this does not cause very significant changes in the result. However, it is dependent on the boundary condition and the frequency. For example the artifacts for the frequency of 160 Hz are higher than for other frequencies. The third row in Figure 6-7 shows that using the local inversion of the Helmholtz equation introduces a significant amount of artifacts. These artifacts are not related to the homogeneity assumption since the region is in fact homogenous. These artifacts are also not due to ignoring the coupling terms since that effect was shown to be small in the second row of simulations. This is simply because the equation is solved locally and the artifacts are caused by the numerical error in the calculation of derivatives in regions with near-zero displacement amplitude or nodal areas. This can also be verified by comparing the position and pattern of the artifacts with the pattern of the zero displacement area shown in Figure 6-6. According to the Helmholtz equation the shear modulus is proportional to the ratio of the displacement over the Laplacian of the displacement. Therefore, wherever the displacement is small, the Laplacian is also close to zero. Since there is always some numerical error in Laplacian calculation, when the value of the Laplacian drops under the error level there will be a significant amount of error in the shear modulus calculation causing the negative values. Since the position of the nodal area changes when the frequency changes, it can be seen that the pattern and level of the artifacts also change with the frequency. Therefore, by combining the data sets from different frequencies, it can be seen that almost all the areas will be covered by large enough displacement from different data sets and the artifacts are significantly reduced. The other way to reduce these artifacts is by increasing the sub-domain size as shown in the fourth row of Figure 6-7. The reason is that when the sub-domain size is small it is more likely that the whole area of a sub-domain will cover a small displacement region which results in a complete failure, while using larger sub-domains increases the chance of covering the larger displacement area around the nodal area which prevents the failure of the inversion in that sub-domain. However, when the homogeneity assumption is used, increasing the sub-domain size blurs sharp boundaries between different elasticities because with the homogeneity assumption only one value of elasticity is assigned to the whole area of the sub-domain. But in the method without the homogeneity assumption the elements inside the sub-domain can have different elasticity values and increasing the sub-domain size does not affect the spatial resolution. The last row in Figure 6-7 shows that using a larger sub-domain in the shear-FEM method (here the size of the entire region of interest) reduces those artifacts present in the local inversion method. However some artifacts remain due

to ignoring the coupling terms and due to zero displacement regions. The remaining artifacts are mostly removed after using the multi-frequency data. The number and spacing of the frequencies is currently determined empirically. In our experience, with the current range of frequency for the current material properties which results in having about half a wavelength within the sub-domain, using three to four frequencies with at least 3% difference in frequency is sufficient to remove most of the artifacts. Basically we do not recommend using the shear-FEM method with single frequency data when only one component of the displacement is used. Due to near zero displacement areas, and due to the effect of ignoring the coupling terms there will be some artifacts in the results. Normally if all three components are available, the regions in which all are small are quite limited. Using multi-frequency data not only solves the problem of near zero displacement regions, but also helps to average out and reduce the effect of ignoring the pressure term. This technique has also been used in previous methods using the local inversion of the Helmholtz equation [32, 52, 53]. In those methods, having access to transient displacement data and taking the Fourier transform of the data, they are able to perform the averaging over a wide range of frequencies. Here we showed that having only a few different frequencies using a simpler system and without needing to acquire transient data, our shear-FEM method is able to produce reasonable results while the local inversion still contains artifacts using as many frequencies.

Similar to the homogenous region, we can see in Figure 6-8 that, for the region with inclusion, the mixed-FEM is producing uniform results with the inclusion clearly detected which can be used as a reference to compare the other methods' results with. In the second row of this figure, the results obtained from using the mixed-FEM with local homogeneity assumption are showed. In this results we can clearly see the effect of homogeneity assumption. This assumption causes biases on the edge of the inclusion where the elasticity variation is high. This effect is very significant and in regions with a more complicated elasticity distribution can completely change the elasticity pattern and cause confusion in locating the stiff area. The third row shows the effect of ignoring the coupling terms. Again it can be seen this effect is not very significant. Some small artifacts can be seen and the CNR is dropped between 20%-50% but still the inclusion is clearly detected. The huge artifacts in the local inversion of the Helmholtz equation are also present for this case. Here the effect of local homogeneity assumption is also added to the artifacts. These artifacts are reduced by increasing the sub-domain size and using multi-frequency data. But as mentioned before increasing the sub-domain size in the local inversion method with homogeneity assumption decreases the resolution. Being able to use a large sub-domain without affecting sharpness of inclusion boundary in the shear-FEM method without homogeneity assumption reduces the artifacts from the zero displacement areas and the remaining artifacts are mostly removed after using multi-frequency data.

The quantitative results presented in Table 6-1 and Table 6-2 confirm the above discussion. For the homogenous region the RMS error decreases when the multi-frequency technique is used; using larger sub-

domains also decreases the RMS error. In this case the method without homogeneity assumption does not really improve the results since the sample is homogeneous. But for the region with the spherical inclusion it can be seen that the CNR values are increased when using the method without the homogeneity assumption.

Figure 6-9 shows that the cylindrical formulation of the shear-FEM without homogeneity assumption performs successfully on simulation data. It can also be seen that using the Cartesian formulation with a data set sampled on a cylindrical mesh and in the radial direction causes underestimating of the Young's modulus and this effect increases away from the axis of the rotation.

The results from the CIRS quality-assurance phantom in Figure 6-11 agree with the simulation results. As in our simulation results, the proposed method without local homogeneity assumption has fewer artifacts and the improvement due to multi-frequency excitation is even more marked. This improvement can also be seen in the CNR values after using the method without the homogeneity assumption and the multi-frequency technique. By comparing the results of the cylindrical formulation and Cartesian formulation in Figure 6-11 we can see that the quality of the result and the CNR value has slightly improved but it is not very significant. By comparing the Young's modulus values obtained for the inclusion and background with the values reported by the manufacturer, we can see that they are underestimated here. The values reported in our previous work [37] (Chapter 5) for the same inclusion in the same phantom obtained using MRE data with our c-FEM method are 45 ± 4 kPa and 23 ± 3 kPa for the inclusion and the background respectively which are close to the values obtained here. As mentioned in that chapter, possible reasons why the values are slightly different from the values reported by the manufacturer include influence of temperature, excitation frequency or the changes of the phantom material properties due to aging of the phantom.

The CIRS prostate phantom results also agree with the simulation results with cylindrical formulation. The inclusion is clearly detected when the cylindrical formulation is used. As expected from the simulation results, using the Cartesian formulation underestimates the Young's modulus values. However, there can be some situations, depending on the displacement wave form and complexity of the region, in which using the Cartesian formulation instead of the cylindrical coordinate formulation may cause more complex artifacts rather than just underestimation of the Young's modulus values.

Unfortunately, for the in-vivo case, a true validation of the elasticity results is not possible since the actual elasticity distribution is not available. Some stiffer areas are observed in Figure 6-14 on the right side of the image (the left side of the patient) which may be a sign of tissue abnormality. According to the pathology report, there was a tumor on the left side of the prostate. However, a correlation between cancer and elasticity is beyond the scope of this study. Looking at the results with the homogeneity assumption, it can be seen that the Young's modulus pattern changes when the homogeneity assumption is not used. As expected from our simulations and phantom studies, the artifacts related to nodal areas are visible in the result with smaller sub-

domains; after increasing the size of the sub-domains, these artifacts are reduced. Furthermore, the computed Young's modulus pattern is totally different from the pattern obtained when the homogeneity assumption was not used. This shows the importance of the effect of the tissue homogeneity assumption on the reconstruction results in cases where there are considerable variations in the elasticity of the region, such as in the prostate region.

6.5 Conclusion

We introduced a new FEM-based inversion technique for US-elastography. The method uses a simplified form of the wave equation without the local homogeneity assumption, suitable for the unidirectional displacement measurements available in typical ultrasound systems. We tested the method on simulation and experiment data. We showed that the artifacts are significantly reduced when the local homogeneity assumption is not used. Also, we showed that the artifacts related to neglected pressure term and the lack of information in regions with near-zero displacement amplitude are greatly reduced by using the multi-frequency vibro-elastography technique. Using the multi-frequency data has also the benefit of noise reduction by providing multiple measurements of data and the averaging effect for the entire region. We showed that for volumetric US displacement data captured on a cylindrical mesh, the data need to be processed with a cylindrical formulation in cases where the angle of rotation is large. Otherwise using regular formulation can cause artifacts in the reconstructed Young's modulus results. In the presented results in this study, this artifact appeared as a radially proportional underestimation of the Young's modulus, but it may not be that simple in practice depending on the wave pattern and the boundary conditions.

The patient results are promising. The huge differences between the results of the methods with and without homogeneity assumption implies a more careful use of this assumption in such cases. The purpose of presenting the in-vivo result here was to show sample results and to compare the behaviour of different methods in an actual in-vivo images. The correlation between cancer and elasticity was not investigated in this study and more clinical research is required to prove the benefits of such elastography imaging in prostate cancer detection.

This method shows the high potential of providing good quality elastograms with ultrasound systems competitive with results obtained from more expensive and time consuming MRE systems. Due to the direct nature of the inversion method, it has even the potential to perform in real-time by using parallel processing in GPU and faster data acquisition with 2D array ultrasound probes.

Chapter 7 - Comparison of inversion techniques

7.1 Introduction

Several methods have been developed for solving the elasticity inverse problem. In previous chapters we introduced direct mixed-FEM with sparsity regularization (Chapter 2) [36], curl-based FEM without homogeneity assumption (Chapter 5) [37] and shear-FEM which is a direct FEM inversion of the simplified wave equation without homogeneity assumption. In this chapter, all these methods are compared with two other established reconstruction algorithms: local frequency estimator (LFE) [81, 82] and curl-based direct inversion (c-DI) [93]. These methods are tested on simulation data and experimental data collected from a CIRS phantom, a custom made agar-phantom, ex-vivo bovine kidney sample and in-vivo human prostate data. The ex-vivo results are also verified using an indentation scan. Since most of these methods require all the three components of the displacement, we use the MRE technique to capture all the experimental data sets.

7.2 Methods

7.2.1 Inversion techniques

The methods introduced in Chapter 2 (Mixed-FEM), Chapter 5 (c-FEM) and Chapter 6 (shear-FEM) are compared with two other state-of-the-art inversion techniques: LFE and c-DI. The first three methods are used with the novel sparsity regularization introduced in Chapter 2.

We will start by providing a brief summary of the methods that we compare.

***Mixed-FEM*:**

In mixed-FEM, the complete wave equation in frequency domain as shown in (7-1) is discretized using FEM and the resulting equations are rearranged with respect to the shear modulus and pressure unknowns and solved directly for those parameters. Equation (7-2) shows the final system of equations after applying the sparsity regularization in which $\mathbf{R}_1$ and $\mathbf{R}_2$ are the regularization filters.

$$\left[\mu\left(u_{i,j}+u_{j,i}\right)\right]_{,j}+p_{,i}=-\rho\omega^2 u_i \tag{7-1}$$

$$[\mathbf{AR_1} \quad \mathbf{CR_2}]\begin{Bmatrix}\boldsymbol{\mu}^* \\ \boldsymbol{p}^*\end{Bmatrix}=\{\boldsymbol{f}'\} \tag{7-2}$$

***c-FEM*:**

In the c-FEM method the curl of equation (7-1) is taken without using the homogeneity assumption as shown in (7-3). The curl operator eliminates the pressure term. Then FEM is used again to discretize this equation and, this time, only the shear modulus is left as unknown (7-4). Again, sparsity regularization is used with this method.

$$\varepsilon_{lmi}\left[\mu\left(u_{i,j}+u_{j,i}\right)\right]_{,jm}=-\rho\omega^2\varepsilon_{lmi}u_{i,m} \tag{7-3}$$

$$\left[\widehat{\mathbf{A}}\mathbf{R}\right]\{\boldsymbol{\mu}^*\}=\{\hat{\boldsymbol{f}}\} \tag{7-4}$$

***Shear-FEM*:**

In shear-FEM the coupling terms in (7-1) are ignored but still the homogeneity assumption is not used. This results in (7-5) which is discretized using the FEM and solved directly for the shear modulus unknowns ((7-6)). Again, sparsity regularization is used with this method.

$$\left[\mu u_{i,j}\right]_{,j}=-\rho\omega^2 u_i \tag{7-5}$$

$$\left[\widetilde{\mathbf{A}}\mathbf{R}\right]\{\boldsymbol{\mu}^*\}=\{\boldsymbol{f}'\} \tag{7-6}$$

LFE:

In LFE the local spatial frequency of the wave is estimated based on filter banks. The filter banks are in pairs; the ratio of the outputs of each pair gives an estimation of the local frequency, provided that the local frequency is within the bandwidth of that pair. Then the spatial frequency is related to the shear modulus based on the shear wave velocity equation. For this method, we use the implementation by Baghani *et al.* in [120].

***c-DI*:**

In c-DI method, again the curl operator is used to eliminate the pressure term but before that, the homogeneity assumption is used to simplify the equation. The resulting Helmholtz equation is shown in (7-7).

$$\mu\nabla^2\boldsymbol{q} = -\rho\omega^2\boldsymbol{q}, \qquad (\boldsymbol{q} = \boldsymbol{\nabla} \times \boldsymbol{u}) \tag{7-7}$$

This equation can be solved directly using a least squares technique. This code was provided by Professor Ralph Sinkus *et al.*, the developers of the method [93]. Since the provided code is not an open source code and it can only process the MRE raw data, for simulation data we used our own implementation of the method. The way we implemented this method is similar to our c-FEM method except that the homogeneity assumption is used. Basically for each point we consider a small sub-domain of size $4 \times 4 \times 4$ around that point and assume one value of elasticity for the entire sub-domain and use c-FEM to solve for the shear modulus. Therefore, this implementation of the method may not produce exactly the same result the original c-DI method would produce but they are fairly similar.

It should be noted that both LFE and c-DI methods have tunable parameters that need to be optimized for specific data sets. Although we have tried to use the best settings we could for these methods, it is still possible these methods could potentially be better with a more appropriate tuning.

7.2.2 Simulations, phantom and data collection

For the simulation study two models, as shown in Figure 7-1, one with a homogeneous region and the other with a hard spherical inclusion, are used to generate the synthetic data. The simulation is carried out using ANSYS (ANSYS Inc., Canonsburg, USA). The background and the inclusion have Young's moduli of 10 kPa and 20 kPa respectively and the Poisson's ratio is assumed to be 0.495 for both regions. The region was discretized using 10-node tetrahedral elements (SOLID187) with element size of 0.5 mm and then the resulting data was interpolated onto a coarser regular rectangular mesh of size 1 mm and used in the inverse problem. In order to see the effect of the excitation frequency on the efficiency of the methods a range of

frequencies from 10 Hz to 400 Hz is used for the homogenous region. Also the effect of inclusion size in the reconstructed result is investigated by changing the radius of the inclusion from 1mm to 7mm and calculating the CNR value for each method. For this study the excitation frequency of 200 Hz is used which is equivalent to r_m ratio of 0.1 (Chapter 4).

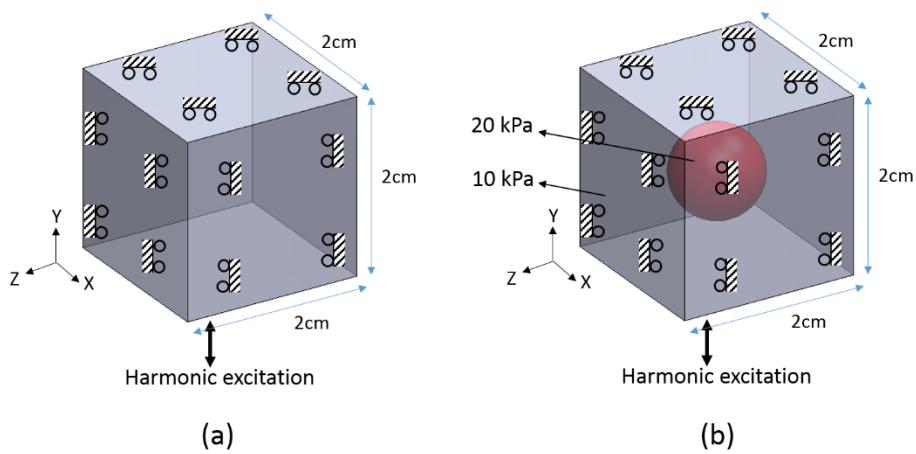

Figure 7-1. Schematic of the models used for generating 3D synthetic data. (a) homogeneous region (b) region with spherical inclusion

The methods were also tested on phantoms. A quality-assurance phantom (Model 049, CIRS Inc, USA) with 8 spherical inclusions of different elasticities and sizes was used (Figure 7-2). Four of the inclusions have a diameter of 2 cm and the other four inclusions have a diameter of 1 cm. Table 2-1 shows the Young's modulus values of the inclusions and of the background. A sinusoidal mechanical excitation of 200 Hz was used for this phantom. The MRE images were acquired in a 3-Tesla scanner (Philips Inc., Netherlands) using a 2D multi-slice multi-shot SE-EPI method with turbo factor 11 [119]. A single sinusoidal cycle was used as the motion encoding gradient with strength of 60mT/m, which captured 8 states of the mechanical motion. The displacements in time domain were converted to complex phasors using the Discrete Fourier Transform and used in the inverse problem. The SNR of the measured displacements for this phantom is 28dB which was estimated using the method explained in Chapter 2.

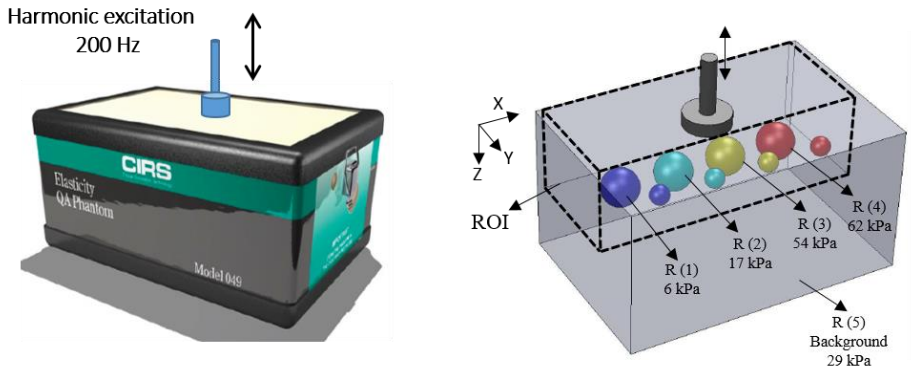

Figure 7-2. CIRS elasticity QA phantom. Only the larger inclusions are located inside the region of interest.

Table 7-1. Young's modulus values of inclusions and background for CIRS phantom reported by the manufacturer. (The density is equal to the density of water)

Region	Young's modulus (kPa)
Type 1	6
Type 2	17
Type 3	54
Type 4	62
Background (5)	29

In order to test the ability of the methods in reconstructing more complex structures, a custom designed phantom was also used. This phantom was made of agar with concentration of 1% agar for the background and 2% for the hard inclusions. To generate T2-weighted and visual contrast, acrylic color was added to the 2% agar solution before being injected into the background solution. The inclusions were injected by a syringe before the gelatine solution was solidified. Many inclusions of various sizes and shapes were created in this manner. Figure 7-3 shows some sample slices of this phantom with irregular shaped inclusions. The MRE images for this phantom were captured in a 7-Tesla scanner (Bruker BioSpin Gmbh., Ettlingen, Germany) using the same method used for the CIRS phantom. A sinusoidal mechanical excitation of 350 Hz was used for this phantom. The SNR of the measured displacements for this phantom is 32dB.

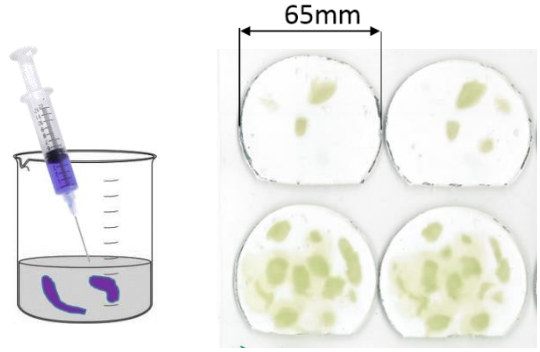

Figure 7-3. The slices of the agar phantom with irregular shape inclusions. The inclusions were made by injecting higher concentration solution into the lower concentration background solution

The methods were also tested on real tissue, both ex-vivo and in-vivo tissue. For the ex-vivo experiment, bovine kidney tissue was used. In order to create lesions inside the sample, first some formalin was injected into the tissue and then the whole sample was kept in formalin for a few hours. Then the sample was embedded in gelatine and it was imaged using the same setup used for imaging the agar phantom. The SNR of the measured displacements for this phantom is 35dB.

For the simulation and phantom study the actual elasticity values and distribution are known and therefore it is possible to validate the reconstructed results with them. But for the real tissue, there is no such a gold standard to compare the results with. One way to achieve a gold standard is to use an indentation tester [151]. Therefore a simple indentation scanner was designed and built for this study to measure relative elasticity maps. As shown in Figure 7-4a, this device has a displacement sensor using a position sensing diode (PSD) and a force sensor (MDB 2.5 , Transducer Techniques, Temecula, CA, USA). In the PSD sensor, a so-called PIN diode, which is rectangular with four electrodes on each side, is exposed to a tiny spot of infrared light. This exposure causes a change in local resistance and thus electron flow in four electrodes. The location of the light spot can be computed from the measured currents of the four electrodes. The sample is moved under the indenter using a 2D automatic motion stage and at each point the sample is poked by the tip of the force sensor and the force-displacement curve is measured. Figure 7-4b shows a sample force-displacement curve during the loading and unloading process. Based on the mathematical solution for the indentation test of a thin elastic layer bonded to a rigid half-space suggested by Hayes *et.al.* [152], the Young's modulus can be predicted using the following equation:

$$E = \frac{(1-\nu^2)}{2a\kappa\left(\frac{a}{h},\ \nu\right)} \cdot \frac{P}{w} \quad , \tag{7-8}$$

where ν is the Poisson's ratio, P is the indentation force, w is the indentation displacement, a is the radius of the indentor, h is the tissue thickness and κ is a function of a/h and ν. Based on this equation if we take the slope of the force-displacement at a specific depth, the resulting value is proportional to the Young's modulus. Therefore if we measure the slope for all the points keeping all the parameters constant, the measured slope can be used as an estimate of the relative Young's modulus. Here the slope of the curve at the end of the unloading path is taken as a measure of relative elasticity. A sample indentation result for a slice of the agar-phantom is shown in Figure 7-4c.

In order to carry out the indentation scan on the ex-vivo sample, the sample was cut into slices after imaging and the indentation measurements were performed on each slice. The registration between the slices and MRE image planes was performed manually based on the visual features in the T2-weighted images.

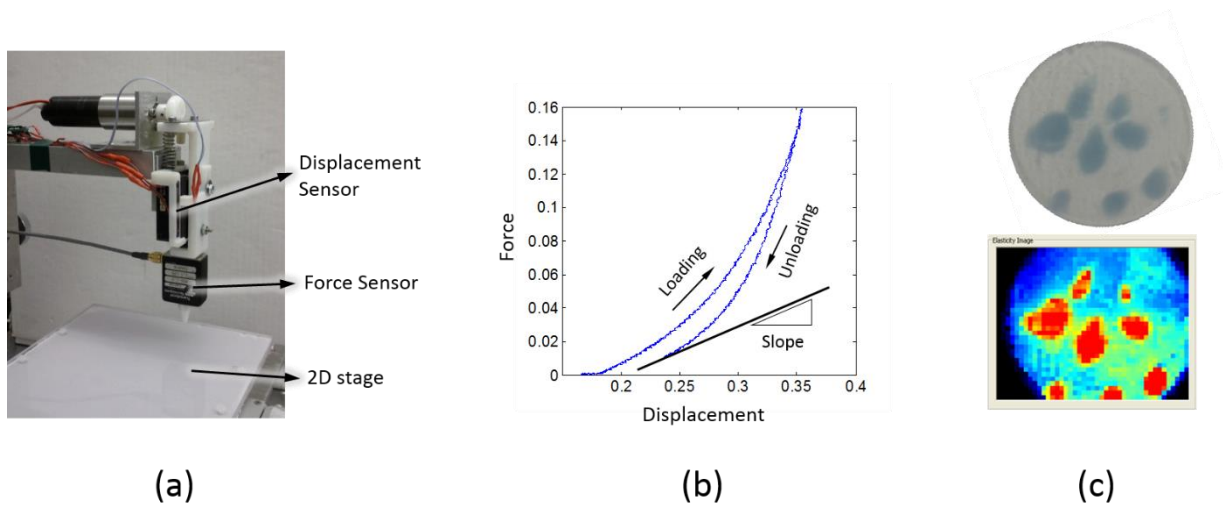

Figure 7-4. (a) The indenter setup used for validation of ex-vivo results. (b) a sample force-displacement diagram obtained for the loading and unloading paths (c) sample indentation result from a slice of agar-phantom

The in-vivo data used in this study is one of the data sets captured by my colleague Ramin Sahebjavaher, under Professor Salcudean's supervision, for a patient study presented in [153]. The patients were diagnosed with cancer and confirmed by biopsy and were scheduled for radical prostatectomy at Vancouver General Hospital (VGH). The studies were approved by the university clinical research ethics board (certificate number: H09-03163) and signed informed consent was provided by all subjects. The details of the setup and acquisition can be found in [153]. The mechanical excitation used for this experiment had the frequency of 70 Hz. The SNR of the measured displacements for this data is 20dB.

7.3 Results

7.3.1 Simulation results

Figure 7-5 shows the results for the homogenous region. In this plot the RMS error is plotted versus the ratio of the voxel size (L) to the wavelength (Λ) : $r_m = L/\Lambda$. The wavelength is calculated from the shear wave speed ($\Lambda = 2\pi/\omega\sqrt{\mu/\rho}$). The dashed lines are the results from noiseless data and the solid lines show the results when white Gaussian noise is added to the displacement data to achieve a SNR of 25dB.

As it can be seen from this figure, similar to our results from Chapter 4, for the FEM methods there is an optimum ratio r_m where the RMS error is minimum. For lower ratios the error increases significantly due to lack of inertial forces and the inaccuracies in calculating the Laplacian for small displacements. For higher ratios we see a slight increase in RMS error which is also due to inaccuracies in computing the derivatives, as discussed in Chapter 4. For the shear-FEM method the observed behaviour may not be related solely to the change of the ratio r_m since in this method the pressure term is ignored for simplification and the effect of this simplification may be different for different cases. The reason for this is that, as the boundary condition or the excitation frequency change, the distribution of the pressure also changes. In some situations the pressure gradients, which are ignored, may be more or less compared to the other terms. The c-FEM result for the case without noise is similar to the mixed-FEM result, but mixed-FEM result is more stable in the presence of noise. Here, the c-DI method has similar results to those of the c-FEM. This is because these methods use similar formulations, except that in the c-FEM, the homogeneity assumption is not used. But this assumption does not deteriorate the inversion since this region is actually homogeneous. In LFE, as opposed to other methods, the RMS error only decreases as the ratio r_m increases but it has an asymptotic decrease.

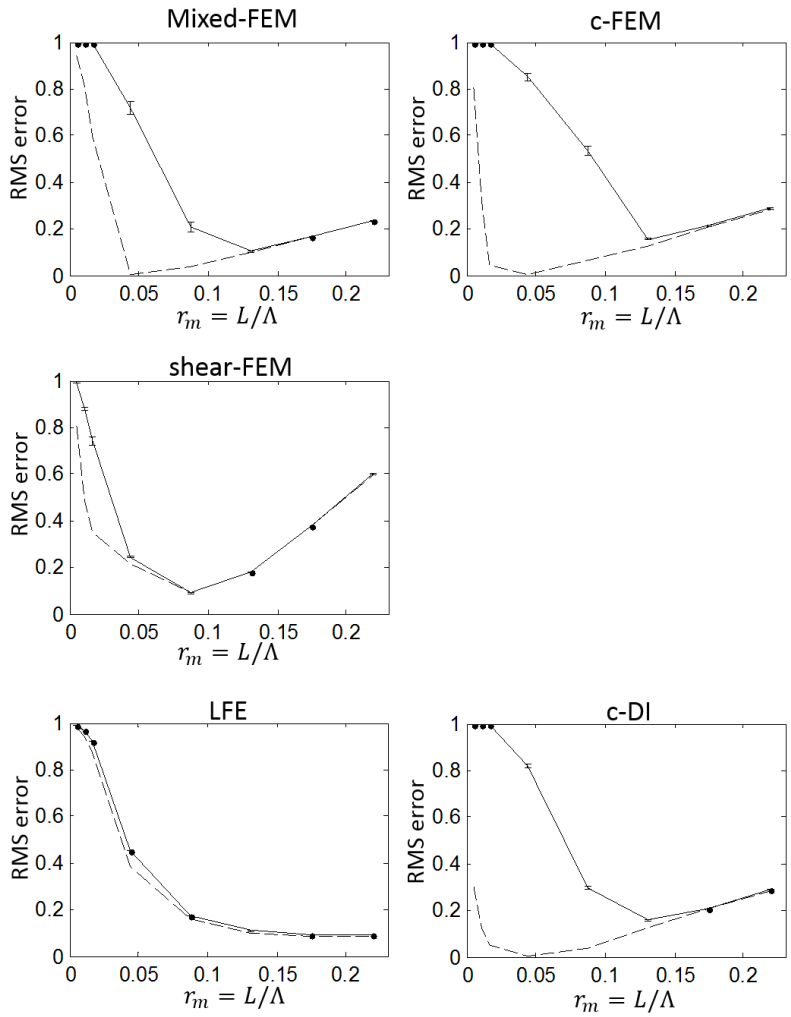

Figure 7-5. RMS error versus the ratio of voxel size / wavelength for a homogeneous region using different methods. (The dash line is for the case without noise and the solid line for the case with noise added with SNR of 25 dB)

For the next study the region with spherical inclusion is used. To investigate the inclusion detectability of each method, the size of the inclusion was changed and the CNR value, which is a measure of detectability (Chapter 4), was calculated for each method. Figure 7-6 shows the CNR value versus the inclusion size using different methods. For this study the excitation frequency of 200 Hz was used. The inclusion size is reported in voxels (D/L) to be independent of the voxel size. D is the inclusion diameter and L is the size of the mesh used in the inverse problem. As before, dashed lines are used for the cases without noise and the solid lines are for the cases with white Gaussian noise added to achieve a SNR of 25 dB.

From these plots it can be seen that the mixed-FEM and c-FEM have the highest CNR values and they have the potential to detect smaller inclusions compared to the other methods. The shear-FEM also has a reasonable high CNR value but, only for larger inclusions compared to mixed-FEM and c-FEM. Among these

methods LFE has the lowest CNR due to smoothing effects in its results, and c-DI also has a low CNR because of the artifacts on the boundaries of the inclusion caused by the homogeneity assumption. When the size of the inclusion increases the area of those artifacts on the boundaries decreases compared to the area of the inclusion and, therefore, the CNR value increases for this method. In all of these results, some local fluctuations are observed which are probably related to resonance modes and can be changed by changing the boundary conditions and frequency. Therefore, it is the global trend that is important and should be considered in our assessment of the methods.

Figure 7-7 shows some sample results of the reconstructed Young's modulus using different methods for regions with different inclusion sizes. Figure 7-8 shows the center profile of the results shown in Figure 7-7 and in Table 7-2 the mean and standard deviation of the Young's modulus for the inclusion and background are listed for the region with inclusion size of $r = 4$ mm. From these sample results it can also be seen that the mixed-FEM and the c-FEM have the most accurate results with the least artifacts. It can be seen that in the shear-FEM results, ignoring the pressure term has caused some artifacts, especially in the case with small inclusions. It should be mentioned again that ignoring the pressure term does not always cause more significant artifacts for smaller inclusions. This depends on the boundary conditions and the frequency. In c-DI, artifacts on the boundaries of the inclusion resulting from the homogeneity assumption are observed as an underestimation of the Young's modulus.

In Figure 7-9 the RMS error and the CNR values are shown vs the displacement SNR for these methods. For this study the size of the inclusion ($r = 4$ mm) and the excitation frequency (200 Hz) are kept constant and only the noise level is changed. From these plots the sensitivity of these methods to noise can be compared. As it can be seen, the c-FEM method is more sensitive to noise as its RMS error and CNR change more compared to the other methods from SNR of 30 to 20. Still, all the FEM methods are superior to the LFE and c-DI.

Just for comparison and to give an estimate of the computational cost of each method, the processing time required for solving the inverse problem for a ROI of size $20 \times 20 \times 20$ as shown in Figure 7-7 are listed in Table 7-3. The processing is done in Matlab® using a standard (Intel® Core2 Duo 2.93GHz) PC with 8GB RAM.

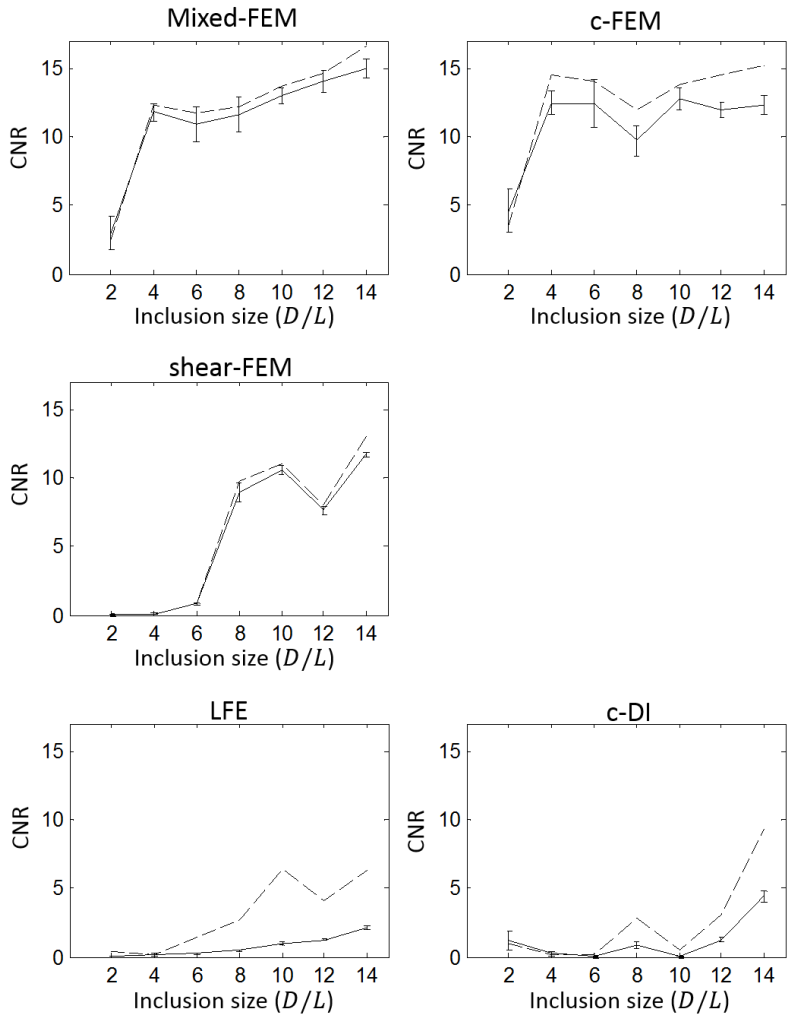

Figure 7-6. CNR values versus the inclusion size for different methods. The frequency of excitation is 200Hz. (The dash line is for the case without noise and the solid line for the case with noise added with SNR of 25 dB)

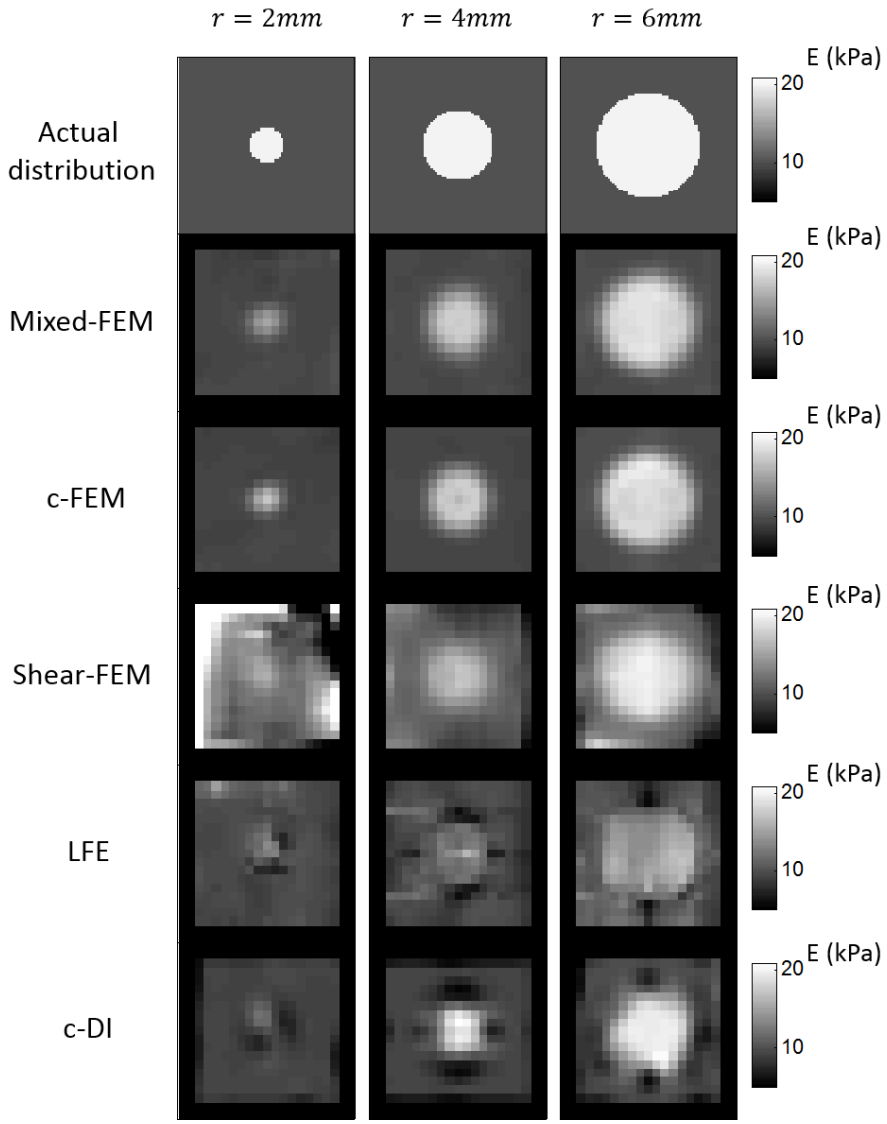

Figure 7-7. Sample reconstructed Young's modulus using different methods for regions with different inclusion sizes. The frequency of excitation is 200Hz.

Table 7-2. The quantitative values of the reconstructed Young's modulus for the region with inclusion of size $r = 4mm$ shown in Figure 7-7

Method	Inclusion E (kPa)	Background E (kPa)
Mixed-FEM	14.7±1.7	9.3±0.8
c-FEM	12.7±1.9	9.4±0.3
Shear-FEM	14.7±1.0	10.5±1.4
LFE	11.2±1.4	9.5±1.0
c-DI	12.7±3.1	8.7±1.1

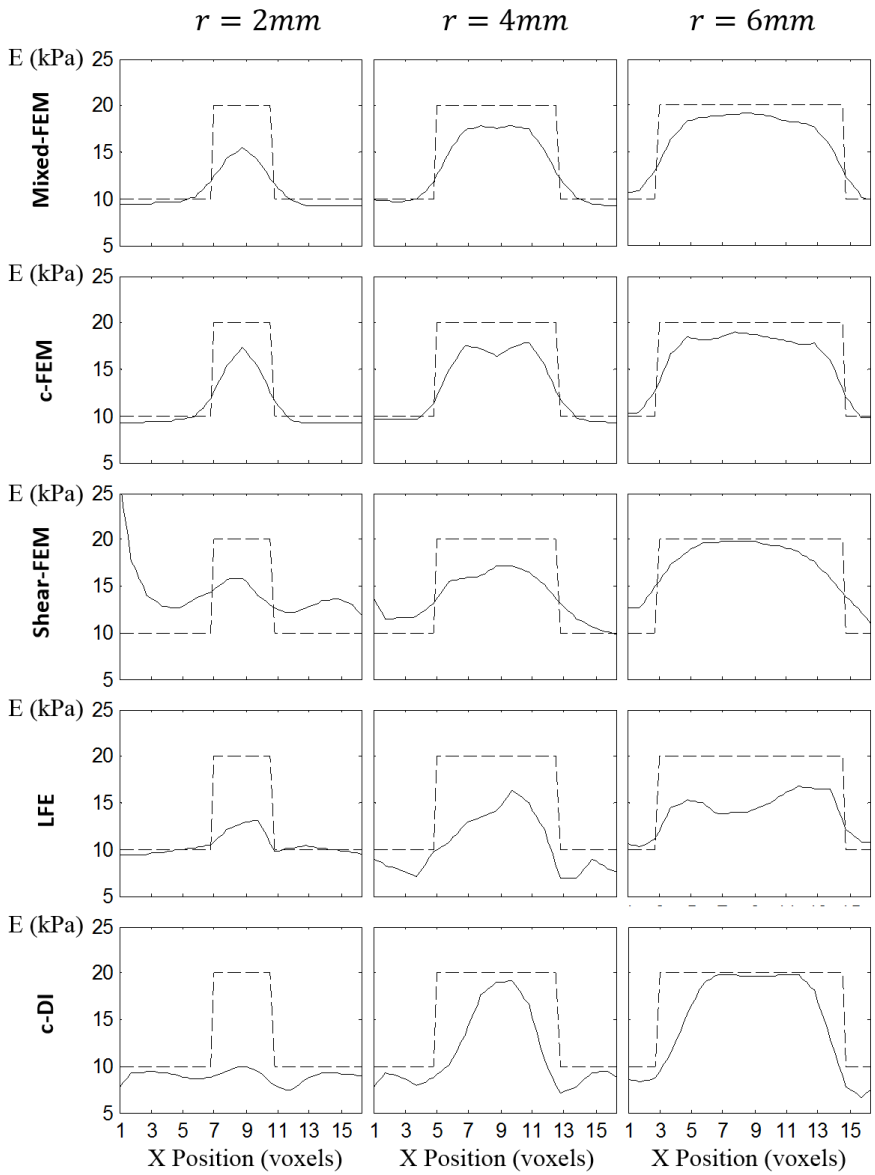

Figure 7-8. The center profile of the reconstructed Young's modulus shown in Figure 7-7.

Table 7-3. The required processing time for solving the inverse problem for region of size $20 \times 20 \times 20$ using different methods. The processing is done in Matlab® using a standard (Intel® Core2 Duo 2.93GHz) PC with 8GB RAM

Method	Processing Time (s)
Mixed-FEM	145
c-FEM	60
Shear-FEM	45
LFE	1
c-DI	10

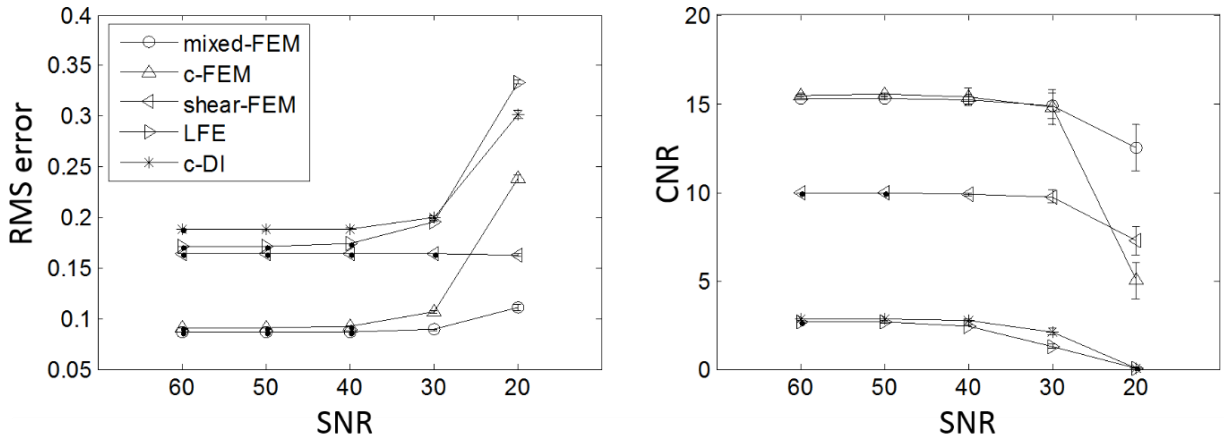

Figure 7-9. RMS error and CNR values versus the noise level SNR for different methods. The inclusion radius is 4mm and the frequency of excitation is 200 Hz.

7.3.2 CIRS phantom results

Figure 7-10 shows the reconstructed Young's modulus for the CIRS phantom using the techniques we tested. In this figure only one cross-section which contains all the larger inclusions is shown. Based on these images it can be seen that the mixed-FEM and c-FEM create fewer artifacts and the inclusions have the clearest boundaries. This is consistent with our simulations results. Artifacts in other methods are due to the simplifications used in deriving their formulations.

In order to have a quantitative comparison between the methods, the mean and standard deviation of the reconstructed Young's modulus of each region were calculated and compared with the values reported by the manufacturer. In order to calculate these values, the regions were segmented by assuming spheres of radius 10 mm, and locating them manually in each region. Figure 7-11 shows the quantitative results.

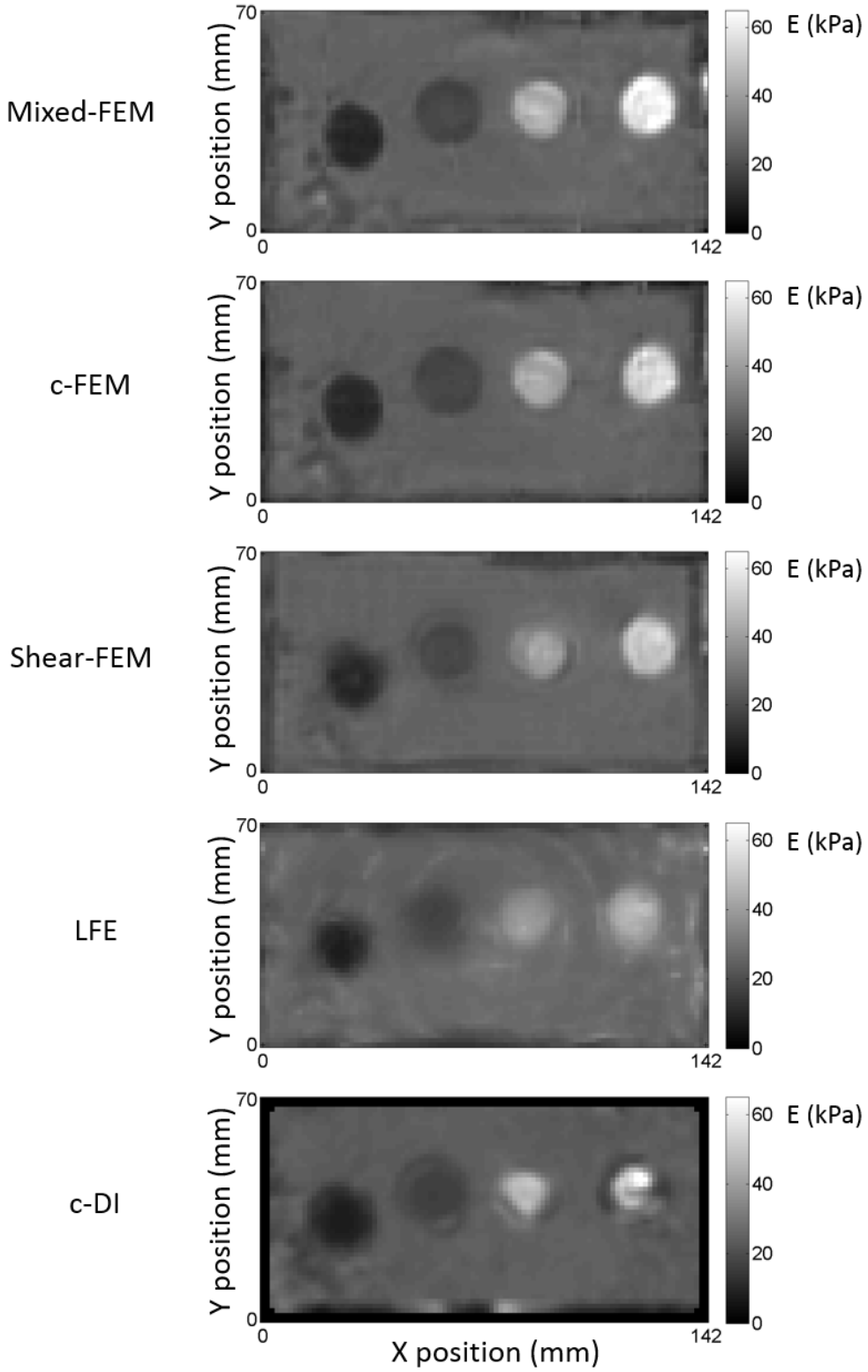

Figure 7-10. A cross-section of reconstructed Young's modulus of CIRS phantom using different methods.

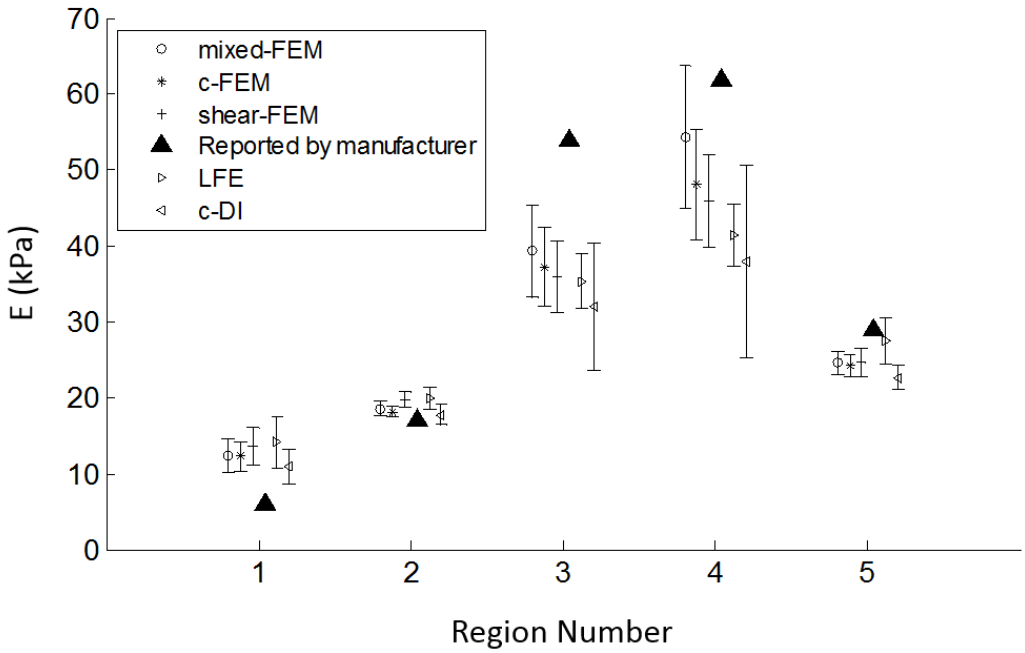

Figure 7-11. The mean and standard deviation of the Young's modulus of each region in CIRS phantom using different methods.

For better comparison of the inclusion profile, the average and variations of the Young's modulus of the elements located at a distance R from the estimated centers are plotted in Figure 7-12. From these plots it can be seen that mixed-FEM and c-FEM have the sharpest edges with the least variations. LFE has the smoothest edges with relatively large variations. c-DI has also large variations on the edges due to the artifacts resulting from the homogeneity assumption.

Table 7-4 shows the required processing time for this phantom using different methods. For FEM methods the processing time is dependent on the sub-domain window size and the overlapping factor of the sub-domains. The relation between the processing time and the sub-domain window size is exponential as shown in Chapter 4 but keeping the sub-domain window size constant the processing time changes linearly with the volume of the region. The processing time for LFE and c-DI also is linearly proportional to the volume of the region.

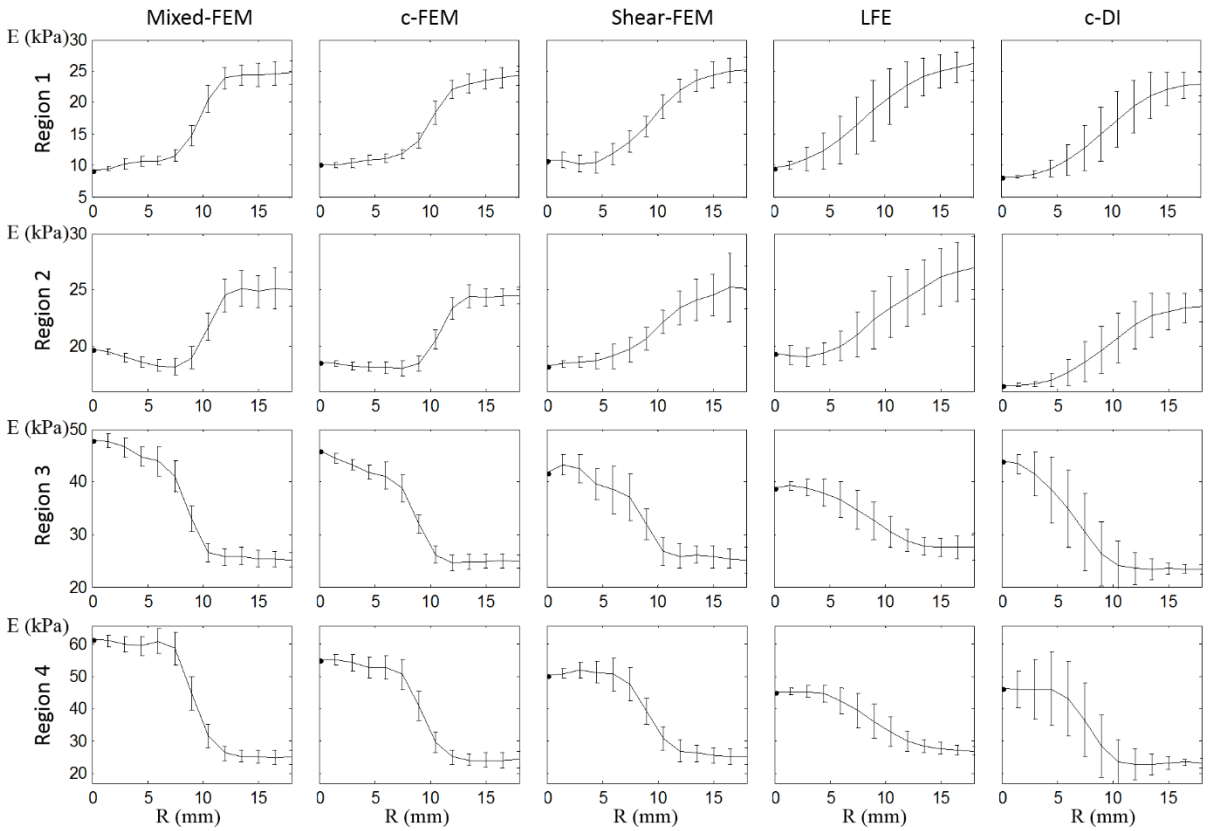

Figure 7-12. Profiles of the average Young's modulus versus distance from the center of the inclusions for different methods.

Table 7-4. The required time for processing the CIRS phantom data using different methods.

Method	Time (s)
Mixed-FEM	1990
c-FEM	960
Shear-FEM	848
LFE	17
c-DI	130

7.3.3 Agar-gelatin phantom results

Figure 7-13 shows different cross sections of the reconstructed Young's modulus using different methods and the corresponding T2-weighted images for the Agar phantom. In this phantom the inclusions are clearly visible in the T2-weighted image therefore the T2-weighted image can be used as a gold standard for the actual pattern of the elasticity. By comparing the Young's modulus maps with the T2-weighted images we can see that the mixed-FEM and c-FEM results nicely match the patterns of the inclusions seen in T2-

weighted images. Shear-FEM results also have a good contrast and resolution but slightly downgraded which is reasonable due to the simplifying assumption used in this method. Since the homogeneity assumption is not used in this method, its results are clearer than c-DI results in which the homogeneity assumption is used. LFE results have a lower contrast and resolution and the inclusions are less visible. c-DI results have a good contrast but the abundance of artifacts on the boundaries of the inclusions makes most of the smaller inclusions undetectable.

Since the actual absolute values of the Young's modulus are not known for this phantom, the RMS error cannot be calculated for this case. But the CNR value can still be used as a quantitative measure for comparison. Therefore the regions are segmented manually based on the T2-weighted images and the CNR value is calculated for each method. Figure 7-14 shows the CNR results. The CNR values also suggest the same trend as expected from the images.

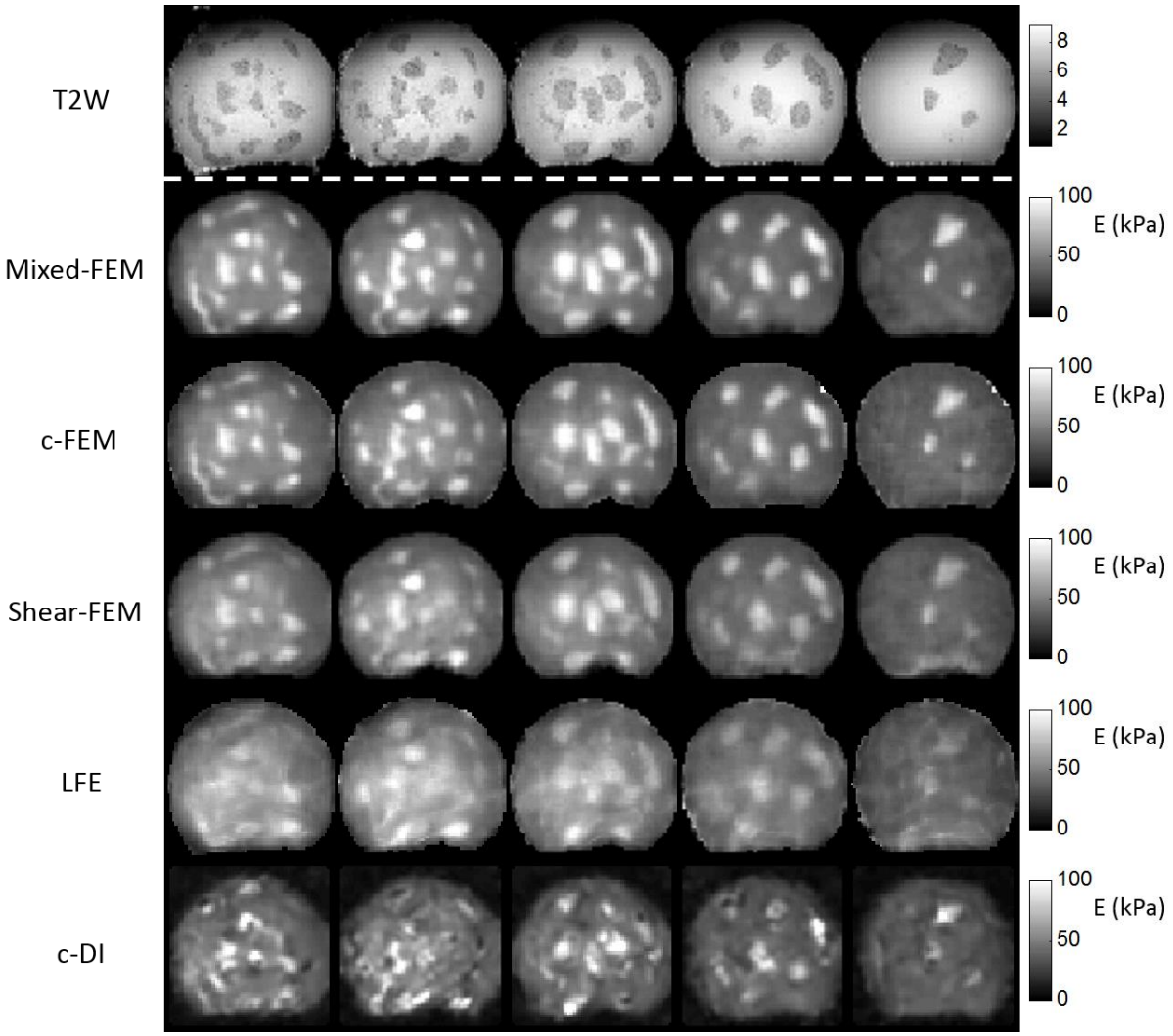

Figure 7-13. Different cross-sections of the reconstructed Young's modulus of the agar-phantom using different methods. The top row is the corresponding T2-weighted image.

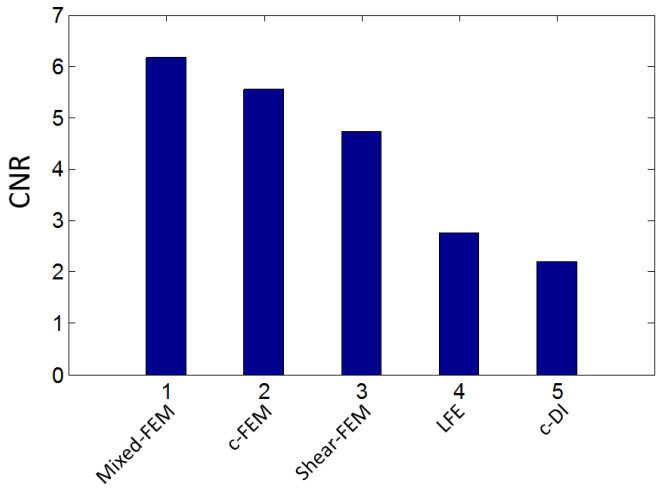

Figure 7-14. CNR values of the agar-phantom results using different methods.

7.3.4 Ex-vivo kidney results

Figure 7-15 shows the reconstructed Young's modulus, T2-weighted images and the indentation results for two different cross sections of the ex-vivo kidney sample. Each row is a different cross section and the columns are the results of different techniques. As mentioned before, for real tissue, the T2-weighted image does not necessarily correspond to the elasticity pattern therefore here the indentation result is used to validate the elasticity results. From these images it can be seen that the FEM results are very similar to each other and also the closest results to the indentation result. These results also make sense since the outer layer of the kidney sample that has been in direct contact with formalin is stiffer than the inside and also there is a stiff area inside the sample, visible in the top row cross section, which is the result of formalin injection inside the sample. In LFE and c-DI results, similar effects as observed in agar phantom results can also be seen here. LFE result is very smooth and unclear and the homogeneity assumption artifacts in c-DI have almost covered the entire stiff outer layer.

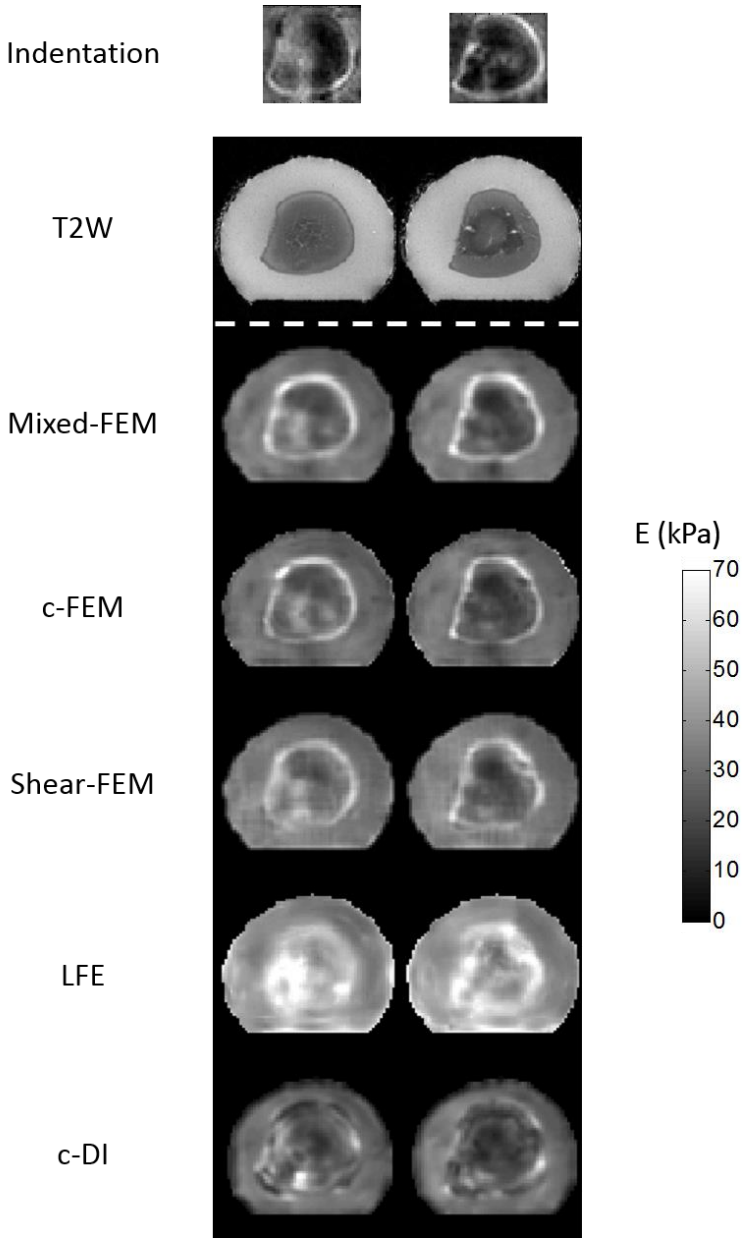

Figure 7-15. Two cross-sections of the reconstructed Young's modulus of the ex-vivo kidney sample using different methods. The two columns on the right side are the corresponding indentation result and T2-weighted images respectively from right to left.

7.3.5 Prostate data

The in-vivo prostate results are shown in Figure 7-16. Here, the columns show different cross sections of the transverse view and each row is the result of a different method. Unfortunately, for the in-vivo case a true validation of the elasticity results is not possible. But it can be seen that all the FEM methods are producing very similar patterns and this consistency can be seen as partial validation of the results. The LFE results in

vivo are worse than the results in phantoms and ex-vivo. Possibly the very low frequency excitation relative to the examined features is the reason of the degradation of LFE result here. The purpose of presenting the in-vivo result here was to show sample results and to compare the behaviour of different methods in an actual in-vivo imaging case. The correlation between cancer and elasticity was not investigated in this study.

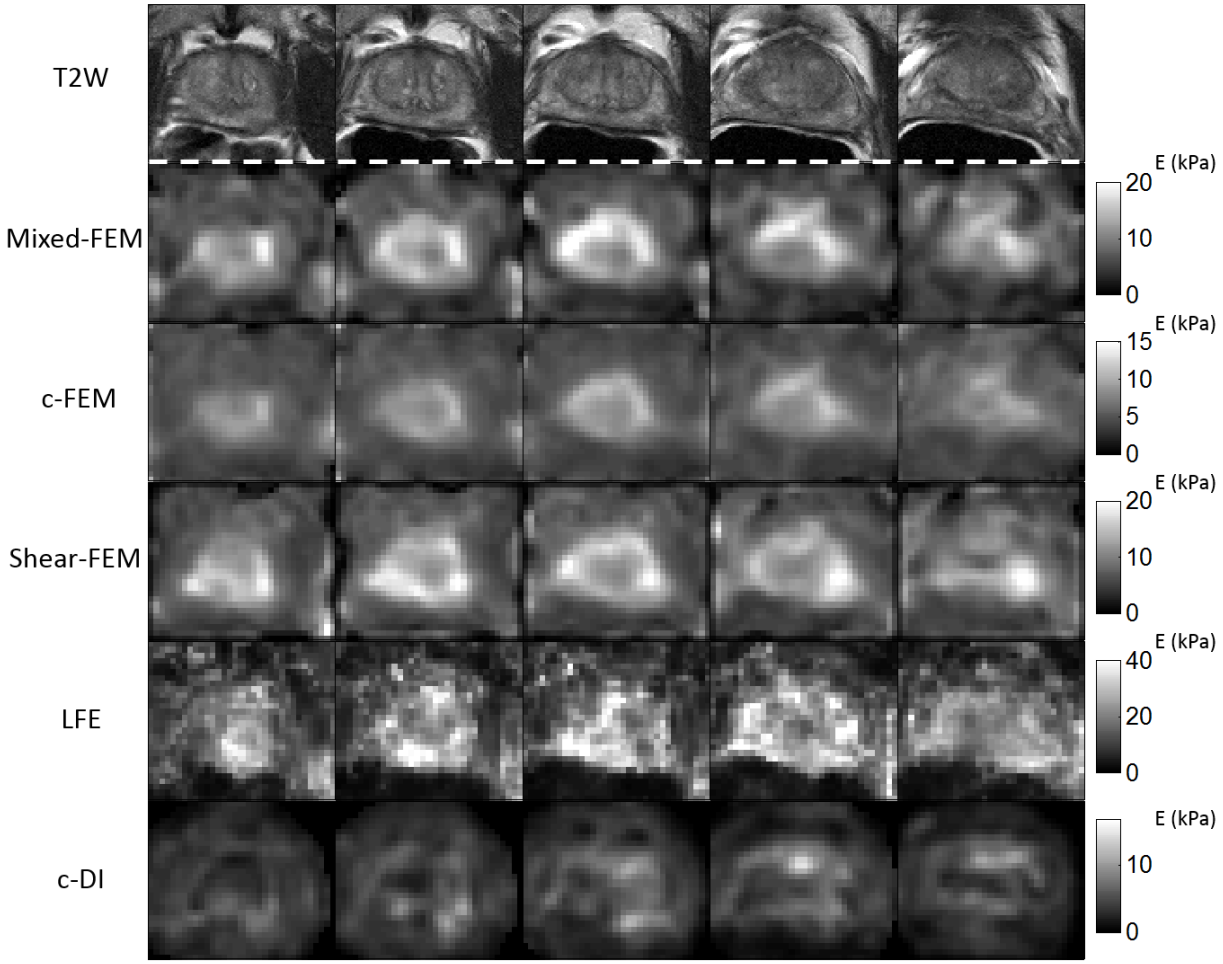

Figure 7-16. Different cross-sections of the transverse view of the reconstructed Young's modulus for the in-vivo prostate data using different methods. The top row is the corresponding T2-weighted image

7.4 Conclusion

In this chapter all of the FEM based inversion techniques proposed in this thesis were compared with two other state-of-the-art methods, LFE and c-DI. All these methods were tested on simulation data, phantoms, ex-vivo and in-vivo data and the results were compared.

It was observed that mixed-FEM and c-FEM methods had the most accurate results since in these methods the complete form of the wave equation is used without any simplification. Simulation results showed that c-FEM is more sensitive to noise compared to mixed-FEM due to the higher order of derivatives required in that method; however, it still works well with the existing noise level in the presented experiment data sets, placing it in a close tie with mixed-FEM results. The advantages of c-FEM method over mixed-FEM are its lower computational cost, since it has fewer unknowns, and the fact that it can be used with multi data sets such as multi-frequency data for further improvement of the results.

Due to the choice of ignoring the pressure term in the shear-FEM method some artifacts were observed in its results, but these artifacts are not as severe as the effects of the homogeneity assumption present in the c-DI results, placing this method in third position after mixed-FEM and c-FEM in terms of its imaging quality. However, since the homogeneity assumption is the only assumption used in c-DI, it should outperform the shear-FEM in cases where the region is actually homogeneous or where the inclusion is very large making the boundary area negligible compared to the inclusion area. It should be mentioned that shear-FEM has been designed for cases where only one component of the displacement is available while c-DI needs all three components of the displacement. Similar to shear-FEM, LFE also has the ability to work with partial data sets and its speed has made this method one of the most common used methods in the field. However for this method to work properly it is important to have a small ratio of shear wavelength to the data voxel size to achieve a reasonable spatial resolution. This can be a limiting factor since in real tissue, higher frequency waves cannot penetrate very deep due to attenuation.

Chapter 8 - Conclusion

8.1 Summary

The imaging of the viscoelastic properties of tissues or elastography has received much attention in the medical field. The inverse problem of elastography using FEM was studied in this research for both MRE and US elastography systems. The goal was to develop novel techniques to accurately measure the absolute value of the shear modulus of soft tissue under the condition of applying continuous harmonic excitation.

In Chapter 2 sparsity regularization was introduced and used in the direct mixed-FEM inversion technique. Simulations were used to compare this method with Tikhonov regularization technique. The results showed that the sparsity regularization is more robust compared to Tikhonov regularization and no parameter readjustment is needed when the frequency or boundary conditions change. It was also shown that using sparsity regularization reduces the computational cost significantly. This method was also tested on MRE data captured from a CIRS elastography phantom. This regularization method is used in all the inversion methods developed in this thesis.

In Chapter 3 the use of quasi-static strain image as a prior knowledge of the elasticity distribution was investigated for the purpose of regularization. Three different ways of constraining the unknown parameters using strain images were introduced and tested on simulation data. The results showed the higher efficiency and stability of the solution using quasi-static strain images in regularization. However the drawback of this method is that it requires additional data collection which may not be feasible in some applications.

In Chapter 4 two forms of direct and iterative FEM inversion techniques used in dynamic elastography were compared. It was shown that the formulations used in these methods are quite similar but solved in a different way. The results showed that the direct method with exact fit generates similar results to the iterative method, while using least-squares fit in the direct method makes this method more stable and accurate compared to the iterative method in the presence of noise. Also the spatial resolution study results showed the higher stability of the CNR value for the direct method with least-squares fit compared to the method with exact fit. It was also shown that the computational cost for the direct method is much lower than that of the iterative method. Therefore, for the linear-in-parameter cases as studied in this Chapter it is recommended that the direct method be used over the iterative method.

In Chapter 5 a new curl-based direct FEM inversion technique without using the homogeneity assumption (c-FEM) was introduced. It was shown that the c-FEM method can be solved faster than the direct mixed-FEM since it has fewer number of unknowns and that it also enables us to use multi-frequency data to improve the resulting shear modulus reconstruction.

In Chapter 6 a new FEM-based inversion technique for US elastography system was introduced (shear-FEM). The methods introduced in previous chapters can be used only with MRE data in which all the three components of the displacement are available. But in US systems usually partial displacement data is available. The method developed in this chapter uses a simplified form of the wave equation without the local homogeneity assumption. The method was tested on simulation and experimental data. It was shown that the artifacts are significantly reduced when the local homogeneity assumption is not used.

In Chapter 7 a comparison of all of the FEM-based inversion techniques proposed in this thesis with two of other state of the art methods, LFE and c-DI was presented. All these methods were tested on simulation data, phantoms, ex-vivo and in-vivo data and the results were compared. It was observed that mixed-FEM and c-FEM methods had the most accurate results since in these methods the complete form of the wave equation is used without any simplification but the downside of these methods is their higher computational cost.

8.2 Contributions

The contributions of this thesis are summarized as follows:

- A novel sparsity regularization technique is developed to be used with direct FEM-based inversion techniques for solving the elasticity inverse problem. The discrete cosine transform (DCT) is used as a sparsifying transform by which the original variables are transformed into a new sparse set of variables. It is assumed in the new domain, the dominant parameters are mostly located in the lower frequency portion of the domain and therefore only those parameters are selected and the original parameters are approximated using those parameters. This approximation decreases the number of the unknowns of the original linear system of equations and results in a new system of equations with higher stability and better conditioning. It also decreases the computational cost and therefore the required processing time.
- Three novel techniques are developed which use quasi-static strain images as a prior knowledge of the elasticity distribution in regularization. In the first technique the region is segmented based on the quasi-static strain image and the elasticity parameters of each segment are lumped together. In the second method, instead of lumping the parameters, the sparsity regularization is applied on each segment separately. For this purpose the sparsity regularization filter is extended to irregular shaped regions using shape adaptive DCT (SA-DCT) algorithm. In the third technique, the sparsity pattern is selected more

efficiently using the quasi-static strain image. The DCT transform of the strain image is calculated and the parameters with higher magnitudes are selected to be inside the sparsity pattern.

- As a by-product of the strain-based regional sparsity regularization, the sparsity regularization filter for irregular shaped regions is developed based on SA-DCT which can be used in cases where the rectangular ROI cannot be used for example in imaging of living organs such as prostate.
- For the first time, the direct and iterative FEM-based inversion techniques are compared in detail resulting in a better understanding of the theory behind these methods. A change is suggested in the formulation of the iterative method, which enables this method to be used with coarser mesh compared to the original formulation. Also it is shown that for linear-in-parameter cases there is no point in using the iterative method since the direct method can produce the same results in a much faster way.
- A novel curl-based direct FEM inversion technique is developed which does not use any simplifying assumptions. The curl operator is used to eliminate the pressure term but unlike the previous curl-based methods, the homogeneity assumption is not used here. The curl-based FEM method has a fewer number of unknowns compared to the mixed-FEM method and is suitable to be used with multi-frequency data. One of the key points observed in this thesis was the importance of the effect of local homogeneity on the reconstruction results, especially in real tissue case where the elasticity variation is high. In the methods developed in this thesis, we tried to avoid this assumption.
- A novel simplified FEM-based direct inversion technique is developed that is suitable for the unidirectional displacement measurements available in typical ultrasound systems. In this method only the coupling terms in the equation of motion are ignored without making the assumption of local homogeneity. This method is called shear-FEM since it uses the shear wave equation without the homogeneity assumption.
- The shear-FEM method is also extended to cylindrical coordinate system since normally the volumetric US displacement data is captured on a cylindrical mesh.
- A thorough comparison of state-of-the-art inversion techniques used in MRE is carried out. The proposed methods in this thesis including mixed-FEM, c-FEM and shear-FEM are compared with LFE and c-DI using simulations, phantom and ex-vivo and in-vivo data.
- Agar-phantoms with many irregular shaped inclusions are fabricated to challenge the proposed inversion techniques. The inclusions in this phantom are made visible in T2-weighted images by adding acrylic color to the inclusions in order to have a gold standard for elasticity pattern for comparing the reconstructed results with.
- An indentation scanner is designed and developed for validating the ex-vivo results.

8.3 Limitations

As mentioned in the introduction chapter, in this thesis we assume the tissue has linear, isotropic, elastic properties and assume the density of the tissue is equal to the density of the water. The linearity assumption is reasonable since we are considering small deformations. However real tissue has nonlinear properties and its elasticity varies for different levels of strains. This may cause discrepancies in our measurements since it is not easy to control the amount of pre-compression in many cases. Also some tissue types, such as muscles, are not really isotropic and the methods developed in this thesis are less appropriate for such cases. The other important limitation of the methods developed in this thesis in real tissue applications is the elastic model used here. This model does not consider the effect of the fluids present in tissue and freely moving within the tissue and interacting with the solid structure of the tissue. This effect can be modeled using a poroelastic model. However this effect differs in different tissue types depending on the porosity and permeability properties of the tissue and also it can vary with excitation frequency. At higher excitation frequencies the fluid may not have a chance to travel through the pores and the model will converge to the elastic model.

The most challenging part of elastography imaging *in-vivo* is accurate and complete motion measurement. Two of the methods presented in this thesis need all three components of the displacement which is only available in MRE data. However the long acquisition time for this technique (more than about 20 mins) introduces artifacts in the results due to subject motion during this long period. US techniques are faster and therefore contain fewer artifacts due to undesired motions but, as mentioned before, they can only measure the axial component accurately. Beam steering methods can be used to measure the other components but these measurements are an order of magnitude less accurate than the axial component and their accuracy depends on the steering angle used. The larger the angle the more accurate the lateral displacement will be, but at the expense of region of overlap between steered images. Furthermore, the accuracy of the lateral displacement is highly dependent on the accuracy of the angle of the beam at low angles, which, in turn, is dependent on the accuracy of the speed of sound estimate in tissue. Therefore the addition of lateral and elevational displacements may not be very helpful because of their poor accuracy.

8.4 Future work

Novel methods have been developed in this thesis for solving the inverse problem of elasticity which can be used in both MRE and US systems. A number of interesting areas of future work can be suggested as follows:

- In the proposed sparsity regularization technique, DCT was used as the sparsifying transform. Other sparsifying transforms such as wavelets can also be used. Also the sparsity patterns used in this thesis

were either manually selected at the lower frequency portion of the DCT domain or were selected based on the DCT transform of the quasi-static strain images. One may also try to find the optimum sparsity pattern using iterative methods by penalizing the weighted magnitude of the DCT coefficients with an l_p-norm.

- The proposed methods in this thesis are based on the finite element method. One may also try to formulate these methods using spectral methods or spectral element methods.
- In this thesis, shear-FEM was extended to cylindrical coordinate systems to be used with US displacement data captured on a cylindrical mesh. In some cases the ultrasound probes have curvature in both directions. Therefore this method should be extended to spherical or some specific coordinate system suitable for such kind of data sets.
- The implementation of the proposed methods in real-time is critical for some clinical applications. This can be achieved by implementing these methods on a graphical processing unit.
- For in-vivo cases, capturing uniformly good quality data is very challenging. In real tissue, there are some areas such as blood vessels or cysts in which displacements cannot penetrate and the measured displacement in those areas is corrupted. It can be useful to develop an algorithm that can automatically find areas with corrupted displacement and remove the equations corresponding to those areas from the system of equations.
- Multi-frequency techniques have been suggested to achieve a more uniform wave illumination and avoid the nodal areas of the standing waves. Since the mechanical properties, namely elasticity and viscosity of tissue, have been shown to be dependent on the frequency of the excitation, the different frequencies need to be relatively close together. However in order to be able to use larger range of frequencies together, one can find a suitable model to relate the elasticity and viscosity to the frequency and solve for the parameters of that model along with the elasticity and viscosity.
- Finding the anisotropic properties of the tissue is another challenging area of research in elastography. Most of the methods developed so far assume isotropy for its simplicity. But this assumption does not hold for some types of tissue such as muscles. The anisotropy assumption introduces more unknowns to the problem, which requires more number of equations. One possible option to increase the number of equations is to use multi-frequency data.
- Poroelasticity is another area which can be investigated. Considering the fact that some tissue types such as the brain contain a great amount of fluid that can freely move within the tissue, the elastic model used in this thesis and most of the elastography techniques may result in artifacts. A similar direct FEM method as presented in this thesis can be developed to model more accurately the interaction between the porous elastic solid and interstitial fluid phase present in such tissues.

- We developed a phantom with many irregular shaped inclusions to create a more sophisticated medium for challenging the proposed inversion techniques. One of the effects we wanted to emphasise more was the effect of homogeneity assumption. Most of the phantoms used for testing the elastography methods contain step inclusions. Since the effect of homogeneity assumption appears only on areas of varying elasticity, for step inclusions, this area is only on the boundary of the inclusion which is usually not noticeable especially when the inclusion is large. While in real cases, in some organs with more complicated structures the elasticity variation exists in larger area of the region. In order to mimic those situations we developed a phantom with many irregular and different sizes inclusions but still the inclusions have a step change in elasticity. A better phantom that is of interest is a phantom with smooth changing inclusions to increase the areas of varying elasticity and better mimicking the actual elasticity distributions in real tissue.

Bibliography

[1] J. Boursier, J. Vergniol, A. Sawadogo, T. Dakka, S. Michalak, Y. Gallois, V. Le Tallec, F. Oberti, I. Fouchard-Hubert and N. Dib, "The combination of a blood test and Fibroscan improves the non-invasive diagnosis of liver fibrosis," *Liver International,* vol. 29, pp. 1507-1515, 2009.

[2] J. Wang, C. Changchien, C. Hung, H. Eng, W. Tung, K. Kee, C. Chen, T. Hu, C. Lee and S. Lu, "FibroScan and ultrasonography in the prediction of hepatic fibrosis in patients with chronic viral hepatitis," *J. Gastroenterol.,* vol. 44, pp. 439-446, 2009.

[3] R. Sinkus, K. Siegmann, T. Xydeas, M. Tanter, C. Claussen and M. Fink, "MR elastography of breast lesions: Understanding the solid/liquid duality can improve the specificity of contrast-enhanced MR mammography," *Magnetic Resonance in Medicine,* vol. 58, pp. 1135-1144, 2007.

[4] M. Tanter, J. Bercoff, A. Athanasiou, T. Deffieux, J. Gennisson, G. Montaldo, M. Muller, A. Tardivon and M. Fink, "Quantitative assessment of breast lesion viscoelasticity: initial clinical results using supersonic shear imaging," *Ultrasound Med. Biol.,* vol. 34, pp. 1373-1386, 2008.

[5] B. S. Garra, E. I. Cespedes, J. Ophir, S. R. Spratt, R. A. Zuurbier, C. M. Magnant and M. F. Pennanen, "Elastography of breast lesions: initial clinical results," *Radiology,* vol. 202, pp. 79-86, Jan, 1997.

[6] A. Thomas, M. Warm, M. Hoopmann, F. Diekmann and T. Fischer, "Tissue Doppler and strain imaging for evaluating tissue elasticity of breast lesions," *Acad. Radiol.,* vol. 14, pp. 522-529, 2007.

[7] D. T. Ginat, S. V. Destounis, R. G. Barr, B. Castaneda, J. G. Strang and D. J. Rubens, "US elastography of breast and prostate lesions," *Radiographics,* vol. 29, pp. 2007-2016, Nov, 2009.

[8] B. Castaneda, K. Hoyt, K. Westesson, L. An, J. Yao, L. Baxter, J. Joseph, J. Strang, D. Rubens and K. Parker, "Performance of three-dimensional sonoelastography in prostate cancer detection: A comparison between ex vivo and in vivo experiments," in *Ultrasonics Symposium (IUS), 2009 IEEE International,* 2009, pp. 519-522.

[9] L. Pallwein, M. Mitterberger, G. Pinggera, F. Aigner, F. Pedross, J. Gradl, A. Pelzer, G. Bartsch and F. Frauscher, "Sonoelastography of the prostate: comparison with systematic biopsy findings in 492 patients," *Eur. J. Radiol.,* vol. 65, pp. 304-310, 2008.

[10] M. Dighe, J. Kim, S. Luo and Y. Kim, "Utility of the ultrasound elastographic systolic thyroid stiffness index in reducing fine-needle aspirations," *J. Ultrasound Med.,* vol. 29, pp. 565-574, Apr, 2010.

[11] S. A. Kruse, G. H. Rose, K. J. Glaser, A. Manduca, J. P. Felmlee, C. R. Jack Jr. and R. L. Ehman, "Magnetic resonance elastography of the brain," *Neuroimage,* vol. 39, pp. 231-237, 2008.

[12] M. A. Green, L. E. Bilston and R. Sinkus, "In vivo brain viscoelastic properties measured by magnetic resonance elastography," *NMR Biomed.,* vol. 21, pp. 755-764, 2008.

[13] L. Xu, Y. Lin, Z. Xi, H. Shen and P. Gao, "Magnetic resonance elastography of the human brain: a preliminary study," *Acta Radiol.,* vol. 48, pp. 112-115, 2007.

[14] T. Elgeti, M. Beling, B. Hamm, J. Braun and I. Sack, "Cardiac magnetic resonance elastography: toward the diagnosis of abnormal myocardial relaxation," *Invest. Radiol.,* vol. 45, pp. 782-787, Dec, 2010.

[15] H. Kanai, "Propagation of spontaneously actuated pulsive vibration in human heart wall and in vivo viscoelasticity estimation," *Ultrasonics, Ferroelectrics and Frequency Control, IEEE Transactions On,* vol. 52, pp. 1931-1942, 2005.

[16] W. Lee, J. Provost, K. Fujikura, J. Wang and E. E. Konofagou, "In vivo study of myocardial elastography under graded ischemia conditions," *Phys. Med. Biol.,* vol. 56, pp. 1155, 2011.

[17] I. Sack, J. Bernarding and J. Braun, "Analysis of wave patterns in MR elastography of skeletal muscle using coupled harmonic oscillator simulations," *Magn. Reson. Imaging,* vol. 20, pp. 95-104, 2002.

[18] J. R. Basford, T. R. Jenkyn, K. An, R. L. Ehman, G. Heers and K. R. Kaufman, "Evaluation of healthy and diseased muscle with magnetic resonance elastography," *Arch. Phys. Med. Rehabil.,* vol. 83, pp. 1530-1536, 2002.

[19] A. A. Oberai, N. H. Gokhale, S. Goenezen, P. E. Barbone, T. J. Hall, A. M. Sommer and J. Jiang, "Linear and nonlinear elasticity imaging of soft tissue in vivo : demonstration of feasibility," *Phys. Med. Biol.,* vol. 54, pp. 1191, 2009.

[20] R. Sinkus, J. Bercoff, M. Tanter, J. L. Gennisson, C. El Khoury, V. Servois, A. Tardivon and M. Fink, "Nonlinear viscoelastic properties of tissue assessed by ultrasound," *IEEE Trans Ultrason Ferroelect Freq Contr,* vol. 53, pp. 2009-2018, Nov., 2006.

[21] A. R. Skovoroda, L. A. Lubinski, S. Y. Emelianov and M. O'Donnell, "Reconstructive elasticity imaging for large deformations," *Ultrasonics, Ferroelectrics and Frequency Control, IEEE Transactions On,* vol. 46, pp. 523-535, 1999.

[22] R. Q. Erkamp, A. R. Skovoroda, S. Y. Emelianov and M. O'Donnell, "Measuring the nonlinear elastic properties of tissue-like phantoms," *Ultrasonics, Ferroelectrics and Frequency Control, IEEE Transactions On,* vol. 51, pp. 410-419, 2004.

[23] Y. C. Fung, *Biomechanics: Mechanical Properties of Living Tissues.* New York: Springer, 1993.

[24] W. S. Slaughter, *The Linearized Theory of Elasticity.* Springer, 2002.

[25] L. E. Kinsler, A. R. Frey, A. B. Coppens and J. V. Sanders, "Fundamentals of acoustics," *Fundamentals of Acoustics, 4th Edition, by Lawrence E.Kinsler, Austin R.Frey, Alan B.Coppens, James V.Sanders, Pp.560.ISBN 0-471-84789-5.Wiley-VCH, December 1999.*, vol. 1, 1999.

[26] M. A. Meyers and K. K. Chawla, *Mechanical Behavior of Materials.* Cambridge University Press Cambridge, 2009.

[27] S. Catheline, J. -. Gennisson, G. Delon, M. Fink, R. Sinkus, S. Abouelkaram and J. Culioli, "Measurement of viscoelastic properties of homogeneous soft solid using transient elastography: An inverse problem approach," *J. Acoust. Soc. Am.*, vol. 116, pp. 3734-3741, 12/00, 2004.

[28] H. Kanai, Y. Koiwa and J. Zhang, "Real-time measurements of local myocardium motion and arterial wall thickening," *Ultrasonics, Ferroelectrics and Frequency Control, IEEE Transactions On*, vol. 46, pp. 1229-1241, 1999.

[29] C. L. de Korte, van der Steen, Anton FW, E. I. Céspedes, G. Pasterkamp, S. G. Carlier, F. Mastik, A. H. Schoneveld, P. W. Serruys and N. Bom, "Characterization of plaque components and vulnerability with intravascular ultrasound elastography," *Phys. Med. Biol.*, vol. 45, pp. 1465, 2000.

[30] S. Wang, W. Lee, J. Provost, J. Luo and E. E. Konofagou, "A composite high-frame-rate system for clinical cardiovascular imaging," *Ultrasonics, Ferroelectrics and Frequency Control, IEEE Transactions On*, vol. 55, pp. 2221-2233, 2008.

[31] M. Fatemi, A. Manduca and J. F. Greenleaf, "Imaging elastic properties of biological tissues by low-frequency harmonic vibration," *Proc IEEE*, vol. 91, pp. 1503-1519, 2003.

[32] J. Bercoff, M. Tanter and M. Fink, "Supersonic shear imaging: a new technique for soft tissue elasticity mapping," *Ultrasonics, Ferroelectrics and Frequency Control, IEEE Transactions On*, vol. 51, pp. 396-409, 2004.

[33] A. P. Sarvazyan, O. V. Rudenko, S. D. Swanson, J. B. Fowlkes and S. Y. Emelianov, "Shear wave elasticity imaging: a new ultrasonic technology of medical diagnostics," *Ultrasound Med. Biol.*, vol. 24, pp. 1419-1435, 1998.

[34] K. Nightingale, R. Bentley and G. Trahey, "Observations of tissue response to acoustic radiation force: opportunities for imaging," *Ultrason. Imaging*, vol. 24, pp. 129-138, Jul, 2002.

[35] O. Rudenko, A. Sarvazyan and S. Y. Emelianov, "Acoustic radiation force and streaming induced by focused nonlinear ultrasound in a dissipative medium," *J. Acoust. Soc. Am.*, vol. 99, pp. 2791-2798, 1996.

[36] M. Honarvar, R. Sahebjavaher, S. Salcudean and R. Rohling, "Sparsity regularization in dynamic elastography," *Phys. Med. Biol.,* vol. 57, pp. 5909, 2012.

[37] M. Honarvar, R. Sahebjavaher, R. Sinkus, R. Rohling and S. Salcudean, "Curl-based Finite Element Reconstruction of the Shear Modulus Without Assuming Local Homogeneity: Time Harmonic Case," *IEEE Trans Med Imaging,* vol. 32, pp. 2189-2199, 2013.

[38] S. Papazoglou, U. Hamhaber, J. Braun and I. Sack, "Algebraic Helmholtz inversion in planar magnetic resonance elastography," *Phys. Med. Biol.,* vol. 53, pp. 3147, 2008.

[39] H. Eskandari, S. Salcudean, R. Rohling and J. Ohayon, "Viscoelastic characterization of soft tissue from dynamic finite element models," *Phys. Med. Biol.,* vol. 53, pp. 6569, 2008.

[40] M. Halliwell, P. N. T. Wells, Y. Yamashita, H. Kancko and M. Kubota, "Elasticity imaging of incompressible biological soft tissue from incomplete ultrasonic displacement data," in Anonymous Springer US, 2002, pp. 461-468.

[41] Z. Yanning, T. J. Hall and J. Jingfeng, "A finite-element approach for Young's modulus reconstruction," *IEEE Trans Med Imaging,* vol. 22, pp. 890-901, 2003.

[42] F. Kallel and M. Bertrand, "Tissue elasticity reconstruction using linear perturbation method," *IEEE Trans. Med. Imag.,* vol. 15, pp. 299-313, 1996.

[43] M. Doyley, P. Meaney and J. Bamber, "Evaluation of an iterative reconstruction method for quantitative elastography," *Phys. Med. Biol.,* vol. 45, pp. 1521, 2000.

[44] M. O'Donnell, A. R. Skovoroda, B. M. Shapo and S. Y. Emelianov, "Internal displacement and strain imaging using ultrasonic speckle tracking," *Ultrasonics, Ferroelectrics and Frequency Control, IEEE Transactions On,* vol. 41, pp. 314-325, 1994.

[45] J. Ophir, I. Cespedes, H. Ponnekanti, Y. Yazdi and X. Li, "Elastography: A quantitative method for imaging the elasticity of biological tissues," *Ultrason. Imag.,* vol. 13, pp. 111-134, 1991.

[46] T. E. Oliphant, J. L. Mahowald, R. L. Ehman and J. F. Greenleaf, "Complex-valued quantitative stiffness estimation using dynamic displacement measurements and local inversion of conservation of momentum," in *Ultrasonics Symposium, 1999. Proceedings. 1999 IEEE,* 1999, pp. 1641-1644 vol.2.

[47] R. Sinkus, J. Lorenzen, D. Schrader, M. Lorenzen, M. Dargatz and D. Holz, "High-resolution tensor MR elastography for breast tumour detection," *Phys. Med. Biol.,* vol. 45, pp. 1649, 2000.

[48] M. M. Doyley, E. E. Van Houten, J. B. Weaver, S. Poplack, L. Duncan, F. Kennedy and K. D. Paulsen, "Shear modulus estimation using parallelized partial volumetric reconstruction," *Medical Imaging, IEEE Transactions On,* vol. 23, pp. 1404-1416, 2004.

[49] E. Park and A. M. Maniatty, "Shear modulus reconstruction in dynamic elastography: time harmonic case," *Phys. Med. Biol.*, vol. 51, pp. 3697, 2006.

[50] R. M. Lerner, S. R. Huang and K. J. Parker, "“Sonoelasticity” images derived from ultrasound signals in mechanically vibrated tissues," *Ultrasound Med. Biol.*, vol. 16, pp. 231-239, 1990.

[51] L. Ji, J. R. McLaughlin, D. Renzi and J. Yoon, "Interior elastodynamics inverse problems: shear wave speed reconstruction in transient elastography," *Inverse Problems*, vol. 19, pp. S1, 2003.

[52] J. Bercoff, S. Chaffai, M. Tanter, L. Sandrin, S. Catheline, M. Fink, J. L. Gennisson and M. Meunier, "In vivo breast tumor detection using transient elastography," *Ultrasound Med. Biol.*, vol. 29, pp. 1387-1396, 2003.

[53] L. Sandrin, M. Tanter, S. Catheline and M. Fink, "Shear modulus imaging with 2-D transient elastography," *Ultrasonics, Ferroelectrics and Frequency Control, IEEE Transactions On*, vol. 49, pp. 426-435, 2002.

[54] S. Catheline, N. Benech, J. Brum and C. Negreira, "Time reversal of elastic waves in soft solids," *Phys. Rev. Lett.*, vol. 100, pp. 064301, 2008.

[55] K. R. Nightingale, M. L. Palmeri, R. W. Nightingale and G. E. Trahey, "On the feasibility of remote palpation using acoustic radiation force," *J. Acoust. Soc. Am.*, vol. 110, pp. 625-634, 2001.

[56] R. Z. Azar, A. Baghani, S. E. Salcudean and R. Rohling, "2-D high-frame-rate dynamic elastography using delay compensated and angularly compounded motion vectors: preliminary results," *Ultrasonics, Ferroelectrics and Frequency Control, IEEE Transactions On*, vol. 57, pp. 2421-2436, 2010.

[57] R. Zahiri-Azar and S. E. Salcudean, "Motion estimation in ultrasound images using time domain cross correlation with prior estimates," *Biomedical Engineering, IEEE Transactions On*, vol. 53, pp. 1990-2000, 2006.

[58] R. Muthupillai, D. J. Lomas, P. J. Rossman, J. F. Greenleaf, A. Manduca and R. L. Ehman, "Magnetic resonance elastography by direct visualization of propagating acoustic strain waves," *Science*, vol. 269, pp. 1854, 1995.

[59] P. Garteiser, R. S. Sahebjavaher, L. C. Ter Beek, S. Salcudean, V. Vilgrain, B. E. Van Beers and R. Sinkus, "Rapid acquisition of multifrequency, multislice and multidirectional MR elastography data with a fractionally encoded gradient echo sequence," *NMR Biomed.*, vol. 26, pp. 1326-1335, 2013.

[60] J. Schmitt, "OCT elastography: imaging microscopic deformation and strain of tissue," *Optics Express*, vol. 3, pp. 199-211, 1998.

[61] R. K. Wang, Z. Ma and S. J. Kirkpatrick, "Tissue Doppler optical coherence elastography for real time strain rate and strain mapping of soft tissue," *Appl. Phys. Lett.*, vol. 89, pp. 144103, 2006.

[62] A. S. Khalil, R. C. Chan, A. H. Chau, B. E. Bouma and M. R. K. Mofrad, "Tissue elasticity estimation with optical coherence elastography: toward mechanical characterization of in vivo soft tissue," *Ann. Biomed. Eng.*, vol. 33, pp. 1631-1639, 2005.

[63] M. Fatemi and J. F. Greenleaf, "Probing the dynamics of tissue at low frequencies with the radiation force of ultrasound," *Phys. Med. Biol.*, vol. 45, pp. 1449, 2000.

[64] M. Fatemi and J. F. Greenleaf, "Vibro-acoustography: an imaging modality based on ultrasound-stimulated acoustic emission," *Proc. Natl. Acad. Sci. U. S. A.*, vol. 96, pp. 6603-6608, Jun 8, 1999.

[65] M. Fatemi and J. F. Greenleaf, "Ultrasound-stimulated vibro-acoustic spectrography," *Science*, vol. 280, pp. 82, 1998.

[66] G. W. Kim, B. H. Han, M. H. Cho and S. Y. Lee, "X-ray elastography: A feasibility study," in *Engineering in Medicine and Biology Society, 2009. EMBC 2009. Annual International Conference of the IEEE*, 2009, pp. 3513-3516.

[67] J. C. Bamber and N. L. Bush, "Freehand elasticity imaging using speckle decorrelation rate," in *Acoustical Imaging*Anonymous Springer, 1996, pp. 285-292.

[68] E. Konofagou, P. Dutta, J. Ophir and I. Céspedes, "Reduction of stress nonuniformities by apodization of compressor displacement in elastography," *Ultrasound Med. Biol.*, vol. 22, pp. 1229-1236, 1996.

[69] e. a. Donald B Plewes, "Visualization and quantification of breast cancer biomechanical properties with magnetic resonance elastography," *Phys. Med. Biol.*, vol. 45, pp. 1591, 2000.

[70] A. Thitaikumar, T. A. Krouskop, B. S. Garra and J. Ophir, "Visualization of bonding at an inclusion boundary using axial-shear strain elastography: a feasibility study," *Phys. Med. Biol.*, vol. 52, pp. 2615, 2007.

[71] H. Ponnekanti, J. Ophir, Y. Huang and I. Céspedes, "Fundamental mechanical limitations on the visualization of elasticity contrast in elastography," *Ultrasound Med. Biol.*, vol. 21, pp. 533-543, 1995.

[72] H. Lee, Y. Yamashita and M. Kubota, "Imaging of the tissue elasticity based on ultrasonic displacement and strain measurements," in *Acoustical Imaging*Anonymous Springer US, 2002, pp. 349-359.

[73] K. R. Raghavan and A. E. Yagle, "Forward and inverse problems in elasticity imaging of soft tissues," *Nuclear Science, IEEE Transactions On*, vol. 41, pp. 1639-1648, 1994.

[74] J. Bishop, A. Samani, J. Sciarretta and D. B. Plewes, "Two-dimensional MR elastography with linear inversion reconstruction: methodology and noise analysis," *Phys. Med. Biol.*, vol. 45, pp. 2081, 2000.

[75] A. Skovoroda, S. Emelianov and M. O'Donnell, "Tissue elasticity reconstruction based on ultrasonic displacement and strain images," *Ultrasonics, Ferroelectrics and Frequency Control, IEEE Transactions On*, vol. 42, pp. 747-765, 1995.

[76] A. Samani, J. Bishop and D. B. Plewes, "A constrained modulus reconstruction technique for breast cancer assessment," *Medical Imaging, IEEE Transactions On,* vol. 20, pp. 877-885, 2001.

[77] A. A. Oberai, N. H. Gokhale and G. R. Feijóo, "Solution of inverse problems in elasticity imaging using the adjoint method," *Inverse Problems,* vol. 19, pp. 297, 2003.

[78] A. A. Oberai, N. H. Gokhale, M. M. Doyley and J. C. Bamber, "Evaluation of the adjoint equation based algorithm for elasticity imaging," *Phys. Med. Biol.,* vol. 49, pp. 2955, 2004.

[79] M. I. Miga, "A new approach to elastography using mutual information and finite elements," *Phys. Med. Biol.,* vol. 48, pp. 467, 2003.

[80] J. Jiang, T. Varghese, C. L. Brace, E. L. Madsen, T. J. Hall, S. Bharat, M. A. Hobson, J. A. Zagzebski and F. T. Lee Jr, "Young's modulus reconstruction for radio-frequency ablation electrode-induced displacement fields: a feasibility study," *Medical Imaging, IEEE Transactions On,* vol. 28, pp. 1325-1334, 2009.

[81] H. Knutsson, C. Westin and G. Granlund, "Local multiscale frequency and bandwidth estimation," in *Image Processing, 1994. Proceedings. ICIP-94., IEEE International Conference,* 1994, pp. 36-40.

[82] A. Manduca, R. Muthupillai, P. J. Rossman, J. F. Greenleaf and R. L. Ehman, "Local wavelength estimation for magnetic resonance elastography," in *Proc. of 3rd IEEE International Conference on Image Processing,* 1996, pp. 527-530 vol.3.

[83] Z. Wu, K. Hoyt, D. J. Rubens and K. J. Parker, "Sonoelastographic imaging of interference patterns for estimation of shear velocity distribution in biomaterials," *J. Acoust. Soc. Am.,* vol. 120, pp. 535-545, 2006.

[84] K. Parker, S. Huang, R. Musulin and R. Lerner, "Tissue response to mechanical vibrations for “sonoelasticity imaging”," *Ultrasound Med. Biol.,* vol. 16, pp. 241-246, 1990.

[85] K. J. Parker and R. M. Lerner, "Sonoelasticity of organs: shear waves ring a bell," *J. Ultrasound Med.,* vol. 11, pp. 387-392, Aug, 1992.

[86] L. Gao, K. J. Parker, S. Alam, D. Rubens and R. Lerner, "Theory and application of sonoelasticity imaging," *Int J Imaging Syst Technol,* vol. 8, pp. 104-109, 1997.

[87] J. McLaughlin, D. Renzi, K. Parker and Z. Wu, "Shear wave speed recovery using moving interference patterns obtained in sonoelastography experiments," *J. Acoust. Soc. Am.,* vol. 121, pp. 2438-2446, 2007.

[88] K. Hoyt, K. J. Parker and D. J. Rubens, "Real-time shear velocity imaging using sonoelastographic techniques," *Ultrasound Med. Biol.,* vol. 33, pp. 1086-1097, 2007.

[89] S. McAleavey and M. Menon, "7B-3 direct estimation of shear modulus using spatially modulated acoustic radiation force impulses," in *Ultrasonics Symposium, 2007. IEEE,* 2007, pp. 558-561.

[90] S. McAleavey, E. Collins, J. Kelly, E. Elegbe and M. Menon, "Validation of SMURF estimation of shear modulus in hydrogels," *Ultrason. Imaging,* vol. 31, pp. 131-150, 2009.

[91] T. E. Oliphant, A. Manduca, R. L. Ehman and J. F. Greenleaf, "Complex-valued stiffness reconstruction for magnetic resonance elastography by algebraic inversion of the differential equation," *Magn. Reson. Med.,* vol. 45, pp. 299-310, 2001.

[92] J. Bercoff, R. Sinkus, M. Tanter and M. Fink, "3D ultrasound-based dynamic and transient elastography : First in vitro results," in *Proc. IEEE Ultrasonics Symposium, 2004,* 2004, pp. 28-31.

[93] R. Sinkus, M. Tanter, S. Catheline, J. Lorenzen, C. Kuhl, E. Sondermann and M. Fink, "Imaging anisotropic and viscous properties of breast tissue by magnetic resonance-elastography," *Magn. Res. Med.,* vol. 53, pp. 372-387, 2005.

[94] A. J. Romano, J. J. Shirron and J. A. Bucaro, "On the noninvasive determination of material parameters from a knowledge of elastic displacements theory and numerical simulation," *IEEE Trans Ultrason Ferroelect Freq Contr,* vol. 45, pp. 751-759, 1998.

[95] P. E. Barbone, C. E. Rivas, I. Harari, U. Albocher, A. A. Oberai and Y. Zhang, "Adjoint-weighted variational formulation for the direct solution of inverse problems of general linear elasticity with full interior data," *Int. J. Numer. Meth. Engng.,* vol. 81, pp. 1713-1736, 2010.

[96] H. Eskandari, S. E. Salcudean, R. Rohling and I. Bell, "Real-time solution of the finite element inverse problem of viscoelasticity," *Inverse Problems,* vol. 27, pp. 085002, 2011.

[97] D. Fu, S. Levinson, S. Gracewski and K. Parker, "Non-invasive quantitative reconstruction of tissue elasticity using an iterative forward approach," *Phys. Med. Biol.,* vol. 45, pp. 1495, 2000.

[98] E. E. W. Van Houten, M. I. Miga, J. B. Weaver, F. E. Kennedy and K. D. Paulsen, "Three-dimensional subzone-based reconstruction algorithm for MR elastography," *Magn. Reson. Med.,* vol. 45, pp. 827-837, 2001.

[99] J. Brum, S. Catheline, N. Benech and C. Negreira, "Shear elasticity estimation from surface wave: the time reversal approach," *J. Acoust. Soc. Am.,* vol. 124, pp. 3377-3380, 2008.

[100] N. Benech, S. Catheline, J. Brum, T. Gallot and C. A. Negreira, "1-D elasticity assessment in soft solids from shear wave correlation: the time-reversal approach," *Ultrasonics, Ferroelectrics and Frequency Control, IEEE Transactions On,* vol. 56, pp. 2400-2410, 2009.

[101] J. McLaughlin and D. Renzi, "Using level set based inversion of arrival times to recover shear wave speed in transient elastography and supersonic imaging," *Inverse Problems,* vol. 22, pp. 707, 2006.

[102] J. McLaughlin and D. Renzi, "Shear wave speed recovery in transient elastography and supersonic imaging using propagating fronts," *Inverse Problems,* vol. 22, pp. 681, 2006.

[103] J. Fowlkes, S. Emelianov, J. Pipe, A. Skovoroda, P. Carson, R. Adler and A. Sarvazyan, "Magnetic-resonance imaging techniques for detection of elasticity variation," *Med. Phys.*, vol. 22, pp. 1771-1778, 1995.

[104] J. Ophir, S. Alam, B. Garra, F. Kallel, E. Konofagou, T. Krouskop and T. Varghese, "Elastography: ultrasonic estimation and imaging of the elastic properties of tissues," *Proc. Inst. Mech. Eng. Part H J. Eng. Med.*, vol. 213, pp. 203-233, 1999.

[105] J. Ophir, S. K. Alam, B. S. Garra, F. Kallel, E. E. Konofagou, T. KROUSKO, C. R. B. Merritt, R. RIGHETT, R. Souchon and S. Srinivasan, "Elastography: Imaging the elastic properties of soft tissues with ultrasound," *J. Med.*, vol. 29, pp. 156, 2002.

[106] H. Ponnekanti, J. Ophir and I. Cespedes, "Axial stress distributions between coaxial compressors in elastography: an analytical model," *Ultrasound Med. Biol.*, vol. 18, pp. 667-673, 1992.

[107] H. Ponnekanti, J. Ophir and I. Cespedes, "Ultrasonic imaging of the stress distribution in elastic media due to an external compressor," *Ultrasound Med. Biol.*, vol. 20, pp. 27-33, 1994.

[108] T. Matsumura, R. Shinomura, T. Mitake, H. Kanda, M. Yamakawa and T. Shiina, "Estimation of pressure-distribution effects upon elasticity imaging," in *Ultrasonics Symposium, 2005 IEEE*, 2005, pp. 1759-1762.

[109] J. F. Greenleaf, M. Fatemi and M. Insana, "Selected methods for imaging elastic properties of biological tissues," *Annu. Rev. Biomed. Eng.*, vol. 5, pp. 57-78, 2003.

[110] Y. Zhang, L. O. Hall, D. B. Goldgof and S. Sarkar, "A constrained genetic approach for computing material property of elastic objects," *Evolutionary Computation, IEEE Transactions On*, vol. 10, pp. 341-357, 2006.

[111] P. E. Barbone and J. C. Bamber, "Quantitative elasticity imaging: what can and cannot be inferred from strain images," *Phys. Med. Biol.*, vol. 47, pp. 2147, 2002.

[112] T. E. Oliphant, "Direct methods for dynamic elastography reconstruction: optimal inversion of the interior Helmholtz problem," 2001.

[113] I. Babuska and M. Suri, "Locking effects in the finite element approximation of elasticity problems," *Numerische Mathematik*, vol. 62, pp. 439-463, 1992.

[114] A. N. Tikhonov, V. I. A. Arsenin and F. John, *Solutions of Ill-Posed Problems.* Washington, DC: Winston, 1977.

[115] B. Jafarpour, V. K. Goyal, D. B. McLaughlin and W. T. Freeman, "Transform-domain sparsity regularization for inverse problems in geosciences," *Geophysics*, vol. 74, pp. R69, 2009.

[116] A. K. Jain, *Fundamentals of Digital Image Processing.* Prentice-Hall, Inc. Upper Saddle River, NJ, USA, 1989.

[117] O. C. Zienkiewicz and R. L. Taylor, *The Finite Element Method.* Oxford, Butterworth-Heinemann, 2000.

[118] R. S. Sahebjavaher, A. Baghani, M. Honarvar, R. Sinkus and S. E. Salcudean, "Transperineal prostate MR elastography: Initial in vivo results," *Magn. Reson. Med.*, 2012.

[119] D. Herzka, M. Kotys, R. Sinkus, R. Pettigrew and A. Gharib, "Magnetic resonance elastography in the liver at 3 Tesla using a second harmonic approach," *Magn. Reson. Med.*, vol. 62, pp. 284-291, 2009.

[120] A. Baghani, S. Salcudean, M. Honarvar, R. Sahebjavaher, R. Rohling and R. Sinkus, "Travelling Wave Expansion: A Model Fitting Approach to the Inverse Problem of Elasticity Reconstruction," *Medical Imaging, IEEE Transactions On,* vol. 30, pp. 1555-1565, 2011.

[121] M. Richards and M. Doyley, "Investigating the impact of spatial priors on the performance of model-based IVUS elastography," *Phys. Med. Biol.*, vol. 56, pp. 7223, 2011.

[122] M. McGarry, C. L. Johnson, B. P. Sutton, E. Van Houten, J. G. Georgiadis, J. B. Weaver and K. D. Paulsen, "Including spatial information in nonlinear inversion MR elastography using soft prior regularization," *Medical Imaging, IEEE Transactions On,* vol. 32, pp. 1901-1909, 2013.

[123] A. S. Khalil, B. E. Bouma and M. R. K. Mofrad, "A combined FEM/genetic algorithm for vascular soft tissue elasticity estimation," *Cardiovascular Engineering,* vol. 6, pp. 93-102, 2006.

[124] L. Floc'h, J. Ohayon, P. Tracqui, G. Finet, A. M. Gharib, R. L. Maurice, G. Cloutier and R. I. Pettigrew, "Vulnerable atherosclerotic plaque elasticity reconstruction based on a segmentation-driven optimization procedure using strain measurements: theoretical framework," *Medical Imaging, IEEE Transactions On,* vol. 28, pp. 1126-1137, 2009.

[125] R. A. Baldewsing, F. Mastik, J. A. Schaar, P. W. Serruys and van der Steen, Antonius FW, "Young's modulus reconstruction of vulnerable atherosclerotic plaque components using deformable curves," *Ultrasound Med. Biol.*, vol. 32, pp. 201-210, 2006.

[126] T. Sikora, "Low complexity shape-adaptive DCT for coding of arbitrarily shaped image segments," *Signal Process Image Commun,* vol. 7, pp. 381-395, 1995.

[127] T. Sikora and B. Makai, "Shape-adaptive DCT for generic coding of video," *Circuits and Systems for Video Technology, IEEE Transactions On,* vol. 5, pp. 59-62, 1995.

[128] E. E. W. Van Houten, K. D. Paulsen, M. I. Miga, F. E. Kennedy and J. B. Weaver, "An overlapping subzone technique for MR-based elastic property reconstruction," *Magn. Reson. Med.*, vol. 42, pp. 779-786, 1999.

[129] E. E. W. Van Houten, J. B. Weaver, M. I. Miga, F. E. Kennedy and K. D. Paulsen, "Elasticity reconstruction from experimental MR displacement data: initial experience with an overlapping subzone finite element inversion process," *Med. Phys.*, vol. 27, pp. 101-107, January 2000, 2000.

[130] E. E. Van Houten, K. D. Paulsen, M. I. Miga, F. E. Kennedy and J. B. Weaver, "Subzone-based nonlinear inversion scheme for viscoelastic tissue properties," in *Medical Imaging 2000*, 2000, pp. 556-563.

[131] M. M. Doyley, Q. Feng, J. B. Weaver and K. D. Paulsen, "Performance analysis of steady-state harmonic elastography," *Phys. Med. Biol.*, vol. 52, pp. 2657, 2007.

[132] K. D. Paulsen, E. E. Van Houten, M. M. Doyley and J. B. Weaver, "Magnetic resonance elastography in the breast: Initial reconstructions of damping coefficient," in *Biomedical Imaging, 2002. Proceedings. 2002 IEEE International Symposium On*, 2002, pp. 157-160.

[133] E. E. Van Houten, M. McGarry, P. Perriñez, I. Perreard, J. Weaver and K. Paulsen, "Subzone based magnetic resonance elastography using a Rayleigh damped material model," *Med. Phys.*, vol. 38, pp. 1993, 2011.

[134] M. D. McGarry and E. E. Van Houten, "Use of a Rayleigh damping model in elastography," *Med. Biol. Eng. Comput.*, vol. 46, pp. 759-766, 2008.

[135] T. E. Oliphant, A. Manduca, M. Dresner, R. Ehman and J. Greenleaf, "Adaptive estimation of piece-wise constant shear modulus for magnetic resonance elastography," in *Proceedings of the 9th Annual Meeting of the ISMRM, Glasgow, Scotland, UK*, 2001, pp. 1642.

[136] P. J. McCracken, A. Manduca, J. Felmlee and R. L. Ehman, "Mechanical transient-based magnetic resonance elastography," *Magn. Reson. Med.*, vol. 53, pp. 628-639, 2005.

[137] R. Sinkus, J. L. Daire, B. E. Van Beers and V. Vilgrain, "Elasticity reconstruction: Beyond the assumption of local homogeneity," *Comptes Rendus Mécanique*, vol. 338, pp. 474-479, 2010.

[138] S. Papazoglou, S. Hirsch, J. Braun and I. Sack, "Multifrequency inversion in magnetic resonance elastography," *Phys. Med. Biol.*, vol. 57, pp. 2329, 2012.

[139] A. Manduca, T. E. Oliphant, M. A. Dresner, J. L. Mahowald, S. A. Kruse, E. Amromin, J. P. Felmlee, J. F. Greenleaf and R. L. Ehman, "Magnetic resonance elastography: Non-invasive mapping of tissue elasticity," *Med. Image Anal.*, vol. 5, pp. 237-254, 12, 2001.

[140] A. J. Romano, J. A. Bucaro, R. Ehnan and J. J. Shirron, "Evaluation of a material parameter extraction algorithm using MRI-based displacement measurements," *Ultrasonics, Ferroelectrics and Frequency Control, IEEE Transactions On*, vol. 47, pp. 1575-1581, 2000.

[141] F. J. Herrmann, D. Wang, G. Hennenfent and P. P. Moghaddam, "Curvelet-based seismic data processing: a multiscale and nonlinear approach," *Geophysics*, vol. 73, pp. A1-A5, 2008.

[142] F. J. Herrmann, "Sub-nyquist sampling and sparsity: How to get more information from fewer samples," in *2009 SEG Annual Meeting*, 2009, .

[143] M. Rao, Q. Chen, H. Shi, T. Varghese, E. L. Madsen, J. A. Zagzebski and T. A. Wilson, "Normal and shear strain estimation using beam steering on linear-array transducers," *Ultrasound in Medicine & Biology,* vol. 33, pp. 57-66, 2007.

[144] M. Rao, Q. Chen, H. Shi and T. Varghese, "Spatial-angular compounding for elastography using beam steering on linear array transducers," *Med. Phys.,* vol. 33, pp. 618-626, 03/00, 2006.

[145] U. Techavipoo, Q. Chen, T. Varghese and J. A. Zagzebski, "Estimation of displacement vectors and strain tensors in elastography using angular insonifications," *Medical Imaging, IEEE Transactions On,* vol. 23, pp. 1479-1489, 2004.

[146] T. Adebar, S. Salcudean, S. Mahdavi, M. Moradi, C. Nguan and L. Goldenberg, "A robotic system for intra-operative trans-rectal ultrasound and ultrasound elastography in radical prostatectomy," in *Information Processing in Computer-Assisted Interventions*Anonymous Berlin Heidelberg: Springer, 2011, pp. 79-89.

[147] A. Baghani, A. Brant, S. Salcudean and R. Rohling, "A high-frame-rate ultrasound system for the study of tissue motions," *Ultrasonics, Ferroelectrics and Frequency Control, IEEE Transactions On,* vol. 57, pp. 1535-1547, 2010.

[148] H. Eskandari, O. Goksel, S. E. Salcudean and R. Rohling, "Bandpass sampling of high-frequency tissue motion," *Ultrasonics, Ferroelectrics and Frequency Control, IEEE Transactions On,* vol. 58, pp. 1332-1343, 2011.

[149] S. Salcudean, R. Sahebjavaher, O. Goksel, A. Baghani, S. Mahdavi, G. Nir, R. Sinkus and M. Moradi, "Biomechanical modeling of the prostate for procedure guidance and simulation," in *Soft Tissue Biomechanical Modeling for Computer Assisted Surgery*Anonymous Springer, 2012, pp. 169-198.

[150] M. Honarvar, "Dynamic Elastography with Finite Element-based Inversion," 2015.

[151] S. Srinivasan, T. Krouskop and J. Ophir, "Comparing elastographic strain images with modulus images obtained using nanoindentation: preliminary results using phantoms and tissue samples," *Ultrasound Med. Biol.,* vol. 30, pp. 329-343, 2004.

[152] W. Hayes, L. Keer, G. Herrmann and L. Mockros, "A mathematical analysis for indentation tests of articular cartilage," *J. Biomech.,* vol. 5, pp. 541-551, 1972.

[153] R. S. Sahebjavaher, "Magnetic resonance elastography of prostate cancer," 2013.

Appendix A – Forward problem of elasticity using finite element method (FEM)

Knowing the distribution of the mechanical properties of the medium and boundary conditions, we can solve equation (A-1) for displacements. This is called the forward problem of elasticity. In order to solve the partial differential equation (A-1) numerically, first we need to discretize the problem. The finite element method is one of the methods used for this purpose.

We start with the boundary value problem of linear elasticity as follows:

$$\left[\mu\left(u_{i,j}+u_{j,i}\right)+\lambda(u_{k,k})\delta_{ij}\right]_{,j}=-\rho\omega^2 u_i \qquad in\ \Omega \tag{A-1}$$

$$u_i=\hat{u}_i \qquad on\ \Gamma_1 \tag{A-2}$$

$$\left[\mu\left(u_{i,j}+u_{j,i}\right)+\lambda(u_{k,k})\delta_{ij}\right]n_j=\hat{T}_i \qquad on\ \Gamma_2 \tag{A-3}$$

where Ω is the region of interest with the boundary of $\Gamma=\Gamma_1\cup\Gamma_2$ and the displacement field $u(x)$ is defined as a function of position $x\in\Omega$. n_i is the unit normal vector on Γ . Vector $\hat{T}_i$ is the traction vector on a part of boundary denoted by Γ_2 and $\hat{u}_i$ is the prescribed displacement vector on a part of boundary denoted by Γ_1.

The first step is to convert this boundary value problem into its equivalent weak formulation. If $u(x)$ a solution of this boundary value problem, then for any smooth function w that is zero on Γ_1 the following equation holds:

$$\int_\Omega \left[\mu\left(u_{i,j}+u_{j,i}\right)+\lambda(u_{k,k})\delta_{ij}\right]_{,j} w\ \mathrm{d}\Omega=\int_\Omega -\rho\omega^2 u_i\, w\ \mathrm{d}\Omega \tag{A-4}$$

Conversely, if u satisfies (A-4) for every smooth function w then one may show that this solution will solve (A-1).

By using integration by parts on the left hand side of (A-4) we obtain:

$$-\int_{\Omega} \left[\mu\left(u_{i,j}+u_{j,i}\right)+\lambda(u_{k,k})\delta_{ij}\right] w_{,j}\,\mathrm{d}\Omega+\int_{\Gamma} \left[\mu\left(u_{i,j}+u_{j,i}\right)+\lambda(u_{k,k})\delta_{ij}\right] n_j w\,\mathrm{d}\Gamma = \int_{\Omega} -\rho\omega^2 u_i\, w\mathrm{d}\Omega \tag{A-5}$$

By substituting the traction boundary condition (A-3) into (A-5) we will have:

$$\int_{\Omega} \left[\mu\left(u_{i,j}+u_{j,i}\right)+\lambda(u_{k,k})\delta_{ij}\right] w_{,j}\,\mathrm{d}\Omega=\int_{\Omega} \rho\omega^2 u_i\, w\,\mathrm{d}\Omega+\int_{\Gamma} \hat{T}_i w\,\mathrm{d}\Gamma \tag{A-6}$$

The next step is to replace the infinite dimensional problem with a finite dimensional version. Based on the Galerkin method we have:

$$\int_{\Omega} \left[\mu^h\left(u^h_{i,j}+u^h_{j,i}\right)+\lambda^h\left(u^h_{k,k}\right)\delta_{ij}\right] w^h_{,j}\,\mathrm{d}\Omega=\int_{\Omega} \rho\omega^2 u^h_i\, w^h\mathrm{d}\Omega+\int_{\Gamma} \hat{T}_i w^h\,\mathrm{d}\Gamma \tag{A-7}$$

where μ^h, u^h_i and w^h are finite dimensional approximations of the actual values. A finite number of nodes are considered on the region for displacements and elasticity and these values are approximated over the region using shape functions. The shape functions have value of one at their corresponding node and value of zero at all other nodes. Then the actual parameters are approximated using the following equations:

$$u_i(x) \approx u^h_i(x) = \bar{u}_{i\alpha}\varphi_\alpha(x) \qquad \alpha = 1, N_u \tag{A-8}$$

$$\mu(x) \approx \mu^h(x) = \bar{\mu}_\beta\psi_\beta(x) \qquad \beta = 1, N_\mu \tag{A-9}$$

$$u_{i,j}(x) \approx u^h_{i,j}(x) = \bar{u}_{i\alpha}\varphi_{\alpha,j}(x) \qquad \alpha = 1, N_u \tag{A-10}$$

where φ_α and ψ_β are shape functions for displacement and elasticity respectively and $\bar{u}_{i\alpha}$ and $\bar{\mu}_\beta$ are nodal values of displacement and elasticity respectively.

In Galerkin's method, the test functions w^h are also approximated using the displacement shape functions as:

$$w \approx w^h(x) = \bar{w}_\alpha \varphi_\alpha(x) \qquad \alpha = 1, N_u \tag{A-11}$$

Since equation (A-7) must be satisfied for any arbitrary $\bar{w}_\alpha$, then $\bar{w}_\alpha$ can be factored out and eliminated, resulting in:

$$\begin{aligned} &\int_\Omega \left[\bar{\mu}_\beta \psi_\beta\left(\bar{u}_{i\gamma}\varphi_{\gamma,j} + \bar{u}_{j\gamma}\varphi_{\gamma,i}\right) + \bar{\lambda}_\beta \psi_\beta\left(\bar{u}_{k\gamma}\varphi_{\gamma,k}\right)\delta_{ij}\right] \varphi_{\alpha,j}\, \mathrm{d}\Omega \\ &\qquad = \int_\Omega \rho\omega^2 \bar{u}_{i\gamma}\varphi_\gamma\, \varphi_\alpha \mathrm{d}\Omega + \int_\Gamma \hat{T}_i \varphi_\alpha\, \mathrm{d}\Gamma \end{aligned} \tag{A-12}$$

Standard pure displacement FEM:

In standard pure displacement formulation of FEM, the only unknown variable is displacement. Knowing the Poisson's ratio, μ and λ can be written with respect to the Young's modulus (E) and the Poisson's ratio (ν) as follows:

$$\begin{aligned} &\int_\Omega \left[\frac{1}{2(1+\nu)} \bar{E}_\beta \psi_\beta\left(\bar{u}_{i\gamma}\varphi_{\gamma,j} + \bar{u}_{j\gamma}\varphi_{\gamma,i}\right) + \frac{\nu}{(1+\nu)(1-2\nu)} \bar{E}_\beta \psi_\beta\left(\bar{u}_{k\gamma}\varphi_{\gamma,k}\right)\delta_{ij}\right] \varphi_{\alpha,j}\, \mathrm{d}\Omega \\ &\qquad = \int_\Omega \rho\omega^2 \bar{u}_{i\gamma}\varphi_\gamma\, \varphi_\alpha \mathrm{d}\Omega + \int_\Gamma \hat{T}_i \varphi_\alpha\, \mathrm{d}\Gamma \end{aligned} \tag{A-13}$$

Then this equation can be written in matrix form as follows:

$$\int_\Omega (\boldsymbol{\Psi}^T \bar{\boldsymbol{E}})(\mathbf{B}^T \mathbf{D} \mathbf{B})\bar{\boldsymbol{u}}\, \mathrm{d}\Omega - \int_\Omega \rho\omega^2 \boldsymbol{\Phi}^T \boldsymbol{\Phi} \bar{\boldsymbol{u}}\, \mathrm{d}\Omega = \int_\Gamma \boldsymbol{\Phi}^T \bar{\boldsymbol{T}}\, \mathrm{d}\Gamma \tag{A-14}$$

where

$$\bar{\boldsymbol{u}} = \left[\bar{u}_{11}, \bar{u}_{21}, \bar{u}_{31}, \dots, \bar{u}_{1n_u}, \bar{u}_{2n_u}, \bar{u}_{3n_u}\right]^T \tag{A-15}$$

$$\bar{\boldsymbol{E}} = \left[\bar{E}_1, \bar{E}_2, \dots, \bar{E}_{n_E}\right]^T \tag{A-16}$$

$$\boldsymbol{\Psi} = \left[\psi_1, \psi_2, \dots, \psi_{n_E}\right]^T \tag{A-17}$$

$$\boldsymbol{\Phi} = \begin{bmatrix} \varphi_1 & 0 & 0 & \varphi_2 & 0 & 0 & \dots & \varphi_{n_u} & 0 & 0 \\ 0 & \varphi_1 & 0 & 0 & \varphi_2 & 0 & \dots & 0 & \varphi_{n_u} & 0 \\ 0 & 0 & \varphi_1 & 0 & 0 & \varphi_2 & \dots & 0 & 0 & \varphi_{n_u} \end{bmatrix} \tag{A-18}$$

$$\mathbf{B} = \begin{bmatrix} \partial x & 0 & 0 \\ 0 & \partial y & 0 \\ 0 & 0 & \partial z \\ \partial y & \partial x & 0 \\ 0 & \partial z & \partial y \\ \partial z & 0 & \partial x \end{bmatrix} \boldsymbol{\Phi} \tag{A-19}$$

$$\mathbf{D} = \frac{1}{(1+\nu)(1-2\nu)} \begin{bmatrix} 1-\nu & \nu & \nu & 0 & 0 & 0 \\ \nu & 1-\nu & \nu & 0 & 0 & 0 \\ \nu & \nu & 1-\nu & 0 & 0 & 0 \\ 0 & 0 & 0 & (1-2\nu)/2 & 0 & 0 \\ 0 & 0 & 0 & 0 & (1-2\nu)/2 & 0 \\ 0 & 0 & 0 & 0 & 0 & (1-2\nu)/2 \end{bmatrix} \tag{A-20}$$

In the finite element methods the region is divided into a number of sub-regions called elements, and local shape functions φ_n are defined for each element to approximate the parameters over the area of the element based on the values of the parameters on the nodes of the element. For example Figure 3-5 shows a rectangular 4 nodes element with linear shape functions N_i which has value of one at node *i* and zero at other nodes.

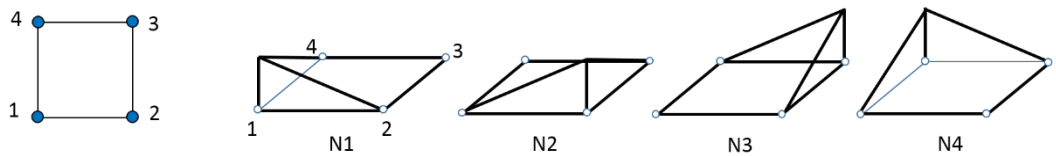

Figure A-1. Sample linear shape functions for a 4-node rectangular element

The integral (A-14) can be taken over each element separately using numerical or analytical methods, and the element matrices $\mathbf{K}_e$, $\mathbf{M}_e$ and $\boldsymbol{f}_e$ are calculated as follows:

$$\mathbf{K}_e = \int_{\Omega_e} (\boldsymbol{\Psi}^T \bar{\mathbf{E}})(\mathbf{B}^T \mathbf{D} \mathbf{B})\, \mathrm{d}\Omega \tag{A-21}$$

$$\mathbf{M}_e = \int_{\Omega_e} \rho \boldsymbol{\Phi}^T \boldsymbol{\Phi}\, \mathrm{d}\Omega \tag{A-22}$$

$$\boldsymbol{f}_e = \int_{\Gamma_e} \boldsymbol{\Phi}^T \overline{\boldsymbol{T}}\, \mathrm{d}\Gamma \tag{A-23}$$

These element matrices are then assembled into the global matrices $\mathbf{K}$, $\mathbf{M}$ and $\boldsymbol{f}$ based on the global node number of each element nodes. These matrices are used in the following equation to find the displacements.

$$(\mathbf{K} - \omega^2 \mathbf{M})\bar{\mathbf{u}} = \boldsymbol{f} \tag{A-24}$$

Mixed displacement-pressure FEM:

Although the pure displacement formulations of finite elements are computationally efficient, their accuracy is dependent on Poisson's ratio or the bulk modulus. In such formulations, the volumetric strain is determined from the displacement derivatives, and is not as accurate as the specific displacements. In almost incompressible conditions, when Poisson's ratio approaches 0.5, the bulk modulus approaches infinity ($\lambda \to \infty$) such that small errors in the predicted volumetric strain appear as large errors in the hydrostatic pressure and also therefore in the

stresses. This error will also influence the predicted displacement because the stresses will balance the external loads. The possible result may be much smaller displacements than required for a particular mesh, or even it may result in no convergence at all. This effect is known as “locking”.

Various methods have been suggested to overcome the locking problem. One solution is to use higher order elements. An alternative modification to the standard displacement formulation which has been shown to reduce the effect of the incompressibility constraint is to use a formulation in which the primary variables are not all of the same type. Such formulations are generally known as ‘mixed methods’. E.g., in a mixed u-p FEM method, a new variable called pressure is introduced as:

$$p = \lambda\left(u_{k,k}\right). \tag{A-25}$$

Substituting (A-25) into (A-7) results in:

$$\int_{\Omega} \left[\mu^h\left(u_{i,j}^h + u_{j,i}^h\right) + p^h \delta_{ij}\right] w_{,j}^h \, \mathrm{d}\Omega = \int_{\Omega} \rho\omega^2 u_i^h \, w^h \mathrm{d}\Omega + \int_{\Gamma} \hat{T}_i w^h \, \mathrm{d}\Gamma \tag{A-26}$$

where

$$p \approx p^h(x) = \bar{p}_\alpha \chi_\alpha(x) \qquad \alpha = 1, N_p \tag{A-27}$$

χ_α are the shape functions for the pressure parameters.

Equation (A-25) can also be written in a weak form and discretized as follows:

$$\int_{\Omega} p^h \, w^h \mathrm{d}\Omega = \int_{\Omega} \lambda^h\left(u_{k,k}^h\right) w^h \, \mathrm{d}\Omega \tag{A-28}$$

By replacing the shape functions in (A-26) and (A-28), we will have:

$$\int_{\Omega} \left[\bar{\mu}_\beta \psi_\beta\left(\bar{u}_{i\gamma}\varphi_{\gamma,j} + \bar{u}_{j\gamma}\varphi_{\gamma,i}\right) + \bar{p}_\gamma \chi_\gamma \delta_{ij}\right] \varphi_{\alpha,j} \, \mathrm{d}\Omega - \int_{\Omega} \rho\omega^2 \bar{u}_{i\gamma}\varphi_\gamma \, \varphi_\alpha \mathrm{d}\Omega = \int_{\Gamma} \hat{T}_i \varphi_\alpha \, \mathrm{d}\Gamma \tag{A-29}$$

$$\int_{\Omega} \bar{p}_{\gamma}\chi_{\gamma}\ \varphi_{\alpha} d\Omega = \int_{\Omega} \bar{\lambda}_{\beta}\psi_{\beta}\left(\bar{u}_{k\gamma}\varphi_{\gamma,k}\right)\varphi_{\alpha}\ d\Omega \tag{A-30}$$

These equations can be written in matrix form similar to standard FEM formulation with some changes as follows:

$$\int_{\Omega} (\boldsymbol{\Psi}^{T}\overline{\boldsymbol{E}})(\mathbf{B}^{T}\mathbf{D}_{d}\mathbf{B})\overline{\boldsymbol{u}}\ \mathrm{d}\Omega - \int_{\Omega} \rho\omega^{2}\boldsymbol{\Phi}^{T}\boldsymbol{\Phi}\overline{\boldsymbol{u}}\ \mathrm{d}\Omega + \int_{\Omega} \mathbf{B}^{T}\boldsymbol{X}\overline{\boldsymbol{p}}\ \mathrm{d}\Omega = \int_{\Gamma} \boldsymbol{\Phi}^{T}\overline{\boldsymbol{T}}\ \mathrm{d}\Gamma \tag{A-31}$$

$$\int_{\Omega} (\boldsymbol{\Psi}^{T}\overline{\boldsymbol{E}})\left(\widehat{\boldsymbol{\Phi}}^{T}\boldsymbol{mB}\right)\overline{\boldsymbol{u}}\ d\Omega - \int_{\Omega} \widehat{\boldsymbol{\Phi}}^{T}\boldsymbol{X}\overline{\boldsymbol{p}}\ d\Omega = \mathbf{0} \tag{A-32}$$

where

$$\widehat{\boldsymbol{\Phi}} = \left[\varphi_{1}, \varphi_{2}, \dots, \varphi_{n_{u}}\right] \tag{A-33}$$

$$\boldsymbol{X} = \left[\chi_{\mathbf{1}}, \chi_{\mathbf{2}}, \dots, \chi_{\boldsymbol{n_p}}\right] \tag{A-34}$$

$$\mathbf{D}_{d} = \frac{1}{2(1+\nu)}\begin{bmatrix} 2 & & & & & \\ & 2 & & & & \\ & & 2 & & & \\ & & & 1 & & \\ & & & & 1 & \\ & & & & & 1 \end{bmatrix} \tag{A-35}$$

$$\boldsymbol{m} = [1\ 1\ 1\ 0\ 0\ 0] \tag{A-36}$$

Therefore, the element matrices $\widehat{\mathbf{K}}_{e}$, $\mathbf{M}_{e}$, $\mathbf{G}_{e}$, $\mathbf{H}_{e}$, $\mathbf{J}_{e}$ and $\boldsymbol{f}_{e}$ can be calculated as follows:

$$\widehat{\mathbf{K}}_{e} = \int_{\Omega_{\mathrm{e}}} (\boldsymbol{\Psi}^{T}\overline{\boldsymbol{E}})(\mathbf{B}^{T}\mathbf{D}_{d}\mathbf{B})\ \mathrm{d}\Omega \tag{A-37}$$

$$\mathbf{M}_{e} = \int_{\Omega_{\mathrm{e}}} \rho\boldsymbol{\Phi}^{T}\boldsymbol{\Phi}\ \mathrm{d}\Omega \tag{A-38}$$

$$\mathbf{G}_e = \int_{\Omega_e} \mathbf{B}^T \boldsymbol{X} \, \mathrm{d}\Omega \tag{A-39}$$

$$\mathbf{H}_e = \int_{\Omega_e} (\boldsymbol{\Psi}^T \overline{\boldsymbol{E}})\left(\widehat{\boldsymbol{\Phi}}^T \boldsymbol{m}\mathbf{B}\right) d\Omega \tag{A-40}$$

$$\mathbf{J}_e = \int_{\Omega_e} \widehat{\boldsymbol{\Phi}}^T \boldsymbol{X} \, d\Omega \tag{A-41}$$

$$\boldsymbol{f}_e = \int_{\Gamma_e} \boldsymbol{\Phi}^T \overline{\boldsymbol{T}} \, d\Gamma \tag{A-42}$$

Then these element matrices are assembled into the global matrices and used in the following system of equations to find both the displacement and pressure parameters:

$$\begin{bmatrix} \widehat{\mathbf{K}} - \omega^2 \mathbf{M} & \mathbf{G} \\ \mathbf{H} & -\mathbf{J} \end{bmatrix} \begin{bmatrix} \overline{\boldsymbol{u}} \\ \overline{\boldsymbol{p}} \end{bmatrix} = \begin{bmatrix} \boldsymbol{f} \\ 0 \end{bmatrix}. \tag{A-43}$$